UNIVERSIDADE DO PORTO
FACULDADE DE ENGENHARIA

Hydrodynamics of Stirred Tank Reactors

A Study with Laser Doppler Velocimetry and Computational Fluid Dynamics

Miroslav Paná̋ek

December 1998

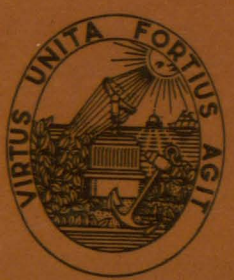

Hydrodynamics of Stirred Tank Reactors

A Study with Laser Doppler Velocimetry and Computational Fluid Dynamics

A Dissertation Presented to the
UNIVERSIDADE DO PORTO
for the Degree of Doctor in Chemical Engineering

by

Miroslav Panáček

December 1998

66(043) PAN Cat
UNIVERSIDADE DO PORTO
Faculdade de Engenharia
BIBLIOTECA
N.º 43759
CDU
Data ___/___/ 19___

Laboratório de Processos de Separação e Reacção
Departamento de Engenharia Química
Faculdade de Engenharia
Universidade do Porto
Porto, Portugal

Acknowledgements

The author wishes to express his thanks and appreciation to those whose contribution was fundamental in the completion of this work.

- Prof. José Carlos Lopes, his Research Advisor, for the suggestion of this research project and for his guidance, counsel and friendship.
- Prof. Madalena Maria Dias, LSRE - Department of Chemical Engineering, FEUP, for her review of the text of this work and many useful suggestions.
- Prof. Alírio Rodrigues, director of LSRE - Laboratory of Separation and Reaction Engineering, FEUP, where this work was carried out.
- Prof. Laginha Palma, for providing of his literature database on LDV technique.
- My colleagues at LSRE for their help, friendship and encouragement. Special thanks to André Teixeira and his family, Peter Spicka, Vera Mata, Isabel Nunes, António Martins, Ricardo Santos and Susana for support, help and living in Portugal.
- Dr. Lígia Ribeiro, Vera Mata and Eng. Tito Vieira who kindly helped in printing of this dissertation.
- To his family and friends for continuos support and encouragement.

Financial support for this work was provided by the Commission of the European Union under the JOULE program, contract JOU2-CT92-012 and by FCT/MCT, project PRAXIS/3/3.1/CEG/2565/95.

To

My Parents and Ingrid

Abstract

The hydrodynamics in the stirred tank agitated with the Rushton impeller was explored both experimentally and numerically. The mixing problem was limited to isothermal flow conditions and to the use of Newtonian fluids. The stirred tank with and without four equally spaced baffles, mounted on the tank wall, was operated under laminar and turbulent flow regimes.

Various regions of the stirred tank were investigated using the LDV — Laser Doppler Velocimetry — technique, and the data was obtained in the form of first order quantities, such as the velocity components, and also in the form of second order quantities such as the turbulent kinetic energy and shear Reynolds stresses. The results showed that the region of the highest magnitudes of velocity, kinetic energy, and shear Reynolds stress is the horizontal plane passing through the impeller centre. Therefore, the large-scale structure of the shear Reynolds stress component was studied in that region for various values of the Reynolds number. The results showed that the flow fields, induced by the Rushton impeller, are scalable with the impeller rotational speed but can not be considered as isotropic mainly for higher values of Reynolds number.

The flow field of a stirred tank was simulated on 2D and 3D computational domains using Computational Fluid Dynamics — CFD — package FIDAP 7.6. The effects of imposed boundary conditions on the predictions of hydrodynamics in the stirred tank were analysed. The results of numerical simulations, based on both steady-state and dynamic computational approaches, were compared with the experimental data and showed good agreement.

The non-reactive tracer study in the stirred tank was accomplished using CFD numerical simulations. The capability of CFD packages to predict the flow hydrodynamics and the situations where the mixing process is coupled with chemical reactions were discussed.

Resumo

Neste trabalho fez-se o estudo da hidrodinâmica num tanque agitado usando uma turbina de Rushton, tanto ao nível experimental como numérico. O problema de mistura foi resolvido em condições isotérmicas e usando fluidos Newtonianos. Estudaram-se os casos em que o tanque agitado opera nos regimes de escoamento laminar e turbulento, na ausência ou na presença de quatro deflectores igualmente espaçados, colocados na parede do tanque.

Investigaram-se várias regiões do tanque agitado usando a técnica LDV – Anemometria de Laser de efeito Doppler — sendo os dados obtidos em termos dos momentos de primeira ordem do campo de velocidades, e ainda em termos dos momentos de segunda ordem, tal como a energia cinética de turbulência e tensões de corte de Reynolds. Os resultados mostraram que a região como os maiores valores de velocidade, energia cinética e tensão de corte de Reynolds, corresponde ao plano horizontal que passa através do centro da turbina. Assim, a estrutura de larga escala da componente da tensão de corte de Reynolds foi estudada nessa região, para vários valores de número de Reynolds.

O escoamento num tanque agitado foi simulado usando pela aplicação comercial FIDAP de CFD – Dinâmica de Fluidos Computacional. Foram analisados os efeitos das condições fronteiras na hidrodinâmica do tanque agitado. Os resultados de simulações numéricas foram comparados com os dados experimentais, tanto em regime estacionário como em regime dinâmico e verificou-se uma boa concordância entre ambos.

O estudo do escoamento de um traçador não-reactivo no tanque agitado foi acompanhado com simulações numéricas de CFD. Foram discutidas as capacidades dos programas de CFD na previsão da hidrodinâmica de escoamento e ainda no caso de processos de mistura com reacção química.

Abstrakt

Rotačné miešadlá sú v chemickom a potravinárskom priemysle používané na intenzifikáciu prenosu hmoty a tepla. Medzi najpoužívanejšie typy patria lopatkové miešadlá, pričom Rushtonovou turbínou sa označuje typ s rovnými lopatkami.
Predmetom tejto dizertačnej práce bolo štúdium hydrodynamiky v miešacom tanku, vybavenom práve s Rushtonovou turbínou, pretože znalosť prúdových charakteristík v premiešavanom systéme slúži k optimalizácii zariadení s mechanickými miešadlami.

Miešanie Newtonovských tekutín bolo vo všetkých prípadoch prevedené pri konštantnej teplote a problematika miešania bola študovaná v dvoch typoch miešacích nádob. V jednom prípade boli na vnútornej strane valcovej nádoby uchytené štyri radiálne narážky siahajúce od vrchu po dno nádoby. Miešanie pri nízkych otáčkach miešadla je opisované ako laminárne a naopak pri vyšších otáčkach ako turbulentné.

Experimentálna časť bola zameraná na tie oblasti miešacích nádob, kde je prúdenie najintenzívnejšie a bola prevedená použitím laserového anemometra a techniky označovanej ako LDV, ktorá je založená na Dopplerovom efekte. Boli namerané a vyhodnotené profily jednotlivých zložiek rýchlosti, tak ako aj veličiny súvisiace s turbulenciou toku vo forme lokálnych kinetických energií, rýchlostí disipácie tejto energie a šmykových Reynoldsových napätí. Z výsledkov vyplýva, že pri vyšších rotačných rýchlostiach miešadla sa turbulencia v nádobe nedá považovať za izotropnú.

Rýchlostné polia a prúdenie tekutiny v miešacích tankoch boli modelované použitím komerčného softwarového programu, FIDAP 7.6, v dvoj ale aj trojrozmernom priestore. Boli študované rôzne modely odlišujúce sa špecifikácou hraničných podmienok, a samotný proces miešania bol simulovaný ako ustálený alebo dynamický. Výsledky týchto numerických simulacií sú vo veľmi dobrej zhode s tými čo boli získané experimentálne. Naviac bola prevedená dynamická simulácia stopovacej zložky po jej vstreku do miešacieho tanku. Na záver sú uvedené perspektívy použitia CFD programov pre simulácie prúdení tekutín spojeného s chemickými reakciami.

Table of Contents

Page

1. INTRODUCTION 1
   1.1 Motivation and Relevance 1
   1.2 Mixing Scenario in the Stirred Tank Reactor 2
   1.3 Thesis Objectives and Dissertation Layout 6
2. STIRRED TANK REACTOR: STATE OF THE ART 8
   2.1 Introduction 8
   2.2 Review of Experimental Research 11
      2.2.1 Single-impeller ST studies by different objectives 12
      2.2.2 Multiple-impeller ST studies 17
   2.3 Review of Numerical Modelling 18
      2.3.1 Steady state modelling of ST 21
      2.3.2 Dynamic simulation of stirred tank 25
   2.4 Chemical Reactions in Mixing Reactor 26
      2.4.1 Experimental methods 27
      2.4.2 Numerical methods 29
3. HYDRODYNAMIC CHARACTERISATION USING LDV 35
   3.1 Introduction 35
   3.2 Experimental Set-up, LDV System and Measurements 36
      3.2.1 Experimental Set-up 36
      3.2.2 LDV System Description 38
      3.2.3 LDV Measurements and Derived Quantities 44
   3.3 LDV Data Analysis 50
      3.3.1 Flow in the Impeller Discharge Region 51
      3.3.2 Flow in the Impeller Region 60
      3.3.3 Flow at the Impeller Centre Plane 69
      3.3.4 Flow in the Baffle Region 84
   3.4 Final Conclusions from Experimental Study 86
4. LAMINAR MIXING — CFD STUDY 89
   4.1 Introduction 89
   4.2 Two Dimensional Stirred Tank 91
      4.2.1 Model description and objectives 91
      4.2.2 Calculated Quantities 94
      4.2.3 Results 96
      4.2.4 Conclusions 105
   4.3 Three Dimensional Study of Stirred Tank 105
      4.3.1 Model description and objectives 105
      4.3.2 Calculated Quantities 107
      4.3.3 Results 107
      4.3.4 Conclusions 116
   4.4 Summary of Conclusions 117
5. TURBULENT MIXING – 3D CFD STUDY 118
   5.1 Introduction 118
   5.2 Steady-State Predictions 120
      5.2.1 Objectives of this work 120
      5.2.2 Computational model description and moving ring approach 121
      5.2.3 Boundary conditions models for the moving ring 130
      5.2.4 Results 137
      5.2.5 Conclusions from steady-state simulations of ST 162

5.3 Dynamic Model Predictions 164
5.3.1 Objective of this work 164
5.3.2 Dynamic model description 164
5.3.3 List of entities and boundary conditions in the dynamic models 165
5.3.4 Results 169
5.3.5 Conclusions from dynamic predictions of ST 184

6. MIXING AND CHEMICAL REACTIONS 186

6.1 Introduction 186
6.2 Coupling of mixing and chemical reaction 187
6.3 Computational methods for laminar reactive flows 189
6.4 Computational methods for turbulent reactive flows 192
6.4.1 Moment methods 197
6.4.2 Micro-mixing models 200
6.5 Application of CFD package for non-reactive mixing in STR 203
6.5.1 Model description and objectives 203
6.5.2 Calculated quantities 207
6.5.3 Results from non-reactive tracer simulations 208
6.6 Conclusions 214

7. CONCLUSIONS AND SUGGESTIONS FOR FUTURE WORK 215

7.1 Conclusions 215
7.2 Suggestions for Future Work 217

8. LITERATURE REFERENCES 220

A. CO-ORDINATE SYSTEM TRANSFORMATIONS 229

A.1 Transformation of Cartesian co-ordinate system 229
A.2 Transformation to cylindrical co-ordinate system 231

B. ELIMINATION OF THE PERIODIC TURBULENCE 234

C. THE CLOSURE PROBLEM IN TURBULENT FLOW AND SPEZIALE'S NON-LINEAR MODEL 239

C.1 Description of the closure problem for turbulent flow 239
C.2 The Reynolds stress equation in non-linear Speziale's model of turbulent flow. 243

List of Figures

Page

Figure 1.1 Possible trajectory scenarios in: (a) the STR and (b) the baffle region 4
Figure 2.1 Impellers used in laminar flow regime: (a) double-flight helical-ribbon impeller; (b) screw impeller; (c) single-flight helical-ribbon; (d) anchor impeller (from Bakker and Gates, 1995). 10
Figure 2.2 Impellers used in turbulent flow regime: (a) pitched blade turbine; (b) high-efficiency impeller;(c) Rushton turbine; (d) simple straight-blade turbine (from Bakker and Gates, 1995) 10
Figure 2.3 Scheme of ST configurations used in industry (red colour highlights the options in this work). 11
Figure 2.4 Illustration of the trailing vortex system formed behind the blade (from Van't Riet and Smith, 1975). 16
Figure 3.1 Schematic representation of the stirred tank used in the experiments. 37
Figure 3.2 Schematic representation of the Rushton impeller used in the experiments. 37
Figure 3.3 Frontal view of the experimental set-up. 38
Figure 3.4 Partial view of the LDV optical system. 42
Figure 3.5 View of the LDV data acquisition system. 42
Figure 3.6 Schematic representation of the LDV system. 43
Figure 3.7 Schematic representation of the mixing tank showing the selected regions for measurements 45
Figure 3.8 Vertical grid for LDV measurements. 52
Figure 3.9 Horizontal grid for LDV measurements. 52
Figure 3.10 Radial and tangential velocity profiles for three values of θ: a) $\theta = \pi/12$; b) $\theta = \pi/4$; c) $\theta = 5\pi/12$ at Re=20000 54
Figure 3.11 Decay of the radial velocity at the impeller centre line for: Re=20000 (present work); Re=26000 (Van der Molen and Van Mannen, 1978); and Re=40000 (Lee and Yianneskis, 1998). 55
Figure 3.12 Dependence of A on the Reynolds number. 56
Figure 3.13 Radial and tangential velocities fluctuations profiles for Re=20000 57
Figure 3.14 Radial and tangential turbulence intensities for Re=20000. 57
Figure 3.15 Radial velocity fluctuation radial profile for: Re=20000 (present work); Re=40000 (correlation from Lee and Yianneskis, 1998); averaged Re=8000 to Re=54000 (correlation from Dyster et al., 1993) 58
Figure 3.16 Flow number radial profile at the impeller centre line position for Re=20000 (present work), and obtained from data averaging on the ranges: Re=8000-22000 (Gunkel and Weber, 1975); Re=14000-43000 (Wu and Patterson, 1989); and Re=29000-46000 (Stoots and Calabrese, 1989). 59
Figure 3.17 The two measurement planes in the impeller region. 60
Figure 3.18 Vertical grid in measurement plane. 61
Figure 3.19 Radial velocity inside of the impeller region for $Re = 5000$ and $N_{pts} = 5000$: a) maps for $\theta = \pi/4$; b) maps for $\theta = 3\pi/8$; c) profiles for various radii at $\theta = \pi/4$ 63
Figure 3.20 Tangential velocity inside of the impeller region for $Re = 5000$ and $N_{pts} = 5000$: a) maps for $\theta = \pi/4$; b) maps for $\theta = 3\pi/8$; c) profiles for various radii at $\theta = \pi/4$ 64
Figure 3.21 Axial velocity gradients: a) contour maps at $\theta = \pi/4$; b) contour maps at $\theta = 3\pi/8$ 65
Figure 3.22 Vector plots of the radial and the axial velocity components. 66
Figure 3.23 Experimental results for $Re = 5000$ and $N_{pts} = 10000$: a) radial velocity; b) axial velocity gradients; c) vector plot of the radial and axial components 67

Figure 3.24 Experimental results for $Re = 10000$ and $N_{pts} = 10000$: a) radial velocity; b) axial velocity gradients; c) vector plot of the radial and axial components....68
Figure 3.25 Measurement grid for the impeller centre plane....70
Figure 3.26 Vectors plots from the radial and tangential velocity components over the impeller centre plane for the different Reynolds numbers....73
Figure 3.27 Normalised kinetic energy k/V_{tip}^2 contour plots for the different Reynolds numbers....74
Figure 3.28 τ_{xy}^t Reynolds stress maps for the different Reynolds numbers....76
Figure 3.29 Time series of two measured components of the velocity filed....77
Figure 3.30 Tangential velocity spectral density functions: a) Re=90, b) Re=450....78
Figure 3.31 Radial and tangential velocity angular profiles for different Re and at three different radii: a) r/R=1.1; b) r/R=1.6; c) r/R=2.1....79
Figure 3.32 τ_{xy}^t Reynolds stress angular profiles for different Re and at three different radii: a) r/R=1.1; b) r/R=1.6; c) r/R=2.1....80
Figure 3.33 Filtered τ_{xy}^t Reynolds stress angular profiles at r/R=1for different Re....81
Figure 3.34 Normalised radial-tangential projections of velocity vector along vertical co-ordinate for $Re = 20000$....82
Figure 3.35 Kinetic energy maps and contours from the radial and tangential fluctuation velocities along axial co-ordinate for $Re = 20000$....83
Figure 3.36 τ_{xy}^t Reynolds stress maps and contours along axial co-ordinate for $Re = 20000$....83
Figure 3.37 Measurement grid for the baffle region....85
Figure 3.38 Results from measurement in the baffle region at Re=5000: a) vector plot; from the radial and tangential velocity components; b) maps of turbulent kinetic energy; c) τ_{xy}^t Reynolds stress maps....85
Figure 4.1 Computational domains for the two-dimensional predictions: (a) unbaffled and (b) baffled stirred tank....91
Figure 4.2 Stream function maps and normalised streamline contour plots for Re=10 at four different positions of the impeller blade set: (a) 0°; (b) 20°; (c) 40°; (d) 60°....98
Figure 4.3 Normalised total viscous stress maps for Re=10 at four different positions of the impeller blade set: (a) 0°; (b) 20°; (c) 40°; (d) 60°....99
Figure 4.4 Normalised streamlines (a, b) and normalised total viscous stress (c, d) maps for Re=1 in baffled (a, c) and unbaffled (b, d) stirred tanks....100
Figure 4.5 Normalised streamlines (a, b) and normalised total viscous stress (c, d) maps for Re=10 in baffled (a, c) and unbaffled (b, d) stirred tanks....101
Figure 4.6 Normalised streamlines (a, b) and normalised total viscous stress (c, d) maps for Re=100 in baffled (a, c) and unbaffled (b, d) stirred tanks....102
Figure 4.7 Normalised streamlines (a, b) and normalised total viscous stress (c, d) maps for Re=1000 in baffled (a, c) and unbaffled (b, d) stirred tanks....103
Figure 4.8 The Power number approximation using 2D simulation....104
Figure 4.9 Normalised speed contour maps overlaid with the radial-axial projection of the velocity vector at two vertical planes $\theta=3\pi/8$ (a, b, c) and $\theta=\pi/4$ (d, e, f), for the three models at Re=10....109
Figure 4.10 Normalised speed maps overlaid with the radial-tangential projection of the velocity vector at different axial co-ordinate values for Re=10 in baffled (a-f) and unbaffled tanks (g-l)....110
Figure 4.11 The baffled and unbaffled ST flow rates ratio....111
Figure 4.12 Normalised total viscous stress maps and contour plots at two vertical planes $\theta=3\pi/8$ (a, b, c) and $\theta=\pi/4$ (d, e , f) and for three models at Re=10....112
Figure 4.13 Normalised total viscous stress maps and contour plots at different axial co-ordinate values for Re=10 in baffled (a-f) and unbaffled tank (g-l)....113

Figure 4.14 Normalised speed maps overlaid with the radial-tangential projection of the velocity vector at the impeller centre plane from the dynamic simulation at Re=10. 114
Figure 4.15 Normalised total viscous stress maps and contour plots at the impeller centre plane from the dynamic simulation at Re=10 115
Figure 4.16 Calculated Power number compared with experimental data 116
Figure 5.1 Schematic representation of the ST geometry and of the mesh of computational domain. 122
Figure 5.2 Moving ring approach and entities specified in the steady-state simulations: SH-shaft, DI-impeller disk, IN-inflow surface, UPS and LOS-upper and lower surfaces, LES and RIS-left and right surfaces, and OUT-outflow surface 122
Figure 5.3 The measured angularity parameter distribution from data obtained by Wu and Patterson (1989) at Re=30000; Mavros et al. (1996) at Re=27000; and from the present LDV study for Re=5000 and Re=2000. 124
Figure 5.4 A schematic representation on how to avoid inconsistency of the boundary conditions at the tank bottom, BT: (a) an ideal solution and (b) a small gap creation 126
Figure 5.5 2D illustration of the velocity boundary conditions specified for: (a) model 1; (b) model 2; (c) model 3; (d) model 4; (e) model 5 and (f) model 6. 131
Figure 5.6 2D illustration of the boundary conditions specified in the TA1turbulence approximation and showing profiles of: (a) turbulent kinetic energy; (b) macro-scale length and (c) the rate of the energy dissipation. 135
Figure 5.7 Comparison of the estimate of the random turbulent kinetic energy used in TA2 approach and data obtained at Re=5000 (from LDV study in Chapter 3) and those found by Wu-Patterson (1989). 136
Figure 5.8 The 2D illustration of the boundary conditions specified in the TA2turbulence approximation and showing profiles of: (a) turbulent kinetic energy; (b) macro-scale length; and (c) rate of the energy dissipation 137
Figure 5.9 Normalised speed maps overlaid with the radial-axial projection of the velocity vector at the vertical plane behind a baffle from steady-state simulations at Re=5000. 139
Figure 5.10 Normalised speed maps overlaid with the radial-axial projection of the velocity vector at the vertical plane passing through the baffle from steady-state simulations at Re=5000. 140
Figure 5.11 Normalised radial-tangential projections of the velocity vector at the impeller centre plane from steady-state simulations using various models at Re=5000. 141
Figure 5.12 Comparison of LDV data with the results of numerical simulations at the three radii and for Re=5000. 142
Figure 5.13 Flow number as a function of the radius from simulations using TA1 turbulent approximation. 145
Figure 5.14 Flow number as a function of the radius; calculated from simulations using the TA2 turbulent approximation 146
Figure 5.15 Normalised turbulent kinetic energy maps and contour plots at the vertical plane behind the baffle from steady-state simulations at Re=5000 and using the TA1 boundary conditions. 148
Figure 5.16 Normalised turbulent kinetic energy maps and contour plots at the vertical plane passing through the baffle from steady-state simulations at Re=5000 and using the TA1 boundary conditions 149
Figure 5.17 Normalised turbulent kinetic energy maps and contour plots at the vertical plane behind the baffle from steady-state simulations at Re=5000 and using the TA2 boundary conditions. 150
Figure 5.18 Normalised turbulent kinetic energy maps and contour plots at the vertical plane behind passing through the baffle from steady-state simulations at Re=5000 and using the TA2 boundary conditions 151

Figure 5.19 Normalised energy dissipation maps and contour plots at the vertical plane behind the baffle from steady-state simulations at Re=5000 and using the TA1 boundary conditions. 152
Figure 5.20 Normalised energy dissipation maps and contour plots at the vertical plane passing through the baffle from steady-state simulations at Re=5000 and using the TA1 boundary conditions 153
Figure 5.21 Normalised energy dissipation maps and contour plots at the vertical plane behind the baffle from steady-state simulations at Re=5000 and using the TA2 boundary conditions. 154
Figure 5.22 Normalised energy dissipation maps and contour plots at the vertical plane passing through the baffle from steady-state simulations at Re=5000 and using the TA2 boundary conditions 155
Figure 5.23 Power number calculated from simulations using steady-state models and (a) TA1 and (b) TA2 boundary conditions 158
Figure 5.24 Comparison of the shear Reynolds stress prediction with LDV data at various radii of the impeller centre plane (z=0) and for Re=5000. 161
Figure 5.25 The contour maps of the shear Reynolds stress at the impeller centre plane: (a) numerical prediction of model 1; (b) LDV data without elimination of pseudo-turbulence. 162
Figure 5.26 Sschematic representation of boundary conditions for dynamic simulations presented in terms of the velocity vectors (a, b) and the turbulent kinetic energy (c, d) for model 7(a, c) and model 8 (b, d). 167
Figure 5.27 Schematic representation s of REF and PER entities. 168
Figure 5.28 Histograms of the normalised speed obtained from simulation of the dynamic model 7at various ST positions (referred to the Cartesian co-ordinate system) 171
Figure 5.29 Normalised speed maps overlaid with the projections of the velocity vector from dynamic simulations using the models 7 and 8 at the tangential co-ordinates $\theta=\pi/4$ (a, d); $\theta=\pi/2$ (b, e); and at the impeller centre plane (c, f). 173
Figure 5.30 Comparison of the results at three radii of the impeller centre plane. 174
Figure 5.31 CFD results vs. LDV data in the baffle region: (a) model 7; (b) model 8; (c) model 1 adjusted; (d) LDV experiment 175
Figure 5.32 Flow number as a function of the radius - predictions versus experimental data. 177
Figure 5.33 Normalised turbulent kinetic energy maps and contour plots from dynamic simulations using the models 7 and 8 at the tangential co-ordinates $\theta=\pi/4$ (a, d); $\theta=\pi/2$ (b, e); and at the impeller centre plane (c, f). 179
Figure 5.34 Normalised dissipation energy maps and contour plots from dynamic simulations using the models 7 and 8 at the tangential co-ordinates $\theta=\pi/4$ (a, d); $\theta=\pi/2$ (b, e); and at the impeller centre plane (c, f). 180
Figure 5.35 The numerical predictions of the Power number and the reference value from Bates et al. (1963). 181
Figure 5.36 Comparison of dynamic models prediction of the shear Reynolds stress with LDV data at various radii of the impeller centre plane (z=0) and at Re=5000. 183
Figure 5.37 Contour maps of the shear Reynolds stress at the impeller centre plane: (a) model 7; (b) model 8; (c) model 1adjusted; (d) LDV data. 184
Figure 6.1 The energy spectrum of velocity fluctuations (from Tatterson, 1991). 193
Figure 6.2 The energy spectrum of concentration fluctuations(from Tatterson, 1991). 194
Figure 6.3 Schematic representation of engulfment mechanism of the species A and B (from Thoenes, 1994) 201
Figure 6.4 Graphical representation of two locations of the tracer injection where (1) stands for the first injection point — FIP, and (2) for SIP. 204
Figure 6.5 Frontal view on temporal images of expansion of the tracer cloud at Re=5000 using laminar flow equations 209
Figure 6.6 Frontal view on temporal images of expansion of the tracer cloud at Re=5000 using laminar flow equations 210
Figure 6.7 The top view on temporal images of expansion of the tracer cloud at Re=5000 using laminar flow equations 211

Figure 6.8 The top view on temporal images of expansion of the tracer cloud at Re=5000 using laminar flow equations....212
Figure 6.9 The segregation curves of non-reactive tracer mixing using the laminar and turbulent flow equations at Re=5000....213
Figure 6.10 The variation of mean concentration of tracer in the STR. 213
Figure A.1 Measurement frame of the reference used in LDV. 230
Figure A.2 Frame of reference for the presentation of results....230
Figure A.3 Cylindrical frame of reference. 232
Figure B.1 (a) Principle of the slotting technique; (b): The R(uv) correlation function....235
Figure B.2 Block diagram of LDV data filtering using LabView software. 237
Figure B.3. Front panel of LDV data filtering using LabView software 238

List of Tables

		Page
Table 3.1	LDV system parameters.	41
Table 3.2	95% confidence interval estimations for LDV statistics.	49
Table 3.3	Typical -relative errors of LDV statistics.	50
Table 3.4	Experimental parameters	61
Table 3.5	List of experiments and their specifications.	70
Table 5.1	Constants used in the Speziale's turbulence model.	129
Table 5.2	Model 1 boundary conditions	132
Table 5.3	Model 2 boundary conditions	133
Table 5.4	Model 3 boundary conditions	133
Table 5.5	Model 4 boundary condition.	133
Table 5.6	Model 5 boundary conditions	134
Table 5.7	Model 6 boundary conditions	134
Table 5.8	Flow number results from predictions using TA1 turbulence approximation.	144
Table 5.9	The flow number results calculated on the $\pi/2$ domain from predictions using the TA1 and the TA2 turbulence approximations.	146
Table 5.10	Literature review of the dissipated energy rate in three ST main regions	156
Table 5.11	The estimates of the energy distribution using the TA2 approximation.	156
Table 5.12	Power number results from predictions using the TA1 and the TA2 turbulence approximations.	158
Table 5.13	Boundary conditions for dynamic models of the stirred tank.	169
Table 5.14	Flow number calculated from dynamic prediction of the stirred tank	176
Table 5.15	Predictions of the energy dissipation.	178

List of Symbols

A_c	empirical constant
a	distance between two locations (m)
B	baffle width (m)
C	bottom clearance (m)
c_A	molar concentration of component A (mol/m^3)
D	impeller diameter (m)
$\mathcal{D}$	Diffusion coefficient (m^2/s)
$\mathcal{D}_t$	turbulent diffusion coefficient (m^2/s)
d_p	optical probe diameter (m)
$eff(t)$	efficiency parameter
F	force to overcome fluid resistance (N)
Fl	Flow (pumping) number
F_b	impeller blade rotational frequency (Hz)
H	liquid height (m)
I	turbulence intensity (%)
k	turbulent kinetic energy (m^2/s^2)
L	impeller blade length (m)
L_s	macro-scale length (m)
m	mass (kg)
N	impeller rotational speed (Hz)
N_P	Power number
N_{pts}	number of data samples per point
N_{FFT}	indirectly measured impeller rotational frequency (Hz)
n_i	molar mass of i-specie (mol)
P	Power draw (W)
p	pressure (Pa)
Q_{ij}	correlation between two variables
Q_r	radial flow rate (m^3/s)
Q_s	flow rate swept by the impeller (m^3/s)
q	energy flux (W/m^2)
R	impeller radius (m)
Re	impeller Reynolds number
R_A	chemical reaction rate of A-specie in molar form
R_{ij}	correlation coefficient
r	co-ordinate in cylindrical system
r_A	chemical reaction rate of A in mass form
r_S	sphere radius (m)
Sc	Schmidt number
Sc_t	turbulent Schmidt number
T	tank diameter (m)
T_I	time of single impeller revolution (s)
t_D	characteristic diffusion time
t_m	characteristic micro-mixing time
t_R	characteristic reaction time
t_F	characteristic flow time
t_{rtd}	characteristic residence time
U	instantaneous velocity component in the x-direction (m/s)
U_i	instantaneous velocity component in the i-direction (m/s)

$\overline{U}$	mean velocity component in the x-direction (m/s)
u	fluctuation velocity component in the x-direction (m/s)
V	instantaneous velocity component in the y-direction (m/s)
$\overline{V}$	mean velocity component in the y-direction (m/s)
V_{ei}	volume of the engulfed fluid (m^3)
V_Q	volume of the mixing reactor (m^3)
V_r	radial velocity component (m/s)
V_S	sphere volume (m^3)
V_θ	tangential velocity component (m/s)
V_{tip}	velocity at the tip of impeller (m/s)
V_z	axial velocity component (m/s)
υ	fluctuation velocity component in the y-direction (m/s)
υ_r	radial velocity fluctuation (m/s)
υ_θ	tangential velocity fluctuation (m/s)
υ_z	axial velocity fluctuation (m/s)
W	blade width (m)
w	wave-number (1/m)
w_i	mass fraction of i-specii
X_S	product distribution
x	co-ordinate in Cartesian system
Y	baffle thickness (m)
y	co-ordinate in Cartesian system
z	co-ordinate in Cartesian system

Greek letters

χ	angularity parameter
δ	striation thickness (m)
δ_0	initial striation thickness (m)
$\delta(t)$	Dirac function
δ_{ij}	Kronecker delta
ε	rate of the kinetic energy dissipation (m^2/s^3)
ε_{ij}	shear rate tensor (1/s)
ε_ϕ	scalar dissipation
ϕ	scalar fluctuation
λ	wavelength (m)
λ_B	Batchelor length-scale (m)
λ_K	Kolmogorov micro-scale (m)
μ	dynamic viscosity (Pa.s)
μ_t	turbulent viscosity (Pa.s)
ν	kinematic viscosity (m^2/s)
ρ	density (kg/m^3)
ρ_A	mass fraction of component A
θ	angle co-ordinate in cylindrical system
σ_{ij}	stress tensor (Pa)
τ	transit time of particle in LDV (s)
τ_ϕ	scalar mixing time
τ_{ij}^t	i-j Reynolds stress component (Pa)
ψ	stream function

Subscripts and upperscripts

i	index
j	index
k	index
m	index
n	index
Δ	difference symbol

List of Abbreviations

CFD	Computational Fluid Dynamics
DNS	Direct Numerical Simulation
FFT	Fast Fourier Transformation
FFW1.0	Find for Windows software (TSI, Inc.)
FIDAP 7.6	commercial CFD package (Fluent, Inc.)
MBC	Moving Boundary Constraint
PDF	Probability Distribution Function
LDV	Laser Doppler Velocimetry
ST	Stirred Tank
STR	Stirred Tank Reactor

1. Introduction

1.1 Motivation and Relevance

Imagine how many mixing reactors make part of the infrastructure of the chemical, petrochemical or biochemical industries. Besides this uncountable amount of mixing devices, consider how many times you performed some mixing process on your own. For example, think on the mixing of your morning's coffee, the mixing of the ingredients for your favourite meal or cake, the mixing of dyes to paint a part of your house and the simple use of your washing machine. Now, you probably would not believe that this so common and fascinating process of mixing has not changed for some centuries. In fact, this is not absolutely true because there have been done some modifications on the mixing tools and the mixing vessels. However, the understanding of the process itself is still a tough nut to crack.

Mixing is not just a simple unit operation, as it is currently taught at chemical engineering courses. It is a rather complex mechanism for contacting with mutually interfering operations in various processes. Tremendous efforts have been applied to optimise almost every chemical process but usually there is always some kind of mixing action to be solved. Therefore, one always comes to a point where the knowledge of mixing is essential for the successful reduction of the operational time and improved quality of the final product.

The importance of the mixing problem has been recognised in this century and substantial progress has been done. Early approaches to the understanding of this problem were solely based on experimental investigations. Different experimental techniques were applied to reveal main characteristics of various mixing tank configurations. Initial studies were limited to determine the most economical configurations and impeller shape in order to reduce the

necessary power input (see Tatterson, 1991). Other works focused on the study of the tank and impeller sizes (Oldshue, 1997), the determination of the main flow patterns (Ottino, 1994; Bakker, 1995), and the time necessary to reach a desirable degree of homogeneity (Moo-Young *et al.*, 1972; Shiue and Wong, 1984).

The major actual problem resides on the applicability of chemical reaction results obtained at laboratory scales and its scale-up to pilot plant and large-scale operations. An important part of the current undergoing research is concerned with the capability to predict mixing computationally. The success for this objective depends mostly on the understanding of the mixing process and subsequent validation of results against experimentally obtained data. Hence some empirical observations and practical experience will find solid background and the progress in mixing can continue. The final goal is to develop numerical models that would reliably predict the reactor productivity, efficiency and the mixing quality. In particular the processing times could be optimised in order to avoid mixing of already well-mixed fluids.

In this way, the time and experimental costs for the design of mixing reactors will be substantially reduced by the use of computational simulations. Final product commercialisation will be also strongly affected by better quality features of the products. The continuously growing demands and regulations on production, safety and ecological issues, are other confirmations of the urgency to resolve the problems related with mixing. Therefore, at the background of scientific interest remain the economical, safety and ecological motivations as the driving forces for the study of mixing.

1.2 Mixing Scenario in the Stirred Tank Reactor

To mix, according to Webster's dictionary (1976) means to combine or blend into one mass, in the act or process called mixing. The mixing and its research were studied, for many years, on a case-by-case basis due to their complexity and different viewpoints. Currently all knowledge and experience related with mixing should be coupled in order to make another step in understanding of the mixing phenomenon. According to Villermaux (1996), the main scientific areas that contributed to mixing research are chemical reaction engineering, fluid mechanics and combustion. In the large spectrum of mixing reactor applications, chemical reaction itself can be implemented in many different ways. Often, mass and heat transfer play an important role, such as, in the impact of mixing in fast competing chemical reactions, in exothermic reactions where heat exchanger configuration is a major part of reactor design, or in combustion processes where product yield and selectivity is totally controlled by these transfer processes. Moreover, sometimes mixing and reaction must take place in multiphase systems like in fermentation and crystallisation. Nevertheless, the final object of all mixing applications is to achieve the best possible homogenisation within the mixing device.

However, the level of success to accomplish this task, will depend on type of the mixing reactor and on the operational conditions. Consequently, the mixing scenario will be rather specific to the particular reactor type, and will also depend on the operational conditions under which the mixing is performed.

The present study will focus on mechanical mixing in a cylindrical flat-bottomed stirred tank reactor — STR — with and without baffles. In this last case, the baffle system consists of four vertical slabs equally spaced and mounted on the tank wall. They are used preferably under turbulent flow regimes (high impeller rotational speeds) to prevent the flow rotation as a solid body. The Rushton-radial type of impeller was selected from a large family of existing agitators due to its ability to generate very complex flow hydrodynamics and its extensive use in industrial practice (Oldshue, 1997). This impeller consists of a flat disk equipped with six vertical, equally spaced, rectangular blades mounted on the impeller shaft.

The hydrodynamics of the selected STR can be described briefly as follows. Tangential flow prevails within the region swept by the blades, referred as the *impeller region.* Strong radial and tangential motion are coming out from the impeller blades. Such flow is continuously pumped towards the reactor wall and the region in the reactor where it takes place is referenced as the *impeller discharge flow region.* This region extends above and below the *impeller centre plane* that passes through the impeller disk. The impeller discharge flow breaks into two parts at the wall, and both of them are redirected to the axial direction. These axial flows originate the two main vortices, one acting above — *top vortex* — and the second below — *bottom vortex* — the impeller centre plane. Hence, the reactor content is agitated by a combination of radial, tangential and axial motions. Some stagnant regions in the upper or lower tank regions might occur if the impeller rotational speed and thus the flow pumping are not strong enough to promote overall fluid motion. The *baffle region* of the STR is also important because the fluid behind it usually rotates in the *baffle vortex* with opposite direction as that of the impeller rotation.

For hydrodynamic conditions under laminar regime, possible trajectory scenarios for a particular particle placed in the STR, could be viewed in the following ways. A particle starting bellow the impeller disk region (see path I in Figure 1.1) will straggle between the blades of the impeller and eventually flows over or below the next incoming blade. Then the particle is directed to the impeller discharge flow and moves along the tank radius until it reaches the wall. Its impact on the reactor wall results in the reduction of its radial momentum and the particle changes its trajectory and follows along the reactor wall below the impeller centre plane. The flow conditions are favourable to proceed within the bottom flow vortex, and the particle continues to flow in the direction parallel to bottom after approaching it and then it turns upward near the shaft axis. The rising particle then re-enters the impeller region and the process is repeated periodically. If the particle starts its travel above the impeller disk (see path II in Figure 1.1), it continues through the impeller discharge flow region until it

reaches the wall where it is redirected into the upper part of the reactor following the top-vortex motion. It can eventually deviate from its travel in the top vortex and enter a stagnant reactor zone below the top liquid surface where it can stay stuck (see path III in Figure 1.1).

If baffles are present in the STR, a particle approaching the wall can be introduced into the region behind the baffle and follow the baffle vortex motion until the moment when it is released to the fluid bulk (see path VI in Figure 1.1).

The global radial-axial motion interacts with the tangential motion generated by the rotating impeller, and very complex three-dimensional flow features arise (see paths IV and V in Figure 1.1). The overall flow patterns under laminar regime are dependent on the ratio of diameters of the impeller and the reactor, and if this ratio is small, large stagnant regions are formed.

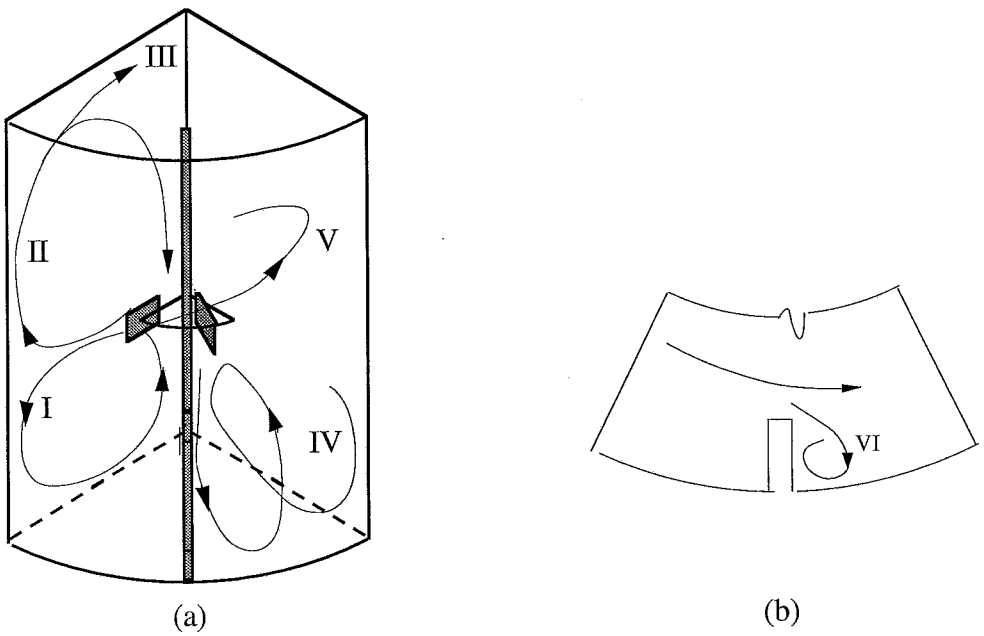

Figure 1.1 Possible trajectory scenarios in: (a) the STR and (b) the baffle region

Close examination of the velocity field under laminar regime reveals a fluctuating nature of the velocity near the impeller. At first, this fact can seem to be contradictory to the laminar character of the flow, but it is due to the periodic blade passages. This situation, where velocity at locations near the impeller is given by the mean and fluctuation components is called the *pseudo-turbulence*.

More complex flow pictures occur under turbulent flow conditions, which is the situation most common in practical applications. Viscous forces, related to the molecular fluid viscosity, are dominant in the laminar regime, while for turbulent regimes, these forces are of small or negligible importance. The inertial forces are dominant for turbulent flows and give origin to flow instabilities. These instabilities can be achieved by increasing the impeller

rotational speed or by the decrease of the fluid viscosity. The mean velocity in all spatial locations will be superimposed by a fluctuating component, as the result. This fluctuating component is of random, real-turbulence nature in all locations except in the impeller vicinity. Here it is composed by the pseudo-turbulence and random fluctuation components. Therefore, the inertial forces are enhanced by the pseudo-turbulence effects. The problem now is to determine what are the effects of turbulence on a particle trajectory.

Considering a particle within the impeller region, its motion can be affected by two kinds of turbulence. The real-turbulence as previously described and a pseudo-turbulence appearing near the impeller and solely due to the periodic passage of the blades. Pseudo-turbulence and real turbulence give origin to a *trailing vortex* system formed between the blades. This trailing vortex system is formed by the pair of vortices behind each blade, above and below the impeller. The diameter of these vortices grows until their effect disappears with increasing distance from the impeller. If the observed particle enters such a trailing system, it starts to rotate within the small vortices until the moment when it is released to the bulk of the fluid. The particle then continues at high velocity into the radial-tangential jet of the impeller discharge flow region. From this point on, the particle path can be identical to the bottom vortex flow. This seems to be a similar mechanism to the one described for the laminar regime. Note, however, that the particle motion can always be affected by the flow instabilities in the turbulent regime. Therefore, a particle re-entering the impeller region, after finishing the bottom vortex travel, can be eventually switched to the above vortex flow and vice-versa. In this way, more intensive mixing is performed and it is believed that also better reactor homogeneity will be achieved.

In turbulent regime, the particle trajectory may be affected by an additional effect. In the case of high impeller rotational speed and in the absence of baffles, a *central air vortex* can be formed along the shaft. This situation can be quite dangerous since the air can be sucked into the impeller region, and the impeller can be damaged due to cavitation. This situation is to be avoided at all cost and will not be considered in the remainder of this work.

Mixing process in the STR can now be easily pictured considering the many particles that are flowing and mutually interacting in the reactor. The term *macro-mixing* is used here to describe the mixing process that occurs according to the above mentioned flow scenario. Macro-mixing occurs on length scales corresponding to the vortex motions that are called *macro-scales*. The energy contained in these macro-scales is next transmitted by a cascade process to the smaller scales until the molecular scale is reached. The processes acting at the *molecular-scale* are referred as *micro-mixing*. The higher energy content present at the macro-scales, the more energy is passed on to the molecular-scale, and faster and more intensive mixing is accomplished.

Finally, the Rushton impeller rotating in the baffled tank reactor creates a very complex flow field that can be thought as a combination of some particular cases well known from fundamental studies of turbulence. One observes, *turbulent shear flow* near the reactor wall and its bottom, *jet flow* developed along the discharge flow, and *wake flow* that occurs behind the baffles and at the edges of impeller blades. All the complexities of the mentioned flow cases and their interactions result in a very difficult, but also very challenging problem to solve, both for the numerical simulations and the experimental studies.

1.3 Thesis Objectives and Dissertation Layout

The objective of this study was to explore both experimentally and numerically the mixing process using the Rushton impeller in a STR. The problem was limited to the isothermal flow conditions and to the use of Newtonian fluids. The experimental part was undertaken using the LDV — Laser Doppler Velocimetry — technique, based on the light scattered by particles passing through the measuring volume created by two-intersecting laser beams. Various regions of the STR were investigated by changing the measuring volume position and the results obtained in two dimensions were used to create the flow field images of the studied regions. The results of experimental study revealed some of the most important features in the STR mixing that were later applied to model the STR hydrodynamics using a commercial CFD — Computational Fluid Dynamics — package. Both laminar and turbulent flow regimes were studied in the STR with and without baffles. The results from numerical simulations, based on both steady-state and dynamic approaches, were validated against the experimental data. The capability of the tested STR models to correctly predict the flow hydrodynamics allowed some experimentation in the numerical simulation of species injection and its spreading in the STR.

The reminder of this thesis dissertation is divided into the following parts:

- The second chapter shows the mixing in a STR in a broad spectrum of works found in the literature. The main and most progressive studies done in both experimental and numerical areas were selected from an abundant amount of available information. Results directly related to the present work are listed along with those that can offer some ideas for future investigation of the STR.

- Chapter 3 highlights the experimental results obtained by LDV in the various regions of the mixing reactor. It provides some important insights on the flow behaviour and describes a flow change in the transition from laminar to turbulent regime. Attention is focused on the evolution of inertial forces with increasing Reynolds number. These forces are demonstrated in terms of the shear Reynolds stresses that are essential for mixing applications with chemical reactions. The contribution of pseudo-turbulence on the shear Reynolds stresses is quantified near the impeller, and found to be higher than

that from real-turbulence. The experimental evidence obtained from the impeller and discharge flow regions is used, in the following chapters, as a support for building of the STR model with suitable boundary conditions.

- Laminar mixing is explored in the Chapter 4 by numerical predictions based on two and three-dimensional STR models. The question whether the Rushton impeller is efficient and economical for applications under laminar regime is addressed. The effect of the baffle presence and its use under studied flow conditions is commented. A comparison of the mixing process predictions to data found in the literature and to data commonly used in industrial mixing-practice is reported. Limitations of numerical modelling based on the laminar flow assumption for higher impeller rotational speeds are clearly demonstrated.

- The main objective of Chapter 5 was to answer the question of whether CFD tools are suitable for hydrodynamic predictions in the STR under turbulent flow conditions. The first part provides detailed analysis of the turbulent mixing in the STR using a steady-state numerical approach called the *moving ring*. Predictions using this approach with different boundary conditions are evaluated. Potential danger and mistakes coming from not-properly-imposed boundary conditions are stressed and limitations of the steady-state numerical modelling of turbulence are highlighted. A new type of dynamical simulation is developed in the second part of this chapter and results compared to those from the steady-state calculations. The results from both steady-state and dynamical numerical predictions are compared to those obtained by the LDV not just in the first-order terms, like velocity components, but also in the second-order terms called the shear Reynolds stress. Parameters of industrial importance are given in terms of the *power* and *flow numbers* and validated against industrially accepted values. It can be concluded that CFD tools are valuable and reliable for the STR predictions also under turbulent regimes.

- At the beginning of Chapter 6 various numerical methods, problems and perspectives to solve turbulent reactive flows, that is, situations where chemical reaction interacts with turbulent flow, are discussed. The success of CFD predictions for the STR hydrodynamics encouraged the idea to observe species injection and its spreading within the STR by means of numerical simulations. CFD possibilities to predict numerically the mixing quality and the reactor performance are outlined at the end.

- Finally, the main conclusions, findings and problems encountered during the research can be found in the Chapter 7. Suggestions for future experimental and numerical work are also outlined here.

2. Stirred Tank Reactor: State of the Art

2.1 Introduction

The Stirred Tank Reactor — STR — can be found in many fields of the world's chemical industry. The mixing of non-miscible fluids, the blending of miscible fluids with different viscosities, and the processing of non-Newtonian fluids are only a few examples of very important processes frequently found in the petroleum, food or pharmaceutical industries. These processes will always require more efficient, more economically and environmentally acceptable equipment for the various applications.

The concept of fluid mixing in chemical reactors has changed over the last decades in many different ways. These changes were performed not just in the field of the stirred tank reactor — STR— but also for other types of the mixing reactors such as T-jet mixers, static mixers, and tubular reactors. In the early 50s and 60s the sudden increase in production of new polymers, synthetic materials and fermentation products started the idea to optimise the mixing process. Some progress has been done in the design and scale-up of reactors and in the understanding of micro-mixing and macro-mixing phenomena. The stirred tank reactor has been improved in many aspects by applying mainly results from experimental research. However, experiments are usually expensive and many times they do not offer all the necessary and desirable information. Furthermore, the fact that today's most reliable experimental techniques in hydrodynamics studies (LDV — Laser Doppler Velocimetry and PIV — Particle Image Velocimetry) are limited to transparent or clear fluids raises the need for alternative forms of research.

Recent progress in the computational area is creating an alternative to deepen the understanding of mixing. Numerical simulations of fluid mixing processes are now seen as a very promising alternative to experimentation. However, it should always be kept in mind that they are just an aid in the effort to solve very specific problems. Hence, it is necessary to take good care in the use of such tools, in their application and interpretation of the results. It is generally understood that further progress can only be made through detailed validation of the results from computational tools against experimental data.

The new emerging tools of Computational Fluid Dynamics — CFD — can solve simultaneously the equations of conservation of mass, energy, momentum, and species in the presence of chemical reaction. These numerical tools are usually based on the finite elements or the finite volume elements methods. CFD can expand our insight into the regions that can not be inspected experimentally, and is especially useful in situations when no other information is available. Moreover, the costs of the experiment set-up and experimental work are significantly reduced, and this is the main advantage of CFD that will play a major role in the future research and development of mixing.

The STR is the main subject of this work, but most of the hydrodynamic studies were concentrated in the study of the stirred tank — ST — where the purpose is solely the homogenisation of the tank contents. The STR accomplishes not only the homogenisation but also the realisation of chemical reactions.

Many configurations of the ST have their own, sometimes specific use, due to its originality or outstanding characteristics. The main parts of any configuration of a ST are the impeller and the tank

Impeller design has undergone the most ample changes since it has been applied to perform the mixing tasks. Today's impeller configurations can be top entering, side entering, or bottom entering with different blade's shapes and with one or more agitators mounted on the shaft. The flow regime and the fluid viscosity must be considered in order to choose properly the impeller type. The helical-ribbon and anchor impellers are very often used for laminar regimes (see Figure 2.1).

Turbine impellers (see Figure 2.2) are preferred for turbulent regimes (Tatterson, 1991). Each configuration has its own characteristics and limitations since the impeller role is to introduce momentum into the ST and through it the main flow pattern is developed. Radial flow fields are promoted by radial impellers such as the Rushton turbine while axial flow patterns dominate the flow fields generated by the axial impellers such as the pitched blade turbine.

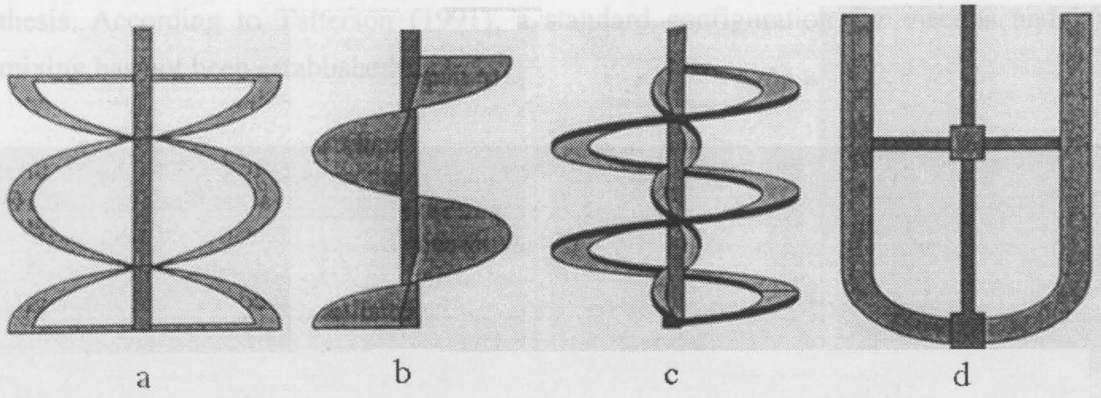

Figure 2.1 Impellers used in laminar flow regime: (a) double-flight helical-ribbon impeller; (b) screw impeller; (c) single-flight helical-ribbon; (d) anchor impeller (from Bakker and Gates, 1995).

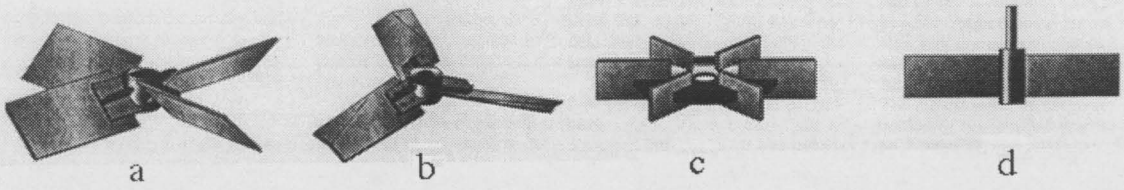

Figure 2.2 Impellers used in turbulent flow regime: (a) pitched blade turbine; (b) high-efficiency impeller;(c) Rushton turbine; (d) simple straight-blade turbine (from Bakker and Gates, 1995).

Mixing tanks can be found in many different shapes and sizes. The shape of the tank bottom plays an important role in mixing of multiphase systems and in drainage of stirred tanks. The sedimentation of a solid phase is less favourable in tanks with a dished bottom than in those with a flat bottom. Baffles are used to avoid the rotation of the fluid as a solid body resulting in poor mixing, and to eliminate the creation of dead zones at the tank top and bottom by re-orienting the flow into the axial direction. The use of baffles also inhibits the formation of the central air vortex and the liquid surface becomes more flat, but this is done at the expense of an increased power draw.

Various ST configurations can be obtained by combining different impeller types with different tank designs. Figure 2.3 summarises the possible schemes for different combinations of impeller type and tank shape to obtain most of the ST configurations found in the industry. The ST configuration highlighted in red in Figure 2.3 is often viewed as *the standard configuration* in turbulent regime studies, and it is used throughout the present

thesis. According to Tatterson (1991), a standard configuration for viscous and laminar mixing has not been established yet.

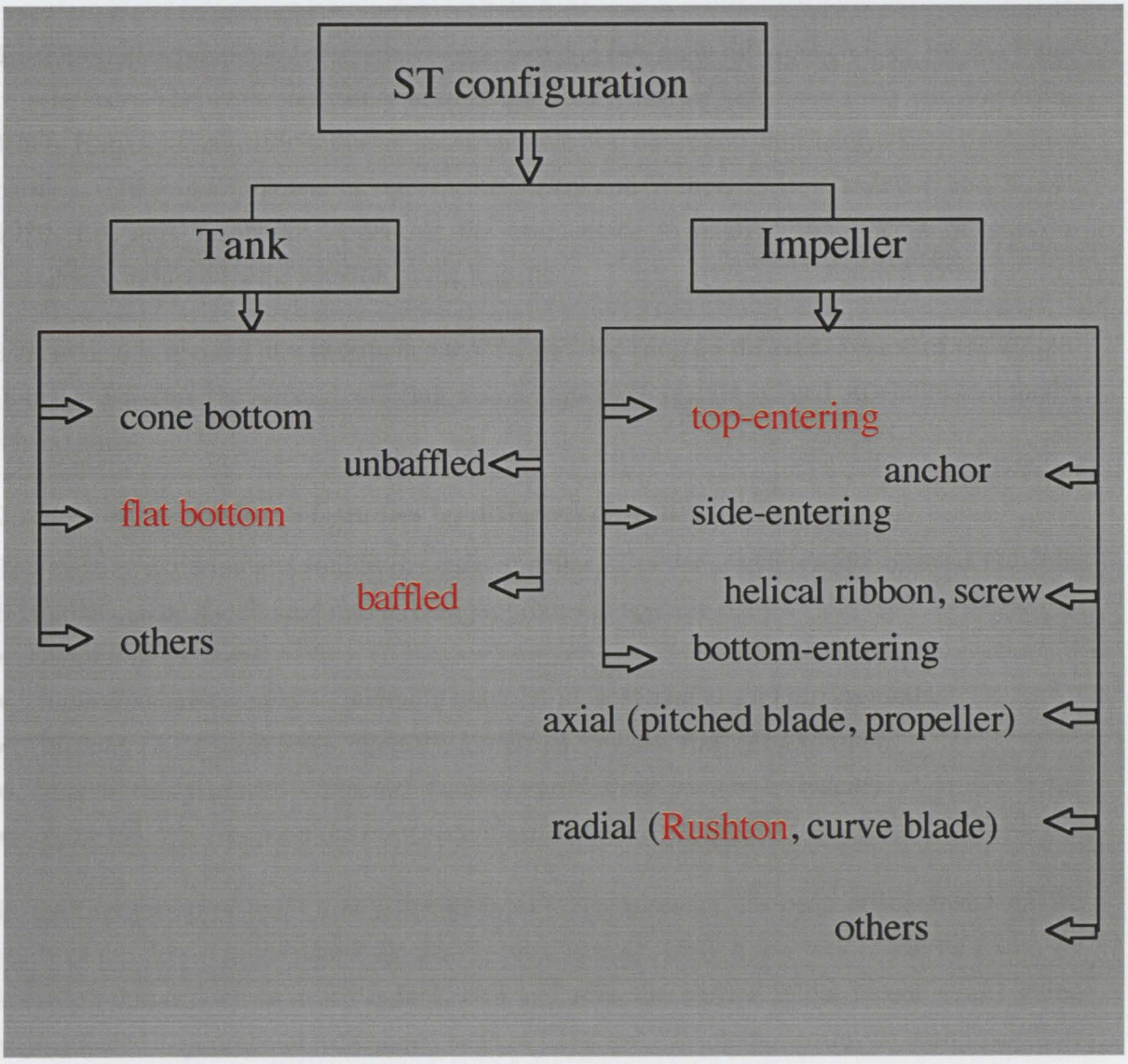

Figure 2.3 Scheme of ST configurations used in industry (red colour highlights the options in this work).

2.2 Review of Experimental Research

The aim of this review is to report on some of the pioneering experimental works and on the most recent experimental research in the field of ST mixing and to draw from them the most relevant conclusions for ST hydrodynamics.

From the various experimental techniques used in the experimental research of ST's, those of non-intrusive nature are generally preferable and the most trusted for hydrodynamic studies. Modern techniques such as LDV, PIV, and LIF — Laser Induced Fluorescence have

substituted methods used in the earlier studies (thermal velocimetry, conductivity or pressure techniques). All these methods have been applied for the analysis of the ST under laminar and turbulent flow conditions.

The reported experimental works have been based in two main different choices for the frame of reference. The most commonly used is the *fixed frame of reference* (Wu and Patterson, 1989; Harvey *et al.*, 1995) that is most suitable for the report and analysis of main flow patterns. The *rotating frame of reference* (Gunkel and Weber, 1975; Calabrese and Stoots, 1989; Lee and Yianneskis, 1994), is the best choice to analyse the effects of pseudo-turbulence induced by the rotation of the impeller.

This review is divided into two main parts, the first focusing on different issues of the single-impeller ST and the second offering some important results related to multiple-impeller stirred tanks.

2.2.1 Single-impeller ST studies by different objectives

The existing experimental studies of single impeller ST cover a wide variety of aspects of the flow, that can be subdivided into five major groups of specific issues:

- *main flow patterns;*
- *main flow parameters — pumping number, power number and mixing time;*
- *turbulence parameters — intensity, kinetic energy and rate of dissipation;*
- *special flow features— impeller trailing vortices and pseudo-turbulence;*
- *some new aspects from the most recent experimental techniques.*

In the first group of *main flow patterns* most of the research has been concentrated on the study of the flow regions where the flow is most intense. Only a few works can be found on specific regions such as near the tank wall and near the baffles. Most recent works using sophisticated experimental techniques, such as LDV and PIV, helped to reveal additional flow features, not observed previously, such as chaotic flow structures and flow instabilities in the ST.

- The earliest studies focused on the description of the velocity field, and the different flow patterns created by various types of impellers in the ST. According to Tatterson (1991) one of the first works on flow patterns was a photographic study using tracer streaks in a four-blade turbine ST by Sachs and Rusthon (1954). Flow patterns between the blades of the impeller have been studied by Gunkel and Weber (1975), and measurements of mean and fluctuating velocities are reported for a large number of positions in the tank using the hot-wire anemometry technique. The flow outside of the Rushton impeller region was found to be driven mainly by the axial motion of the fluid. More recently, Reed *et al.* (1977) studied main flow patterns for the Rushton impelled ST using LDV. These visualisation results confirmed the formation of two main vortices in the flow field (above

and below the impeller position) and the occurrence of strong mixing between the two vortices at the impeller discharge flow region. Harvey *et al.* (1995) reported LDV data in the ST using the pitched-blade impeller.

- Most of the experiments reported in the literature were focused on the impeller and discharge flow regions, however, Stuersson *et al.* (1995) provided a study of the velocity field in the near wall and bottom regions. The velocity data near the solid boundaries was found to scale with the impeller speed.

- Bakker *et al.* (1996) focused their work on the flow patterns under laminar and turbulent conditions for a pitched blade impeller. Both LDV and PIV techniques were used to obtain flow patterns at a vertical plane of the ST. Close agreement between the results of two techniques was reported. The large-scale chaotic flow structures were clearly revealed by PIV, but these temporal instabilities are completely smoothed out by time averaging with LDV.

- An interesting study on the flow above the axial impeller was reported by Montes *et al.* (1997). They analysed the macro-instability phenomenon generated by the impeller rotation using LDV and flow visualisation with a laser-sheet technique, and found that these instabilities are rather organised modifications of the flow patterns in the upper part of the ST. These instabilities were dependent on the macro eddies formed between the impeller and the liquid free surface and that they were strongly coupled with the blade passage frequency.

The main hydrodynamic flow properties are quantified in the second group of works by the following set of flow parameters: the *flow number* to express the intensity of radial flow generated by the impeller; the *power number* to measure the power draw supplied to the mixing process; and the *mixing time* as the time necessary to achieve a prescribed degree of homogeneity. These parameters are mainly important for the comparison of performance of different types of ST's.

- Mavros *et al.* (1996) measured the effect of impeller type (Rushton and two different axial impellers) and liquid viscosity on flow fields by LDV. The Rushton impeller yielded the highest overall liquid circulation but at the expense of an increased power draw. The results showed that increasing the liquid viscosity the pumped (radial) and circulated (tangential) flows were reduced. However, only a small effect of the viscosity on the velocity maps was observed. Flow number studies can also be found in the works of Gunkel and Weber (1975), Wu and Patterson (1989) and Stoots and Calabrese (1995).

- The results of Bates *et al.* (1963) on power studies are most commonly used in ST design. They reported effects of impeller type and size on the impeller power draw. Hockey and Nouri (1996) recently studied the power characteristics of a pitched impeller

in a baffled stirred tank. Mean and fluctuation velocities measured fields are reported with angle resolution of the one degree. The data on power number was computed from the measured induced torque. Their results showed a sharp drop in the power number at $\mathrm{Re} = 1200$, due to the change in the flow pattern from radial to axial. Anisotropic turbulence was found in the discharge flow region while isotropic turbulent flow dominated in the bulk of the tank. Comparison of the Rushton-impelled ST with the tank agitated by the pitched blade impeller showed a better pumping efficiency per unit power input of the pitched blade impeller. This makes it a better choice for applications where high flow rate is required. Pinho *et al.* (1997) reported an experimental study of three new hyperboloid impellers and their power characteristics.

- Manna (1997) used two methods for measuring the mixing times of the STR with Rushton impellers. Chemical and physical (conductivity) methods were employed to evaluate theoretical hypotheses that were determined by the local mass transfer equations with boundary and initial conditions. The measured mixing times confirmed the theoretical results. Bouwmans *et al.* (1997) carried out a study of mixing times in the ST for liquids of different viscosities and densities. Three regimes — impeller, gravity, and intermediate regime — were defined for buoyant additions and the mixing times values were found to be dependent on the particular regime.

Most of the hydrodynamic studies in ST have been conducted under the turbulent regime. In the third group of experimental works *turbulence parameters* are usually reported in terms of the turbulence intensity, kinetic energy and its rate of dissipation. Studies on the macro-scales of turbulent eddies and of the Reynolds stresses are less common, but very important for the understanding of turbulent mixing.

- Wu and Patterson (1989) reported detailed measurements, in a baffled tank with the Rushton impeller, of turbulence intensities, kinetic energy, energy dissipation rates, energy spectra, and turbulence macro-scales. Mean and fluctuation velocities were measured by LDV in three directions and the random and periodic contributions to measured quantities were separated. Corrections for the effect of pseudo-turbulence were achieved using the auto-correlation function. The results showed that the region close to the impeller was dominated by the pseudo-turbulence and its effect diminished towards the reactor wall. The maximum turbulent energy dissipation rate occurred at the central part of impeller discharge flow and it was accompanied by small macro-scales and high turbulence intensities. Similar results were obtained from LDV studies of Calabrese and Stoots (1989). Data acquisition of the rotating frame velocity data was made at a fixed point in the tank. The LDV signal was coupled to an optical encoder that sent information about the blade position to the signal processor. The authors found that the variation of the velocity with angular position is much greater than the variation of instantaneous

velocity using the fixed frame of reference. Turbulence parameters near the impeller (kinetic energy and energy dissipation rate) were reported in the study of Lee and Yianneskis (1998). A new relationship for the velocity decay along the tank radius was proposed based on this data. Time scales were calculated from the time-resolved measurements and spectral analysis was performed in order to obtain the estimates of length scales and energy dissipation rates. One important conclusion from this work is that the macro-scale length near the blade tip, frequently approximated as 20% of the impeller radius (Kresta, 1991) may be overestimated by a factor of two.

- The main parameter studied by Zhou and Kresta (1996) was the energy dissipation rate and its dependence on the tank geometry and the impeller type. Maximum values for turbulent energy dissipation rates were estimated using velocity fluctuation data near the impeller region. The results showed that the Rushton impeller produced larger dissipation rates than the axial impellers and a significant effect of the impeller diameter on energy dissipation values was observed.

- Schaefer *et al.* (1997) carried out high-resolution LDV measurements of a Rushton impelled stirred tank. Large scale flow fields and turbulence length scales (about the half of the blade width) were found to be in agreement with previous works. In addition, the flow within the impeller region was studied in detail.

- Pettersson and Rasmuson (1998) performed rather exceptional measurements of the complete 3D velocity fields in a tank agitated by a pitched-blade impeller. Complete Reynolds stress tensor measurements were reported to quantify the growing inertial forces, and results indicated that the normal stresses were larger than the shear stresses. Additional studies of the macro-scales, auto-correlation coefficients and velocity comparisons between the suspended particles and fluid were given. Differences between the two phases were generally small in all regions but the discharge flow.

The hydrodynamics of the ST were described from qualitative and quantitative points of view in previous paragraphs, while special attention was given to the overall turbulent flow field. Other group of ST studies were dedicated to more detailed and *specific flow features*, such as impeller trailing vortices and pseudo-turbulence.

- Considering the location near the impeller blade, a very erratic nature of fluctuation velocity arises. Measurements of the velocity or any other variable near the impeller (for example concentration fields, Reigth, 1965; see Wu and Patterson, 1989) are influenced by periodic motion of the blades. According to Van't Riet *et al.* (1975), the turbulence data, measured with a stagnant probe, contains an additional signal that can not be clearly interpreted as turbulence. This phenomenon was also observed by other researchers (Mujumbar *et al.*, 1970; Gunkel and Weber, 1975) and was recognised by Van't Riet *et*

al. (1976) as pseudo-turbulence. Photographic velocity measurements in the discharge flow of the Rushton impeller has revealed a trailing vortex system (see Figure 2.4) formed behind each blade (Van't Riet *et al.*, 1975). The position of the vortex axis has been determined and the results were consistent with the pressure measurements.

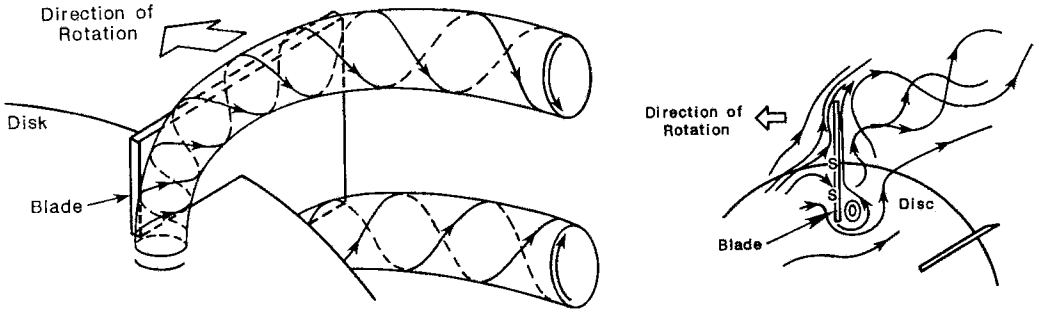

Figure 2.4 Illustration of the trailing vortex system formed behind the blade (from Van't Riet and Smith, 1975).

- Measurements using a rotating frame of reference are the best choice to study the pseudo-turbulence caused by the periodic motion of the blades. Gunkel and Weber (1975) measured flow parameters in the baffled ST with an anemometry probe mounted on the Rushton impeller. They performed measurements using hot-wire anemometry and obtained data between the impeller blades. Four vortices were detected between each pair of the blades, two above and two below the impeller disk. The energy spectra from measurements in the impeller discharge flow confirmed the slope $(-5/3)$ inclination in the *inertial-convective range* (low frequency range). Some peaks corresponding to the impeller blade frequency were observed on these spectra. The bulk of the tank was found approximately turbulent, homogeneous and as the region with the highest energy dissipation. This last conclusion was unique and contradictory with many other different studies (Cutter, 1966; Wu and Patterson, 1989; Zhou and Kresta, 1996).

- Periodically fluctuating flow in the impeller discharge region was measured by Van Der Molen and Van Maanen (1978) for various sizes of the stirred tank. The decay of mean and fluctuation velocity components with radius was verified. The amplitude and phase of the periodic contribution were determined by measurements triggered with the correlator at the impeller blade frequency. This study confirmed that the time-averaged velocities scale with the impeller speed and that the trailing vortices give origin to random velocity fluctuations that decrease with increasing radius.

- Yianneskis *et al.* (1987) obtained detailed LDV data on the trailing vortex system in the baffled ST with the Rushton impeller. The results were used to determine the vortex

centre and equation for the vortex axis. Data from the fixed and rotating frames of reference were compared and significant differences were reported.

- The extent of the flow periodicity and the vortex structure were determined in the study of Stoots and Calabrese (1995) using 3D flow measurements. The term *clinging vortex* was introduced for the part of the vortex that wraps around the blade while the part acting far away from the blade tip was referred as the *trailing vortex*. Moreover, they noted that the tangential velocity could exceed the blade tip speed due to the acceleration over the blade. The thickness of the *clinging vortex* was found to grow with distance from the blade. The *trailing vortex* had a diameter of one blade width at the tip of the blade and the vortex axis extended in a 30 degrees outside direction behind the blade. In addition, some calculations of the pumping numbers, deformation and energy dissipation rates were presented based on the angle-resolved data. It was found that deformation rates near the blade tip can exceed the impeller rotational frequency by as much as two orders of magnitude and these rates were independent of the angular position.

The last group of studies provides *some new aspects of the most recent experimental techniques* for the stirred tank research.

- Letellier *et al.* (1997) analysed the velocity field, in a stirred tank mixed with the Rushton impeller, using the concepts from the theory of non-linear dynamical systems. They demonstrated that the dynamical behaviour of the ST contains a quasi-periodic motion with three frequencies. Two of these frequencies were associated with the rotation of blades. The origin of the third, unexpected, frequency was not completely understood but the authors claimed that it could be a characteristic of the mechanical driving system.

- Lee and Yianneskis (1997) employed the liquid crystal thermographic technique to measure the transient mixing characteristics in the ST. Liquid crystals (tracer) sensitive to the temperature were tracked in the fluid, and these displayed temperature patterns analysed by image processing in order to determine the mixing times and temperature fields at the vertical plane of the ST. The obtained mixing times were compared with the results from previous studies. The results indicated that measured data could be affected by the tank size and the velocity of tracer injection. The technique needs some additional developments and tests for future measurements of mixing times.

2.2.2 Multiple-impeller ST studies

This section gives some interesting findings from experimental studies of multiple- impellers in the ST.

- Lee and Yianneskis (1994) presented a study of the extent of periodicity of the flow with a double Rushton impeller system. The trailing vortices formed around the blades were

investigated using both the fixed and rotating frame of reference. Measurements showed an anisotropic character of the trailing flow vortex and the periodic flow was determined to act in the blade vicinity. The trailing vortex and flow patterns for the double Rushton impeller system were found to be dependent on the impeller spacing. The trailing vortex structure appeared to loose its identity at one impeller radius away from the blade tip and it was observed that the vortex is nearly horizontal in the impeller discharge flow. The last observation suggests that the trailing vortices do not extent above or below the impeller blades. This study has also indicated that the flow can be considered as steady outside the region of strong periodicity.

- Three stable flow patterns and four unstable ones were observed by Rutherford *et al.* (1996) in vessels equipped with two Rushton impellers. This study focused on the effect of the lower *impeller clearance* (distance from the tank bottom), the distance between two impellers and the effect of the submergence of the upper impeller (into the ST) on the flow. Anisotropic behaviour inside the ST was determined. The study of various tank sizes revealed that the main flow features such as the stream inclination and turbulence levels are scaleable and well established.

- Baudou *et al.* (1997) studied the optimisation of impeller configuration and number in the ST using LDV and flow visualisation methods. Flow field patterns were dependent on the spacing between the impellers. If this spacing exceeded certain value the impellers worked independently. The three-stage configuration offered better energy distribution than the double impeller ST.

All the reported experimental studies cover large spectra of aspects that are most relevant to the ST mixing. However, research on ST is still a very strong area for new developments, and future research must provide more relevant information on the specific field of mixing with chemical reactions. In particular, the study of turbulent shear stresses is one important example that has been found very challenging for the present thesis. The behaviour of turbulent shear stresses in the stirred tank field is almost unknown but it plays a crucial role in processes involving chemical reactions.

2.3 Review of Numerical Modelling

Numerical modelling of the ST hydrodynamics became a very attractive alternative to the experimental studies mainly due to substantially reduced costs and savings of time in order to obtain the desired information.

Numerical modelling of fluid flow produces predictions of flows for a given situation and is based on the conservation equations. These equations are transformed to their numerical analogues by numerical discretization. Numerical analogues of fluid flow equations are

solved by numerical techniques on each point of the grid of a flow domain. A set of initial and boundary conditions is required in order to produce the flow predictions. The domain of the ST studied will consist of the two main parts: the tank and the impeller. These main parts may be divided on the particular entities of the tank — top, bottom, tank wall and fluid — and those of the impeller — blades, disk and shaft. The initial and boundary conditions must be defined for all entities.

The aim of this review is to report on numerical studies of the ST found in the literature. This is done in order to facilitate the choice of the simulation strategy for the present work and for better understanding of steps taken in the numerical simulations.

Numerical simulations of ST's can be categorised by the following aspects.

- *laminar or turbulent flow conditions;*
- *steady-state or transient simulation;*
- *ST configuration (unbaffled or baffled tank).*

This categorisation helps to foresee the difficulties related with numerical simulations and gives better perspectives to explain the weaknesses and strong points of the simulation strategy chosen.

First, the numerical simulations depend on *laminar or turbulent flow conditions*. Numerical modelling of mixing in the ST under laminar flow conditions is solely based on the equations of conservation of mass, momentum and energy. Modelling of turbulent flows requires additional conservation equations for the turbulence properties. Moreover, these equations need to be supplied, in contrast to the laminar case, with some semi-empirical constants and with additional boundary conditions. As a result, numerical simulations of the ST operating under turbulent regime is both more complicated and more time consuming than those of laminar regime. Numerical predictions of specific flow regime, for the ST configuration studied, should approximate a flow scenario described in Chapter 1.

Second, independently of the flow regime, the flow can be approached by *steady-state or transient simulation.* The rotation of the impeller in a stirred tank can be seen as a quasi steady-state or periodic problem due to the regular passage of the blades. In this way, the mixing process can be simplified to a steady-state simulation. The main difficulty is the specification of the boundary conditions in the region swept by the blades of the impeller. Boundary conditions at the impeller are set properly if they mimic its rotational motion. The impeller can be modelled as *the blades set* (steady-state approach) and the mixing process is obtained by a sequence of various positions of the blades relative to the tank wall. The results of this sequence of numerical simulations are then averaged in space to get the suitable

steady-state description of the flow field. Results acquired in this way are only approximations because the inertial effects and time dependence of the flow are ignored.

Another steady-state possibility is to consider the fluid swept by the impeller blades, as the moving ring, and to provide this virtual fluid body with proper boundary conditions. This idea comes from the time averaging point of view on the periodic motion of the impeller and has some analogy in the LDV measurements. The problem remains to find the proper boundary conditions for the moving ring created by the impeller rotation.

Dynamic simulations are easier to understand because the change of position of the blades is simulated exactly, in space and time, and in contrast to steady-state situation, no approximations of the impeller rotation are necessary.

As mentioned before, numerical methods need a set of boundary and initial conditions to produce the predictions of flow fields. This set is usually obtained from experimental data. According to Xu and McGrath (1996) the boundary conditions in the impeller region can be defined in three different ways:

- *Experimental boundary conditions*, where measured profiles of velocity or pressure variables are imposed within the impeller region. Unfortunately, experimental data is not available for each impeller type and the ST configuration.

- *Momentum source boundary conditions*, where some experimental data (e.g. velocity, pressure or Reynolds stresses) is required to impose boundary conditions in the impeller region but a direct simulation of the flow around the blades of the impeller is not available.

- *Direct boundary conditions* are specified from a dynamic, time dependent calculation with no experimental data requirements, offering the possibility to resolve all flow details inside the impeller region.

The third aspect of numerical modelling is related to the *ST configuration (unbaffled or baffled tank)*. The effect of the presence of wall baffles on the flow scenario in a stirred tank has been described in the Chapter 1. Again, it may be recalled that the baffles enhance the mixing process but introduce a very complex pattern of the flow.

The hydrodynamics of ST without baffles is conceptually easy to predict. The great majority of earlier numerical ST hydrodynamic simulations was done for the unbaffled ST or for the particular case where *impeller-baffle interactions* (time dependency of the impeller's blades position relative to the baffles) are not present. In this case, the impeller region can be modelled as a motionless part while the tank wall is rotating. The approach of the rotating wall and motionless impeller can be performed using both steady-state and dynamic

simulations. Numerical modelling is more complex for baffled tanks due to the impeller-baffle interaction. In this case, the rotating wall frame of reference is not acceptable and a different approach needs to be applied. For example, the blades set approach or the moving ring approach. The moving ring is the most often used approach in current CFD packages, but there are also other very promising approaches.

A review of previous numerical studies of the hydrodynamics of ST's follows. This review is organised in two main parts, the first dealing with the steady-state modelling and the second focused on dynamical simulations.

2.3.1 Steady state modelling of ST

The reviews in this section are divided on the following topics.

- *earliest numerical predictions of stirred tanks;*
- *numerical predictions o funbaffled stirred tanks;*
- *numerical predictions of baffled stirred tanks with Rushton impeller;*
- *numerical predictions of baffled stirred tanks with various types of impellers.*

The first group of works reports on the *earliest numerical predictions* of the ST in two and three dimensional domains.

- One of the first reports on flow field prediction in the ST was accomplished by Harvey and Greaves (1982). They performed the simulation of turbulent flow on a two-dimensional grid assuming symmetry in the tangential direction and a non-linear distribution of the radial velocity at the impeller blade tip. The boundary conditions for the turbulence parameters, k and ε (turbulent kinetic energy and dissipation), were set to null. According to the authors, the use of zero values for k and ε, in the standard turbulence model $k-\varepsilon$, allowed the best match with experimentally found velocity patterns. The quantitative agreement with experimental data was not satisfactory, however, because of adjusted zero turbulence level.

- Middletton *et al.* (1986) were the first to present a full 3D simulation. The frame of reference was stationary and the impeller somewhat simplified in a way that the periodic flow arising from the passage of the blade was time averaged and not modelled in detail. The impeller boundary conditions were taken from experimental data and the predictions showed promising agreement with their measurements.

Numerical predictions of hydrodynamics in the *unbaffled stirred tanks* are conceptually easier to perform and only more recent works are referenced. These studies were done on

three-dimensional domains and differ mainly on the methodology used to resolve the turbulent flow.

- Turbulent flow in closed and free surface unbaffled tanks stirred by radial impellers was studied by Ciofalo (1996). In this study, no recourse to experimental data was required in order to specify the boundary conditions. Simulations with the wall as the rotating frame of reference were performed to predict a free-surface formation under turbulent flow conditions. Two models, the standard two-equation (eddy-viscosity) $k-\varepsilon$ model and the differential stress model were investigated. The use of the differential stress model was found more satisfactory in terms of its capability to handle turbulence. Agreement between the two models was observed in the overall patterns, the vortex shape, and global parameters such as the power and the pumping number.

- Numerical predictions of the pitched-blade impeller in the unbaffled STR were done by Armenante *et al.* (1997). Turbulence effects were simulated using either the $k-\varepsilon$ and the algebraic stress model and compared to experimental data. Velocity predictions based on the algebraic stress model were found superior to those based on the $k-\varepsilon$ model.

Numerical studies of the turbulent flow in a baffled ST are more complex. Some works on the *ST with the Rushton impeller*, are introduced as the third group. These studies differ mainly on the specifications for the boundary conditions and in the models used to handle the turbulence.

- As previously mentioned, Harvey and Graeves (1982) were the first to compute the ST turbulent flow with standard $k-\varepsilon$. Pericleous and Patel (1987) used the turbulence model based on the Prandtl mixing length hypothesis. Here, the additional term called turbulent viscosity is a function of the flow density, a length scale in the flow and the local mean flow velocity. This model is suitable only for simple turbulent flows so their predictions of the ST had limited accuracy.

- Kresta and Wood (1991) prescribed the turbulent kinetic energy and the rate of energy dissipation at the vertical boundary swept by the impeller and performed their predictions with the $k-\varepsilon$ model. However, the standard $k-\varepsilon$ model is based on the assumption of isotropic turbulence, that is turbulence constant in all directions. The Rushton impelled ST flow field is not close to this assumption, as it was confirmed by various experimental works (for example Hockey and Nouri, 1996; Rutherford *et al.*, 1996; Lee and Yianneskis, 1994). In addition, the present LDV data will also show that motions in ST's exhibit clear anisotropic turbulence (see Chapter 3).

- Bakker and Akker (1994) prescribed the turbulence boundary conditions at the vertical surface swept by the Rushton impeller using the two different profiles: in the shape of a

double peak and as a parabolic profile. The double peak profile is in accordance with experimental data measured by Wu and Patterson (1989) and the parabolic profile was reported in the experimental work of Ranade and Joshi (1990). The authors concluded that the calculated rate of dissipated energy is realistic only for the case of a double peak profile. On the other hand, the use of the parabolic profile resulted in a reasonable agreement between the overall energy-dissipation rates and the power draw measurements. However, the question on which of these profiles is the best choice remained open. Bakker and Akker(1994) also studied which of two models (averaged stress model and standard $k-\varepsilon$ model) is more appropriate to handle the turbulence. The standard $k-\varepsilon$ model is based on a concept of isotropic turbulence and the averaged stress model assumes the anisotropy turbulence. Their predictions showed that the averaged stress model produces more feasible results than the $k-\varepsilon$ model. This last conclusion confirms the experimental findings, as mentioned in the previous paragraph, and demonstrates a need to employ anisotropic models of turbulence for numerical modelling of the ST hydrodynamics. Turbulence models, as the one of Speziale (1987), where the Reynolds stresses are non-linear functions of the strain rate, seem to be a very good alternative. Another option is to solve individual transport equations for each of the Reynolds stress components, as it is accomplished in the second-moment closures.

Numerical simulations of the ST agitated by the Rushton impeller were reported in previous paragraphs, where special attention was given to the proper adjustment of the boundary conditions and to the selection of best model for the turbulent regime. Other group of studies were dedicated to *stirred tanks agitated by various types of the impellers*. The goal here is to introduce various modelling approaches and to compare their ability to model properly the velocity fields and turbulence characteristics.

- Dong (1994) focused on the flow induced by an eight-bladed-flat-paddle impeller in an unbaffled tank. The flow characteristics were predicted from a 3D computation in conjunction with the standard $k-\varepsilon$ turbulence model. The results showed satisfactory agreement with the measurements of velocities and the turbulent kinetic energy. Small discrepancies between the predictions and experiments were observed in the impeller discharge flow and in the shaft vicinity.

- Bakker and Akker (1994) modelled the radial (Rushton) and the axial pumping impellers (A315 impeller and pitched blade turbine—PBT) in the single-phase stirred tank. The radial and tangential velocities, and values of k and ε were prescribed on the boundary swept by the tip of the impeller using a parabolic approximation. The predictions agreed quite well with experimental data and a change of position of the centre of the axial vortices was observed before and behind the baffle. Harvey *et al.* (1995) performed CFD simulations of the baffled pitched-blade impelled stirred tank. This approach called the

blades set was applied and the steady-state results were approximated by spatial averaging of a sequence of predictions. Numerical predictions of the velocity field were compared to the LDV data. A better match of data was obtained far away of the impeller than in the impeller vicinity. The authors claimed that the approach used in the study offers a reasonable accuracy of the ST velocity fields only for very low Reynolds numbers.

- Xu and McGrath (1996) presented the momentum source model for prediction of the ST agitated by the pitched-blade impeller. The impeller blades were divided into vertical strips and approximated as an airfoil. The radial momentum source was derived from the impeller-fluid interaction. The results were compared against CFD predictions using LDV data as boundary conditions. Two models exhibited similar predictions and these were compared with LDV experimental data. The authors reported a very good agreement in the axial and radial components of velocity but the tangential velocity was found to be over-predicted.

- The flow generated by the pitched-blade turbine was the objective of another Bakker *et al.* (1996) study using various experimental and numerical methods (LDV, PIV, CFD). They found that laminar flow can be fairly well predicted using the proper boundary conditions. To prescribe the boundary conditions for the rotating shaft of the impeller was found as necessary in order to ensure a correct magnitude of the tangential velocity at the top of the stirred tank. Some of the features of the flow field in turbulent regime were correctly predicted but the total energy dissipation rate was dramatically under-predicted.

- Most of the above mentioned works treated the impeller as a block box by specifying the boundary conditions at the surfaces drawn by the impeller rotation. Ranade and Dommeti (1996) proposed a method called "snapshot", with a possibility to predict the flows between and around the blades of the impeller. Quasi steady-state equations are calculated with no recourse to experimental data. The authors explored the idea that the flow starts to behave periodically after resolving temporal variation within and outside of the impeller region. Therefore, they tried to make a shortcut through the evolution of the flow and to go directly to the periodic state, generally reached after a few impeller rotations. The knowledge of the impeller geometry and of the rotational speed was sufficient to define the source terms at the fixed front sides of the blades and sink terms at the backsides of the blades. Acquired results were then spatially averaged for various positions of the impeller blades concerning the baffles. The predicted results showed good qualitative, as well as, quantitative agreement with published experimental data and in addition, the flow details between the impeller blades were presented.

- Goetz *et al.* (1997) studied the effect of pitched-blade impeller on the velocity distribution in the ST. Their model balanced the drag and lift forces around impeller blades and the comparisons of numerical results to LDV data showed satisfactory agreement.

The impeller region is often specified using boundary conditions that are taken from experimental data. The future goal of numerical predictions is to minimise recourses for these experiments. The momentum source approach(e.g. the moving ring) is currently regarded as the most suitable for practical applications. Therefore, it is very stimulating for the present work to study the effects of imposed boundary conditions on the ST predictions.

2.3.2 Dynamic simulation of stirred tank

Steady-state approaches of the ST have been mostly applied in numerical works reported in the literature. This fact was due to the lack of suitable tools to resolve the impeller-baffle interactions. Novel techniques of sliding and clicking meshes can solve the problem of interactions and therefore are seen as valuable instruments for further investigation. These techniques are already available in some commercial CFD packages and are now being tested for ST predictions. Only a few works can be found in the literature on dynamic simulation of the baffled ST, and majority of them focused on flow patterns under laminar conditions, as it is reported in the following paragraphs.

- Hamill *et al.* (1994) presented an application of the sliding and the clicking mesh tools to single and multiphase flows in the ST. The mixing tank was filled with silicon oil and agitated by a pitched-blade turbine at small rotational velocity. Their predictions compared well to the experimental data in terms of the magnitudes, the direction of velocity components and the vortex centres. Slight differences in the radial velocity between the clicking and the sliding approaches were contributed to a finer grid used in the sliding mesh calculation. The advantage of dynamic modelling of the baffled stirred tank remains in the fact that there is no need of experimental data input for the impeller boundary conditions.
- Bakker *et al.* (1997) used the sliding mesh to resolve the flow field in the baffled tank agitated by a pitched-blade turbine. Low Reynolds number conditions were responsible for the mainly radial flow patterns, similar to those in the work of Hamill *et al.* (1994). In this work, a constant time step and about 40 impeller revolutions were performed until the periodic steady state was reached. It was observed that the number of revolutions to achieve the periodic state increases with the Reynolds number. The results compared quite well to the experiments at low impeller Reynolds numbers ($Re < 400$).
- Jaworski *et al.* (1997) predicted baffled ST working under laminar flow regime using a sliding mesh approach. The authors reported a very good predictability of the stirred tank hydrodynamic and proposed the model/experiment error ratio to be generally adopted as a criterion for the quality of CFD modelling.

Dynamic simulations of the ST are advantageous because they can reveal flow details not available from steady-state simulations and require no experimental data. The main disadvantage remains in the excessive time and storage expenses. For example, the ST hydrodynamic can be resolved as a steady-state problem within a few hours of computer time,

while the same problem computed by dynamic modelling and using the same computational domain can be completed only after weeks or months.

Dynamic simulation of the ST with baffles, operating under turbulent regime, is still not explored and it is a challenging task. This was one of the motivations for the present study and the results of dynamic prediction will be compared against those of steady-state simulations. In this way, the CFD capability to resolve very complex flow problems can be tested and the advantages and weaknesses of both modelling methods will be stressed.

2.4 Chemical Reactions in Mixing Reactor

Fluid mixing is very important in reacting processes of chemical technology. Molecules of the reactants are contacted at the molecular scale and chemical reaction can be started. The zone where chemical reaction takes place is accompanied by diffusion and convection of reactants from the surrounding fluid and these processes can be promoted by mechanical mixing. The transport processes may depend on the chemical reaction kinetics and these are faster if the concentration gradients grow. The ability to describe these transport processes is essential for good numerical predictions.

Experimental works dominated the first attempts to characterise the quality of fluid mixing with chemical reactions. They have been performed mainly in the tubular or stirred tank reactors. The combination of fast and slow chemical reactions was found as the most feasible for such a purpose. In the case of a slow reaction, the mixing and thus the micro transport processes have no effect on the final product, since they are already finished when the reaction starts. A fast chemical reaction, however, can be influenced by both the micro and macro-mixing. The reaction time can be of the order of the micro-mixing time and the reactant transport is affected indirectly by macro processes that give origin to the small-scale effects.

Two systems of reactions have been used to describe the quality of mixing with chemical reactions. The first system refers to the competitive-consecutive reactions and was studied by Bourne and co-workers (1981-1983).

$$\begin{aligned} A + B &\xrightarrow{k_1} R \\ R + B &\xrightarrow{k_2} S \end{aligned} \qquad (2.1)$$

Here, the first reaction gives the desired product, R, at a much higher rate ($k_1 >> k_2$) than that of the second reaction that produces the by-product S. In the case of perfect mixing, and

considering an excess of the reactant A, B is consumed preferably until depletion by the first-faster reaction. The yield of product S grows with the poor mixing quality of the reactor.

The second reaction system employs competitive and parallel reactions ($k_2 < k_1$) and was proposed by Villermaux *et al.* (1994):

$$\begin{aligned} A + B &\xrightarrow{k_1} P \\ C + B &\xrightarrow{k_2} Q \end{aligned} \tag{2.2}$$

The first reaction is quasi-instantaneous and the rate of the second one is comparable to that of the micro-mixing process. If the incoming reactant B becomes segregated for a time long with respect to that of the second reaction, it reacts both with A and C. The mixing performance of reactor can be determined from the relative amounts of B going to P and Q.

The product of the second reaction (S or Q), independently of the reaction system used is negligible if the system is premixed before the chemical reaction takes place. However, the case of non-premixed system is more interesting for practical purposes. The selectivity, in the case of non-premixed STR, depends on the impeller speed, power input, feeding time, and the reactor hydrodynamics. The distribution of the feeding pipes, their location in the reactor, viscosity of the reactants, and initial concentrations of the reactants are not less important. The reactor configuration and its operating conditions are other possible variables that have an impact on the reaction selectivity.

The main objective of this review is to introduce experimental and numerical methods used for studies of reactive flows, micro-mixing phenomena, and quality of mixing in the STR. This will be helpful to set the strategy in future simulations of ST mixing involving chemical reactions and for interpretation of difficulties related with this subject.

This review is composed by two main parts, the first part focusing on experimental studies and the second part reports on numerical methods.

2.4.1 Experimental methods

The following group of experimental works describes the effects of feed location, impeller speed, and of the feeding time on the product distribution in the STR and the tubular reactor.

- The first system of reactions was introduced by Bourne and collaborators in series of excellent papers (1981-1983). The competitive, consecutive reaction system was considered to produce dyestuffs (monoazo, R, and biazo, S) by use of the 1-naphtol and diazotised sulphanilic acid. The product inhomogeneity was measured by a spectrophotometer.

- The work of Angst *et al.* (1983) showed that for nine investigated feed points, the radial jet leaving the impeller gives the fastest micro-mixing due to high values of local energy dissipation.

- The work of Li and Toor (1986) was dedicated to the determination yield in non-premixed, series-parallel reactions (Equation 2.1) in a tubular reactor. They noted that the yield of product R was higher with increasing Re, for both single and multi-jet feed configurations. Their results are similar to the STR results of Bourne *et al.* (1981), where the yield of the desired product decreased with slower impeller speed and with increasing reactant concentrations.

- Experiments in a stirred tank reactor reported by Bourne and Hilber (1990) referred to the reaction system of consecutive competitive reactions. The feed addition time was under investigation, and it was found that if this time exceeds a critical value, the product distribution is independent of feeding time, being a function only of the micro-mixing. The proper feed distribution and number of nozzles was also studied. It was observed that less by-product S was formed in the case of the multiple feed nozzles and some decrease of the critical time value was observed. More of the S by-product was formed for times smaller than the critical one. In addition, a visualisation study to check if multiple feed zones are mutually independent was performed. The study of the viscosity effect showed that higher viscosity values cause formation of more by-product. The results on the reactor scale-up study were approximated by empirical relation reasoning that the critical time of feeding increases with the rising reactor volume.

- Villermaux *et al.* (1994) suggested the use of the second parallel reaction system. The system of parallel-competing reaction (Equation 2.2) based on reactions producing iodine was applied into the STR to characterise micro-mixing. The yield of by-product S was evaluated as a function of the impeller speed and its type, at different locations. Additional experiments involved gas-liquid and liquid-solid dispersion.

- Study of micro-mixing based on precipitation in a liquid-solid suspension was reported by Guichardon *et al.* (1995). The same iodide-iodate test reactions were used to study micro-mixing in liquids of different viscosity by Guichardon *et.al.* (1997).

- Different reactants were used to describe micro-mixing in the study of Bourne and Yu (1994). The parallel reaction system consisted of the competition for sodium hydroxide between neutralisation with hydrochloric acid and alkaline hydrolysis of ethyl monochloracetate. Investigation of various operational conditions (impeller speed, initial concentrations, feed positions) showed an agreement with previous studies published in the literature.

Additional experimental studies focused on the mixing time parameter, on distribution of the tracer concentration in the STR and are introduced in the following group of works.

- Most of above mentioned studies used classical spectrophotometry methods to determine the concentration distributions in the reactor. Distelhoff *et al.* (1997) obtained non-intrusive measurements of the scalar concentration in a fully baffled mixing reactor using LIF (Laser Induced Fluorescence) technique. Time dependent measurements of a passive scalar were adopted to determine the mixing time. It was observed that the mixing was slowed down due to a scalar that remained in the lower vortex region, before it mixed with the fluid in the region above the Rushton impeller. In the this work, radial impellers were characterised by higher mixing time values than those from axial impellers.

- The extent and intensity of the partial segregation in a semi-batch reactor were evaluated by Mann *et al.* (1997) using 3D visualisation. These 3D visualisations of the inert and reactive tracer were based on the acid/alkali reaction and on the use of coloured indicators.

- Concentration differences at the macro-scale were measured by Strizhak and Menzinger (1998) using the spatial microelectrode scans in the discharge flow of continuous STR. These concentration differences at the macro-scale were contributed to the spatial dependence of the interaction between the micro-mixing and the chemical reaction.

2.4.2 Numerical methods

The main difficulty in numerical predictions of turbulent flow is often referred as *closure problem*, where the number of unknown variables exceeds the number of available equations. If chemical reaction occur in this flow, the process is called *turbulent reactive flow*. Two extra-unclosed terms arise in the governing equations of turbulent reactive flow: the non-linear convective term called *turbulent flux* and the *reaction term*. The turbulent flux term can be solved by application of the gradient diffusion theory while the reaction term is more complicated in nature. The reason is that an additional covariance of the concentration fluctuation appears in the reaction term. This is a quite difficult term to close due to its simultaneous dependence on the turbulence and chemical reaction (Fox, 1996).

The next group of works gives a brief literature review on the numerical studies that are related to the mixing problem involving chemical reactions. The text is divided into three main categories, according to the method used for prediction of the reactive flow:

- *turbulent closure models;*
- *phenomenological models of micro-mixing;*
- *models using Probability Distribution Function —PDF methods.*

The relevant assumptions and background of these numerical models is beyond the scope of this section but more detailed description of selected models and additional key references to this subject are provided in Chapter 6.

The first category of studies reports on methods that are based on the *turbulent closure models*. The difficulty to close the reaction term is resolved by assuming the various simplifying assumptions, or using DNS simulation, or by coupling of CFD with simplified micro-mixing models.

- Toor (1969) assumed that the covariance of concentration fluctuations, arising in the reaction term, is independent of the speed of the reaction when the reactants are fed in stochiometric proportions (assumption based on the limit of fast and slow reactions). This approach results into an assumption that this covariance depends only on the hydrodynamics and not on the reaction rate what is often referred as the *Toor's hypothesis.*

- Some closure models for parallel-consecutive reactions have been proposed by Bourne and Toor (1977). According to Dutta and Tarbel (1989), the covariance of concentration fluctuations is unaffected by the second-slow reaction and its value can be taken from measurements performed on the case of a fast single-step reaction.

- Dutta and Tarbell (1989) studied four closure models: the coalescence-redispersion — CRD — model of Curl (1963); the interaction by exchange with the mean — IEM — model of Villermaux and Devillon (1972); the three-environment — 3E — model of Ritchie and Togby (1979); and the four environment — 4E — model of Mehta and Tarbell (1983). These were tested against experimental data for both single and multiple reactions. All models were also examined to satisfy the limits of slow (pure mixing) and fast reactions. The authors found that the closures based on the CRD, 3E and 4E models provide very good predictions of all the experimental data, while other models derived in their work or found in the literature were not adequate.

- In Wang and Tarbell (1993) the accuracy of the 3E model was evaluated by comparison with the Direct Numerical Simulation — DNS — of Gao and O'Brien (1991), and some discrepancy was observed. The extension from one to multidimensional geometry of the 3E model was presented by Wang and Tarbell (1993). This extension lead to some improvements in the predictability of concentration fluctuations.

- DNS is more precise than the closure models, due to accurate description of the physical process expressed by the Navier-Stokes equations and the mass conservation equation for all species present in the system. An example is the above mentioned work of Gao

and O'Brien (1991). However, despite of being an effective tool for the study of reactive flow, DNS is not applicable for higher values of Re and Schmidt number, Sc, due to computational limitations.

Application of CFD packages to turbulent reactive flows suffers by the fact that the effects at the smallest scales are substituted by the averages corresponding to the grid dimensions. Therefore, the CFD packages should be coupled with micro-mixing models in order to resolve correctly the events at the scales smaller than the grid cell. An alternative option is to assume that each computational cell is perfectly mixed, as it is reported in the following group of studies.

- Micro-mixing and chemical reaction were modelled by Hannon (1994) with a CFD package implementing some simple closure models of mixing at the molecular scale. The standard CFD package was supplied by the modified laminar model, combustion model, and a simplified version of the cascade model. It should be noted here that the modified combustion model is suitable for gas phase but not for liquids, where the $Sc > 1$. These coupled models predicted correct trends of the yield with Re, but the magnitude of change was incorrect. Togatorop *et al.* (1994) predicted an inert tracer mixing and multiple reaction in a batch reactor using a CFD package. A noteworthy resemblance with experimental visualisation was reported. Numerical predictions were performed using the assumption of perfect micro-mixing within each cell of the computational domain. The reaction rate was given as a function of the average concentrations while the covariance of concentration fluctuations was set to zero.

- Time dependent prediction of turbulent reactive flow inside a STR was performed by Bakker and Fasano (1994). They used a slightly modified version of the combustion model, present in the CFD package used, and obtained good agreement with experiments. This model for competitive-consecutive reaction system showed correct trends of effects of increasing impeller speed and feed locations on the product yield, S. A combination of a CFD package with micro-mixing models was applied in the study of Bakker and Van den Akker (1994) to both the parallel and consecutive pairs of competitive reactions. Various micro-mixing models were incorporated into the available CFD package but all of the models overpredicted the experimental data.

Some analogies with the above mentioned CFD studies can be seen in the first work of the following group while the second study reported gives a useful link on decoupling of the effects at various scales.

- The approach introduced by Wang and Mann (1992) represented the semi-batch mixing reactor using a network of mixing zones. The pair of reactions $A + B \rightarrow R$ and $A \rightarrow S$ was studied (R being desired product). The mass flows through each zone of a 2D

network and material balance equations have been written in terms of the accumulation, input and output by the flow exchange with surrounding zones. Perfectly mixed zones were assumed and the results were presented for laboratory and production scale reactors. Since the assumption of perfectly mixed zones can be justified for sufficiently slow reactions, in order to eliminate the effect of micro-mixing, a close reproduction of experimental results was obtained.

- The study of Ranade (1992) offers a useful discussion on the decoupling of the micro and macro-mixing effects at the computational grid scale. A comparison of results of the numerical prediction against experiments was promising.

In previously reported works, the mixing at molecular and small scales was neglected, substituted by grid averages or resolved by various micro-mixing models. The *phenomenological micro-mixing models* are based on empirical data and some of them are introduced in the second category of reported numerical studies.

- Belevi *et al.* (1981) reported the numerical diffusion-reaction model where the reactant B is fed into an environment of reactant A, forming small spherical elements. Only diffusion and chemical reaction occur within such spheres. Results from this model have shown that an increase of the stochiometric ratio, as well as, an increase of the impeller speed suppresses the formation of the S by-product. High viscosity values increase the formation of S. *Back-mixing* phenomenon was reported as the effect of product formation inside the feeding pipe, due to small feeding velocity relative to the flow field in the reactor. The most economical and the highest selectivity position of feeding pipe was found to be below the impeller. All these results were confirmed by experimental data. The reaction zone, however, was found smaller than the Kolmogorov scale (length scale in turbulence theory).

- Therefore, Angst *et al.* (1982, 1983) developed a new model of diffusion and reaction within a deforming fluid element. The initial reaction zone corresponds to the scale of Kolmogorov, and this is thinned out by the laminar shear into slab elements but the model avoids the complexities arising from turbulence. The thickness of these slabs is reduced progressively as a function of the shear rate. Less by-product, S, is formed by stretching mechanism relative to the non-stretched case. Smaller quantity of S is formed in case where reactant B is assumed to diffuse within the reaction zone, irrespective of its shape (sphere or slab). Due to the larger specific surface of the spherical reaction zone, less by-product is formed than in a slab of the equal thickness. Angst *et al.* (1982), in another study, claimed that the production of undesired product, S, can be reduced by increasing the impeller speed, reducing viscosity, increasing the stochiometric ratio and by the use of dilute reagent solutions.

- In the work of Bolzern and Bourne (1983), the reaction zone underwent extensional and shear forces that accelerate the molecular transport. Their numerical predictions showed that the model including an extensional flow causes a faster mixing and less S formation than the model including pure shear forces at constant energy. However, the comparison with experimental data showed that the model using the shear deformation gives better results. Baldyga and Bourne (1983) derived the velocity at which deforming laminae are shrinking. Comparison to the model of shear deformation showed that this model produces faster shrinkage of the fluid elements. However, both models were reported to predict the experimental data well.

- A different model was developed for the case of fast competitive-consecutive reactions by Ranade and Bourne (1991). The authors assumed complete macro-mixing and a fine scale engulfment process and predictions showed good agreement against experimental data. Fox and Villermaux (1990) derived an unsteady-state version of the IEM model in order to predict dynamic behaviour of the continuous stirred tank reactor. Their model was tested using a simple reaction system for both premixed and non-premixed reactants. The authors reported that numerical predictions exhibit dynamic behaviours similar to that observed experimentally.

- Interaction between the micro and macro-mixing was numerically studied by Thoma *et al.* (1991). They extended the one-dimensional engulfment model of Baldyga and Bourne (1989) to a multidimensional system. This study investigated the effects of feed location, impeller speed, reactor size, and multiple feeds on products by a pair of azo-coupling reactions.

- A numerically favourable scheme of the IEM (called random replacement IEM model) was proposed by Change *et al.* (1996). Such scheme was found superior to the unsteady IEM model for systems with stiff chemistry (high value of ratio of the reaction rates).

A different approach to close the reaction term in modelling of turbulent reactive flows is the use of *Probability Density Function methods —PDF*. These methods treat the reaction term exactly and are performed using the concept of notional particles that travel through the reactor. The trajectories of notional particles are calculated by Monte-Carlo methods. Some of the studies employing PDF methods are reported in the last category of numerical studies. Detailed description of these promising numerical methods and their combination with commercial CFD packages can be found elsewhere (Fox and Grier, 1993; Fox, 1992 and 1996).

- Baldyga (1989) used the Beta presumed PDF method to evaluate a decay of the concentration variance in the reactor with homogeneous and instantaneous reactions. Later, Fox (1996) argued that the presumed PDF method, using the Beta functions, have

some limitations for practical purposes. Another model based on the PDF method was derived by Natu and Shenoy (1990). Micro-mixing was characterised in a convenient way and the results were different from those of presumed PDF method.

- Tsai and Fox (1994) computed series-parallel reactions in a tubular reactor by a joint velocity-composition PDF method. The tubular low-density polyethylene reactor was modelled by PDF and a CFD package in another study of Tsai and Fox (1996). Problems arise with closing of the scalar dissipation rate. Progress has been reported later using the spectral relaxation model (Tsai and Fox, 1996) for predictions of series-parallel reactions in a single jet-tubular reactor.

It is advantageous to combine CFD packages with software using PDF methods. The reactor hydrodynamics can be computed using a CFD package and its predictions are then supplied to a software using PDF where the interactions of mixing with chemical reactions are coupled and solved. Currently, some CFD packages (Fluent, CFX) are commercialised with optional built-in PDF software. These are usually based on models developed by Hannon (1994) who developed the *PFD reaction model*, and Pope (1995) who developed the *pdf2ds model.*

3. Hydrodynamic Characterisation using LDV

3.1 Introduction

Radial impellers, such as the Rushton turbine, have been widely accepted in industrial practice for mixing in stirred tanks. Detailed knowledge of the mixing scenario is important for the understanding of transport processes in these devices. The experimental studies are essential in the effort to discover the mixing scenario and play a major role in the development of models to predict these transport processes. Consequently, the ST performance can be optimised using the experimental and numerical studies.

Despite of the considerable progress in this field, as described in the previous chapter, the mixing in the ST is still subject to study mainly due to its complexity. The main goal of the present experimental work is to specify the flow features of the most important regions in the ST agitated by the Rushton impeller. This chapter presents the results of measurements that demonstrate the hydrodynamics of this tank, and special emphasis is made on the results that are mainly relevant for proper specification of boundary conditions in numerical simulations. Some of the results from this work are compared with those already published in the literature. The shear Reynolds stresses induced by the rotating impeller are inspected for a range of Reynolds number. These second order quantities are a particular and novel criterion for validation of CFD predictions.

Among many experimental methods (photographic, Pitot-tube pressure studies, hot-wire anemometry or acoustic techniques), the Laser-Doppler Velocimetry (LDV) and the Particle-Image Velocimetry (PIV) have been receiving the highest attention in the last years. The LDV method was selected for the present study due to its ability to offer time averaged

information. In this way, a good insight on the quasi steady-state ST problem is given and the necessary information for numerical simulation is then obtained.

This chapter is divided into three main parts. In the first part it is described the experimental set-up, the basic principles of experimental technique and the LDV system used in this study. Measured and calculated quantities are introduced here together with the analysis of experimental and statistical uncertainties. The second part of this chapter presents the results of LDV experiments obtained in the ST. The flows in the impeller discharge region, in the impeller region, at the impeller centre plane and baffle region are reported separately. Finally, the last part is the summary of all main findings of this experimental study.

3.2 Experimental Set-up, LDV System and Measurements

3.2.1 Experimental Set-up

Figure 3.1 shows a schematic representation of the stirred tank used in the experiments. The stirred tank is a cylindrical vessel made of Plexiglas with diameter $T = 0.294\,\mathrm{m}$. For easy reference, all geometrical parameters were chosen to scale with T. Four baffles were mounted on the wall, equally spaced around the cylinder. Baffles are made of Plexiglas slabs of width $B = T/10$ and thickness equal to $T/100$.

The ST was filled with liquid to the height, H, equal to the tank diameter, T. The Rushton impeller of diameter, $D = T/3$ is mounted on a shaft entering the tank from the top. A schematic representation of two of the six blades symmetrically distributed at the impeller disk is shown in Figure 3.2. The impeller off-bottom clearance, C, which is the distance between the impeller and the tank bottom is in this case $C = T/3$. This particular value was optimised by researchers from their power studies of the Rushton impeller in the ST (Tatterson, 1991). The ST with these characteristic dimensions is often reported in the literature as the *standard ST configuration* for turbulent flow.

The impeller shaft is powered by the 0.9 kW electric motor (EFACEC, BF580M). Rotational speed is controlled within ±0.01% by a speed drive controller (Control Techniques Ltd., Commander CDE). Figure 3.3 shows a photograph of the frontal view of the experimental set-up.

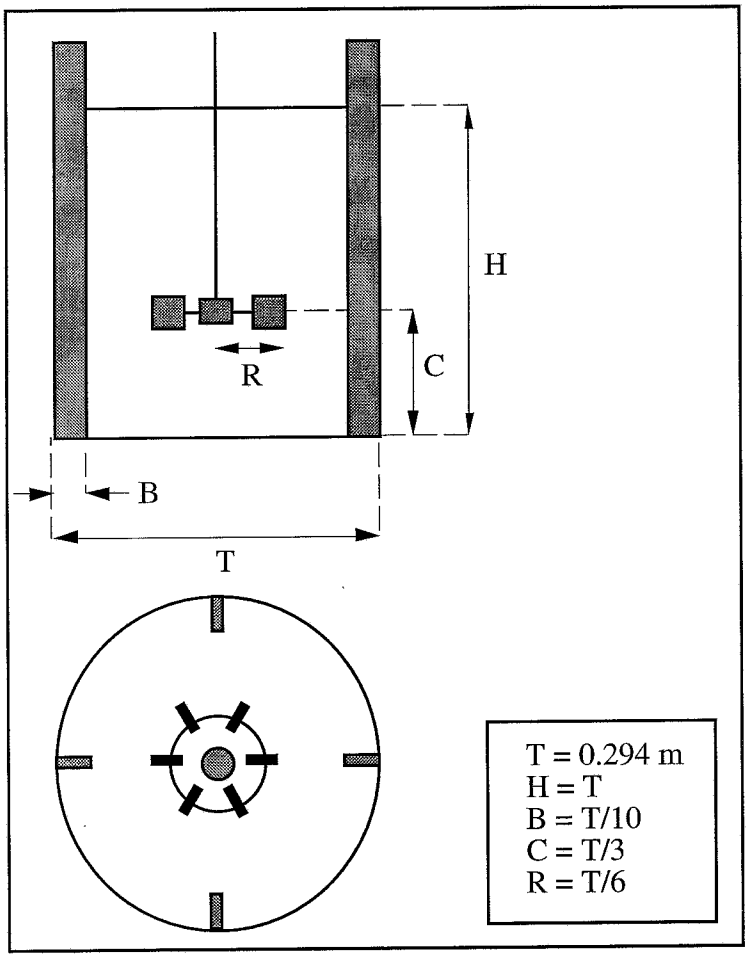

Figure 3.1 *Schematic representation of the stirred tank used in the experiments.*

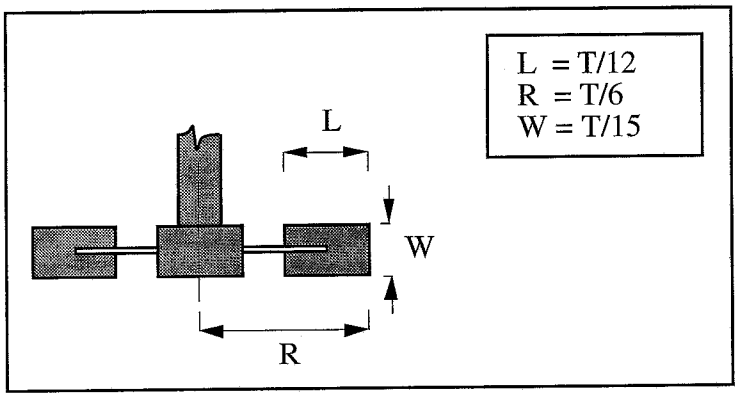

Figure 3.2 *Schematic representation of the Rushton impeller used in the experiments.*

1 - Plexiglas ST

2 - Speed commander drive

(Control Techniques, Ltd., CDE)

3 – Electrical motor

(EFACEC, BF580M)

Figure 3.3 Frontal view of the experimental set-up.

3.2.2 LDV System Description

The hydrodynamics of the ST was studied using the Laser-Doppler Velocimetry (LDV) technique. The basic principles of LDV are rather simple and are briefly described in this section. The theory behind this powerful technique is complex and received extensive attention during the last decades. A significant progress has been done and results of LDV theory were applied to practical use. Currently the LDV system involves very sophisticated mainly electronic and optical components. The LDV system used in this work presents *the state of the art* in hydrodynamics studies. More details of LDV principles and description of each system component can be found elsewhere (Durst *et al.*, 1976; TSI manuals, 1991).

The 2D LDV system used in the present work operates on the *backscatter mode* (the light is transmitted and received from the same optical probe) and two velocity components can be measured simultaneously. The laser source produces a monochromatic and coherent light beam, which is collimated and then mirrored to the multicolour beam separator. The light beam is there separated into four beams by wavelength (two green with wavelength $\lambda = 514.5$ nm, and two blue ones with $\lambda = 488.0$ nm) and these are focused to the optical couplers connected to fibre-optical cables. The cables carry the parallel beams to the head of the optical probe. These beams are focussed and crossed, with a transmitting lens of the optical probe, into a very small measuring volume. The crossing beams of the same colour

create an interference pattern composed of planar layers of high and low intensity light, usually called *fringes*. When a moving particle passes through the fringes, it scatters the light of a certain frequency. This scattered light is proportional to the velocity of particle that corresponds to the fluid flow velocity if the particle is neutrally buoyant. The velocity normal to the fringes can be calculated with the frequency measured from the signal (scattered light) and with the known distance between the fringes (length between high and low intensity layers).

A basic LDV system can not distinguish between forward or reverse flows and low velocity flows because the frequency of the signal goes to zero at zero velocity of a particle. The *frequency shift* eliminates this ambiguity by the addition of known frequency for one beam of each colour. This is performed in the Bragg cell of multicolour beam separator, in order to bring the frequency measured into the range of the signal processor and to resolve directional ambiguity of a moving particle.

The laser beam power and the way in which it is transmitted to the optical probe are of vital importance for experiments. The fibre-optical cables are employed in order to obtain the maximum benefit of the laser power transmitted and of the scattered light which is focused by receiving lens of the optical probe into these cables for transmission to the photo-detectors. Photo-detectors convert the received scattered light into an electrical-voltage signal using the photo-multiplier system.

The signal processor (TSI, IFA 750) receives a voltage signal from photo-multiplier system, and this signal is then filtered, analysed and converted into velocity information. The signal processor communicates with a PC computer through, a direct memory access card (TSI, DMA model 6264) and FFW 1.0 software (TSI, Inc.) is used to collect velocity data and to provide complete velocity statistics for LDV data.

The filtered signal from the processor can be monitored on the oscilloscope (ITT Instruments, model OX 750 B) allowing a better adjustment of LDV operational parameters (band-pass filters, frequency shift, threshold).

The optical probe, which transmits the four laser beams and receives the scattered light, is mounted on an automatic 3D positioning system called *traverse table* (TSI, Isel). The traverse table allows automated measurements on a grid of positions by a very precise displacements of the optical probe position. Optical probes of two different sizes, $d_p = 15$ mm (TSI, model 9802) and $d_p = 83$ mm (TSI, model 9253), were used in the measurements. The probe with smaller focal distance was only used when immersed from the top into the ST. The second of longer focal distance was placed below the bottom of the ST and allowed totally non-intrusive measurements. The measurements using the probe of longer

focal distance were performed on a coarser grid of positions near the impeller, baffle and wall. The main characteristics for each probe are shown on Table 3.1.

The higher power of laser beam increases the signal to noise ratio and the velocity information is available at the higher data rates. In addition, small nylon particles of diameter 4 μm (TSI, Pt-900845) and neutrally buoyant relative to the fluid flow, were added to the stirred tank This in order to improve the quality of a signal to noise ratio resulting in a higher data rate.

The complete LDV system consists of: a 5W Argon-Ion laser (Coherent, Innova 305); a beam collimator (TSI, model 9108); a multicolour beam separator (TSI, Colorburst model 9802); four optical couplers (TSI, model 9271); a two-velocity components probe (TSI, model 9802 or 9253-350) with connecting fibre-optical cables; receiving optics equipment (TSI, Colorlink 9230); and a signal processor (TSI, IFA 750 Digital Burst Correlator). Two different views of the LDV system are shown in Figure 3.4 and Figure 3.5, and a schematic representation of the system is presented in Figure 3.6.

The hardware and software settings are also reported on Table 3.1. The hardware settings (band-pass filters, frequency shift) were adjusted after the calculation of the expected frequency of Doppler signal. This calculation was based on the expected average flow velocity (e.g. impeller rotational speed) and on the optical fringe spacing. The value of the expected Doppler frequency plus the frequency shift was then placed into the frequency limits of band-pass filters.

The software settings (measuring volume parameters on Table 3.1) related to changes of refractive index of used liquids were carefully readjusted. Fluid 1 and Fluid 2 on Table 3.1 refer to glycerol mixtures with viscosity of 40 mPa·s and 134 mPa·s, respectively.

Table 3.1 LDV system parameters.

Probe	**15 mm**		**83 mm**	
Channel	**1**	**2**	**1**	**2**
Beam parameters:				
Nominal power (Watt)	5	5	5	5
Wavelength in vacuum (nm)	514.5	488.0	514.5	488.0
Beam diameter (mm)	0.5	0.5	0.5	0.5
Measuring volume parameters:				
Half-angle of intersection in air	3.81°	3.81°	3.95°	3.95°
Half-angle of intersection in water	2.86°	2.86°	-	-
Half-angle of intersection in fluid 1	2.66°	2.66°	-	-
Half-angle of intersection in fluid 2	2.66°	2.66°	-	-
Diameter in air (mm)	0.11	0.11	0.090	0.078
Diameter in water (mm)	0.11	0.11	-	-
Diameter in fluid 1 (mm)	0.11	0.11	-	-
Diameter in fluid 2 (mm)	0.11	0.11	-	-
Length in air (mm)	1.68	1.59	1.3	1.3
Length in water (mm)	2.10	1.99	-	-
Length in fluid 1 (mm)	2.44	2.31	-	-
Length in fluid 2 (mm)	2.49	2.37	-	-
Number of fringes:				
air	23	23	24	24
water	20	20	-	-
fluid 1	20	20	-	-
fluid 2	20	20	-	-
Fringe spacing (μm):				
air	3.87	3.67	3.72	3.52
water	5.15	4.88	-	-
fluid 1	5.55	5.29	-	-
fluid 2	5.62	5.33	-	-
Band-pass filters:				
low impeller rotational speeds	0.1-1MHz	0.1-1MHz	0.1-1MHz	0.1-1MHz
high impeller rotational speeds	0.3-3MHz	0.3-3MHz	-	-
Frequency shift parameters:				
low impeller rotational speeds	+500 kHz	-500 kHz	+500 kHz	-500 kHz
high impeller rotational speeds	+2 MHz	-2 MHz	+2 MHz	-2 MHz

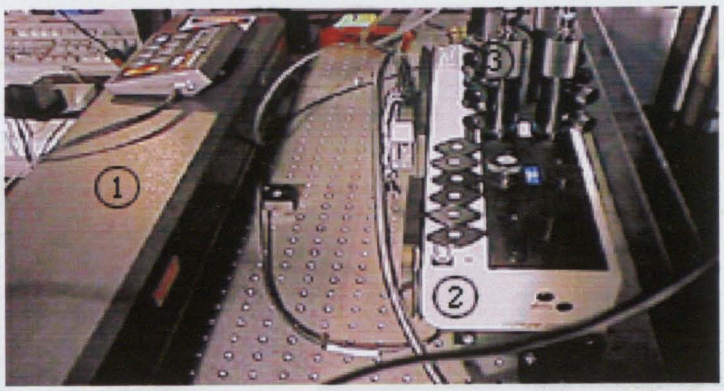

1 - Laser source
(Argon-Ion, 5 watts)

2 - Bragg cell
(TSI, Colorburst model 9201)

3 - Optical couplers
(TSI, model 9271)

Figure 3.4 Partial view of the LDV optical system.

1 - Signal receiver
(TSI, Colorlink 9230)

2 - Signal processor
(TSI, IFA 750)

3 - IBM PC 350+ software
(TSI, FFW 1.0)

4 - Oscilloscope
(ITT, OX 750B)

Figure 3.5 View of the LDV data acquisition system.

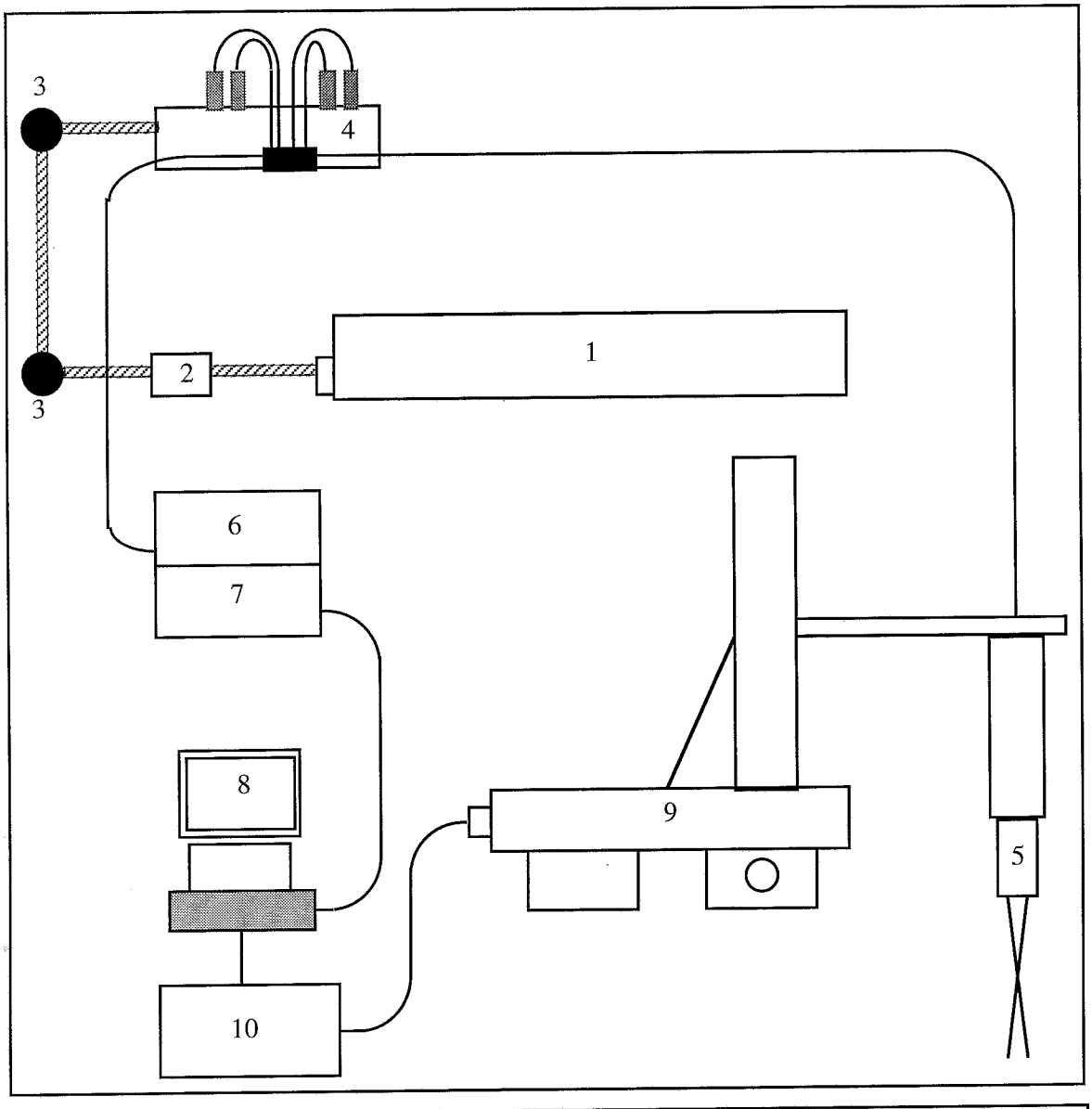

1 - Laser source (Argon-Ion, 5 watts)
2 - Collimator (TSI, model 9108)
3 - Mirrors (TSI, model 9109)
4 - Bragg cell (TSI, Colorburst model 9201)
5 - Optical probe (TSI, 15 mm or 83 mm)
6 - Signal receiver (TSI, Colorlink 9230)
7 - Signal processor (TSI, IFA 750)
8 - IBM PC 350 (TSI, FFW 1.0 software)
9 - Traverse table (TSI, Isel)
10 - Traverse table controller (TSI, Isel)

Figure 3.6 Schematic representation of the LDV system.

3.2.3 LDV Measurements and Derived Quantities

This section provides some details on LDV measurements, and makes a list of all measured and derived quantities as they are presented in this chapter. An analysis of uncertainties associated with the measurements is also given and therefore, the text is organised by the following items:

- *realisation of LDV experiments;*
- *measured quantities ;*
- *calculated quantities ;*
- *analysis of experimental and statistical uncertainty.*

The first item on *realisation of LDV measurements* introduces the measured regions and describes the experimental conditions and data acquisition. The second item covers the *measured quantities* — mean and fluctuation velocities, turbulence intensity and shear Reynolds stresses — as they are obtained by the LDV technique. The first of them is used to express the *derived quantities* — impeller Reynolds number and Flow number — as specified in the third item. The measured and independent variables are presented in dimensionless forms also reported in the third item. The sources of *experimental and statistical uncertainties* are summarised in the last item.

- ***Realisation of LDV Experiments***

According to Tatterson (1991), mixing can be considered to occur in two areas. The flow passing through the vortex systems of the Rushton impeller and the area where the impeller discharge flow is disrupted by the flow in the bulk of a tank.

The *impeller region* and the *impeller discharge flow region* (see Figure 3.7) were investigated experimentally due to the occurrence of abrupt hydrodynamic changes caused by the impeller rotation or the presence of a baffle. The two specific regions — the *impeller centre plane* and the *baffle region* — that were also inspected make part of the impeller discharge flow region. Selection of these regions was based on a careful analysis of studies in the literature, as reported in Chapter 2, and the data provided a good insight on the characteristic of flow patterns.

All presented experiments were performed using the LDV system on the experimental set-up as described in previous sections. Measurements were always conducted at the laboratory temperature (20°C) and room pressure. The temperature changes of the fluid due to viscous dissipation were assumed negligible. The liquids used varied from the pure water to glycerol mixtures. The range of fluid densities varied from 1000 $kg \cdot m^{-3}$ to 1230 $kg \cdot m^{-3}$ measured with a pycnometer. The fluid viscosity varied from 1 $mPa \cdot s$ to 143 $mPa \cdot s$ and these values

were determined by measuring the refractive index with a refractometer (Bausch & Lomb, Abbe-3L). The dependence of viscosity on the refractive index was obtained from data on physical properties of glycerol mixtures.

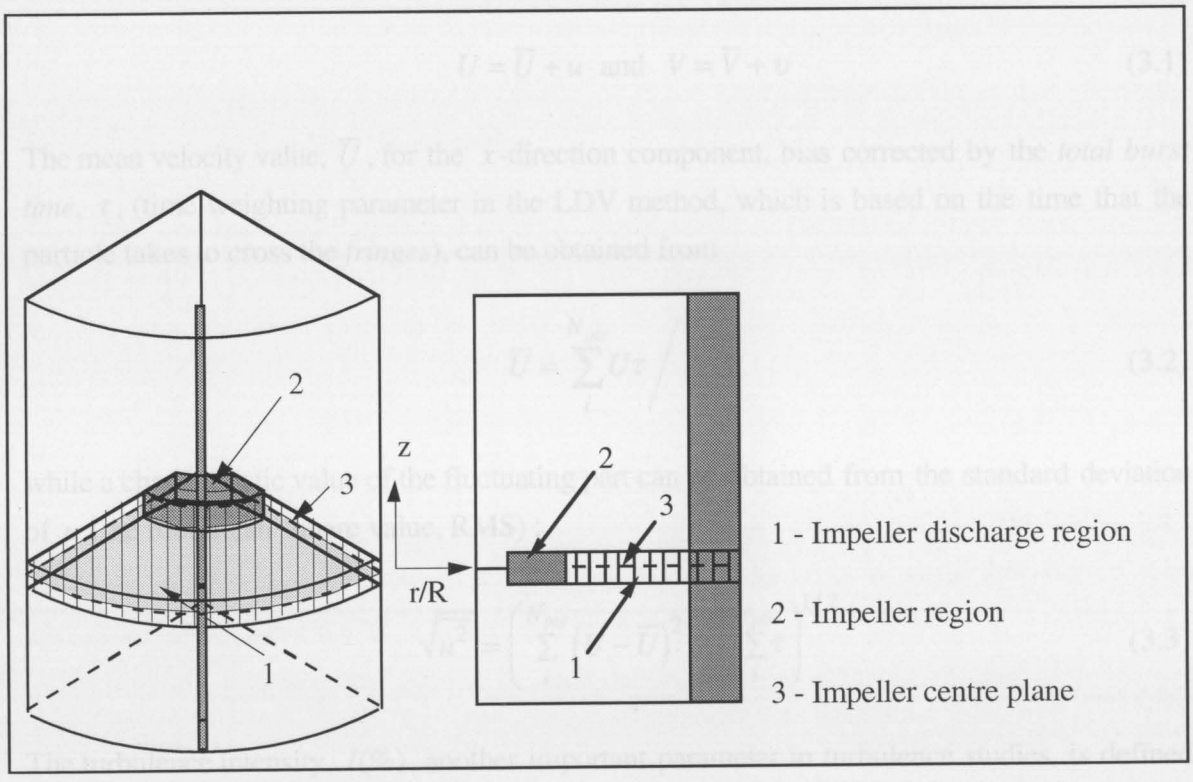

Figure 3.7 *Schematic representation of the mixing tank showing the selected regions for measurements.*

A fixed frame of reference was used to compute the local velocity components (Figure 3.7). The data was obtained in the Cartesian co-ordinate system with its origin located at the centre of the impeller. Some of the velocities are reported in a cylindrical co-ordinate system using relationships derived in Appendix A, but the axial-vertical axis is identical for both co-ordinate systems.

The number of samples, N_{pts} required to achieve statistically meaningfull results, depends on the local velocity fluctuations and is reported in each section individually. Also, two different modes of data acquisition were used. The *random mode* acquired and validated the data from two channels for each velocity component independently. In the *coincidence mode* signals from two channels about the two velocity components were acquired and validated within a specified time coincidence window. The selected mode is reported for each measurement.

- ***Measured Quantities***

Taking U and V to be the instantaneous velocity components in two arbitrary normal x and y directions, and by applying the decomposition of the U velocity on the mean plus the fluctuating part, then:

$$U = \overline{U} + u \quad \text{and} \quad V = \overline{V} + \upsilon \tag{3.1}$$

The mean velocity value, $\overline{U}$, for the x-direction component, bias corrected by the *total burst time*, τ, (time weighting parameter in the LDV method, which is based on the time that the particle takes to cross the *fringes*), can be obtained from

$$\overline{U} = \sum_{i}^{N_{pts}} U\tau \Big/ \sum_{i}^{N_{pts}} \tau \tag{3.2}$$

while a characteristic value of the fluctuating part can be obtained from the standard deviation of u (the root mean square value, RMS) :

$$\sqrt{\overline{u^2}} = \left(\sum_{i}^{N_{pts}} \left(U - \overline{U}\right)^2 \tau \Big/ \sum_{i}^{N_{pts}} \tau \right)^{1/2} \tag{3.3}$$

The turbulence intensity, $I(\%)$, another important parameter in turbulence studies, is defined as

$$I(\%) = 100 \times \sqrt{\overline{u^2}} / \overline{U} \tag{3.4}$$

The same statistical values can be obtained for the other velocity component, V.

For a liquid of density, ρ, the τ_{xy}^{t} Reynolds stress component can be calculated as:

$$\tau_{xy}^{t} = -\rho \overline{u\upsilon} = -\rho(\overline{UV} - \overline{U}\ \overline{V}) \tag{3.5}$$

where $\overline{UV}$ is obtained from:

$$\overline{UV} = \sum_{i}^{N_{pts}} UV\Delta t_o \Big/ \sum_{i}^{N_{pts}} \Delta t_o \tag{3.6}$$

with the *overlap time* Δt_o, being the smallest of the two measured burst times for each coincident detection of the two velocity components, U and V.

- ***Derived Quantities***

The *impeller Reynolds number*, Re, for the ST is defined as:

$$Re = \frac{4\rho NR^2}{\mu} \tag{3.7}$$

where N is *the impeller rotational frequency*, R is the impeller radius, and ρ and μ are the liquid density and viscosity, respectively.

The *flow or pumping number*, Fl, is a dimensionless parameter often used for the characterisation of the radial flow in the ST. Its value expresses the ratio between the radial and the tangential flow rates and is dependent on the relative radial position, r/R. This is defined as:

$$Fl = \frac{Q_r}{8NR^3} \tag{3.8}$$

where Q_r is the radial flow rate at a certain radial position, r/R, N is the impeller rotation and R is the impeller radius. The radial flow rate away from the impeller, Q_r, between the lower horizontal plane at the position $-z_l$ and the upper plane at z_u, is computed as:

$$Q_r = R\int_{-z_l}^{z_u} dz \int_0^{2\pi} (r/R)V_r d\theta \tag{3.9}$$

at three radial positions $r/R = 1.1,\ 1.3, 1.5$.

All the reported measured and derived quantities are expressed in dimensionless values. Main flow patterns are constructed from the mean velocity data normalised by the velocity at the tip of impeller given by:

$$V_{tip} = 2\pi NR \tag{3.10}$$

The normalised radial, tangential and axial components of the local velocities are expressed as V_r/V_{tip}, V_θ/V_{tip} and V_z/V_{tip}, respectively.

Turbulence parameters, such as the velocity fluctuations, are also normalised by V_{tip}. The turbulent kinetic energy can be computed using the velocity fluctuations v_r, v_θ and v_z in cylindrical co-ordinate system as

$$k = \left(v_r^2 + v_\theta^2 + v_z^2\right)/2 \tag{3.11}$$

and the k is always reported normalised by the square of V_{tip}, that is k/V_{tip}^2.

The measured Reynolds stresses are given in dimensionless form by:

$$\tau_{xy}^t/\rho V_{tip}^2 = -\overline{uv}/V_{tip}^2 \tag{3.12}$$

Furthermore, the independent variables are also expressed in dimensionless form where the radial co-ordinate is normalised by the impeller radius, r/R, and the axial co-ordinate by the impeller blade width, $2z/W$.

- ***Analysis of Experimental and Statistical Uncertainty***

To establish the experiment precision and final accuracy the all sources of uncertainty must be discussed. The uncertainties of LDV measurements originate from the instruments precision and statistical uncertainty. The instruments uncertainty vary from the overall precision of the LDV system, to the adjustment of the speed drive controller and the accuracy of the traverse table.

A possible reason for experimental uncertainty is related to the adjustment of the frequency of the impeller rotation. The speed drive controller works from 0.1 Hz to 100 Hz with the 0.01%accuracy. The rotational speed of the impeller was checked by a video camera and the uncertainty was found less then 1%. The probe is mounted on the positioning traverse table with the step resolution of 0.01 mm. Thus, the traverse table positioning uncertainty is less then 1% for the maximum number of consecutive steps performed in one experiment. In addition, the position of measuring volume was regularly checked on a reference mark of known co-ordinates that was located on the impeller disk.

The overall LDV system uncertainty can be decomposed into the following contributions. Focal length error of TSI lenses is reported as 1%. Likewise, the error in the angle of the focusing lens is known to be within 1%. The accuracy of the fringe spacing is within 0.2%, and the total error in the velocity data from the signal processors is within 0.5% accuracy.

The main source of statistical uncertainty of mean velocity values is biasing, based on the realisation that more particles at a higher velocity pass through the measuring volume than those at lower velocities. However, measurement biasing can be corrected. The transit time weighting, τ, was automatically performed by the software to correct for velocity bias. Mean velocities and standard deviations were corrected using Equations 3.2 and 3.3, respectively. By applying the analysis of Buchhave *et al.* (1979), the Reynolds stresses data can be unbiased by weighting using the overlap time of two transit times, as shown in Equation 3.6.

The 95% confidence interval for the estimation of the mean velocities, based in a normal distribution, is:

$$\overline{U} \pm 1.96\left(\overline{u^2}/N_{pts}\right)^{1/2} \tag{3.13}$$

and this confidence interval is symmetric about the estimate and simple to calculate.

Unfortunately, most turbulence flow quantities are not always normally distributed and equations for confidence intervals of higher moments are difficult to find if the type of distribution is unknown (Benedict and Gould, 1996). For these cases, Kendall and Stuart (1958) presented the general equations for the sampling variance of univariate and bivariate central moments based on theory of large samples (see Benedict and Gould, 1996). These equations are valid for arbitrary distribution functions as long as N_{pts} is large, and were applied by Benedict and Gould (1996) to the turbulence quantities with the simple requirement of independence between the samples. The estimations of variance for the mean, fluctuating velocities, and Reynolds stresses are given on Table 3.2 for the normal distribution and for any general distribution shape (for details see Benedict and Gould, 1996).

Table 3.2 95% confidence interval estimations for LDV statistics.

	Normal distribution	**General distribution**
Mean velocity	$\pm 1.96\left(\overline{u^2}/N_{pts}\right)^{1/2}$	$\pm 1.96\left(\overline{u^2}/N_{pts}\right)^{1/2}$
Velocity fluctuations	$\pm 1.96\left(\overline{u^2}/2N_{pts}\right)^{1/2}$	$\pm 1.96\left(\left(\overline{u^4}-\left(\overline{u^2}\right)^2\right)/4\overline{u^2}N_{pts}\right)^{1/2}$
Reynolds stresses*	$\pm 1.96\left(\left(1+R_{uv}{}^2\right)\left(\overline{u^2}\right)\left(\overline{v^2}\right)/N_{pts}\right)^{1/2}$	$\pm 1.96\left(\left(\overline{u^2v^2}-\left(\overline{uv}\right)^2\right)/N_{pts}\right)^{1/2}$

* $R_{uv} = \left(\overline{uv}\right)/\left(\sqrt{\overline{u^2}}\sqrt{\overline{v^2}}\right)$ correlation coefficient.

Estimations on the relative errors for the all measured LDV quantities, based on these 95% confidence intervals are given on Table 3.3. As can be seen, the uncertainty of the mean and the fluctuating velocity is small and therefore is not reported in the velocity results. The uncertainty of the measured Reynolds stresses is not negligible and is reported when necessary.

Table 3.3 Typical -relative errors of LDV statistics.

	Normal distribution			General distribution		
Re	5000	10000	20000	5000	10000	20000
Mean velocity	0.8%	0.8%	0.9%	0.8%	0.8%	0.9%
Velocity fluctuations	1.4%	1.4%	1.4%	1.6%	1.5%	1.4%
Reynolds stresses	5.0%	11.0%	15.0%	4.0%	11.0%	8.0%

The uncertainty of the impeller Reynolds number is related with the precision of measurements of the impeller rotational speed (less then 1%), and with determination of the viscosity and the density. The uncertainty of density measurements is 0.3% and the uncertainty of the viscosity determination, based on the measurement of refractive index, is 0.2%. Therefore, the maximum uncertainty of the Reynolds number determination is within 1.5%.

3.3 LDV Data Analysis

The results of LDV experiments are organised in four independent sections by the region inspected:

- *flow in the impeller discharge region;*
- *flow in the impeller region;*
- *flow at the impeller centre plane ;*
- *flow in the baffle region.*

The main goals of examinations in each investigated region are summarised here.

- Understanding the nature of the *impeller discharge flow* is very important for modelling the mixing process in the ST (Tatterson, 1991). A comprehensive body of investigation has been dedicated to this region in the literature (see for example Stoots and Calabrese, 1995; Wu and Patterson, 1988) and in the present work. The velocity mean and the fluctuating velocity near the surface swept by the impeller blades are studied in Section 3.3.1. The effect of the impeller off-bottom clearance on the impeller discharge flow is commented. Data measured in this region is necessary for the specifications of the boundary conditions necessary for numerical predictions, as it will be shown in Chapters 4 and 5.

- Investigation of the flow in the *impeller region* has obtained less attention in experimental studies of the ST (see Chapter 2). Main experimental difficulties using LDV technique

are due to the regular intersection of the measuring volume (created by two pairs of four laser beams) by passages of the impeller blades. Nonetheless, it was stimulating for the present work to explore the flow in the impeller region, since the information could be very useful in the modelling of the ST mixing process. Section 3.3.2 shows the results of the study in the impeller region.

- The region given at the *impeller centre plane* was examined for velocity components and shear Reynolds stresses in the transition from the laminar to turbulent regime and in the turbulent flow regime in Section 3.3.3. The shear Reynolds stresses are difficult to measure, but their knowledge is very important for mixing with chemical reactions. The main goal is to clarify their spatial structure with increasing values of Reynolds number and to use the data for comparisons with numerical predictions.

- Baffles are used to enhance the axial motion in the ST at the expense of tangential motion. Therefore, it is interesting to observe also the flow in the *baffle region*. The goal of study presented in Section 3.3.4 is to examine the shear stresses generated near the baffles.

Each section is subdivided into three subsection with experiment description, results and conclusions.

The results are presented in the form of profiles of measured data along the radial or tangential directions and in the form of maps visualising the data distributions in the regions under investigation. These maps were created by interpolation and smoothing of the measured data within the specified regions and overlaid with contour plots in order to facilitate their interpretation.

3.3.1 Flow in the Impeller Discharge Region

3.3.1.1 Experiment description

The radial and tangential velocities were measured outside of the tip of the impeller blades. This region, known as the impeller discharge flow region, (see Figure 3.7) is dominated by a strong radial stream coming out of the Rushton impeller. Profiles of the mean velocity and intensity of velocity fluctuations were measured using the $d_p = 15$ mm probe. Due to its short focal distance, the probe was immersed in the fluid from the top of the ST, and it was assumed that the probe creates negligible disturbance in the flow due to its small size. This assumption will be validated in the following sections.

Plain tap water was used as a working medium in the stirred tank. The experiment was conducted at $Re = 20000$, corresponding to the impeller rotation of $N = 2.0$ Hz. Local radial and tangential components were acquired in the LDV random mode.

The acquired data provide information on that part of the impeller discharge flow region where the pseudo-turbulence is present. For this purpose, the area corresponding to the horizontal plane where the radial co-ordinate spans from the impeller blade tip to double of the impeller radius was assumed satisfactory.

Data was taken at seven horizontal planes with 0.5 cm distance in between, according to Figure 3.8.

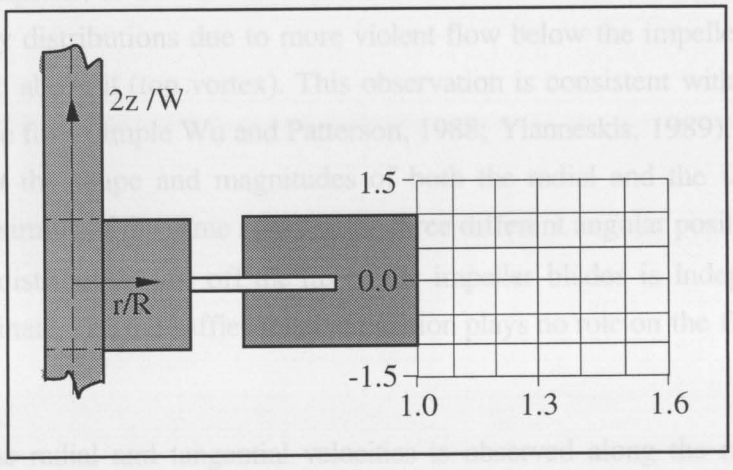

Figure 3.8 Vertical grid for LDV measurements.

The measurement grid depicted in Figure 3.9 was used to collect data at each of the seven planes. The grid covers a range of θ from $\pi/12$ to $5\pi/12$ with $\Delta\theta = 5\pi/180$, and a range of radii from $r/R = 1.0$ to $r/R = 1.6$ with a spacing of $\Delta r/R = 0.1$. The total number of measured grid points was 637. The number of measured samples per point was, $N_{pts} = 2048$.

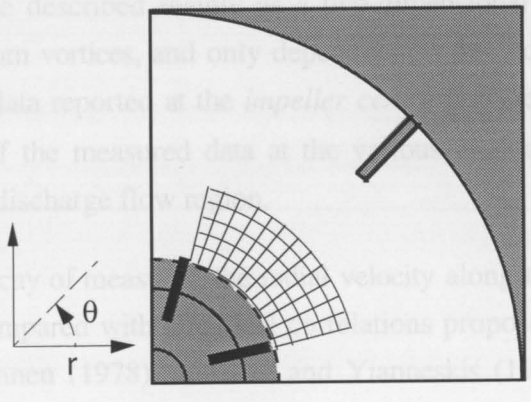

Figure 3.9 Horizontal grid for LDV measurements.

3.3.1.2 Results

Figure 3.10 shows the evolution along the radial direction of the normalised velocity profiles for the radial and the tangential components at three different angular positions ($\theta = \pi/12$, $\pi/4$ and $5\pi/12$).

First analysis of these plots demonstrates the effect of the impeller off-bottom clearance. The position of the impeller, at the $C = T/3$ from the tank bottom, results into an asymmetric profile of velocity distributions due to more violent flow below the impeller (bottom vortex) than in the region above it (top vortex). This observation is consistent with data reported by many authors (see for example Wu and Patterson, 1988; Yianneskis, 1989). Furthermore, the results show that the shape and magnitudes of both the radial and the tangential velocity profiles are very similar at the same radii for the three different angular positions. This proves that the velocity distribution just off the tip of the impeller blades is independent of the θ tangential co-ordinate, i.e., the baffles relative position plays no role on the flow-field near the impeller.

Decay in both the radial and tangential velocities is observed along the radial direction. A narrow peak (approximately a range of $2z/W = \pm 0.5$) of a strong radial stream, originating at the impeller tip, proceeds towards the wall at magnitudes higher than those of the tangential motion at the same radial co-ordinate. However, the tangential motion starts to prevail with increasing axial distance from the *impeller centre line*. This flow image supports the main characteristic of radial impellers. In general, it can be seen as the radial stream being injected into the overall rotational motion.

The *impeller centre plane* is a very specific part of the discharge flow region. Near this plane the flow field that can be described mainly as a two-dimensional parallel flow, occurring between the top and bottom vortices, and only dependent on the radial co-ordinate along the impeller centre line. The data reported at the *impeller centre line* are presented for each radii as the spatial averages of the measured data at the various angular co-ordinates, θ of the measurement grid of the discharge flow region.

Figure 3.11 shows the decay of measured the radial velocity along the impeller centre line in this work. This data is compared with empirical correlations proposed independently by Van der Molen and Van Mannen (1978), and Lee and Yianneskis (1998), based on their own LDV data for the standard ST configuration, taken at different values of Re.

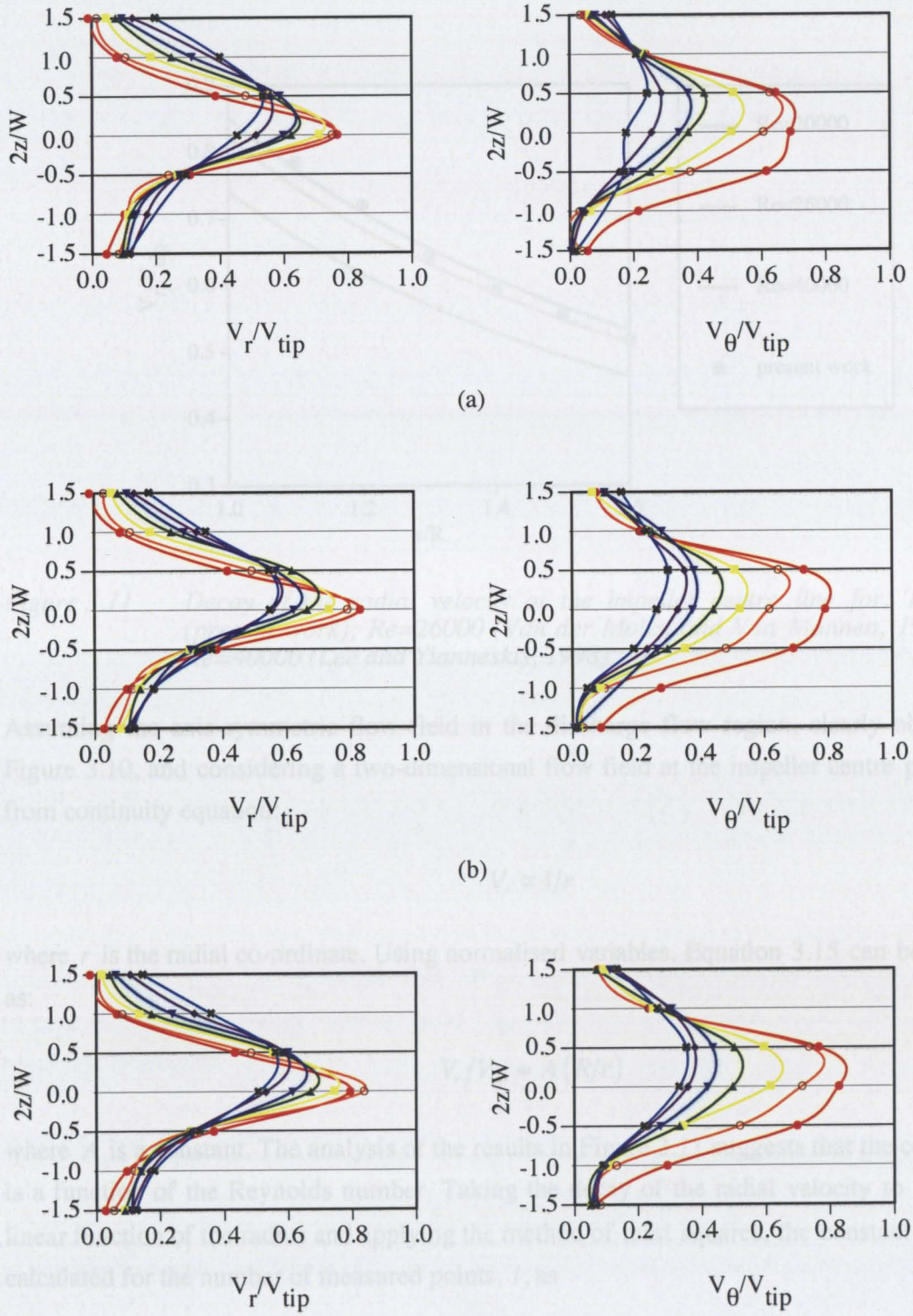

Figure 3.10 *Radial and tangential velocity profiles for three values of θ: a) $\theta = \pi/12$; b) $\theta = \pi/4$; c) $\theta = 5\pi/12$ at Re=20000.*

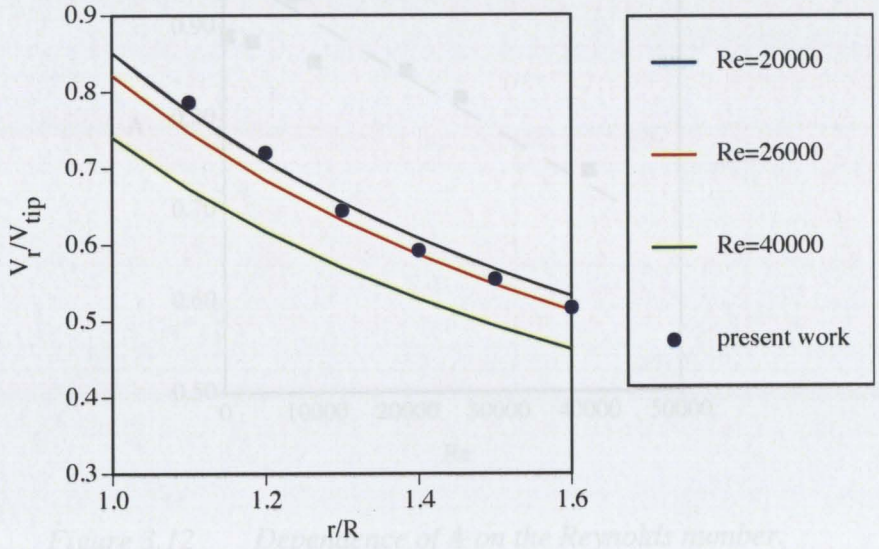

Figure 3.11 *Decay of the radial velocity at the impeller centre line for: Re=20000 (present work); Re=26000 (Van der Molen and Van Mannen, 1978); and Re=40000 (Lee and Yianneskis, 1998).*

Assuming the axis-symmetric flow field in the discharge flow region, clearly observed in Figure 3.10, and considering a two-dimensional flow field at the impeller centre plane, then from continuity equation:

$$V_r \propto 1/r \tag{3.14}$$

where r is the radial co-ordinate. Using normalised variables, Equation 3.15 can be rewritten as:

$$V_r/V_{tip} = A\left(R/r\right) \tag{3.15}$$

where A is a constant. The analysis of the results in Figure 3.11 suggests that the constant A is a function of the Reynolds number. Taking the decay of the radial velocity to be a non-linear function of the radius and applying the method of least squares, the constant A can be calculated for the number of measured points, i, as

$$A = \sum_i (RV_r)/(rV_{tip}) \Big/ \sum_i (R/r)^2 \tag{3.16}$$

Figure 3.12 presents the dependence of the constant A with the Reynolds number. And it shows clearly that A decreases with Re. To confirm this trend a few additional points were taken from other measurements using different liquid viscosities, and are plotted also in Figure 3.12. These points were obtained for Re = 450; 900; 3100 and 10000 from the experiments that will be presented in Section 3.3.3.

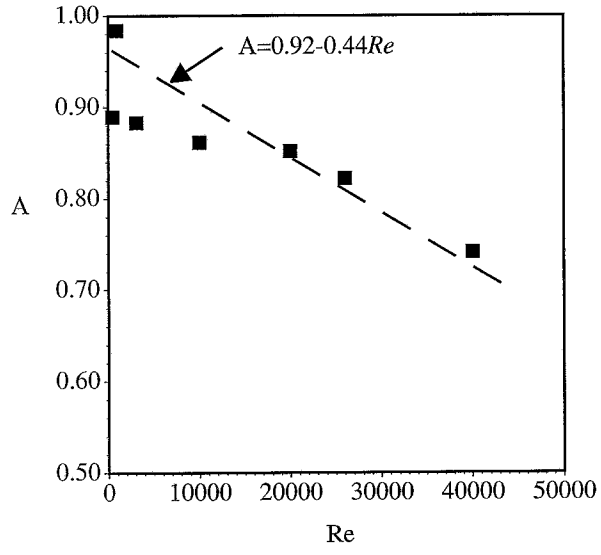

Figure 3.12 Dependence of A on the Reynolds number.

Figure 3.13 show the axial profiles of radial and tangential velocity fluctuations at $\theta = \pi/4$, and Figure 3.14 show the same profiles for radial and tangential turbulence intensities for the same region.

The radial and tangential velocity fluctuations profiles are quite similar, indicating the periodic and pulsating nature of the flow induced by the impeller rotation. Also, it is clear from these data that the turbulent flow inside the impeller discharge flow region is homogeneous but strongly anisotropic in the radial and axial directions. Moreover, this is particularly clear in the turbulence intensity plots. This reinforces the idea of difference in the flow of the top and bottom vortices. In Figure 3.14, the top vortex has a stronger rotation with higher radial turbulence intensities, and the bottom vortex has a stronger axial motion with larger tangential turbulence intensities.

Figure 3.15 plots the decay of the radial velocity fluctuation along r/R. The data follows similar trends to previously published data, condensed into Dyster *et al.* (1993) correlation, $v_r/V_{tip} = 0.48 - 0.16(r/R)$. More recently, Lee and Yianneskis (1998) proposed a different correlation $v_r/V_{tip} = 0.45 - 0.13(r/R)$ based on data taken at $Re = 40000$. The differences found in the data, do not follow a consistent trend with Re, as it was observed for the mean radial velocity profile.

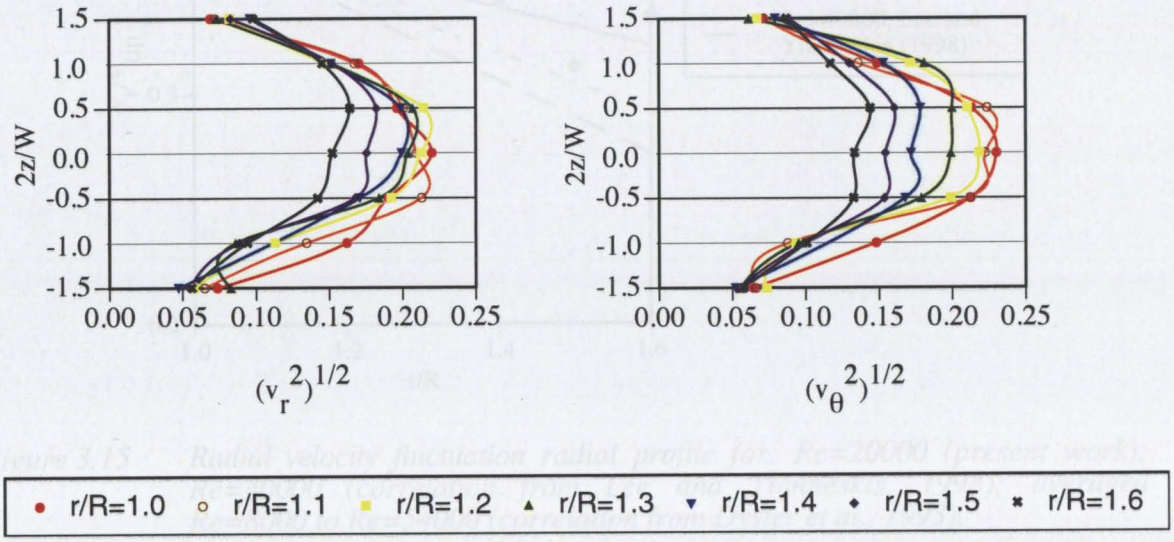

Figure 3.13 Radial and tangential velocities fluctuations profiles for Re=20000.

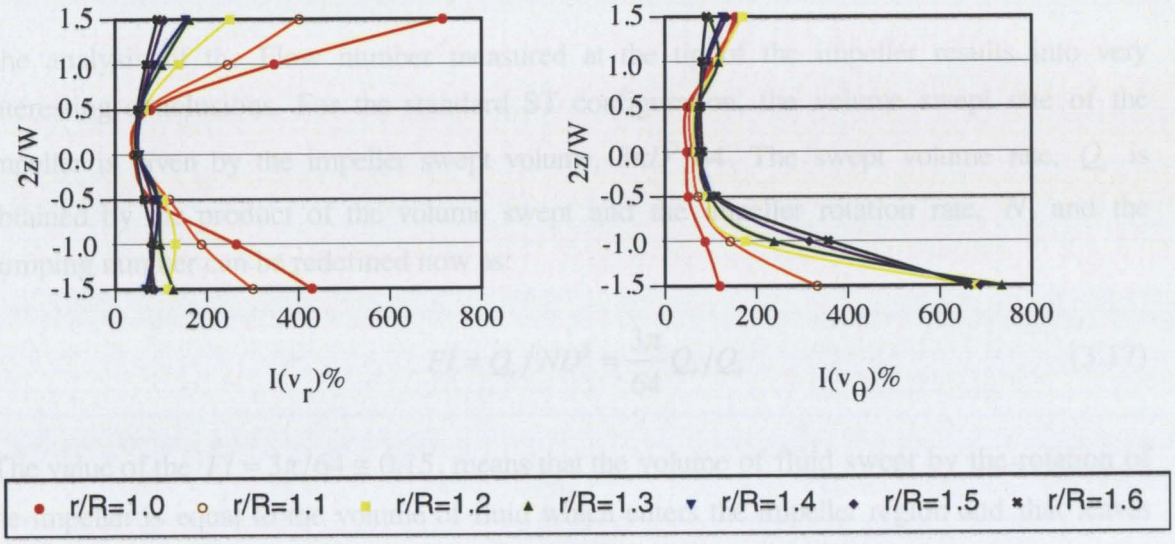

Figure 3.14 Radial and tangential turbulence intensities for Re=20000.

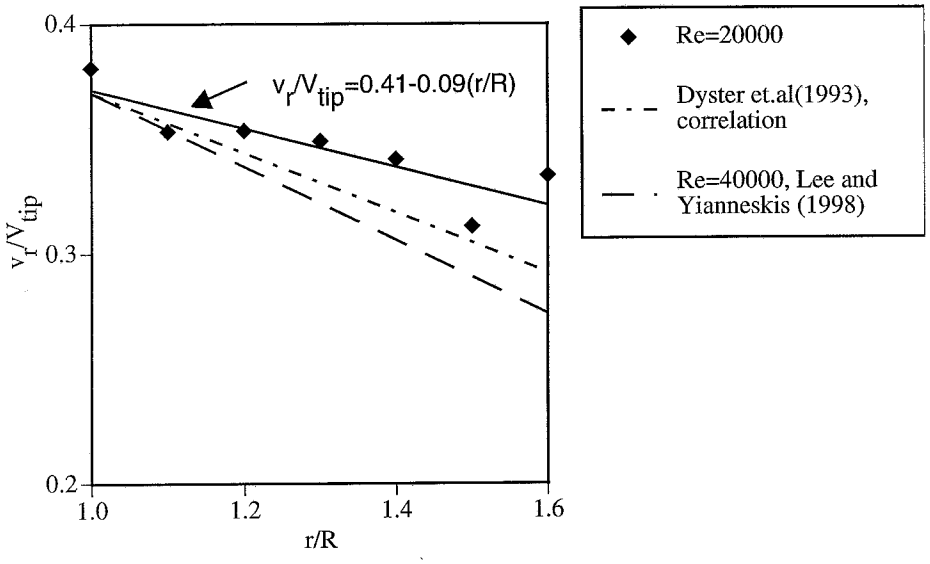

Figure 3.15 *Radial velocity fluctuation radial profile for: Re=20000 (present work); Re=40000 (correlation from Lee and Yianneskis, 1998); averaged Re=8000 to Re=54000 (correlation from Dyster et al., 1993).*

Figure 3.16 shows the Flow number values obtained in the present work and from the literature. Data from the present work agrees very well with data of Gunkel and Weber (1975). However, it should be noted that data from the present work might be slightly underestimated at the values of $r/R = 1.3$ and 1.5. Since the measured limits (see Equation 3.9) of the axial range can be narrower than the real range where the radial jet extends.

The analysis of the Flow number measured at the tip of the impeller results into very interesting conclusions. For the standard ST configuration, the volume swept rate of the impeller is given by the impeller swept volume, $3\pi D^3/64$. The swept volume rate, Q_s is obtained by the product of the volume swept and the impeller rotation rate, N, and the pumping number can be redefined now as:

$$Fl = Q_r/ND^3 = \frac{3\pi}{64} Q_r/Q_s \tag{3.17}$$

The value of the $Fl = 3\pi/64 \cong 0.15$, means that the volume of fluid swept by the rotation of the impeller is equal to the volume of fluid which enters the impeller region and that leaves this region per unit time. For $Fl = 0.0$, the impeller region rotates only as a solid body. The flow number can provide fundamental information about the impeller effectiveness. Results from other works (Gunkel and Weber, 1975; Wu and Patterson, 1989; Stoots and Calabrese, 1989) shown in Figure 3.16, indicate that increasing the impeller rotational speed, higher Reynolds number, does not offer an expected improvement of the pumping performance in terms of the radial jet coming out of the impeller, decreasing the measured values of Fl at the impeller tip.

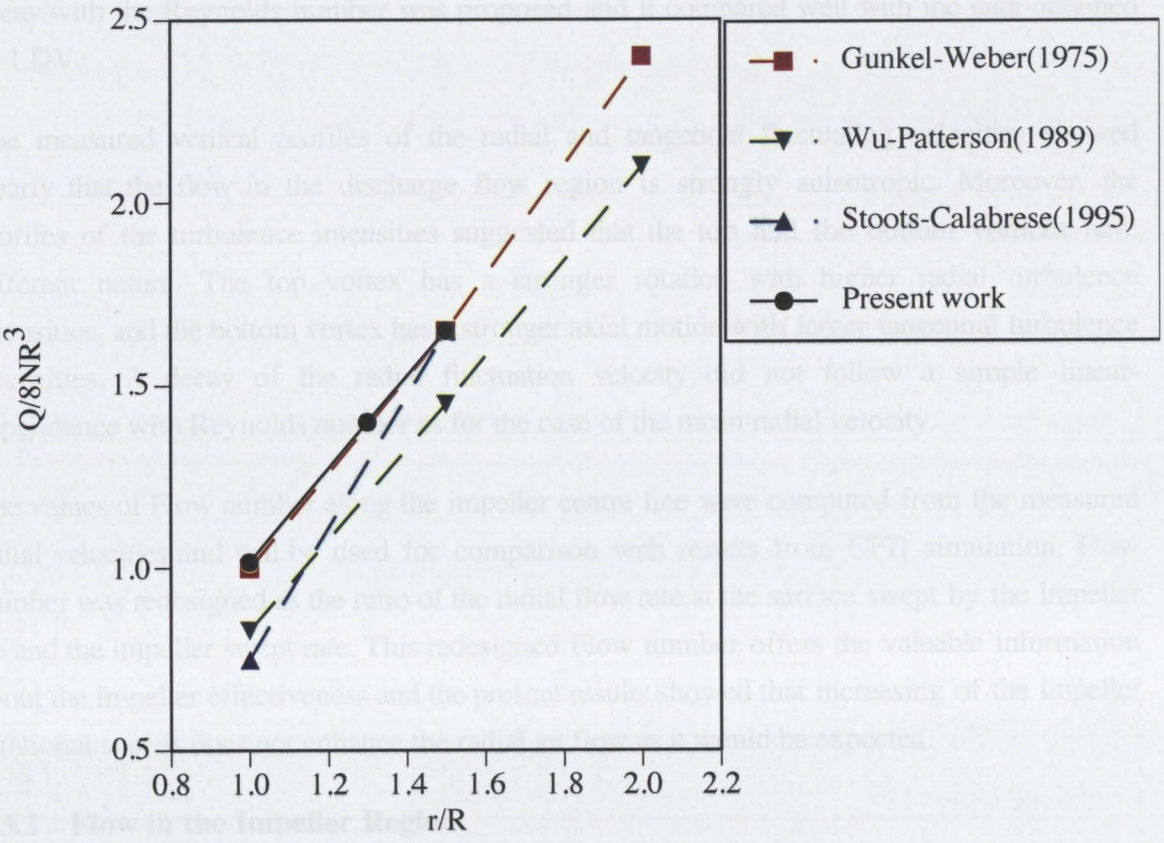

Figure 3.16 *Flow number radial profile at the impeller centre line position for Re=20000 (present work), and obtained from data averaging on the ranges: Re=8000-22000 (Gunkel and Weber, 1975); Re=14000-43000 (Wu and Patterson, 1989); and Re=29000-46000 (Stoots and Calabrese, 1989).*

3.3.1.3 Conclusions

The radial and tangential velocity profiles obtained in this work were found consistent with other data reported in the literature. The analysis of these velocity profiles at the three different values of the angular θ co-ordinate showed that the flow at the tip of the impeller and in the investigated region of the impeller discharge flow is axis-symmetric. This is very important conclusion that will be helpful for the specification of boundary conditions in CFD simulations presented in Chapter 5.

The impeller off-bottom clearance, C, imposed a non-symmetrical shape of vertical profiles of the mean velocity components in the discharged flow field.

The experimental results showed that decay of the mean radial velocity along the impeller centre line depends on the Reynolds number. The function of this decay was derived theoretically based on simple assumptions of the axis-symmetric and two-dimensional parallel flow at the impeller centre plane. The theoretical dependence of the radial velocity

decay with the Reynolds number was proposed and it compared well with the data obtained by LDV.

The measured vertical profiles of the radial and tangential fluctuating velocities showed clearly that the flow in the discharge flow region is strongly anisotropic. Moreover, the profiles of the turbulence intensities suggested that the top and the bottom vortices have different nature. The top vortex has a stronger rotation with higher radial turbulence intensities, and the bottom vortex has a stronger axial motion with larger tangential turbulence intensities. A decay of the radial fluctuation velocity did not follow a simple linear-dependence with Reynolds number as for the case of the mean radial velocity.

The values of Flow number along the impeller centre line were computed from the measured radial velocities and will be used for comparison with results from CFD simulation. Flow number was redesigned as the ratio of the radial flow rate at the surface swept by the impeller tip and the impeller swept rate. This redesigned Flow number offers the valuable information about the impeller effectiveness and the present results showed that increasing of the impeller rotational speeds does not enhance the radial jet flow as it would be expected.

3.3.2 Flow in the Impeller Region

3.3.2.1 Experiment description

Measurements of the radial and tangential velocities were performed in the *impeller region* (see Figure 3.7). The data was obtained using the $d_p = 15$ mm probe and the random mode of LDV data acquisition, in the same way, as described in Section 3.3.1.

Measurements were conducted at two vertical planes with angles θ within the impeller as shown in Figure 3.17. The *first plane* crosses the baffle plane ($\theta = \pi/4$) while the *second plane* is placed halfway between the baffles ($\theta = 3\pi/8$). The assumption of symmetric flow in the θ-direction in the *impeller region* can thus be investigated.

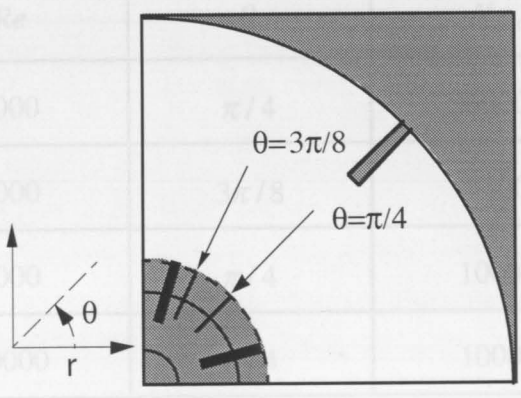

Figure 3.17 The two measurement planes in the impeller region.

A grid (20×20 mm) with 121 nodes, as shown in Figure 3.18, was used for measurements in both planes. The range of the radial co-ordinate r/R extends from $3/5$ to $5/5$. However, the measurements at the second plane were taken with a smaller range (from $18/25$ to $25/25$) due to technical limitations.

The water in the tank was seeded with nylon particles. Measurements were made at two Reynolds numbers, $Re = 5000$ and $Re = 10000$, corresponding to the impeller rotation of $N = 0.5rps$ and $N = 1.1rps$, respectively.

Data sets of different sizes ($N_{pts} = 5000$ and $N_{pts} = 10000$), were used to test possible differences in the statistical averages.

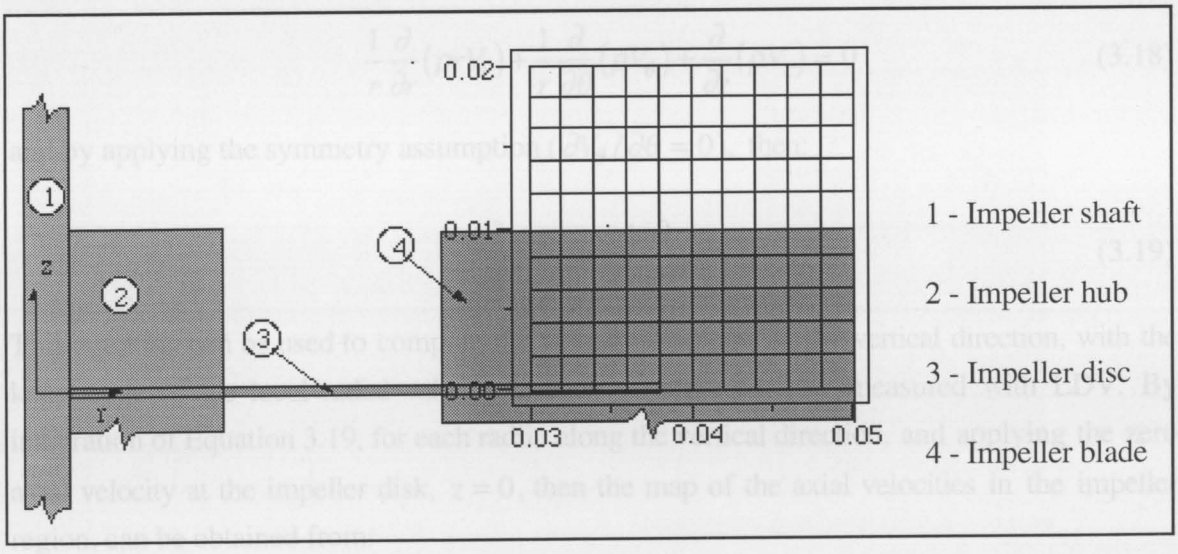

Figure 3.18 Vertical grid in measurement plane.

In order to study independently the effects of N_{pts} and Re, measurements were performed at various combinations of the parameters Re, θ and N_{pts}, summarised in Table 3.4.

Table 3.4 Experimental parameters.

Re	θ	N_{pts}
5000	$\pi/4$	5000
5000	$3\pi/8$	5000
5000	$\pi/4$	10000
10000	$\pi/4$	10000

3.3.2.2 Results

The main question here, arises of what is flow pattern inside the impeller region. Although the tangential motion of the rotating blades should be dominant, the question now is what are the magnitudes and profiles of the radial velocity. The axial velocity might be even more interesting, since its knowledge will reveal if the flow mainly enters between blades from the top and bottom of the impeller. These questions should be answered by the following results.

Since only the two horizontal velocity components were obtained, the third axial component can only be computed. The periodic flow inside the impeller region can be taken as a pseudo steady-state problem. Taking the conservation mass equation in cylindrical co-ordinates:

$$\frac{1}{r}\frac{\partial}{\partial r}(\rho r V_r)+\frac{1}{r}\frac{\partial}{\partial \theta}(\rho V_\theta)+\frac{\partial}{\partial z}(\rho V_z)=0 \tag{3.18}$$

and by applying the symmetry assumption ($\partial V_\theta / \partial \theta = 0$), then:

$$\frac{\partial}{\partial z}(V_z)=-\frac{1}{r}\frac{\partial}{\partial r}(rV_r) \tag{3.19}$$

This equation can be used to compute the velocity gradients in the vertical direction, with the knowledge of the local radial velocity at each vertical i-position measured with LDV. By integration of Equation 3.19, for each radii, along the vertical direction, and applying the zero axial velocity at the impeller disk, $z=0$, then the map of the axial velocities in the impeller region, can be obtained from:

$$V_z(i)=-\frac{1}{r}\int_0^{z(i)}\frac{\partial}{\partial r}(rV_r)dz \tag{3.20}$$

Figure 3.19 and Figure 3.20 show the maps of two measured velocity components for $Re = 5000$ and $N_{pts} = 5000$ in the impeller region. In Figure 3.19, the radial velocity profiles are presented, and as expected, there is present a velocity maximum at the impeller centre line and at the tip of impeller blade. The decay of the radial velocity component towards the shaft and with increasing axial distance can be seen clearly. The contour maps at the two planes ($\theta = \pi/4$ and $3\pi/8$), provide additional evidence of the flow symmetry in the θ-direction inside the impeller region. The dominance of the tangential velocity is evident from its magnitude in Figure 3.20. It should be noted that the magnitude of tangential component is practically constant inside the impeller region, and it decays mainly outside of the impeller region above the edge of the blade. A small disturbance is observed in the upper right corner of the blade. This is probably caused by the trailing vortices formed behind the impeller blades.

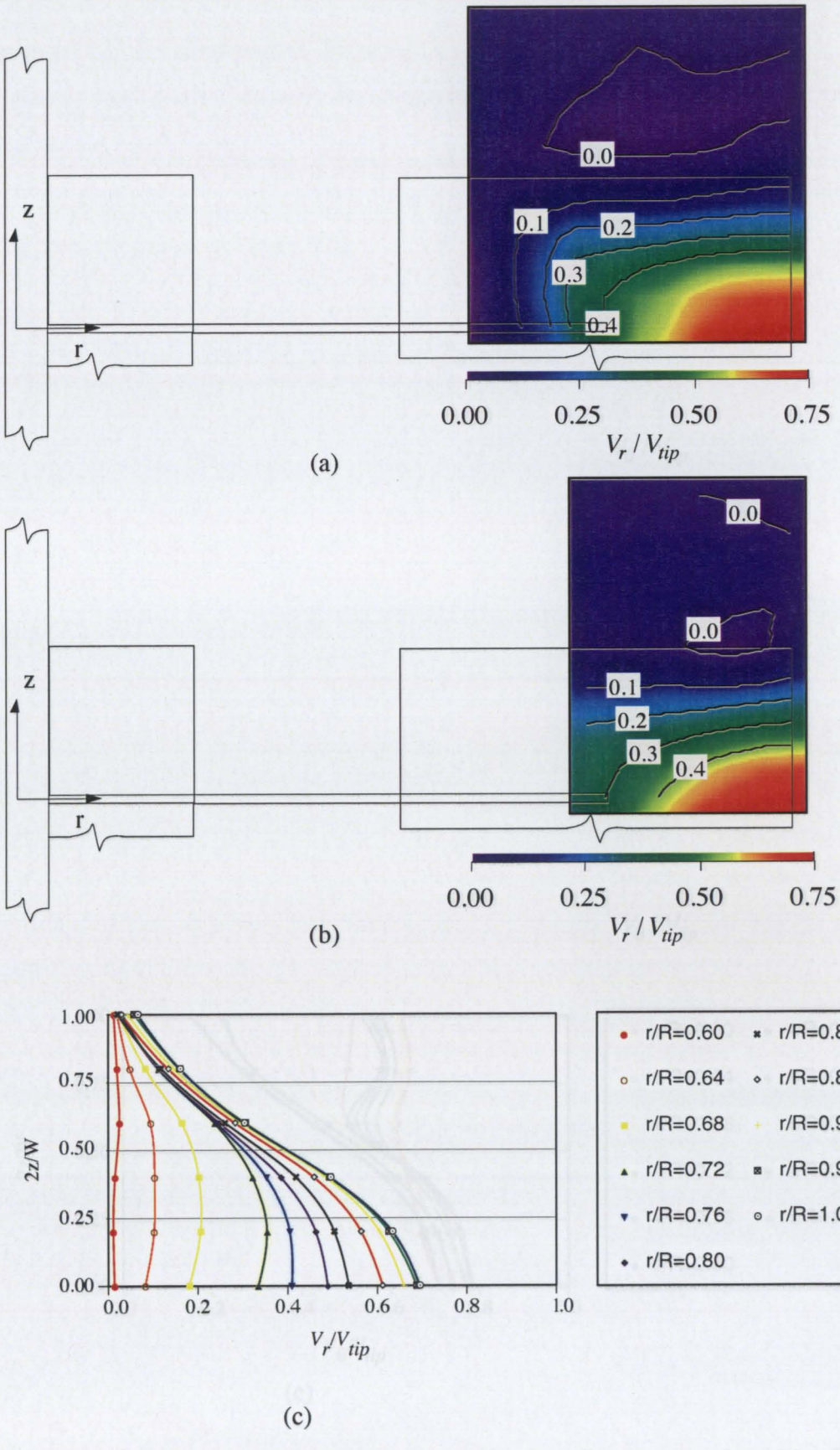

Figure 3.19 *Radial velocity inside of the impeller region for* $Re = 5000$ *and* $N_{pts} = 5000$*: a) maps for* $\theta = \pi/4$*; b) maps for* $\theta = 3\pi/8$*; c) profiles for various radii at* $\theta = \pi/4$.

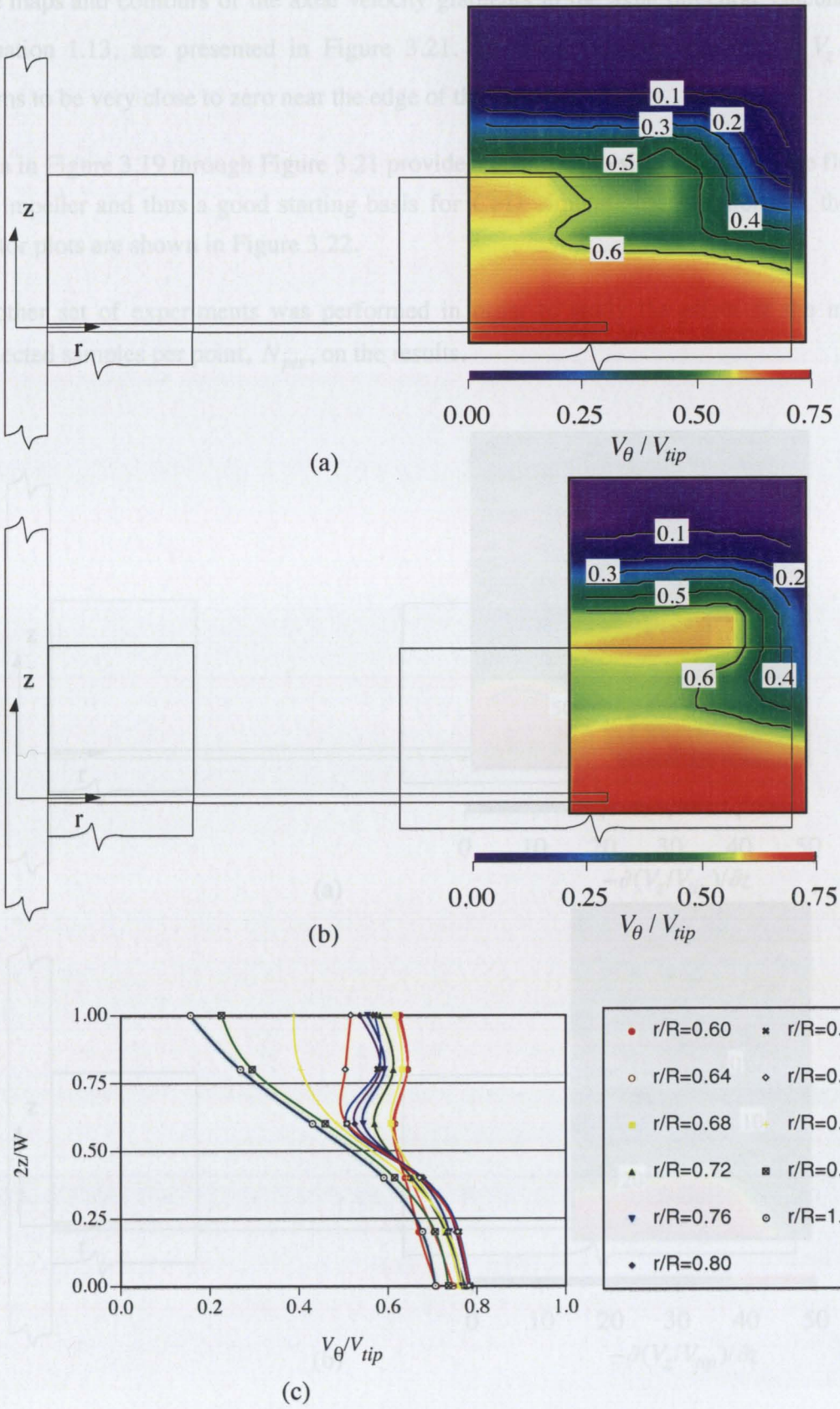

Figure 3.20 *Tangential velocity inside of the impeller region for* $Re = 5000$ *and* $N_{pts} = 5000$*: a) maps for* $\theta = \pi/4$*; b) maps for* $\theta = 3\pi/8$*; c) profiles for various radii at* $\theta = \pi/4$.

The maps and contours of the axial velocity gradients in the axial direction, calculated using Equation 1.13, are presented in Figure 3.21. The axial velocity gradient, $\partial\left(V_z / V_{tip}\right)/\partial z$, seems to be very close to zero near the edge of the blade.

Data in Figure 3.19 through Figure 3.21 provide a detailed physical picture on the flow inside the impeller and thus a good starting basis for CFD simulations. Additionally, the velocity vector plots are shown in Figure 3.22.

Another set of experiments was performed in order to study the effect of the number of collected samples per point, N_{pts}, on the results.

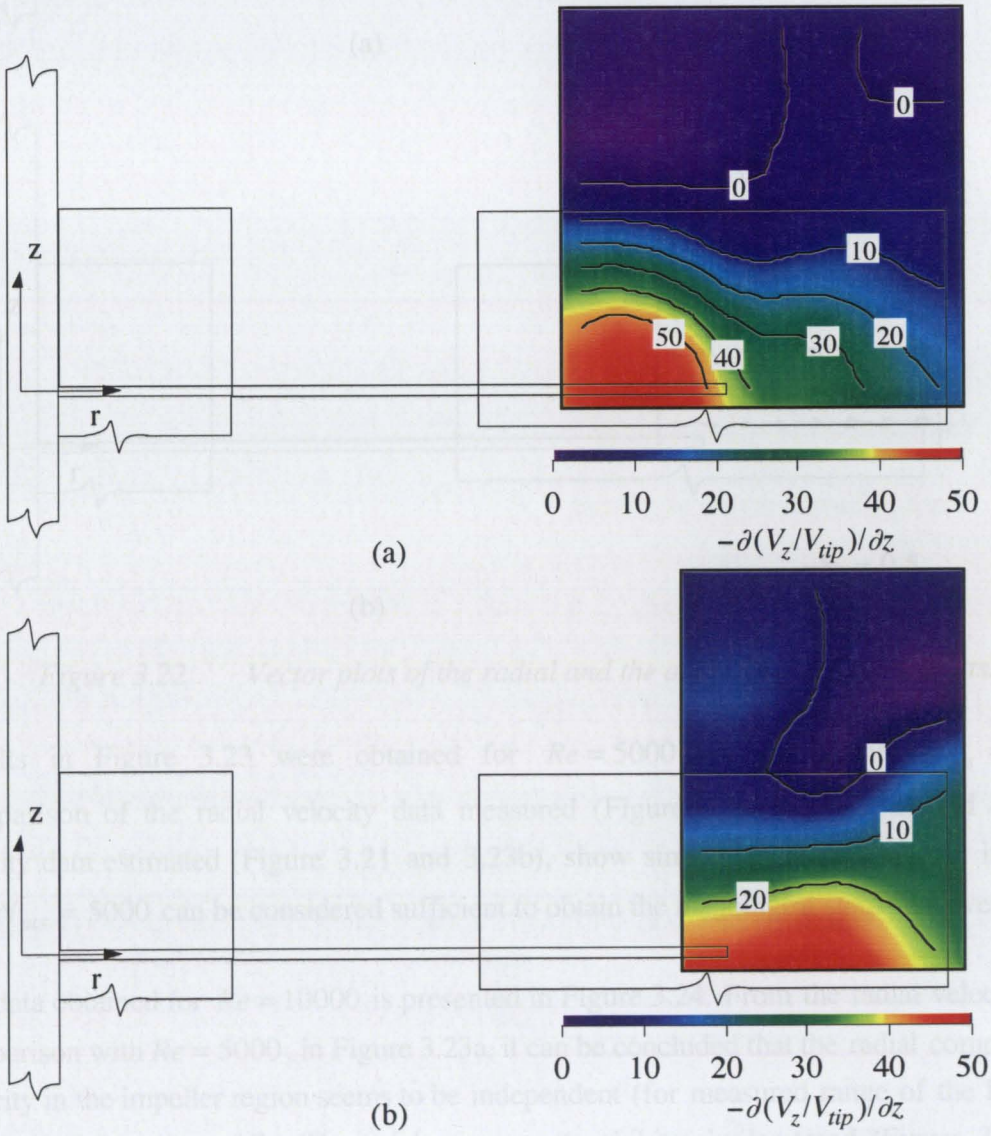

Figure 3.21 *Axial velocity gradients: a) contour maps at $\theta = \pi/4$; b) contour maps at $\theta = 3\pi/8$.*

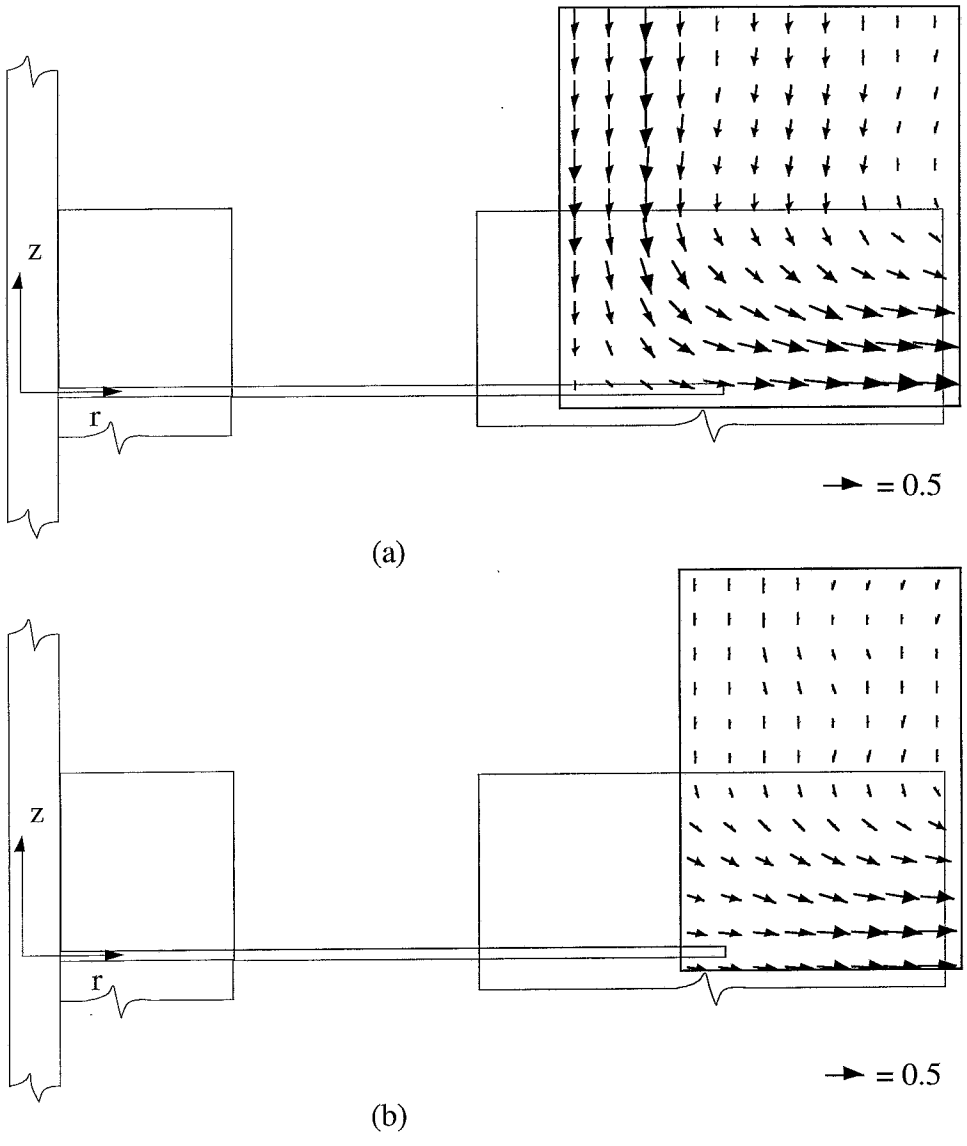

Figure 3.22 Vector plots of the radial and the axial velocity components.

Results in Figure 3.23 were obtained for $Re = 5000$, $\theta = \pi/4$ and $N_{pts} = 10000$. Comparison of the radial velocity data measured (Figure 3.19 and 3.23a) and the axial velocity data estimated (Figure 3.21 and 3.23b), show similar qualitative results, indicating that $N_{pts} = 5000$ can be considered sufficient to obtain the meaningful statistical averages.

The data obtained for $Re = 10000$ is presented in Figure 3.24. From the radial velocity maps comparison with $Re = 5000$, in Figure 3.23a, it can be concluded that the radial component of velocity in the impeller region seems to be independent (for measured range of the Reynolds number) of the value of Re. The axial component exhibits similar trend (Figure 3.24c and Figure 3.23c). Moreover, the gradient of the axial velocity (Figure 3.23b) in the case of $Re = 10000$ has a tendency to be zero along the horizontal edge of the impeller blade. From results in Figure 3.23 and Figure 3.24, can be observed a good agreement between the radial velocity measured for the two of Re.

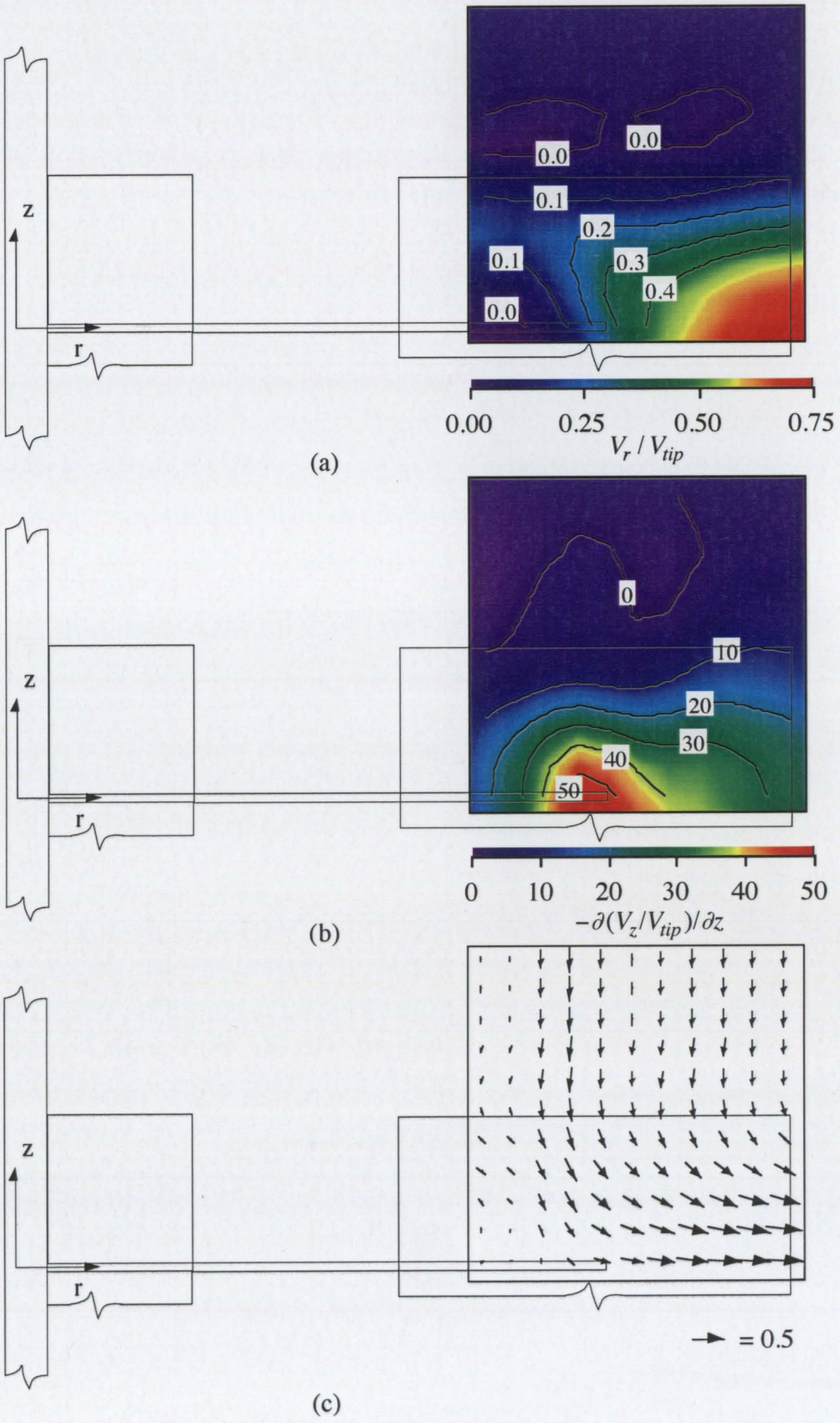

Figure 3.23 *Experimental results for* $Re = 5000$ *and* $N_{pts} = 10000$*: a) radial velocity; b) axial velocity gradients; c) vector plot of the radial and axial components.*

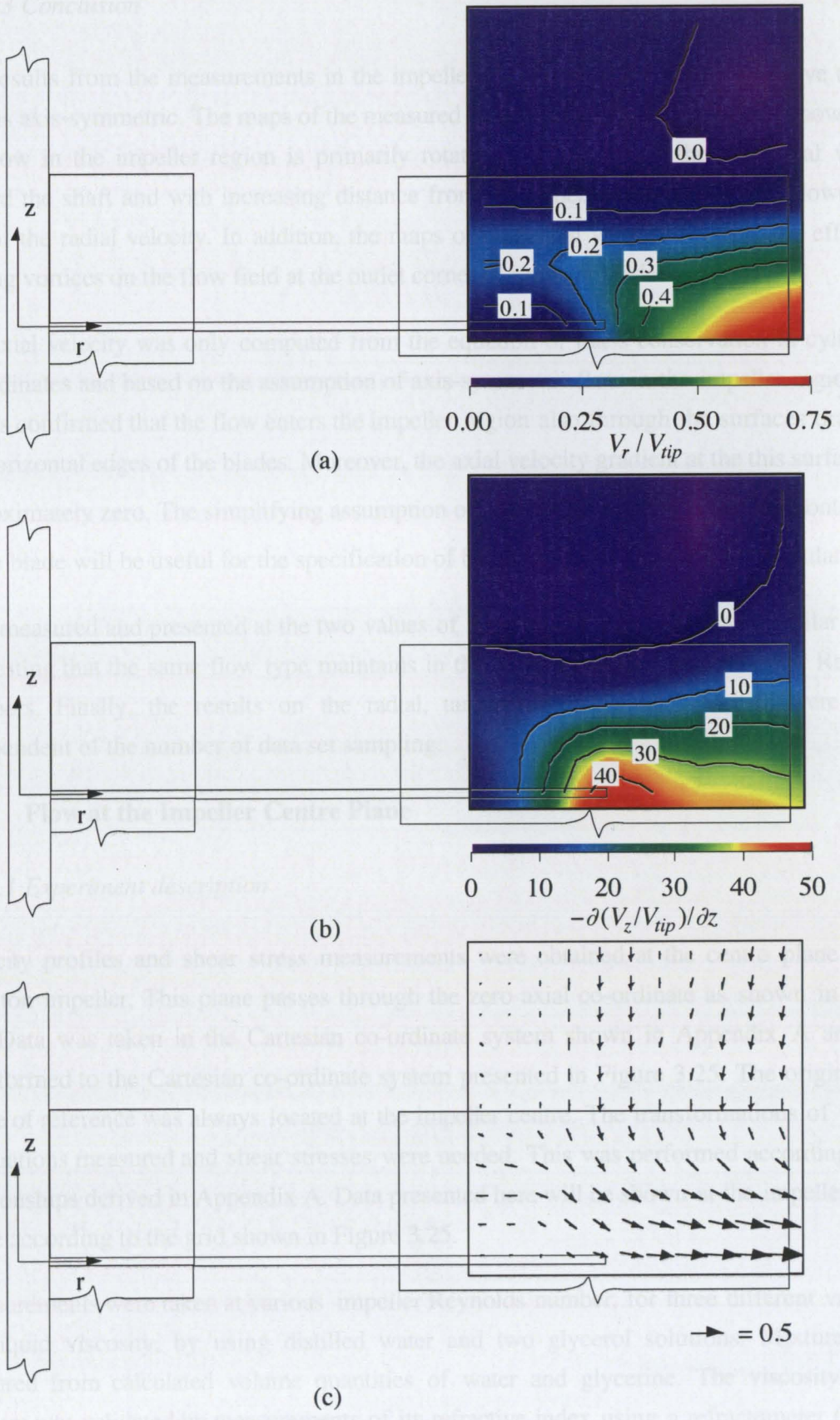

Figure 3.24 *Experimental results for Re = 10000 and N_{pts} = 10000: a) radial velocity; b) axial velocity gradients; c) vector plot of the radial and axial components.*

3.3.2.3 Conclusion

The results from the measurements in the impeller region provided additional prove that the flow is axis-symmetric. The maps of the measured radial and tangential velocities showed that the flow in the impeller region is primarily rotational. A decay of the tangential velocity toward the shaft and with increasing distance from the impeller centre line was slower than that of the radial velocity. In addition, the maps of tangential velocity revealed the effects of trailing vortices on the flow field at the outlet corner of impeller blade.

The axial velocity was only computed from the equation of mass conservation in cylindrical co-ordinates and based on the assumption of axis-symmetric flow in the impeller region. The results confirmed that the flow enters the impeller region also through the surfaces drawn by the horizontal edges of the blades. Moreover, the axial velocity gradient at the this surface was approximately zero. The simplifying assumption of $\partial\left(V_z / V_{tip}\right)/\partial z = 0$ at the horizontal edge of the blade will be useful for the specification of boundary conditions in CFD simulations.

Data measured and presented at the two values of Reynolds number exhibited similar results suggesting that the same flow type maintains in the impeller region for the higher Reynolds numbers. Finally, the results on the radial, tangential, and axial velocities were found independent of the number of data set sampling.

3.3.3 Flow at the Impeller Centre Plane

3.3.3.1 Experiment description

Velocity profiles and shear stress measurements were obtained at the centre plane of the Rushton impeller. This plane passes through the zero axial co-ordinate as shown in Figure 3.7. Data was taken in the Cartesian co-ordinate system shown in Appendix A and then transformed to the Cartesian co-ordinate system presented in Figure 3.25. The origin of the frame of reference was always located at the impeller centre. The transformations of velocity fluctuations measured and shear stresses were needed. This was performed according to the relationships derived in Appendix A. Data presented here will be shown at the impeller centre plane according to the grid shown in Figure 3.25.

Measurements were taken at various impeller Reynolds number, for three different values of the liquid viscosity, by using distilled water and two glycerol solutions. Mixtures were prepared from calculated volume quantities of water and glycerine. The viscosity of the mixture was validated by measurements of its refractive index using a refractometer (Bausch & Lomb, model Abbe-3L) and the mixture density was obtained by pycnometry. All liquids were seeded with Nylon particles (TSI, Pt900845), neutrally buoyant with an average diameter of 4 μm and density of 1100 $\mathrm{kg \cdot m^{-3}}$.

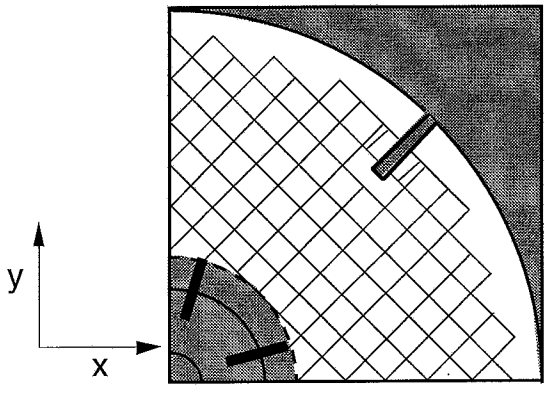

Figure 3.25 Measurement grid for the impeller centre plane.

Table 3.5 shows the list of covered Reynolds numbers, Re, and associated experimental parameters, including: the liquid viscosity, μ; the imposed impeller frequency, N, and the indirectly measured impeller frequency form LVD data, N_{FFT}, the rotational velocity at the tip of the impeller, V_{tip}; the number of measuring grid points collected at the plane; and the number of samples for each point, N_{pts}. Information on the data rate at the impeller tip and the used probe size is also provided.

Table 3.5 List of experiments and their specifications.

Re	$\mu \times 10^3$ (Pa·s)	N (Hz)	N_{FFT} (Hz)	V_{tip} (m·s^{-1})	Number grid points	N_{pts}	Data Rate (Hz)	d_p (mm)
45	134	0.5	0.4	0.15	164	4096	830	15
90	134	1.0	1.0	0.3	164	4096	980	15
125	40	0.4	0.3	0.12	164	4096	100	15
450	134	5.0	4.9	1.5	164	4096	140	15
640	40	2.25	2.2	0.69	164	4096	60	15
900	134	10.0	9.8	3.0	164	4096	120	15
1250	40	4.4	3.1	1.35	164	4096	40	15
3100	40	11.0	*	3.40	164	4096	5	15
5000	1	0.5	0.5	0.17	138	10000	60	83
10000	1	1.1	1.2	0.33	138	10000	280	83
20000	1	2.2	2.0	0.67	164	1024	40	15
20000	1	2.2	2.2	0.67	138	10000	260	83

* not determined due to small data rate and high impeller rotation

All measurements were performed under LDV coincidence mode. Simultaneous measurement of two velocities provides information essential for understanding the flow dynamics. The two velocity components, measured at the same time, are needed in order to compute the time averaged Reynolds stress component through Equation 3.5.

The main problem to measure shear stresses by LDV is the random sampling of particles in the LDV measuring volume. In order to ensure that the measurement is simultaneous in the two velocity components, a time *coincidence window* between the two different velocity component detection has to be selected properly. Menon (1987) proposed the selection of the coincidence window as follows. The minimum window value can be estimated as the time interval during which the particle passes the measuring volume. The maximum value should be estimated as one order of magnitude less than the time between successive data (the time between to successive particles is obtained as the inverse value of the average data rate). In this work, the narrower interval of the time (coincidence window) was chosen. The minimum of coincidence corresponds to the time a particle takes to cross four fringes of the measuring volume, since this number is sufficient to produce LDV data. To ensure that velocities are really measured simultaneously, the maximum window was selected as the time a particle takes to cross the measuring volume.

Another difficulty is related to the particular frame of reference used for the LDV set-up. In certain spatial locations of the impeller centre plane, one of the velocity components dominates the other by order of magnitudes and the selection of coincidence window is especially difficult. This because the time interval of a particle to cross the measuring volume in one measured direction can exceed and/or does not match the interval estimated for second direction. In this case, the measurements could proceed with the minimum value of two time intervals. However, this leads to measurements with an error dependent on the spatial location. Another option is to take measurements for each location with a frame of reference where the velocity components are of the same order, that is, to adjust the frame of reference in certain locations. This is a complicated and elaborate procedure. In this work, a modification of the width of coincidence window through spatial location was performed during data acquisition.

$N_{pts} = 4096$ data samples were taken with the $d_p = 15$ mm probe for the majority of plane points. The time necessary to obtain the data samples increases when the data rate decreases. For a few locations, mostly near the wall, a data acquisition time of 15 minutes was used. It was observed that the data rate decreases with distance from impeller to very small values near the solid wall or the baffle. This is due to lower velocities in these locations resulting into smaller number of particles passing the measuring volume.

From LDV theory is known that data rate is also a quadratic function of the probe diameter. For this reason, it was easier to take more data samples per point, $N_{pts} = 10000$, using the $d_p = 83$ mm probe.

LDV experiments in this study were time-averaged and performed over several revolutions of the impeller. To evaluate some characteristics of turbulent flow, the pseudo-turbulence must

be eliminated. In the following section a procedure used to eliminate the pseudo-turbulence is described.

3.3.3.2 Results

The mean and fluctuation velocities and the shear Reynolds stress were measured. Statistical quantities are reported in terms of the normalised velocity vector, the turbulent kinetic energy, k, and the Reynolds stress, τ^t_{xy}. The tip velocity, V_{tip}, is the normalisation variable for the velocity vector, while values of the kinetic energy and of the shear Reynolds stress are normalised by $V_{tip}{}^2$. Data is plotted within one quarter of the investigated plane (see Figure 3.25) and missing data, between the tip of the impeller and the impeller disk, was interpolated along rows and columns using a linear interpolation (weighted fill) method. The velocity at the impeller disk consists only of the tangential component. The kinetic energy and Reynolds stresses are zero at the physical boundaries such as the impeller disk and the tank wall.

Figure 3.26 shows the average liquid velocity vector projection plots over the impeller centre plane for all the Reynolds numbers. At this plane the two vertical vortices (top and bottom vortex) separate and the axial velocity is very close to zero. Measurements were performed at eleven impeller rotations. The general flow picture is very similar for $Re > 125$ and the liquid speed always reaches its maximum near the impeller tip region. The flow is dominated by the radial component and the liquid is mainly pumped against the wall by the radial flow.

The maps of the normalised turbulent kinetic energy are presented in Figure 3.27 with overlaid contour plots. The turbulent kinetic energy values were computed by Equation 3.11, from the measured radial and tangential velocity fluctuations and considering the axial fluctuations value to be zero, due to the 2D nature of the flow at the impeller centre plane. In Figure 3.27 it can be observed that the magnitude of the kinetic energy increases with the Reynolds number, indicating that the turbulence also increases with Re. The maximum of normalised value approximates 10% of the squared tangential velocity fluctuation, $V_{tip}{}^2$. The contour levels for $Re > 450$ are nearly the same. The highest region of the turbulent kinetic energy, k, is associated with the periodic motion of the blades. A decay of the turbulent kinetic energy away from blades is also evident. And a similar trend is observed in the opposite direction (towards the impeller disk). The two contour maps for $Re = 20000$ obtained with two different size LDV optical probes, suggest that the measured quantities are independent of the probe used for measurement. The last observation supports idea that the small probe does not disturb the flow in the ST significantly.

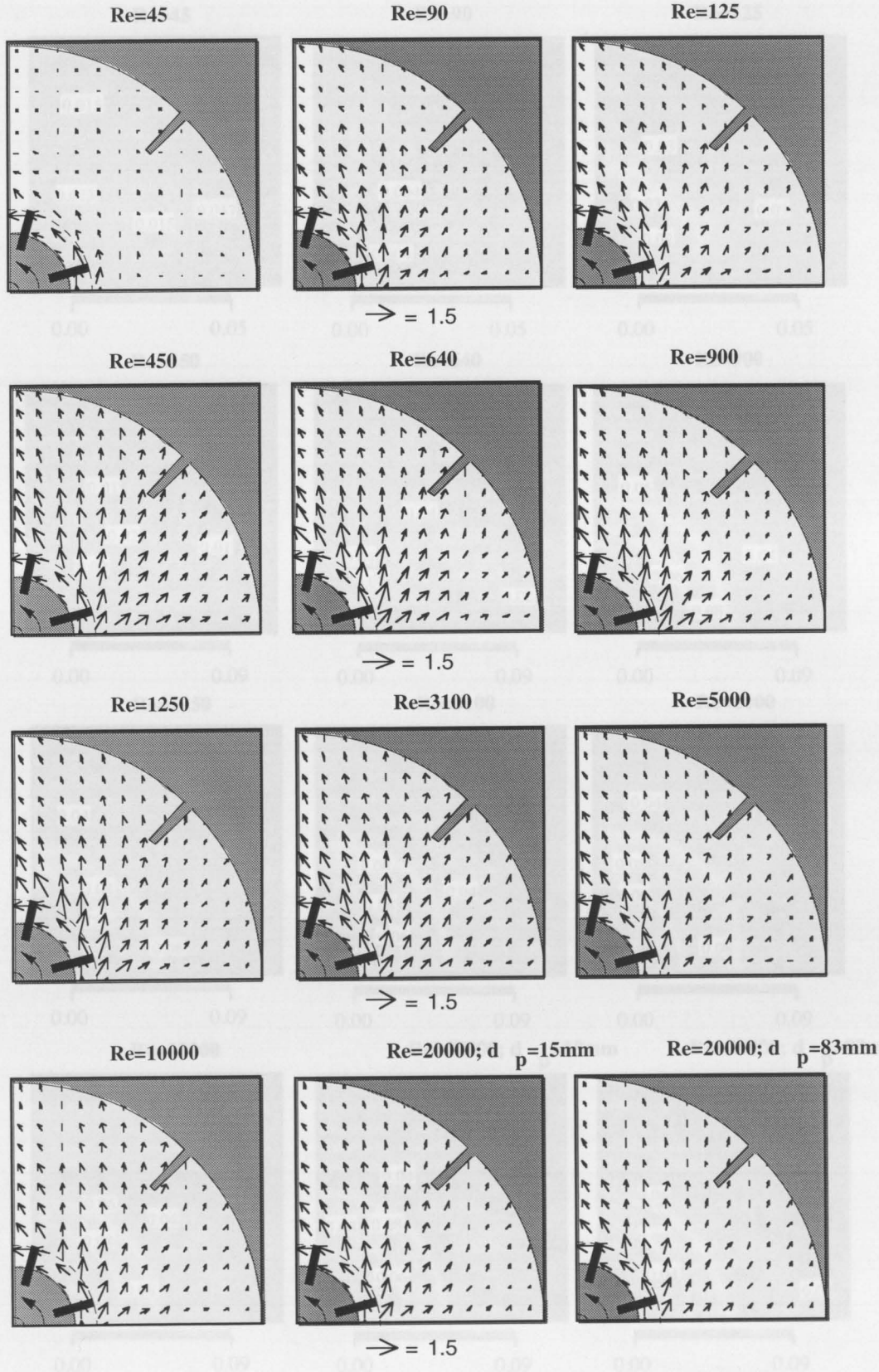

Figure 3.26 *Vectors plots from the radial and tangential velocity components over the impeller centre plane for the different Reynolds numbers.*

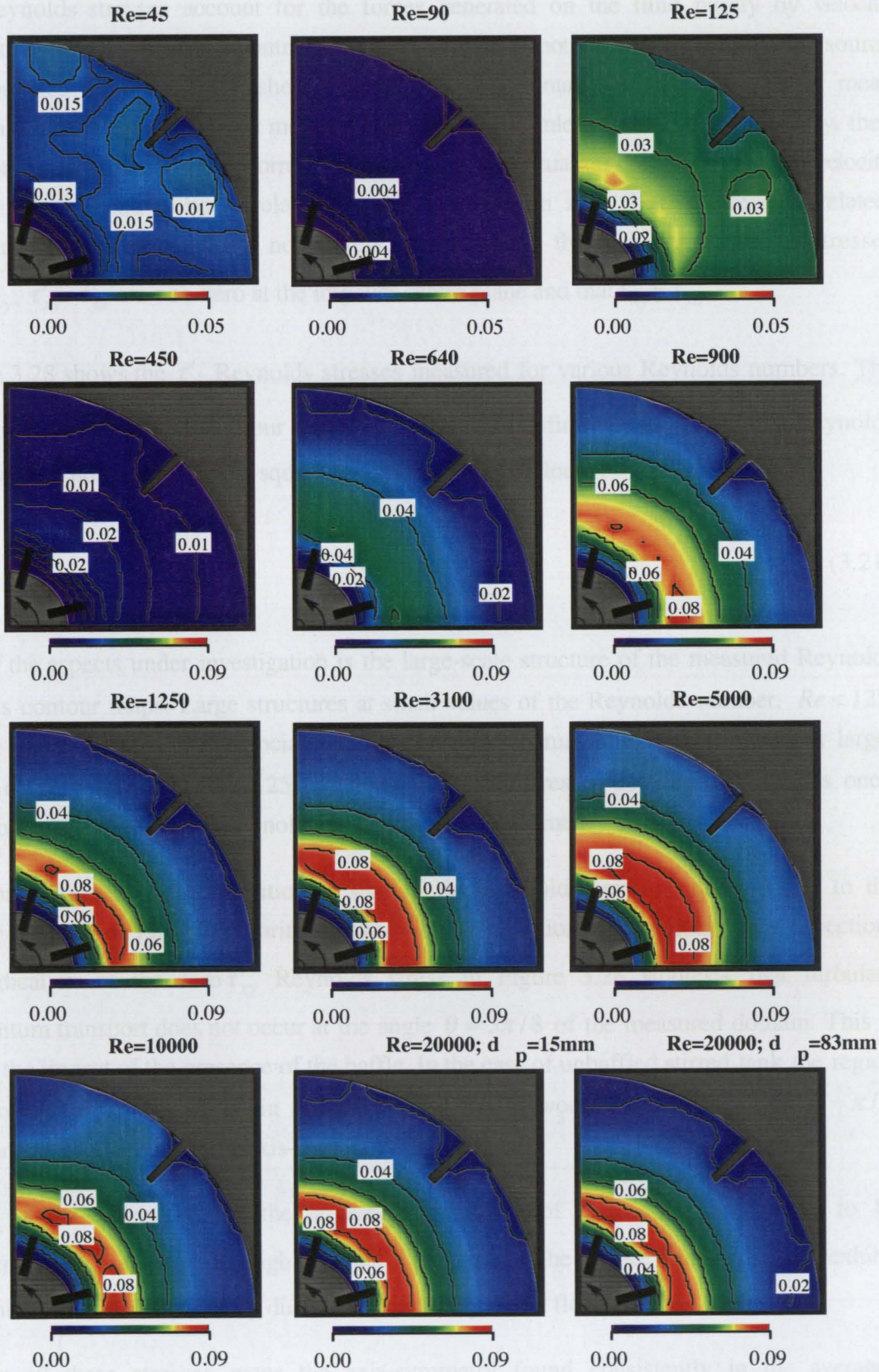

Figure 3.27 *Normalised kinetic energy k / V_{tip}^2 contour plots for the different Reynolds numbers.*

The Reynolds stresses account for the forces generated on the fluid purely by velocity fluctuations. They represent a contribution to the turbulent motion, which decays if the source of turbulence disappears. The shear stresses play a dominant role in the theory of mean momentum transfer by turbulent motion (Tennekes and Lumley, 1972). Mathematically, they represent the covariance or the correlation between two fluctuation components. Two velocity fluctuations are said to be correlated if their value is non zero. If they are uncorrelated, turbulent momentum transfer is not present. It is expected that only the Reynolds stresses τ^t_{xx}, τ^t_{yy}, τ^t_{xy}, τ^t_{yx} are non-zero at the impeller centre plane and that $\tau^t_{xy}=\tau^t_{yx}$.

Figure 3.28 shows the τ^t_{xy} Reynolds stresses measured for various Reynolds numbers. The contour maps overlaid by contour plots are shown (by definition) as negative τ^t_{xy} Reynolds stress values, normalised by the square of the impeller tip velocity:

$$\frac{\tau^t_{xy}}{\rho V_{tip}{}^2} = -\frac{\overline{uv}}{V_{tip}{}^2} \tag{3.21}$$

One of the aspects under investigation is the large-scale structure of the measured Reynolds stresses contour maps. Large structures at small values of the Reynolds number, $Re < 125$, are not well formed, and the associated data is one order of magnitude smaller then for larger values of $Re > 125$. For $Re > 125$, where the Reynolds stresses dominate the viscous ones, the two regions of different Reynolds stress polarity are formed.

The spatial region of the transition in sign of the Reynolds stresses, corresponds to the change in the strain rate (the polarity changes with the direction of the velocity in x direction) An indication of the zero τ^t_{xy} Reynolds stress in Figure 3.28 suggests that turbulent momentum transport does not occur at the angle $\theta \approx 3\pi/8$ of the measured domain. This is due to the impact of the presence of the baffle. In the case of unbaffled stirred tank the region of zero momentum transport (in this Cartesian system) would pass through the $\theta \approx \pi/4$ angular co-ordinate, due to its axis-symmetry.

These results illustrates that the large-scale structure of turbulent flows tends to be independent of viscosity for high Reynolds numbers . The τ^t_{xy} Reynolds stresses exhibit maximums near the impeller tip due to the periodicity of the flow.

And in all these stresses maps the axis-symmetry found consistently in the averaged velocities maps, is now broken in the Reynolds stresses maps.

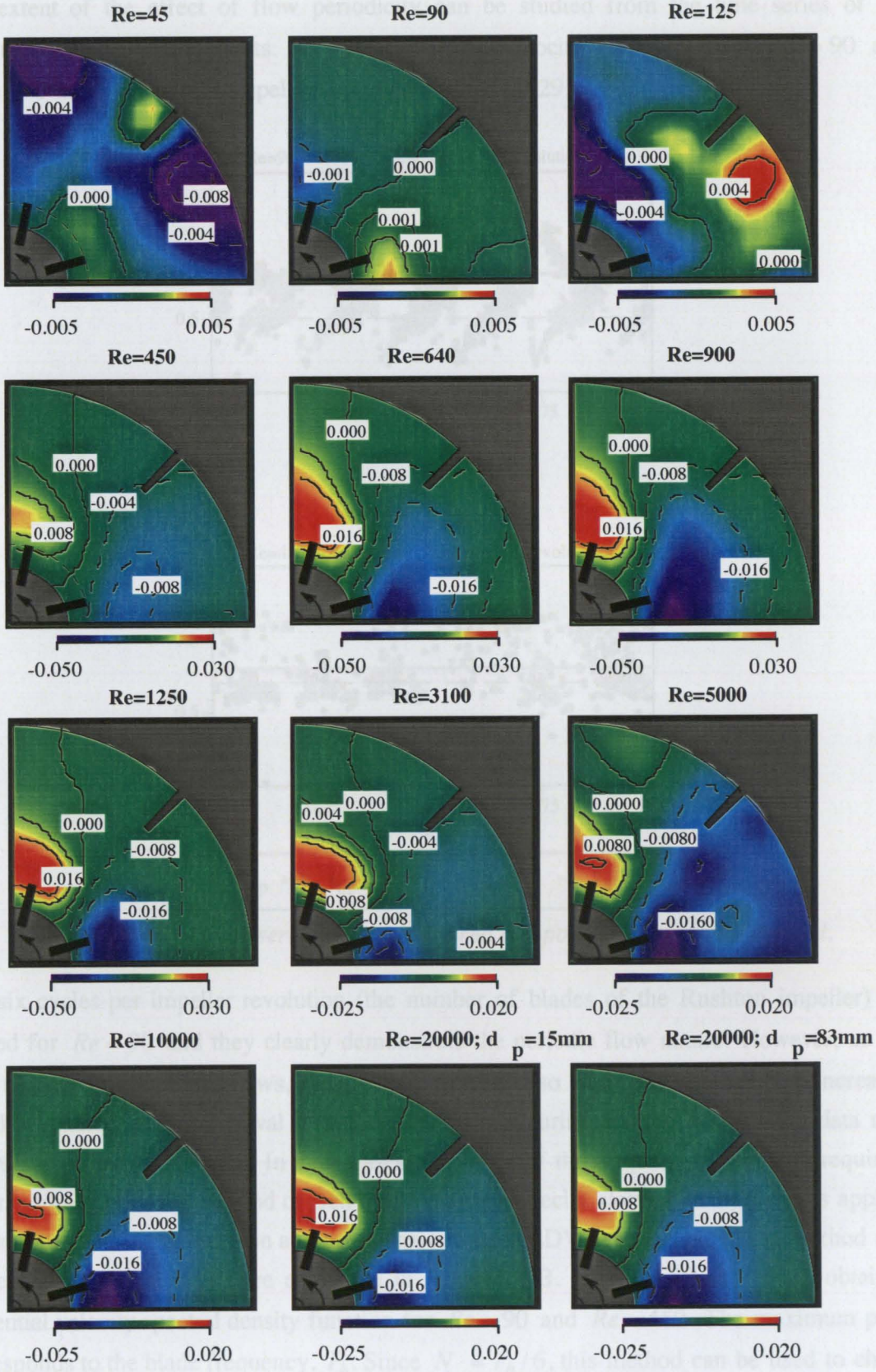

Figure 3.28 τ'_{xy} *Reynolds stress maps for the different Reynolds numbers.*

The extent of the effect of flow periodicity can be studied from the time series of the measured velocity components. An example of the velocity time series for $Re = 90$ and $Re = 450$ at the vicinity of impeller is plotted in Figure 3.29.

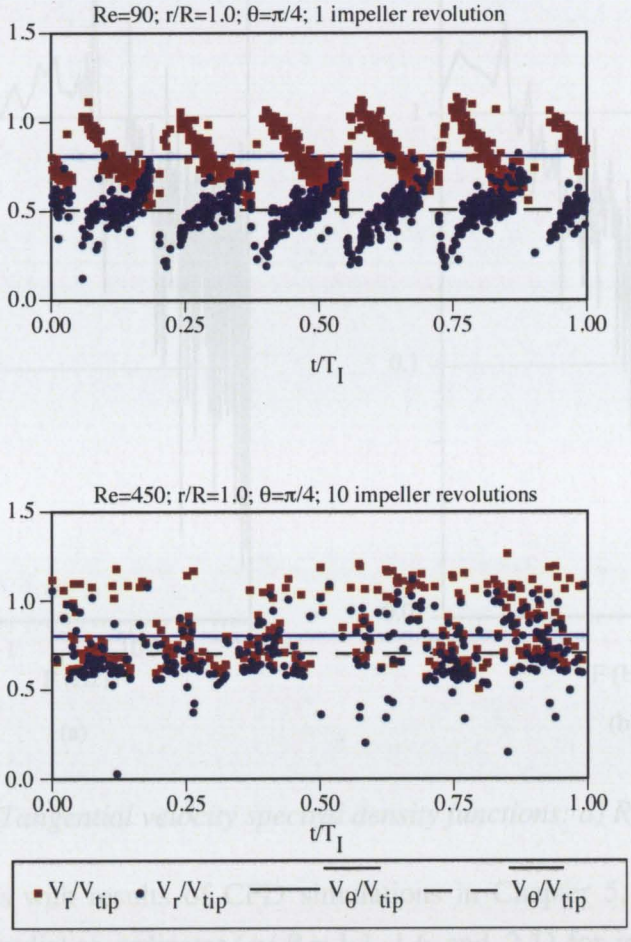

Figure 3.29 Time series of two measured components of the velocity filed.

The six cycles per impeller revolution (the number of blades of the Rushton impeller) are plotted for $Re = 90$ and they clearly demonstrate the periodic flow nature. However, as the time series of $Re = 450$ shows, the periodicity is not so clear for higher Re. Increased impeller rotation, random arrival of particles to the measuring volume, and smaller data rate, result into an unclear picture. In such cases, the study of the frequency spectra is required. The random correlation method of Bell (1986) using a special *slotting technique* was applied to compute FFT transformation and power spectra from LDV data. Details of the method and procedure for data analysis are explained in Appendix B. Figure 3.30 shows the obtained tangential velocity spectral density function for $Re = 90$ and $Re = 450$. The maximum peak corresponds to the blade frequency, F_b. Since $N = F_b / 6$, this method can be used to check the rotational speed of the impeller adjusted for each measurement. The N_{FFT} column in Table 3.5 shows the results for the impeller rotation obtained by random correlation technique and FFT transformation.

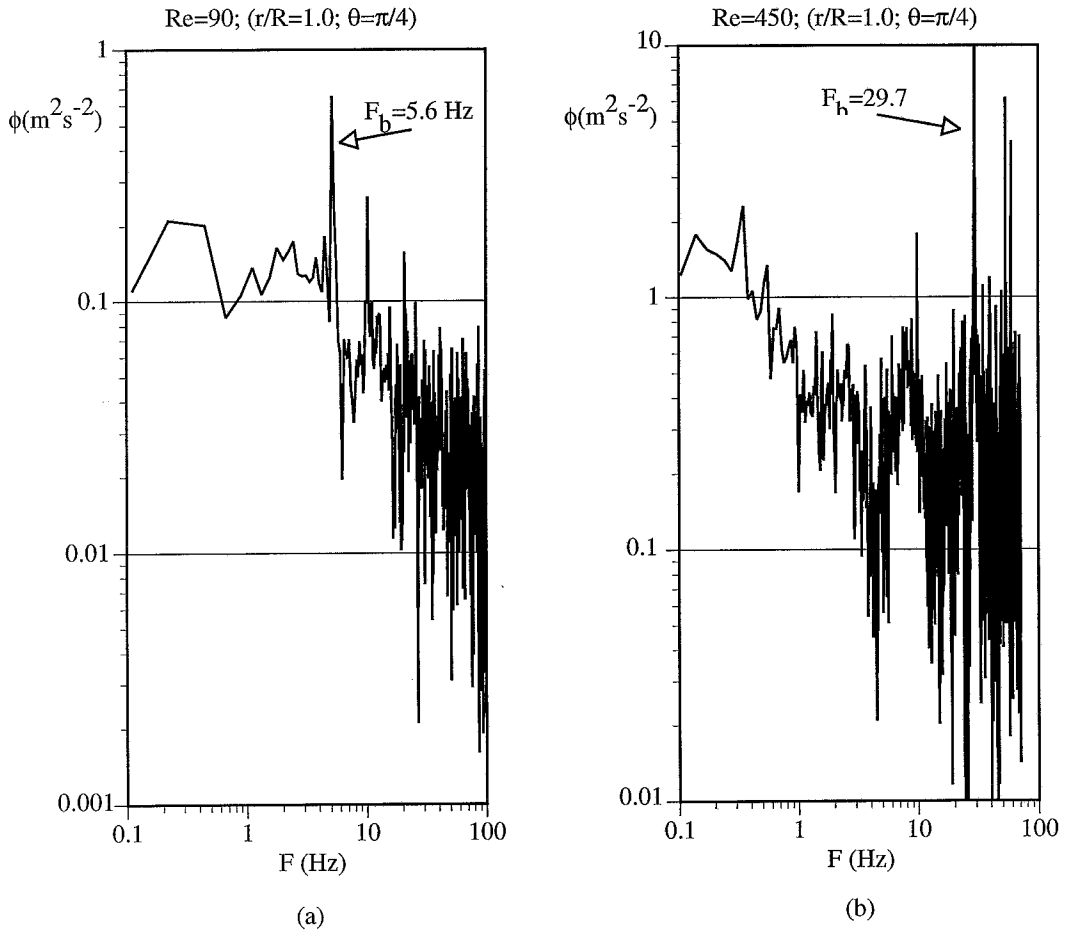

Figure 3.30 Tangential velocity spectral density functions: a) Re=90, b) Re=450.

For future comparisons with results of CFD simulations in Chapter 5, some data profiles were extracted at three radial co-ordinates ($r/R = 1.1$, 1.6 and 2.1) for increasing values of *Re*=5000 , 10000 and 20000.

The normalised radial and tangential vector components are plotted as a function of the angle co-ordinate in Figure 3.31. In Figure 3.31 are plotted the obtained experimental values as points, and a linear fitting is made for each Reynolds value. These fitted lines express clearly once again, that the average velocity are essentially axis-symmetric, i.e., independent of angular position. Radial and tangential velocity values are quite similar at the impeller tip, and they become increasingly different as the positions further away from the impeller with the predominance of radial motion.

The same type of diagrams is presented in Figure 3.32 for the Reynolds stress angular profiles. However in these profiles, the axis-symmetry is clearly broken at $\theta \approx \pi/4$ value for the angular co-ordinate. Also, there is a five times decrease in the level of Reynolds stress from $r/R = 1.1$ to $r/R = 1.6$, and only a small change from $r/R = 1.6$ to $r/R = 2.1$

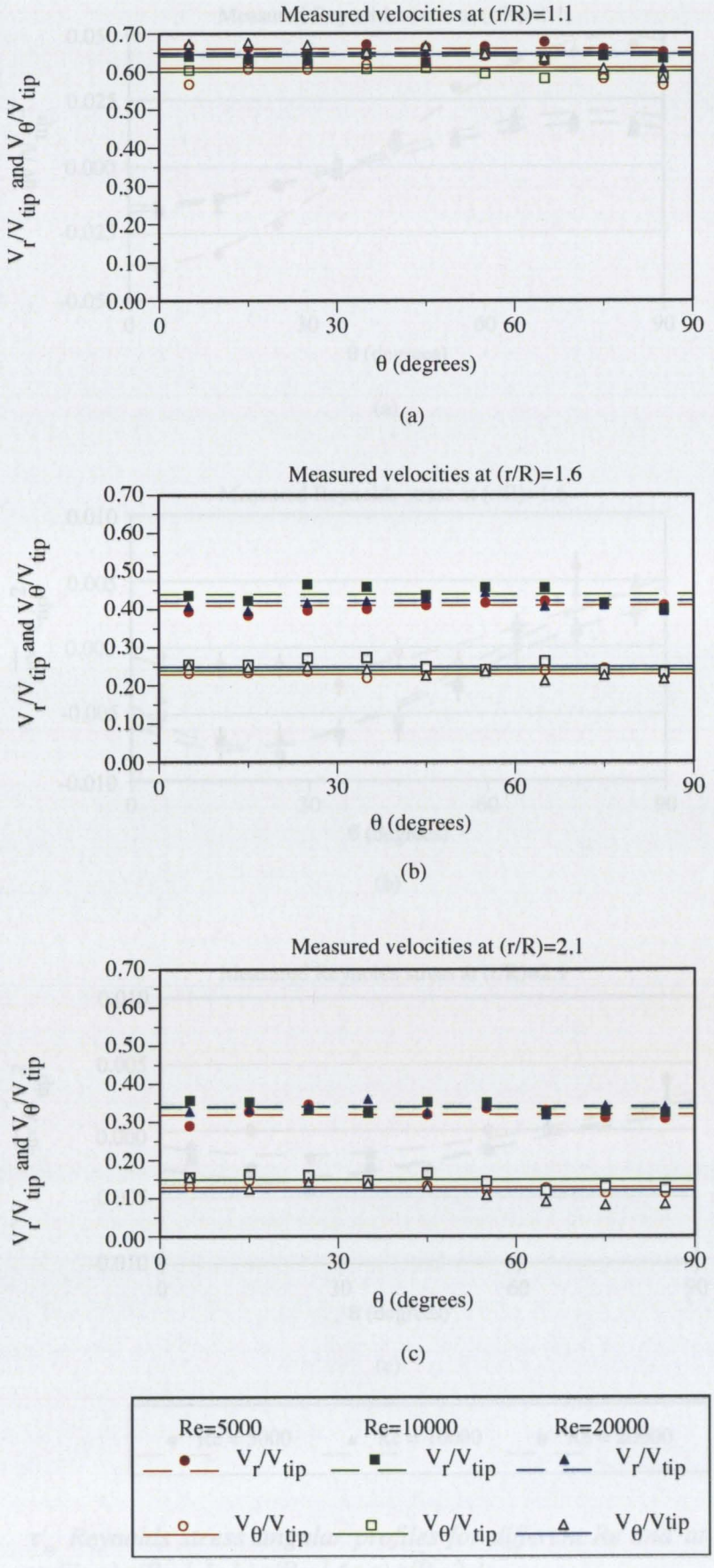

Figure 3.31 *Radial and tangential velocity angular profiles for different Re and at three different radii: a) r/R=1.1; b) r/R=1.6; c) r/R=2.1.*

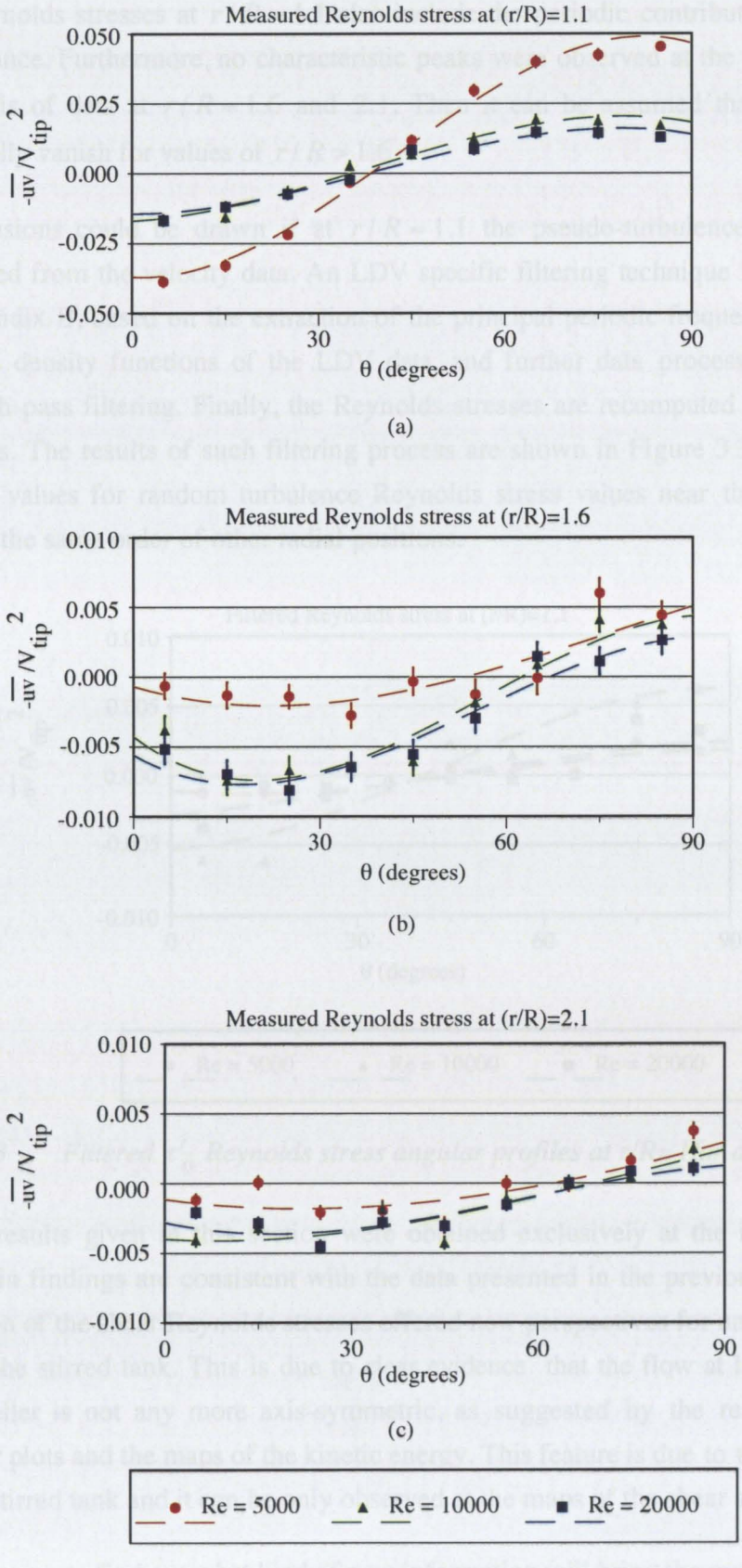

Figure 3.32 τ^{I}_{xy} *Reynolds stress angular profiles for different Re and at three different radii: a) r/R=1.1; b) r/R=1.6; c) r/R=2.1.*

Measured Reynolds stresses at $r/R = 1.1$ also include the periodic contribution caused by pseudo-turbulence. Furthermore, no characteristic peaks were observed at the power spectral density analysis of data at $r/R = 1.6$ and 2.1. Then it can be assumed that the pseudo-turbulence totally vanish for values of $r/R > 1.6$.

Similar conclusions could be drawn if at $r/R = 1.1$ the pseudo-turbulence contributions could be filtered from the velocity data. An LDV specific filtering technique is presented in detail in Appendix B, based on the extraction of the principal periodic frequencies from the power spectral density functions of the LDV data, and further data processing by digital Chebishev high-pass filtering. Finally, the Reynolds stresses are recomputed on the filtered velocity signals. The results of such filtering process are shown in Figure 3.33, where now the reminding values for random turbulence Reynolds stress values near the impeller are found to be of the same order of other radial positions.

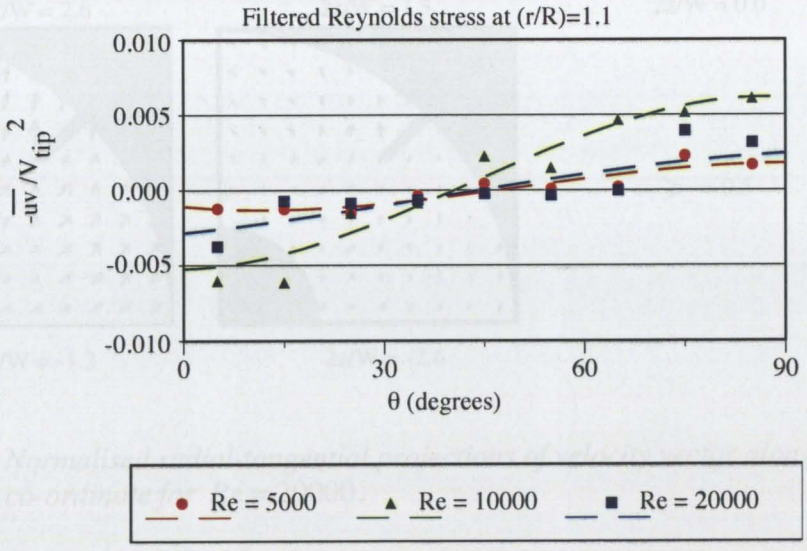

Figure 3.33 Filtered τ'_{xy} Reynolds stress angular profiles at r/R=1for different Re.

All the LDV results given in this section were obtained exclusively at the impeller centre plane. The main findings are consistent with the data presented in the previous sections but the examination of the shear Reynolds stresses offered new perspectives for understanding of flow fields in the stirred tank. This is due to clear evidence that the flow at larger distances from the impeller is not any more axis-symmetric, as suggested by the results from the velocity vector plots and the maps of the kinetic energy. This feature is due to the presence of baffles in the stirred tank and it can be only observed at the maps of the shear stresses.

It is interesting now to find out what kind of new information will bring the maps of the shear Reynolds stress at the horizontal planes of different vertical co-ordinates. Data obtained at five planes, parallel with the impeller centre plane, are presented for this purpose at the value of $Re = 20000$.

Firstly, the vector plots created from the measured radial and tangential velocity components are shown in Figure 3.34. It is observed that the strong jet of mainly radial flow decays quickly with increasing distance from the impeller centre plane ($2z/W = 0$). This suggests that the flow at the larger distances from the impeller centre plane is driven predominantly by the axial velocity. In addition, the effect of the impeller off-bottom clearance can be again observed at the presented parallel planes.

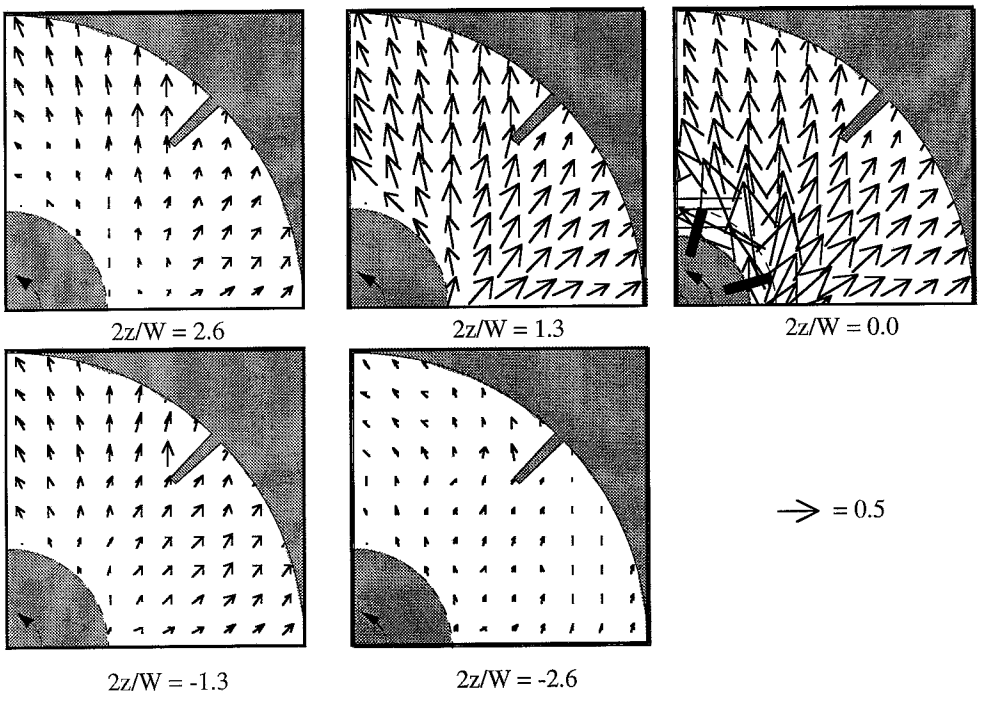

Figure 3.34 *Normalised radial-tangential projections of velocity vector along vertical co-ordinate for* $Re = 20000$.

The turbulent kinetic energy was computed from the radial and tangential velocity fluctuations and the maps in Figure 3.35 present the same horizontal planes along the vertical direction. These maps demonstrate the concentration of the turbulent kinetic energy at the impeller centre plane but this can be misleading since the fluctuations of axial velocity components were not measured and included in the turbulent kinetic energy.

The maps of the shear Reynolds stress are shown in Figure 3.36 at different vertical positions. As can be seen, the magnitudes and distributions of the Reynolds stress values vary noticeably thus confirming the strong anisotropic flow nature in the stirred tank. The maximum values of the τ^t_{xy} Reynolds stress are observed at the impeller centre plane and the magnitudes decay quickly with increasing distance from the impeller centre plane. Moreover, different distributions of the positive and negative Reynolds stresses along the vertical axis justify the fact that the top and bottom vortices have distinct turbulent flow features.

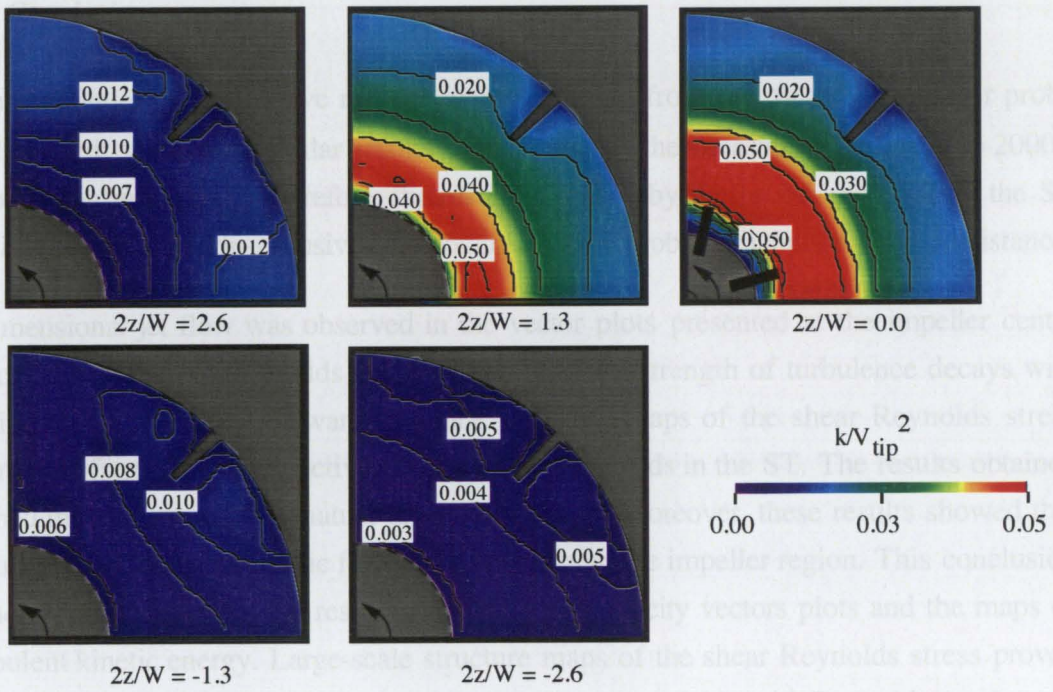

Figure 3.35 *Kinetic energy maps and contours from the radial and tangential fluctuation velocities along axial co-ordinate for* $Re = 20000$.

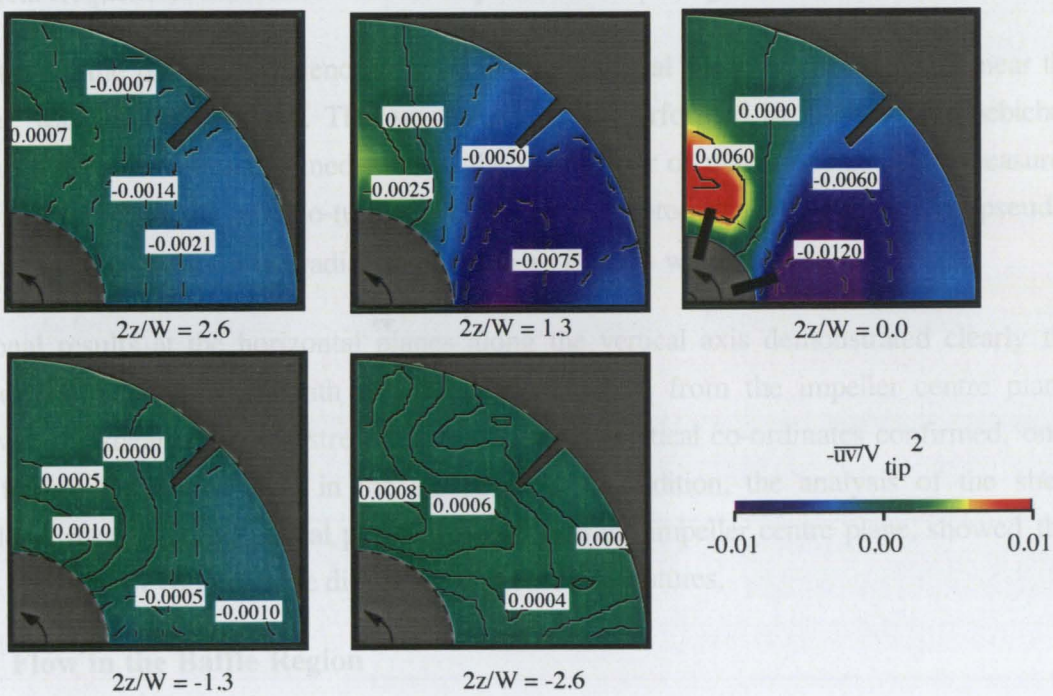

Figure 3.36 τ^t_{xy} *Reynolds stress maps and contour along axial co-ordinate for* $Re = 20000$

3.3.3.3 Conclusion

Initial uncertainties about invasive measurements resulting from the use of the smaller probe were dismissed, since very similar results were found in the measurements at $Re = 20000$ using both configurations. Therefore, the results obtained by the probe immersed in the ST are equivalent with the non-intrusive data obtained by the probe with the longer focal distance.

Two dimensional jet flow was observed in the vector plots presented at the impeller centre plane for all the range of Reynolds numbers studied. The strength of turbulence decays with increasing radial co-ordinate towards the tank wall. The maps of the shear Reynolds stress distributions offered new perspectives to study the flow fields in the ST. The results obtained confirmed the anisotropic flow nature in the stirred tank. Moreover, these results showed that the assumption of axis-symmetric flow is valid only near the impeller region. This conclusion could not be obtained from the results presenting the velocity vectors plots and the maps of the turbulent kinetic energy. Large-scale structure maps of the shear Reynolds stress proved that turbulent stresses are independent of the viscosity and scalable with Reynolds number.

The random correlation technique was employed for the study of velocity time series. The FFT transformation of these results to the power spectral density functions clearly showed the typical frequencies associated with the impeller blades passages.

Separation of the pseudo-turbulence contribution to the total shear Reynolds stress, near the impeller, was found necessary. This was successfully performed by high pass Chebichev filtering, and the data thus obtained were of the same order of magnitude as those measured in the region where the pseudo-turbulence vanished. Moreover, the tendency of pseudo-turbulence to disappear for the radial co-ordinate $r/R > 1.6$ was observed.

Additional results at the horizontal planes along the vertical axis demonstrated clearly the decay of the radial flow jet with the increasing distance from the impeller centre plane. Moreover, the shear Reynolds stress maps at different vertical co-ordinates confirmed, once again, the anisotropy of flow in the stirred tank. In addition, the analysis of the shear Reynolds stress at the horizontal planes, parallel with the impeller centre plane, showed that the top and bottom vortices have different turbulent flow features.

3.3.4 Flow in the Baffle Region

3.3.4.1 Experiment description

Description of the primary flow pattern around the baffle was the objective of this last LDV study. Measurements were conducted at the zero axial co-ordinate (impeller centre plane) for

$Re = 5000$, and LDV data was obtained with the $d_p = 83$ mm probe located below the ST bottom.

A very fine grid was used since the baffle presence creates the abrupt changes in its vicinity. The rectangular region of 145 points around the baffle was investigated with resolution of 2 mm. Unfortunately, the points in close proximity of the baffle could not be measured due to larger beams separation of the used probe.

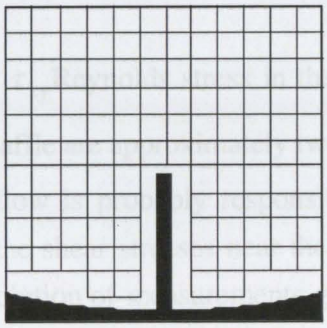

Figure 3.37 Measurement grid for the baffle region.

Ten thousand samples per point were collected in LDV coincidence mode. Water was the working fluid and seeded by neutrally buoyant nylon particles.

3.3.4.2 Results

Figure 3.38 shows the results obtained in the baffle region. The flow near the wall is strongly redirected into the axial direction due to the baffle presence.

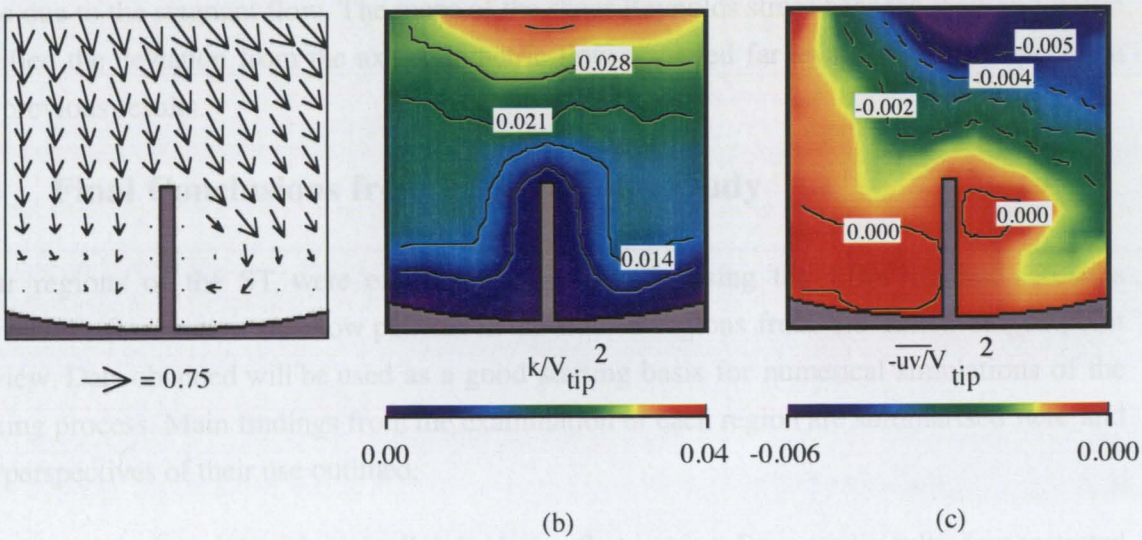

Figure 3.38 Results from measurement in the baffle region at Re=5000: a) vector plot; from the radial and tangential velocity components; b) maps of turbulent kinetic energy; c) τ^t_{xy} Reynolds stress maps.

From the map of the vector plot (Figure 3.38a), a small vortex formed behind the baffle can be observed. This vortex rotates in opposite direction of the impeller rotation. The turbulent kinetic energy was computed only from the measured radial and tangential velocity fluctuations (Equation 3.11) and therefore, the presented maps in Figure 3.38b can be under-estimated. Figure 3.38b shows the map of the normalised turbulent kinetic energy in the baffle region. The contours in Figure 3.38b illustrate the decay of turbulence towards the tank wall as it was expected. In addition, these contours suggest the assumption of the axis-symmetric flow near the wall.

Figure 3.38c shows the map of the τ_{xy}^{t} Reynolds stress in the baffle region. As can be seen, the τ_{xy}^{t} Reynolds stresses near the baffle are approximately two orders of magnitudes smaller then in its vicinity. The stagnant flow is probably responsible for this phenomenon. The expected increasing magnitude of the shear stresses near the baffle was not observed. This probably due to the insufficient resolution of measurements grid near the baffle and the tank wall. Other components of the Reynolds stress tensor are expected to rise significantly due to the strong and abrupt flow change into the axial direction. Here again, the Reynolds stress data confirmed that the assumption of axis-symmetric flow, suggested by the vector plots and the maps of the turbulent kinetic energy, is not valid in the regions far away from the impeller.

3.3.4.3 Conclusion

A small re-circulation zone was found behind the baffle of a stirred tank. The length scale of this vortex is around two thirds of the baffle width, B. The tendency of turbulence to decay towards the stirred tank wall was confirmed. Very small τ_{xy}^{t} Reynolds stresses near the baffle arise due to the stagnant flow. The maps of the shear Reynolds stress near the wall and baffle justified the deviation from the axis-symmetric flow observed far away from the impeller in the previous results.

3.4 Final Conclusions from Experimental Study

Four regions of the ST were explored experimentally using the LDV method. Results showed the flow nature and flow patterns in the studied regions from the time averaged point of view. Data obtained will be used as a good starting basis for numerical simulations of the mixing process. Main findings from the examination of each region are summarised here and the perspectives of their use outlined.

The first study focused on the impeller discharge flow region. Presented results demonstrated clearly that the velocity profiles close to the impeller region are independent of the tangential co-ordinate. The impeller off-bottom clearance imposes a non-symmetrical shape of vertical profiles of the radial and tangential velocity.

The radial and tangential velocities were found to decay along the impeller centre line and this decay depends on the Reynolds number. The theoretical dependence of the radial velocity decay with the Reynolds number was proposed and it compared well with the data obtained by LDV.

The measured vertical profiles of the radial and tangential fluctuating velocities showed clearly that the flow in the discharge flow region is strongly anisotropic. Moreover, the profiles of the turbulence intensities suggested that the top and the bottom vortices have different nature. The top vortex has a stronger rotation with higher radial turbulence intensities, and the bottom vortex has a stronger axial motion with larger tangential turbulence intensities. The values of Flow number at various radii were computed from the measured radial velocities and these will be used for comparisons with results from CFD simulation.

The second study was dedicated to the impeller region. The results showed that the flow in the impeller region is axis-symmetric and mainly rotational. This is a very important conclusion that will significantly simplify CFD simulations of the stirred tank hydrodynamics.

The maps of tangential velocity revealed the effects of trailing vortices on the flow field at the outlet corner of impeller blade. The axial velocity in the impeller region was only computed and the obtained results showed that the flow enters the impeller region also through the surfaces drawn by the horizontal edges of the blades. Moreover, the axial velocity gradient at this surface was approximately zero. This observation will be useful for the specification of boundary conditions in CFD simulations.

The third study provided the flow field quantities at the impeller centre plane for a range of Reynolds numbers. The behaviour of the flow field with increasing Reynolds number was reported using the maps of the velocity vectors, turbulent kinetic energy and shear Reynolds stress. Large-scale structure maps of all studied quantities were found to scale with the rotational speed of the impeller and were influenced by the pseudo-turbulence near the impeller.

The study of kinetic energy revealed that the strength of turbulence decays with distance from the impeller and its highest magnitudes were determined at the impeller tip. The results presented in terms of the shear Reynolds stress maps offered new perspectives to study the flow fields in the ST. This data confirmed the anisotropic flow nature in the stirred tank but also showed that the assumption of axis-symmetric flow is valid only near the impeller region. This conclusion was in contradiction with those obtained from the plots of the velocity vectors and the maps of turbulent kinetic energy but is more reliable due to change in the flow field caused by the baffle presence.

The presented results of the shear Reynolds stress are novel and very important for the ST applications with chemical reactions. It is believed that the shear Reynolds stress will be a good criterion for validation of the results produced by the existing CFD tools.

The last experimental study, in the baffle region, revealed a small vortex behind the baffle rotating in the opposite direction of the impeller rotation. The maps of the shear Reynolds stress provided additional confirmation that the flow far away from the impeller can not be assumed as axis-symmetric.

4. Laminar Mixing — CFD Study

4.1 Introduction

Mixing is considered a process where the uniformity of a desired quantity is progressively improved. To achieve such a goal in the stirred tank — ST, its contents must be put into motion by the forces of a rotating impeller. In any flow regime, the external forces imposed on the impeller must overcome the resisting forces of the fluid. The inertial forces are important in the case of change of direction or velocity of the liquid. The other important type of forces is the viscous-stresses. The inertial forces are essential for low viscosity fluids and the viscous-shear forces play an important role for viscous materials. In both cases, the major resistance determines the method by which the impeller momentum is transferred into the tank bulk.

The impeller design and the shape of the stirred tank are fundamental for optimal mixing performance. Their main impact is on the increase of interfacial area that promotes the mixing enhancement. The creation of new surface area can be made by shear or normal deformations in the material, induced by the rotating impeller. In laminar mixing, the major mechanism is shear, since turbulence is not present and diffusion has not significant impact. The quality of mixing depends on the ability of the impeller to create thinner and thinner layers, and this characteristic property of the laminar mixing processes is called *striation*. Striation thickness is related to the created interfacial area and can be pictured as the scale for segregation. According to Uhl (1966), the smaller the striation thickness is, the smaller is the segregation, and consequently mixing is better. Therefore, the creation of surface area and the lowering of striation thickness intensify the mixing processes. Usually, large impellers with diameter close to that of the tank are preferred in laminar regime. They create high shear forces

between the blade tip and the wall of the ST, thus decreasing striation thickness, and promoting in this way the overall laminar mixing.

The aim of this chapter is to characterise the mixing process in stirred tanks operating under laminar regime. This objective is achieved by means of numerical simulations using the CFD tool FIDAP, on two and three-dimensional computational domains. The steady-state simulations of flow fields in the baffled and unbaffled stirred tanks are performed using the blade set and the moving ring approaches. The results from these approaches are validated and analysed here with a purpose to build the most appropriate simulation strategy for the ST mixing process under turbulent regime that will be studied in Chapter 5. The ability of CFD tools to predict the ST hydrodynamics and mixing efficiency under a laminar regime is investigated.

Numerical predictions are based on the conservation of mass and the conservation of momentum for laminar flow. The inertial terms, in laminar regime are either not present or not important due to their small magnitude. As the impeller Reynolds number increases, the inertial forces start to dominate the viscous forces of the liquid and the equations valid for laminar regime become inadequate. More complicated approaches must be employed for numerical simulations of higher Reynolds numbers.

The instantaneous flow patterns of the ST operating under laminar regime vary periodically due to passages of the blades for baffled tanks. This variation depends on the impeller rotational velocity, impeller type, and liquid properties. The velocities can be negligible in some regions of the stirred tank mainly for high viscosity liquids. This gives origin to stagnant zones and their presence results in poor performance of the mixing since it becomes an area-controlled process. This study will determine the effect of the presence of a baffle in the creation of these stagnant zones and in the overall ST mixing.

This chapter is organised in four main sections. The study of two-dimensional ST is given in Section 4.2. The section 4.3 is dedicated to numerical simulations obtained using the three-dimensional model of ST. Both Sections 4.2 and 4.3 are subdivided into four parts:

- *model description and objectives;*
- *calculated quantities;*
- *results;*
- *conclusions.*

The two and three-dimensional simulations are compared and the limitation of numerical modelling based on equations used for laminar flow is demonstrated in Section 4.3. The main findings and conclusions from this study are summarised last, in Section 4.4.

4.2 Two Dimensional Stirred Tank

Two-dimensional steady-state predictions of the ST operating under a laminar regime are given here. The results are presented in terms of the streamlines, total viscous stresses, and Power number for the range of Reynolds numbers from 1to 1000. Descriptions of the equations and numerical model used, calculated quantities and results from predictions follow.

4.2.1 Model description and objectives

The computational domain of integration is formed by a single horizontal cut through the ST at the impeller centre plane (Figure 4.1). Here the analysis is limited to two-dimensional flow where there is no axial motion and the geometrical model consists only on the impeller and on the tank wall with or without baffles. The impeller and tank wall are fixed entities in the steady-state simulation.

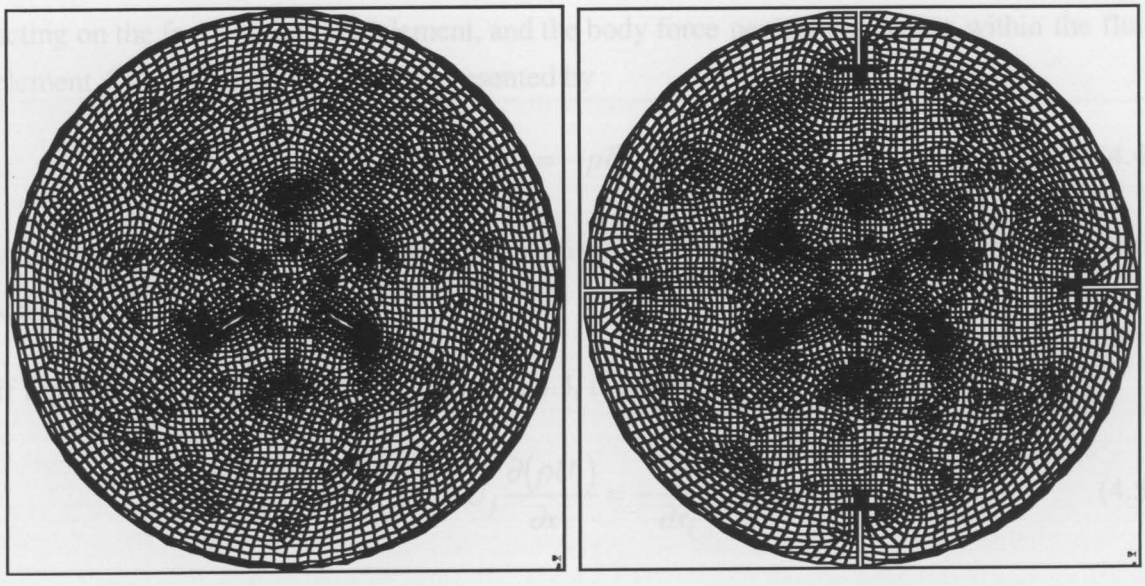

Figure 4.1 Computational domains for the two-dimensional predictions: (a) unbaffled and (b) baffled stirred tank.

The flow is considered incompressible and isothermal and fluid Newtonian. Numerical simulations are accomplished by the solution of the equations of conservation of mass and momentum. These equations form a closed system of equations. The equations are written in Cartesian co-ordinates using the *double-indexing scheme* where repeated indices in any term indicate a summation over all three values of the index (see Appendix C). The equation of mass conservation is given by

$$\frac{\partial \rho}{\partial t} + \frac{\partial \rho U_i}{\partial x_i} = 0 \tag{4.1}$$

where the U_i is component of the velocity vector in the x_i direction, and ρ is the liquid density. For liquids of constant density Equation 4.1 simplifies to

$$\frac{\partial U_i}{\partial x_i} = 0 \tag{4.2}$$

The conservation of momentum is derived by applying Newton's laws of motion along each direction for fluid element in a differential control volume, that is:

$$\frac{\partial(\rho U_i)}{\partial t} + U_j \frac{\partial(\rho U_i)}{\partial x_j} = \frac{\partial}{\partial x_j}\sigma_{ij} + \rho g_i \tag{4.3}$$

Here, σ_{ij} is the *stress tensor* and $g_i$is the component of the gravitational acceleration. The terms on the left hand-side represent the net accumulation rate of momentum within the control volume and the net transport of momentum across the faces of the control volume. The terms on the right hand-side of Equation 4.3 represent the sum of forces per unit volume acting on the faces of the fluid element, and the body force per volume acting within the fluid element. The stress tensor can be represented by

$$\sigma_{ij} = -p\delta_{ij} + \tau_{ij} \tag{4.4}$$

where the p is hydrodynamic pressure, δ_{ij} is the Kronecker delta, and τ_{ij} is the viscous stress tensor.

If Equation 4.4 is substituted into Equation 4.3, it can be obtained

$$\frac{\partial(\rho U_i)}{\partial t} + U_j \frac{\partial(\rho U_i)}{\partial x_j} = -\frac{\partial p}{\partial x_i} + \frac{\partial \tau_{ij}}{\partial x_j} + \rho g_i \tag{4.5}$$

The forces acting on the faces of the control volume are now expressed by the sum of two terms: the pressure on an element per unit volume, $\partial p/\partial x_i$, and the viscous force on a fluid element per unit volume, $\partial \tau_{ij}/\partial x_j$.

For viscous incompressible Newtonian fluids the viscous stress tensor, τ_{ij}, can be expressed as

$$\tau_{ij} = 2\mu\varepsilon_{ij} \tag{4.6}$$

where the ε_{ij} is *shear rate tensor* and the μ is the dynamic molecular viscosity and is a function of temperature and species concentration. The shear rate tensor is defined by

$$\varepsilon_{ij} = \frac{1}{2}\left(\frac{\partial U_i}{\partial x_j} + \frac{\partial U_j}{\partial x_i}\right) \tag{4.7}$$

For laminar flow of constant density and viscosity, Equation 4.5 can be rewritten as:

$$\rho\frac{\partial U_i}{\partial t} + \rho U_j\frac{\partial U_i}{\partial x_j} = -\frac{\partial p}{\partial x_i} + \mu\frac{\partial^2 U_i}{\partial x_j^2} + \rho g_i \tag{4.8}$$

and this equation can be simplified for steady-state simulation as:

$$\rho U_j\frac{\partial U_i}{\partial x_j} = -\frac{\partial p}{\partial x_i} + \mu\frac{\partial^2 U_i}{\partial x_j^2} + \rho g_i \tag{4.9}$$

This equation is used for the two dimensional study of stirred tanks that totally neglects inertial terms corresponding to dynamic change of the relative position of the impeller and the baffle. In this way, the dynamic simulation can be obtained as a sequence of pseudo steady-state simulations.

Boundary conditions were specified only in terms of the velocity. The rotational motion of the impeller was specified by the velocity on its blades and at the impeller disk. This is called *the blades set approach* and it was applied in steady-state model to resolve the various positions between the impeller blades and baffles in the case of the baffled ST. The tank wall is considered a static region with non-slip boundary conditions.

The inertial effects between the successive positions of the blades relative to the baffle were ignored but the predictions can be used to study the extent of periodic flow generated by the rotational motion of the impeller.

The model equations were discretized and solved by the commercial software FIDAP 7.6 using the finite element method. Two-dimensional four node quadrilateral elements were used with bilinear velocity and discontinuous constant pressure approximations. An iterative method was used for the solution of the numerical system of equations using a fixed point iteration algorithm known as successive substitution. For 6190 number of elements used, represented in Figure 4.1, the required core memory was of 40 MB and computational time was of the order of 800 seconds in an IBM RS6000 machine, model 25T.

The *penalty* approach was selected for the pressure approximation. In this approach, the pressure is eliminated from the global system of unknowns. This significantly reduces the total number of equations that must be solved and the pressure is then recovered in a post-solution operation once the other variables have been determined.

The convergence criteria was set to DTOL = 0.001 for all degrees of freedom solved (the two or three components of velocity and pressure) in both types of simulations. This means that iteration for the steady-state solution or at a given time step was terminated when the relative error (change between two consecutive steps) for the solution vector was less than the convergence criteria.

4.2.2 Calculated Quantities

The velocity patterns are presented in terms of stream functions. For two-dimensional incompressible flows, the stream function is defined by

$$U = \frac{\partial \psi}{\partial y}; V = -\frac{\partial \psi}{\partial x} \tag{4.10}$$

where U and V are velocity components in the x and y directions of Cartesian co-ordinate system, respectively. On the streamlines diagrams, the streamline function is normalised by the streamline function at the wall and these normalised values represent the fraction of the total tangential flow rate between the impeller tip and the tank wall.

The equation governing the dynamics of the fluid kinetic energy can be obtained by multiplying Equation 4.3 by U_i. Assuming steady-state, incompressible flow and neglecting body forces, this equation becomes

$$\rho U_j \frac{\partial}{\partial x_j}\left(\frac{1}{2}U_i U_i\right) = U_i \frac{\partial}{\partial x_j}\sigma_{ij} = \frac{\partial}{\partial x_j}\left(\sigma_{ij} U_i\right) - \sigma_{ij}\frac{\partial}{\partial x_j}U_i \tag{4.11}$$

The first term on the right-hand side of Equation 4.11 represents the transport of fluid kinetic energy by the stress σ_{ij}. This term integrates to zero, if the integration refers to a control volume on whose surface either σ_{ij} or U_i vanish (Tennekes and Lumley, 1972). In this case, only the second term $\sigma_{ij}\,\partial U_i/\partial x_j$ can change the total amount of kinetic energy in the control volume. Furthermore, the second term can be expressed as the deformation work, $\sigma_{ij}\varepsilon_{ij}$, since the shear rate tensor must be symmetric. Then from Equation 4.11, the deformation work must be equal to the loss of kinetic energy. The deformation work can be defined using Equation 4.4 as

$$\sigma_{ij}\varepsilon_{ij} = -p\delta_{ij}\varepsilon_{ij} + \tau_{ij}\varepsilon_{ij} \tag{4.12}$$

For incompressible fluids, the contribution of the first term of Equation 4.12 is zero and the deformation work can finally be derived, from Equation 4.6, as

$$\sigma_{ij}\varepsilon_{ij} = 2\mu\varepsilon_{ij}\varepsilon_{ij} \tag{4.13}$$

where the term $2\mu\varepsilon_{ij}\varepsilon_{ij}$ is the *viscous dissipation rate* per unit volume of fluid.

The results in this study are presented in terms of the total viscous stress,

$$\left(\tau_{ij}{}^2\right)^{1/2} = 2\mu\left(\varepsilon_{ij}\varepsilon_{ij}\right)^{1/2} \tag{4.14}$$

that can be normalised by:

$$\frac{\left(\tau_{ij}{}^2\right)^{1/2}}{\rho V_{tip}{}^2} = \frac{2\mu\left(\varepsilon_{ij}\varepsilon_{ij}\right)^{1/2}}{\rho V_{tip}{}^2} \tag{4.15}$$

In addition, by substitution of the tip velocity, $V_{tip} = 2\pi NR$, the last equation may be rewritten and rearranged into:

$$\frac{\left(\tau_{ij}{}^2\right)^{1/2}}{\rho V_{tip}{}^2} = \frac{2\left(\varepsilon_{ij}\varepsilon_{ij}\right)^{1/2}}{\pi^2 N\,\mathrm{Re}} \tag{4.16}$$

where the N is impeller rotational frequency and the R is impeller radius.

Equation 4.16 shows that the normalised total viscous stress is a non-linear function of the Reynolds number and of the impeller rotational frequency. This function is studied here by analysis of numerical predictions at various Reynolds numbers.

The power draw, P, is the energy per unit time which is transferred to the ST through the impeller to compensate the energy losses by viscous dissipation. The power draw can be measured using the torque-meters or it can be estimated from numerical simulations of the flow field in the ST.

From dimensional analysis arises that the power draw has the same fundamental units as the product of $\rho N^3 R^5$ or the product $\mu N^2 R^3$. Experimental power studies are usually reported in terms of dimensionless parameter called the *Power number*, N_P, defined as

$$N_P = \frac{P}{\rho N^3 (2R)^5} \tag{4.17}$$

or as

$$N_P = \frac{P}{\mu N^2 (2R)^3} \tag{4.18}$$

Here $(2R)^5$ and $(2R)^3$ are used in order to be consistent with definition found in Tatterson (1991), where the power draw is defined in terms of the impeller diameter.

Since the present simulations are performed on a 2D domain, the value of P in the entire 3D stirred tank may be only estimated. The approximation is based upon the assumption that the power draw dissipated on the calculated area, A, is then multiplied by the blade width, W, representing the energy input into the impeller and the impeller discharge flow regions, that is

$$P \approx 2W\mu \int_A \left(\varepsilon_{ij}\varepsilon_{ij}\right) dA \tag{4.19}$$

The power draw estimated in this way is smaller than the real value since it does not account for the viscous heating in the bulk of the tank.

4.2.3 Results

In the results of 2D numerical simulation presented, the periodic change of the impeller blade to baffle position is considered as a pseudo steady-state problem. In this case, the steady-state situation is solved for each particular position independently. The numerical results in the ST are visualised as the normalised stream functions on the computational domain. The stream function contours are the streamlines for the flow and fluid flows parallel to them. Streamlines, at four different impeller to baffle relative positions, are plotted in Figure 4.2 overlaid on the stream function map. The stream function map is only represented for the region outside of the impeller radius.

The overall picture is maintained throughout Figure 4.2a-d and is independent of the blade to baffle position. The higher density of streamlines near the blades suggests that the velocity and shear rates are higher in that region. Asymmetric shape of the streamline is found near the baffles. It is an important aspect that 80% of the total tangential flow takes place only in the inner half of the tank radius. In addition, the striation thickness can be represented by the spacing between the streamlines. The striation thickness is smaller in the impeller vicinity. This confirms the physical picture of the flow obtained from the experiments.

The maps of the normalised total viscous stress for $Re = 10$ are illustrated in Figure 4.3 at various positions between the blades and baffles. Larger values of the total viscous stress are found near the impeller tip and they also increase at the tips of the baffles. This tendency is caused by dramatic changes in the velocity gradients in the mentioned regions. From the maps in Figure 4.3a-d can also be observed that the total viscous stress values on the regions away from the source of the momentum are not dependent on the relative position of the impeller blades. This is in contrast with the regions near the blade vicinity, where the total viscous stress varies periodically with passages of the blades. These maps show that the flow periodicity extends from the impeller tip up to a distance twice the size of the impeller radius.

Noteworthy is the fact that the quantities studied, in the computational domain, maintain the overall periodicity in each quarter of the tank that contains a baffle at its middle position. This suggest that it would be possible to use only one quarter of the tank coupled with periodic boundary conditions to obtain the global simulation of the tank flow field. This fact will be used for the 3D simulations.

The simulation results for the baffled and unbaffled tanks can be seen in Figure 4.4 through Figure 4.7 for four different values of the Reynolds number, $Re = 1, 10, 100, 1000$. For the baffled and unbaffled tanks, differences in the streamlines are negligible near the impeller but, with the increasing radial position, the flow fields start to differ. The tangential flow rate is greater for the ST without a baffle than that for the baffled tank. The flow rate decreases because of the presence of the baffles. A similar trend is observed at higher impeller rotations, thus suggesting that the baffles inhibit homogenisation during the mixing process under laminar regimes. When the impeller rotates at higher speeds, the streamlines extend more towards the wall indicating better mass and heat transfer. However, for the baffled tanks, four recirculation vortices can be found between the baffles, thus inhibiting the global circulation.

The maps of the normalised total viscous stress are displayed in Figure 4.4c,d through Figure 4.7c,d. Looking at the shape of the maps, the impact of the baffles is evident. The baffles deform the stress maps and increase its value only at the tip of the baffles but they decrease the total viscous stress in the regions between the baffles. The size of these regions of poor mixing performance is reduced with increasing Reynolds number but the magnitude of the total viscous stress also decreases. The trend of the total viscous stress to decrease with Reynolds number, as derived theoretically in Equation 4.16, can thus be confirmed.

The baffles in the stirred tank diminish the overall circulation and significantly reduce the mixing performance in laminar regime.

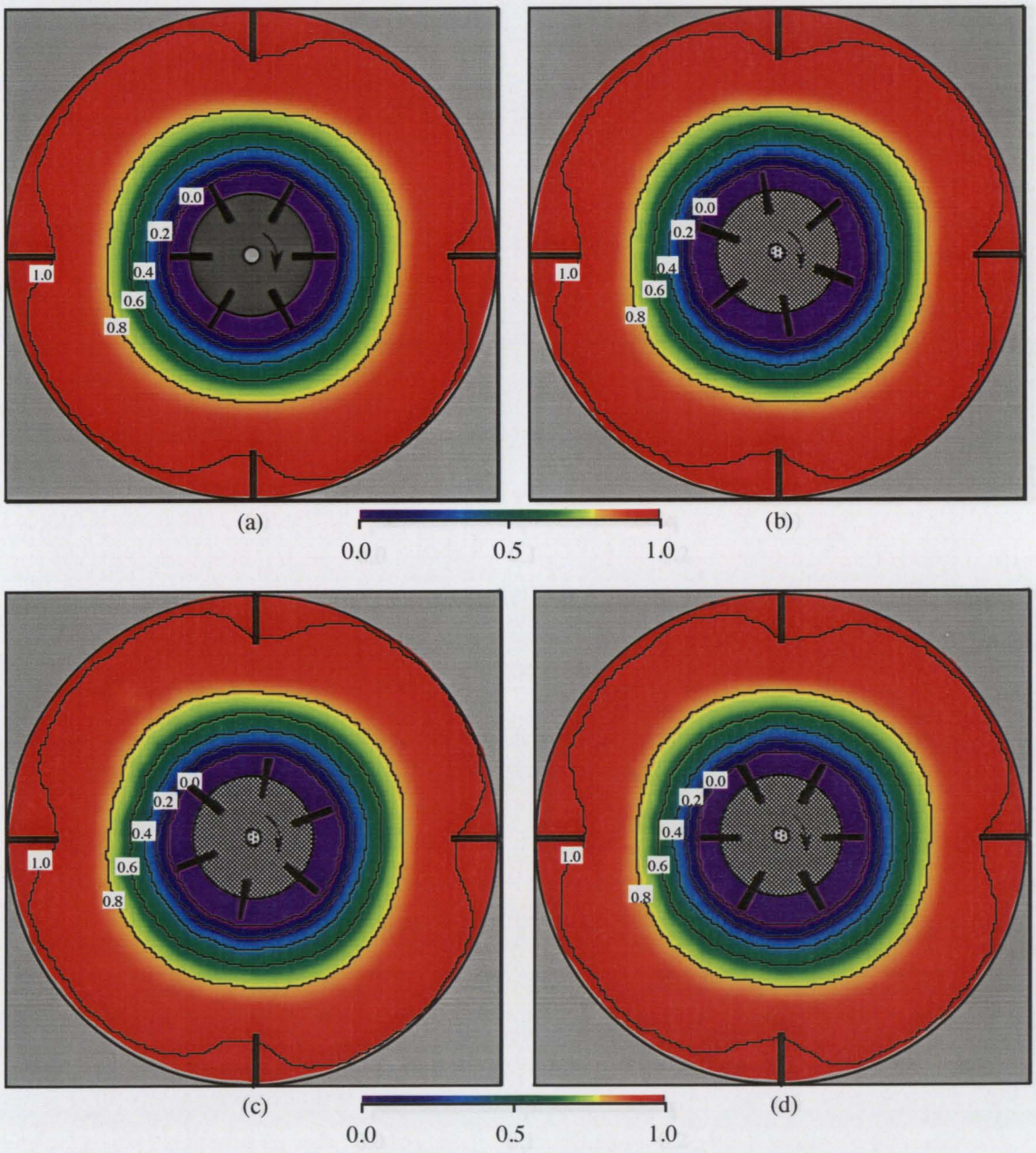

Figure 4.2 *Stream function maps and normalised streamline contour plots for Re=10 at four different positions of the impeller blade set: (a) 0°; (b) 20°; (c) 40°; (d) 60°.*

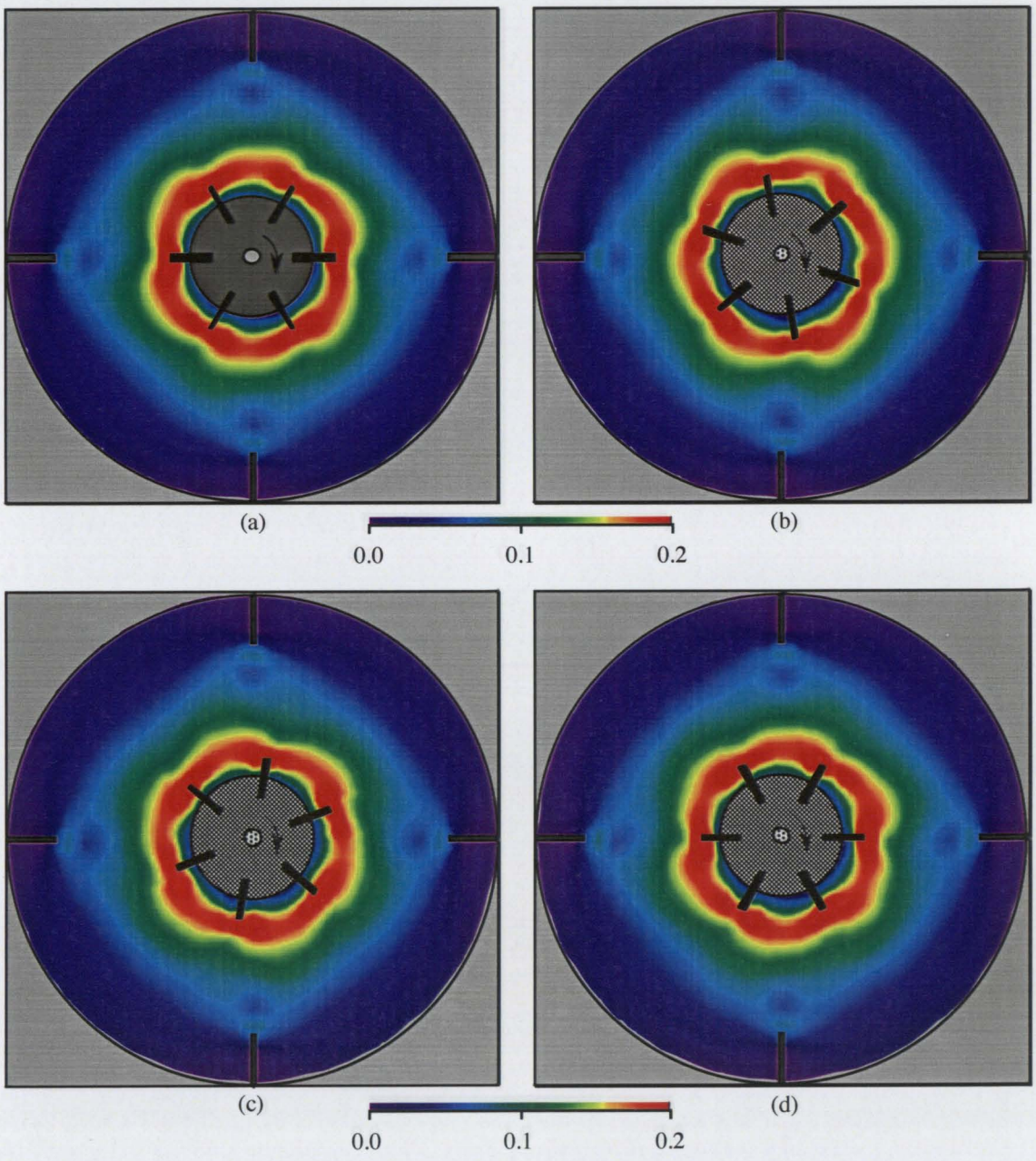

Figure 4.3 *Normalised total viscous stress maps for Re=10 at four different positions of the impeller blade set: (a) 0°; (b) 20°; (c) 40°; (d) 60°.*

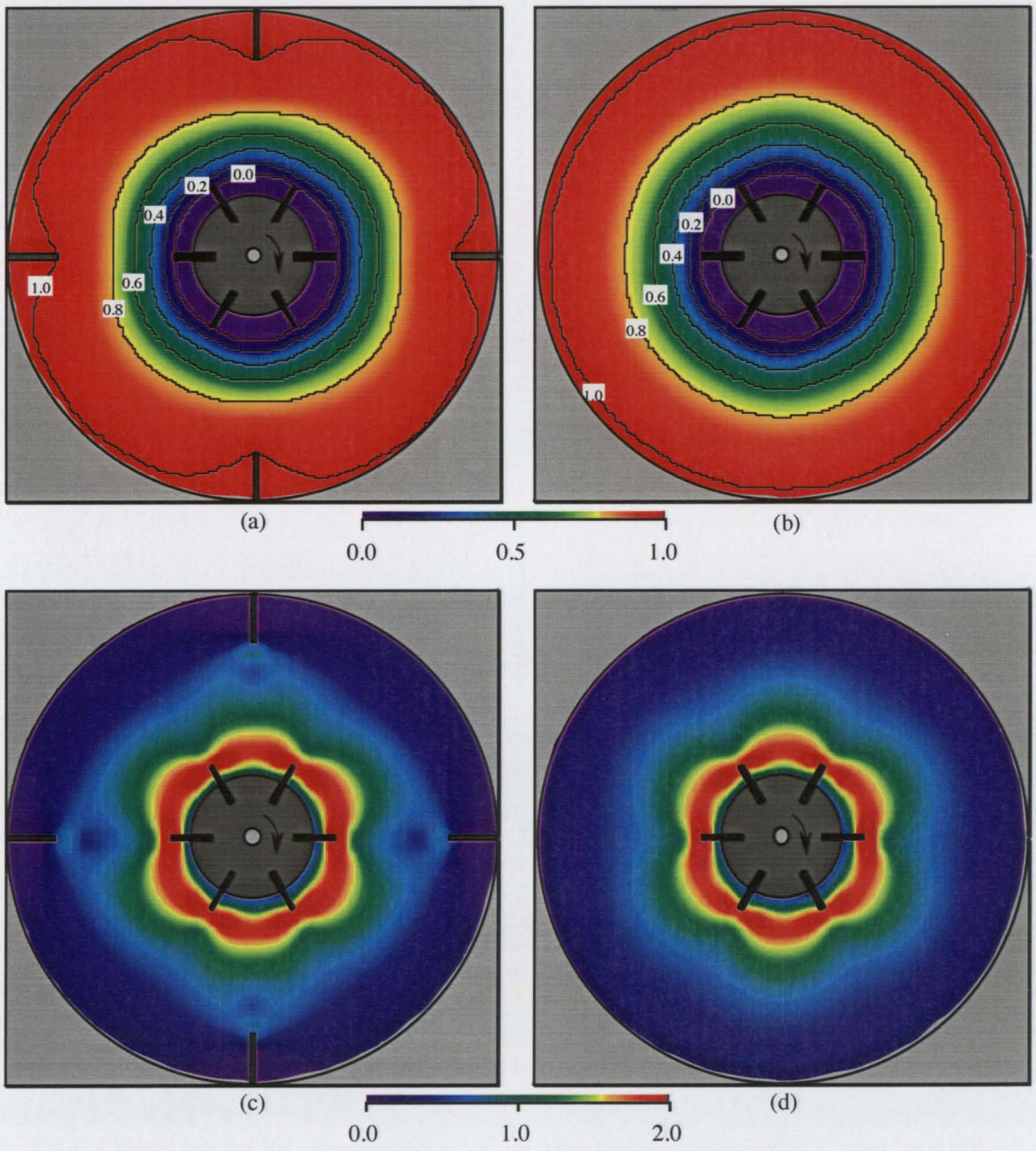

Figure 4.4 *Normalised streamlines (a, b) and normalised total viscous stress (c, d) maps for Re=1 in baffled (a, c) and unbaffled (b, d) stirred tanks.*

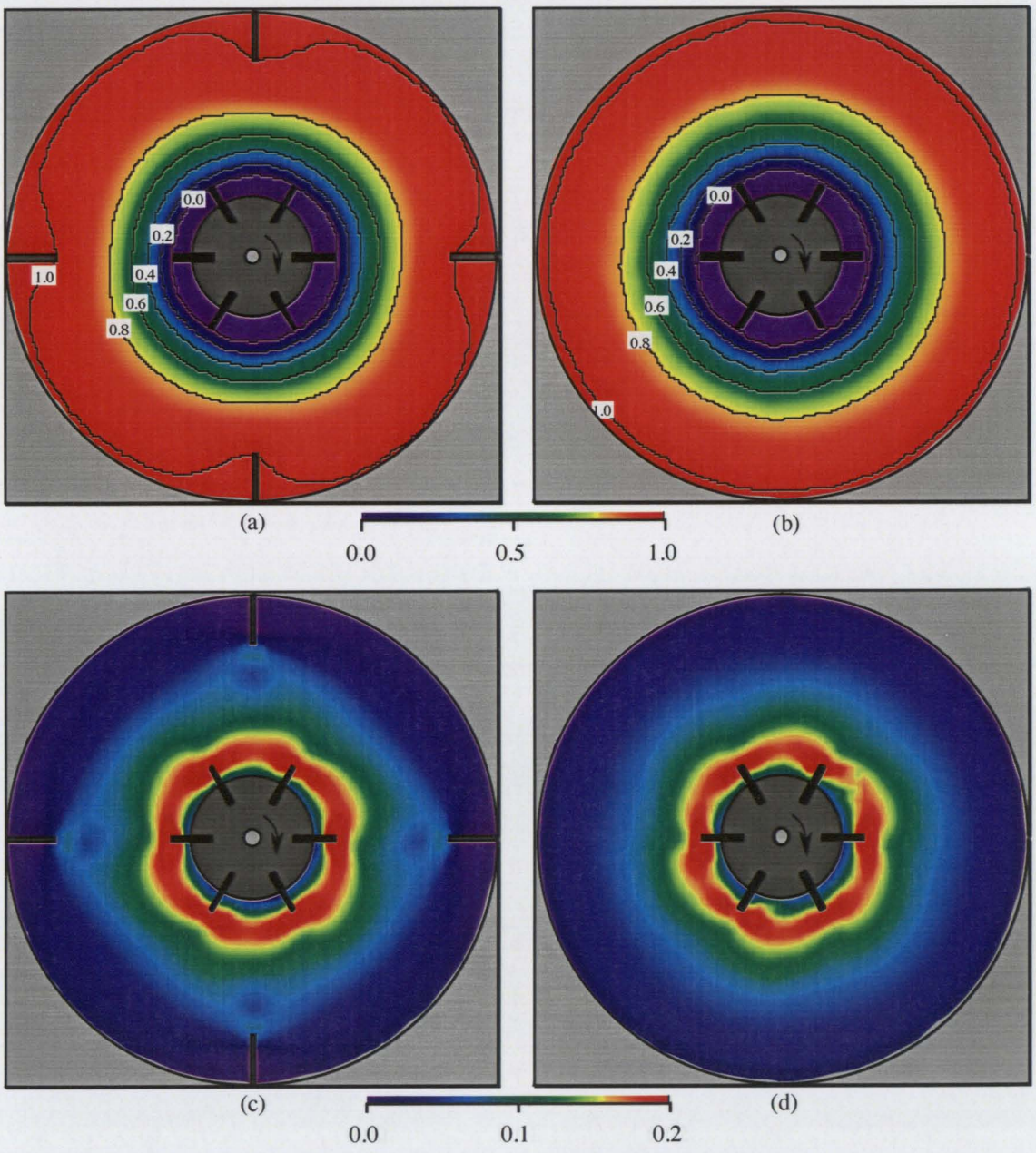

Figure 4.5 *Normalised streamlines (a, b) and normalised total viscous stress (c, d) maps for Re=10 in baffled (a, c) and unbaffled (b, d) stirred tanks.*

BIBLIOTECA F.E. PORTO

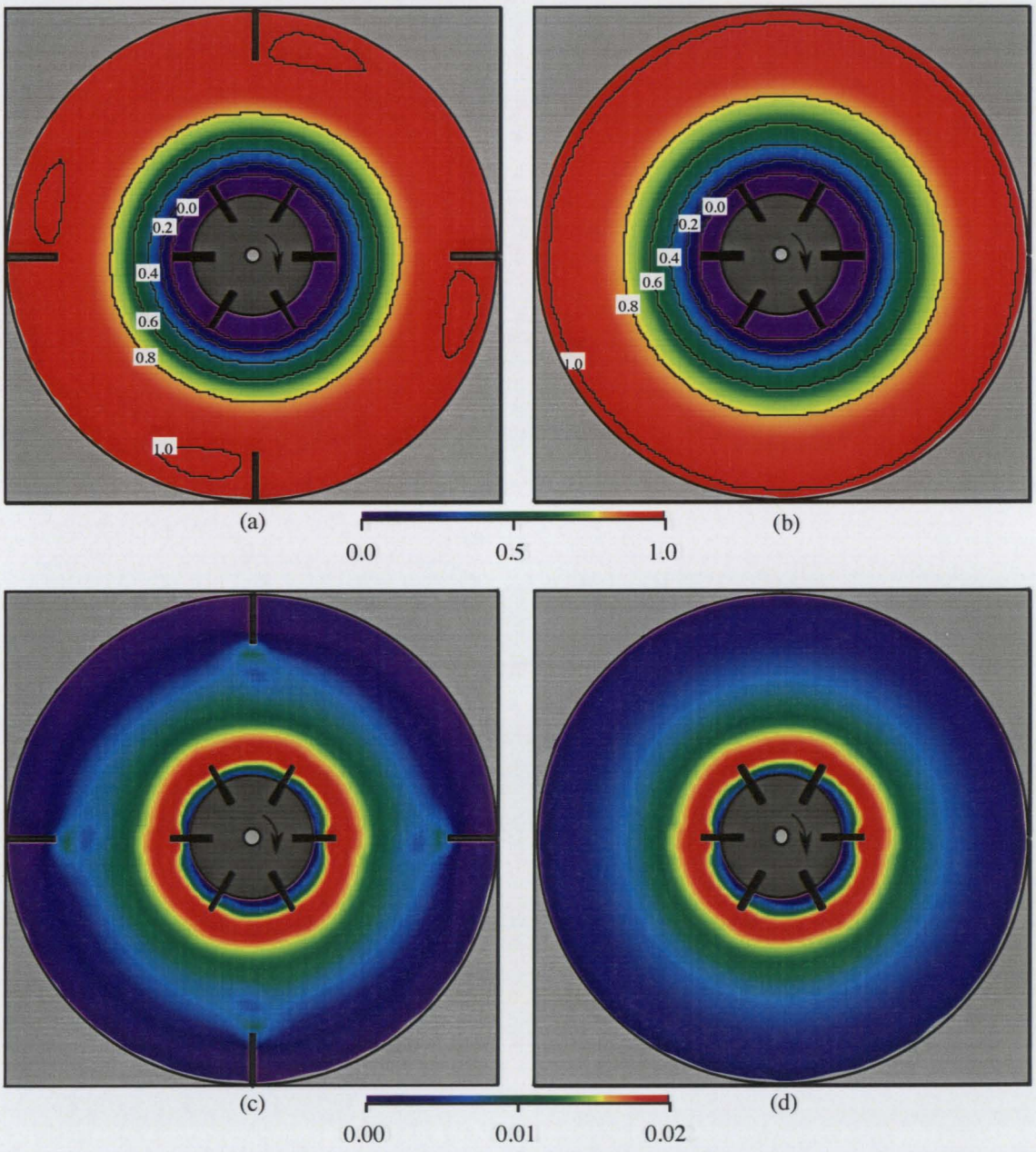

Figure 4.6 *Normalised streamlines (a, b) and normalised total viscous stress (c, d) maps for Re=100 in baffled (a, c) and unbaffled (b, d) stirred tanks.*

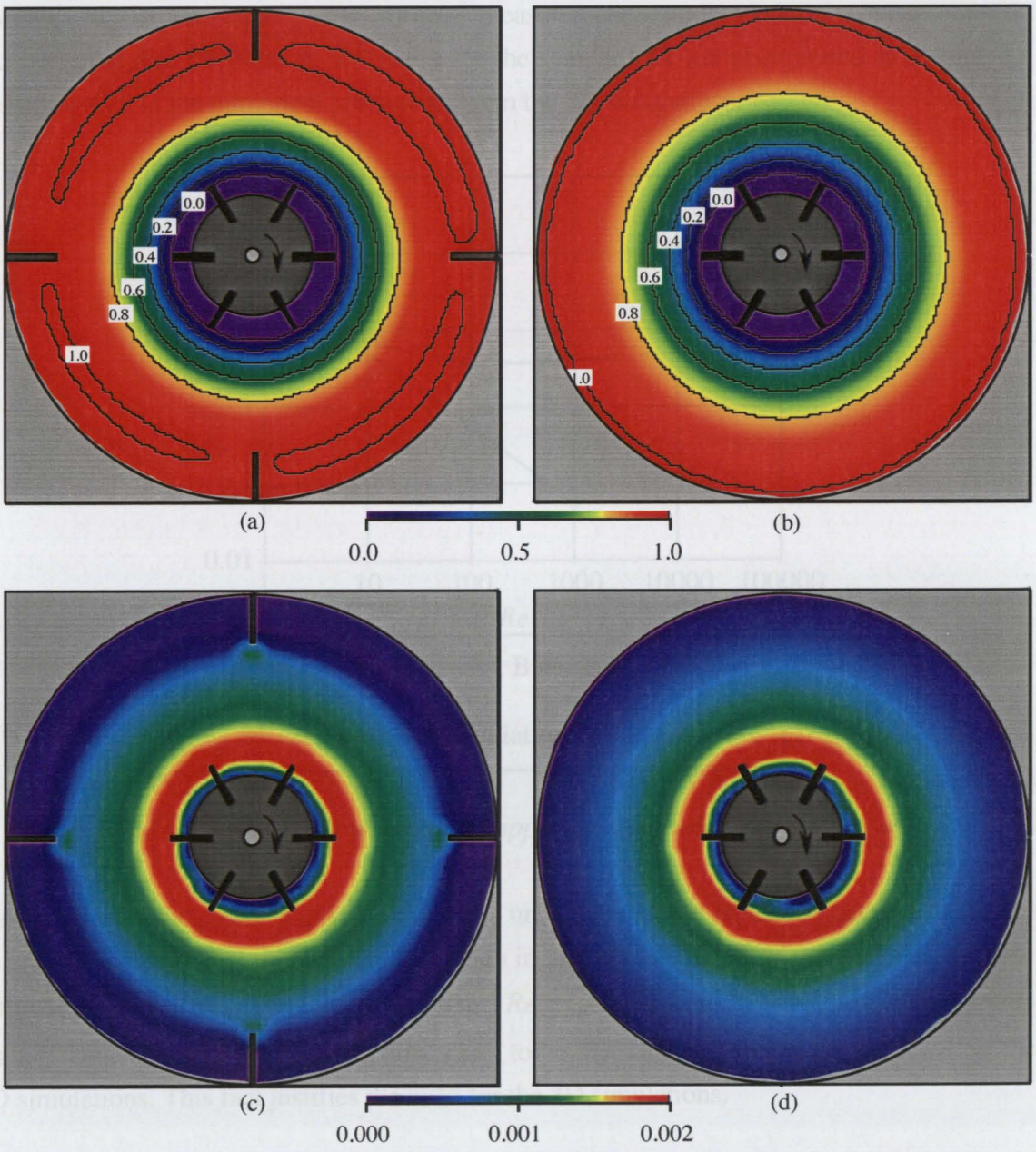

Figure 4.7 *Normalised streamlines (a, b) and normalised total viscous stress (c, d) maps for Re=1000 in baffled (a, c) and unbaffled (b, d) stirred tanks.*

The predicted total viscous stress was used to compute the power draw of the ST, as explained in the previous section, and plotted in Figure 4.8. This quantity can also be investigated experimentally by torque measurements and torsional dynamometers. Experimental data by Bates *et al.* (1963) for the standard ST are also plotted in Figure 4.8 and compared to the numerical predictions from the 2D simulations.

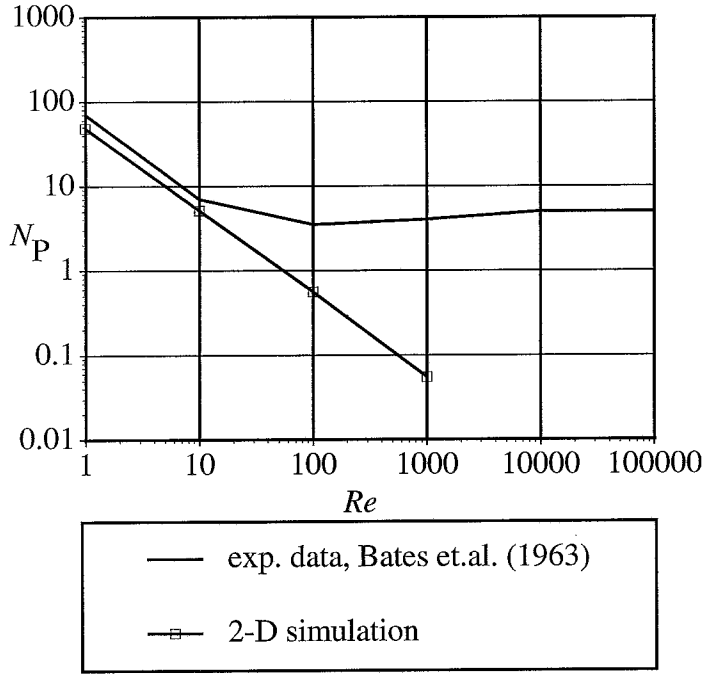

Figure 4.8 The Power number approximation using 2D simulation.

As can be seen, the power number estimations under-predict the measured data but it should be emphasised here that the viscous dissipation in the bulk of the ST is not included in these estimations. However, the trend of N_P versus Re is correct until $Re < 10$, where the flow is mainly tangential. For $Re > 10$ the flow starts to be 3D, and this cannot be predicted by the 2D simulations. This fact justifies the need for the 3D simulations.

In addition, there are a few relevant conclusions on the power draw observed experimentally by various researches (for example Martin, 1946; Rushton, 1946; Nagata *et al.*, 1955 see Tatterson, 1991):

- viscosity has little effect on power consumption except for small Re
- power number tends to a constant value at high Re
- a constant value is reached sooner in baffled tanks at lower Re than for unbaffled tanks

According to Tatterson (1991), the power number is not a constant quantity for a particular impeller at a specific Reynolds number, nor is it uniquely determined by the impeller Reynolds number and impeller geometry. In different geometric configurations, the flow

patterns and the fluid mechanical environments of the impeller are different and consequently, the power number changes.

4.2.4 Conclusions

The 2D flow field in the ST was found to be symmetric and the computational domain of one ST quarter with the baffle in its middle position would be sufficient for simulation purposes. The results showed that the 2D tangential flow rate in the unbaffled tank is higher than that in the baffled tank. Consequently, the presence of the baffles in the stirred tank operating under 2D laminar regime results into reduction of the mixing performance.

The effect of position of the impeller relative to the baffles, on the flow field, was observed in the region with the size up to twice of the impeller radius. This region can be approximated as the zone of extent of pseudo-turbulence.

The total viscous stress was found to be inversely proportional to the impeller rotational speed and to the Reynolds number. The predictions of power draw to the ST underestimated the experimental data of Bates *et al.* (1963) and this was attributed to the fact that the flow development in the axial direction was not accounted for in 2D simulations.

4.3 Three Dimensional Study of Stirred Tank

The non-existence of axial motion in the previous 2D simulations of the ST limited the analysis and comparisons with the 3D experimental results. This is mainly due to the absence of the top and bottom vortices that are particularly important in the case of the baffled tank. The 3D simulations, presented in this section, should eliminate problems found in the 2D study of stirred tanks. The geometric model of the ST standard configuration used here, for experiments and simulations, is discussed in detail in Chapter 5. The calculated quantities and the simulation results are introduced after a very brief model description. The results are compared to those from the 2D simulations. Calculated total viscous stresses are compared at different Re and their special trend with increasing values of Re is emphasised. The Power number computations and its comparison to the results of 2D predictions follow.

4.3.1 Model description and objectives

The computational domain of integration is formed by the $\pi/2$ segment of the ST. This domain is considered sufficient for the 3D numerical simulations, as it was discussed in previous Section 4.2. The geometrical model is described in detail in Chapter 5 where the views on the calculated domain are also presented.

Three different CFD models were used for the 3D simulations of the ST. Two pseudo steady-state models were used for both baffled and unbaffled ST, and one dynamical model was used to perform the dynamic simulations but only for the case of baffled ST.

The same conservation equations introduced in the 2D study are now solved for the 3D flow.

Boundary conditions for the impeller region differ for each one of the three models. The stirred tank bottom, walls, and baffles if present were defined with non-slip boundary conditions. The free liquid surface is modelled as a flat surface with zero axial velocity, thus preventing the formation of the central air vortex. This is acceptable mainly for small Re in the unbaffled ST and for moderate impeller speeds in the baffled ST.

The objective of using three different kinds of boundary conditions in the impeller region is to compare the results of:

- *steady-state simulation using the blades set approach;*
- *steady-state simulation using the moving ring approach;*
- *dynamic simulation;*

and to determine which of the ST models is the most appropriate for simulations of laminar mixing.

- The first steady-state model is an extension of the 2D model, described in Section 4.2.1, to the axial direction, z. Therefore, only the tangential velocity is defined at the surface of the blades while other velocity components are assumed negligible. The tangential velocity, V_θ, at the impeller disk as well as at the shaft, is considered as a linear function of the radius.

- In the second steady-state model the impeller region is specified using the moving ring concept. The region swept by the blades motion is substituted by a virtual fluid-body and boundary conditions are applied on its surfaces. However, here only the tangential velocity is defined at the surface swept by the blade tip. This moving ring approach is analysed and explained in detail in the first part of Chapter 5.

- The third model uses the boundary conditions developed in the first steady-state model and now solved in a dynamic way. The change of relative position between the impeller and the baffles is solved explicitly as it is described in more detail in the second part of Chapter 5.

The equations describing the flow throughout the flow domain are discretized with finite elements using eight node brick, with tri-linear velocity and discontinuous constant pressure

approximations. The system of ordinary differential equations is solved on each element of the computational domain using a segregated solver for each independent variable.

The symmetric linear equation part of the system is solved by the conjugate residual method (CR) and solution of the non-symmetric part of system is provided by generalised minimal residual method (GMRES). The number of elements is 50445, and the simulations required 24MB of core memory for each independent variable. The computational time was of the order of 5 hours for the steady-state simulation and 100 hours for dynamic simulation on an IBM RS6000 machine model 3CT.

The convergence criterion was set to DTOL = 0.001 for all degrees of freedom solved (the three components of velocity and pressure) in all simulations.

4.3.2 Calculated Quantities

Speed, S, contour maps are calculated from three velocity components where all velocities presented are normalised by the velocity at the impeller tip, as

$$S = \left(\Sigma U_i^2\right)^{1/2} / V_{tip} \tag{4.20}$$

The power draw parameter can be calculated from the volume integral of the viscous dissipation in the ST, as discussed in Section 4.2.2. The equation relating the viscous dissipation to the power draw is expressed as

$$P = 2\mu \int_V \varepsilon_{ij}^{\ 2} dV \tag{4.21}$$

In addition, the Power number for the present 3D simulation is given by:

$$N_P = \frac{P}{\rho N^3 (2R)^5} \tag{4.22}$$

4.3.3 Results

Since the results for the simulations of the two steady-state models (the blades set and the moving ring approach) were equivalent, only those results from the moving ring approach are shown here.

Figure 4.9 shows the normalised speed maps overlaid by the radial-axial projections of the velocity vector at two vertical planes of the stirred tank. Figure 4.9a,b,c illustrates the flow pattern at the plane $\theta = 3\pi/8$ behind the baffle (see Chapter 3 for the location of the co-ordinate system considered), and Figure 4.9d,e,f at the vertical plane $\theta = \pi/4$, which passes

through the baffle. The numerical simulations using the steady-state model are also displayed for the baffled tank (Figure 4.9a,d) and the unbaffled tank (Figure 4.9b,e).

Time dependent simulations were performed only for the baffled tank, started with the fluid at rest and continued until a pseudo-steady state flow field was reached in the tank bulk. The results of simulations revealed some variation in the flow field caused by the time dependent position between the impeller blades and the baffle. The overall flow fields in Figure 4.9c,f are presented as the average from the results of the last eight time steps. The dynamic model predictions are similar to those of the steady-state models (Figure 4.9a,d). The flow is centred on the impeller and the magnitude of the speed attains a maximum of 20% of V_{tip}.

Figure 4.10 shows the normalised radial-tangential projections of the velocity vectors, at horizontal planes of different axial co-ordinate values, predicted by the steady-state simulations. The axial co-ordinate values are normalised by the blade width, W. The maps of the speed are overlaid with $V_r - V_\theta$ vector plots. Flow rates of the baffled tank are smaller than in the unbaffled tank, and the presence of baffles is responsible for the formation of stagnant zones near the wall.

It is necessary to have a mass flow in and out of the high-dissipation zone for effective mixing. Since the mixing with the Rushton impeller occurs in a small region of the stirred tank, the fluid above the impeller remains almost completely segregated. Therefore, the flow is almost stagnant in the upper part of the stirred tank, suggesting that the use of a single impeller is not sufficient to promote the overall mixing. Comparing the results of steady-state models in the baffled and unbaffled tanks, it is evident that the flow rate is higher in the tank without baffles. Figure 4.11 shows the ratio of tangential flow rates of the baffled and unbaffled tanks for various Reynolds numbers as obtained using the 2D and 3D simulations. The tangential flow rate through the radius of the calculated domain is taken from 2D simulations, whereas for the 3D simulations an average of the tangential flow rate through the vertical planes of the ST was considered. These results confirm clearly that the presence of baffles decreases overall flow in the stirred tank at higher impeller speeds.

The results at the vertical plane of ST show clearly that the Rushton impeller does not promote mixing of the whole tank content. These results also illustrate that the presence of a baffle decreases the mixing efficiency in a laminar regime. Moreover, the Rushton impeller seems inadequate for laminar mixing, due to the formation of stagnant regions in the bulk of the stirred tank.

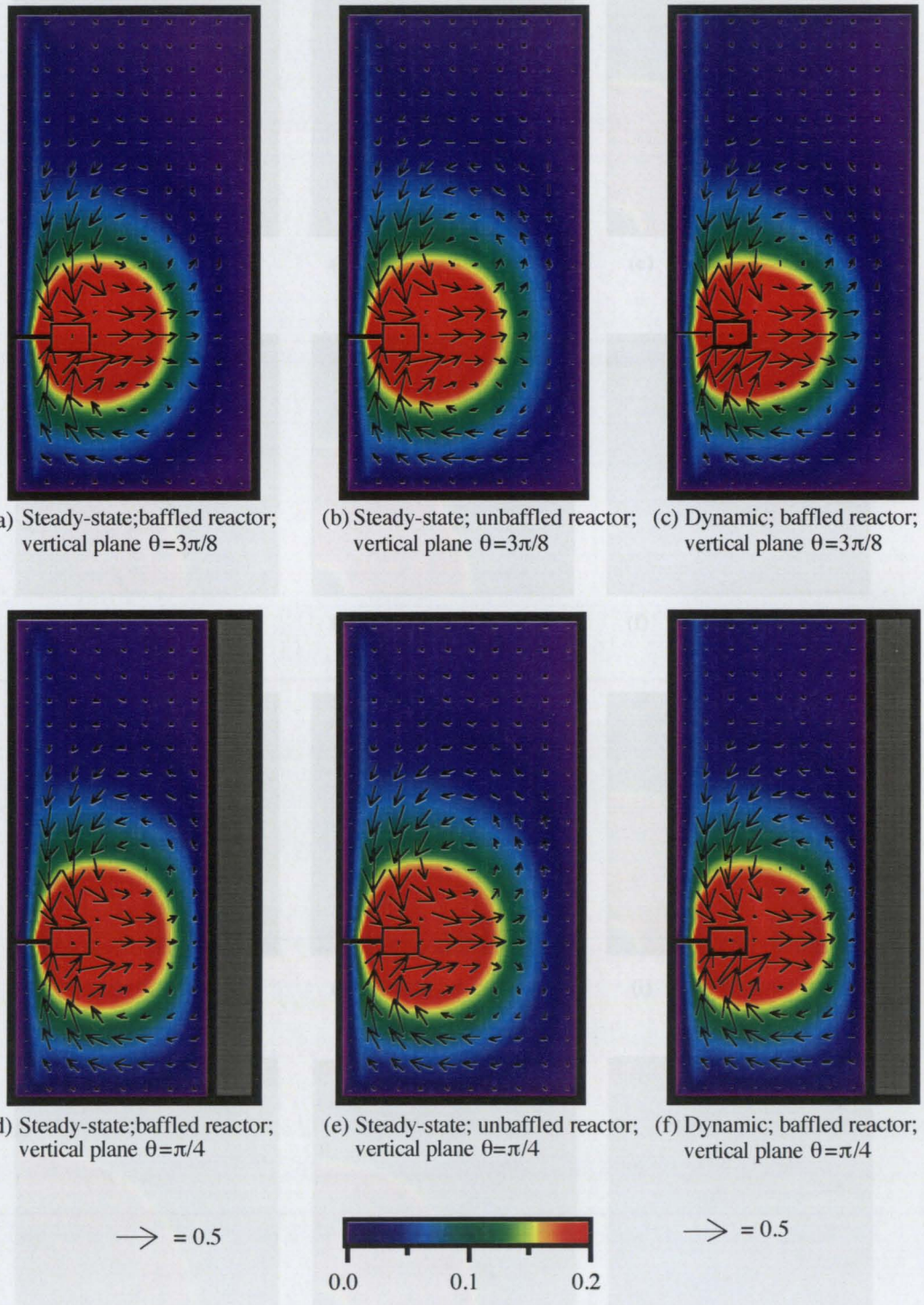

Figure 4.9 *Normalised speed contour maps overlaid with the radial-axial projection of the velocity vector at two vertical planes θ=3π/8 (a, b, c) and θ=π/4 (d, e, f), for the three models at Re=10.*

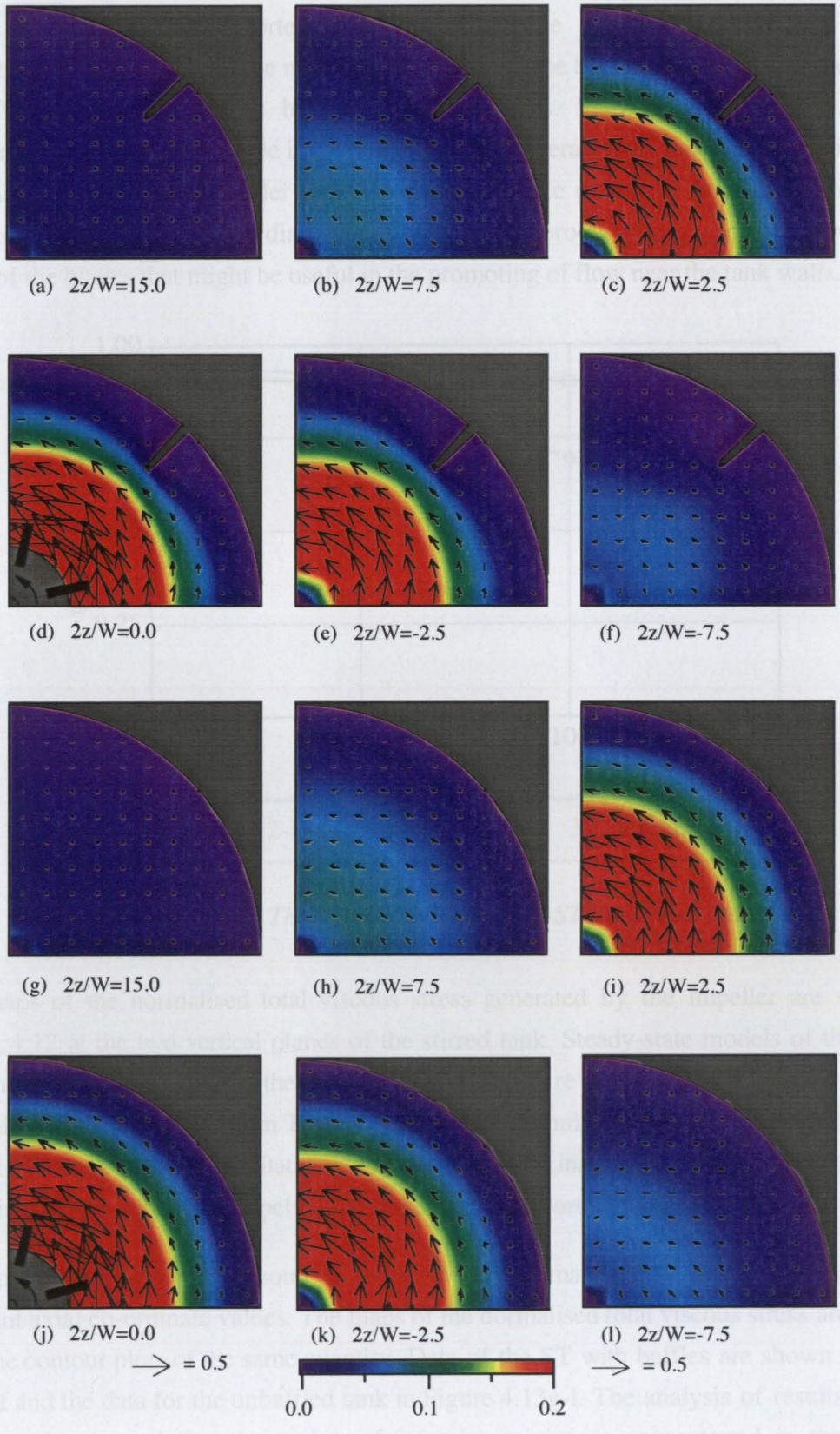

Figure 4.10 *Normalised speed maps overlaid with the radial-tangential projection of the velocity vector at different axial co-ordinate values for Re=10 in baffled (a-f) and unbaffled tanks (g-l).*

Hoogendoorn and Den Hartog (1967) reported similar observations of stagnant regions behind the baffles and reported that removal of the baffles enhanced the pumping characteristics and improved the mixing performance in the ST. For practical applications, the use of multiple impellers can help to solve problems. Metzner *et al.* (1961) reported advantages in the use of multiple impellers to promote overall fluid motion. The other option is the use of a different impeller type. Poor performance of the Rushton impeller may be enhanced by impellers of large diameters. These should produce high viscous stresses at the edges of the blades that might be useful in the promoting of flow near the tank walls.

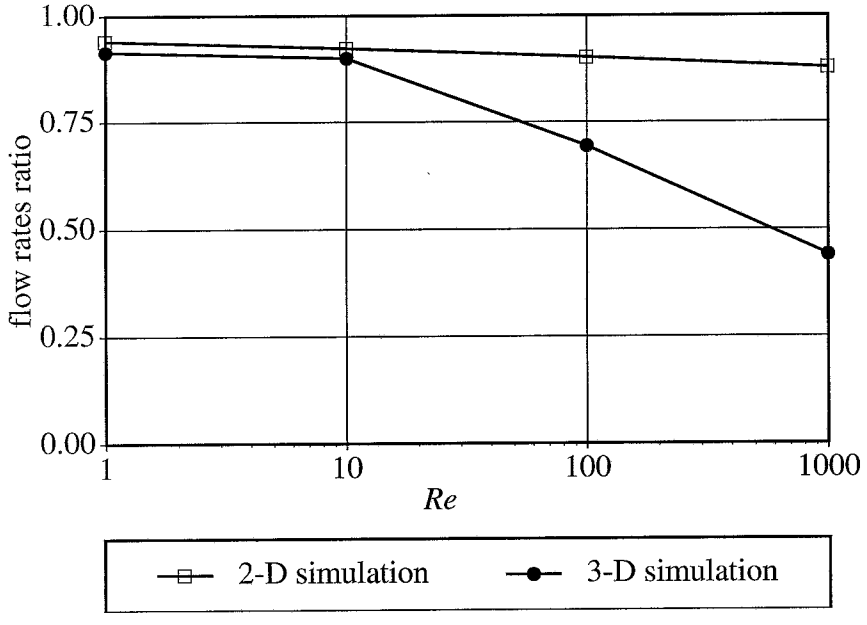

Figure 4.11 The baffled and unbaffled ST flow rates ratio.

The maps of the normalised total viscous stress generated by the impeller are shown in Figure 4.12 at the two vertical planes of the stirred tank. Steady-state models of the baffled and unbaffled tanks produce the results shown in Figure 4.12a,b,d,e, and those from the dynamic model are depicted in Figure 4.12c,f. The simulations from the models studied exhibit close resemblance qualitatively and quantitatively, indicating the highest values of the total viscous stress near the impeller and increased values around the baffles.

The horizontal planes throughout the computational domain are shown in Figure 4.13 at different axial co-ordinate values. The maps of the normalised total viscous stress are overlaid with the contour plots of the same quantity. Data of the ST with baffles are shown in Figure 4.13a-f and the data for the unbaffled tank in Figure 4.13g-l. The analysis of results for both stirred tanks showed that the region of intensive mixing is concentrated in the impeller vicinity while mixing in the bulk of the tanks is very poor.

From Figure 4.9 and Figure 4.12, it is evident that dynamic simulations confirm the results obtained by steady-state models.

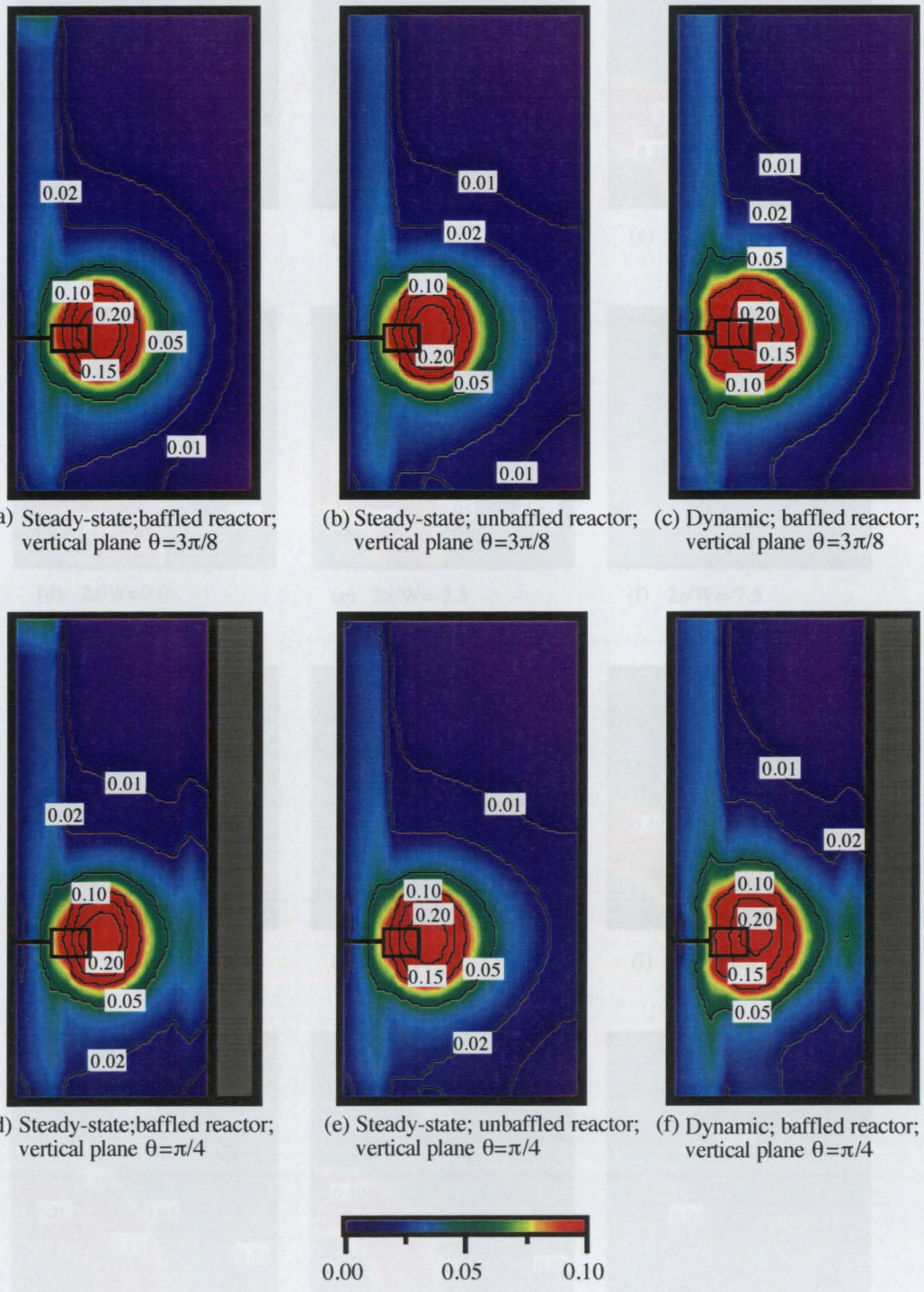

(a) Steady-state;baffled reactor; vertical plane $\theta=3\pi/8$

(b) Steady-state; unbaffled reactor; vertical plane $\theta=3\pi/8$

(c) Dynamic; baffled reactor; vertical plane $\theta=3\pi/8$

(d) Steady-state;baffled reactor; vertical plane $\theta=\pi/4$

(e) Steady-state; unbaffled reactor; vertical plane $\theta=\pi/4$

(f) Dynamic; baffled reactor; vertical plane $\theta=\pi/4$

Figure 4.12 *Normalised total viscous stress maps and contour plots at two vertical planes $\theta=3\pi/8$ (a, b, c) and $\theta=\pi/4$ (d, e , f) and for three models at Re=10.*

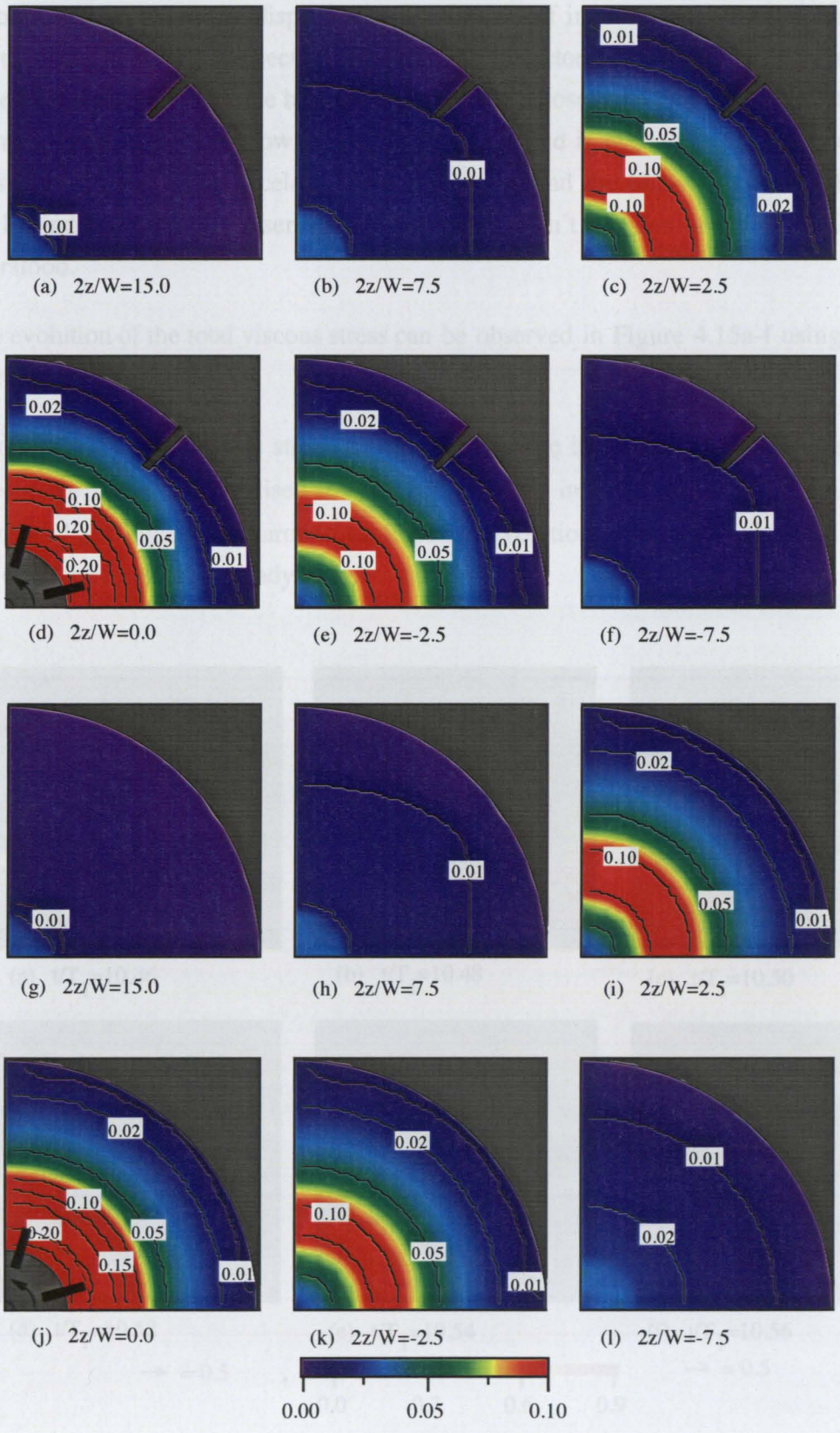

Figure 4.13 *Normalised total viscous stress maps and contour plots at different axial co-ordinate values for Re=10 in baffled (a-f) and unbaffled tank (g-l).*

Time evolution of the flow field at the impeller centre plane is illustrated in Figure 4.14. Various instants of time are displayed in Figure 4.14a-f in terms of the speed maps overlaid with the radial-tangential projections of the velocity vector. An interesting observation is that the velocity vectors behind the blades are greater than those in its front. This fact comes from the mechanism of the fluid flow around the blades. Fluid is pushed in front of the blade and flows over it resulting in acceleration in regions behind the blade. Therefore, the pressure drop behind the blades, as observed in experiments (Van't Riet and Smit, 1975, 1976) can be understood.

Time evolution of the total viscous stress can be observed in Figure 4.15a-f using the results at the impeller centre plane.

Regions of high total viscous stress are formed near the blades and are trailed behind as the blades move. Time is normalised for one period of the impeller revolution, T_I. As shown in Figure 4.14 and Figure 4.15, around ten impeller revolutions were necessary to drive the flow field of ST into a pseudo-steady state.

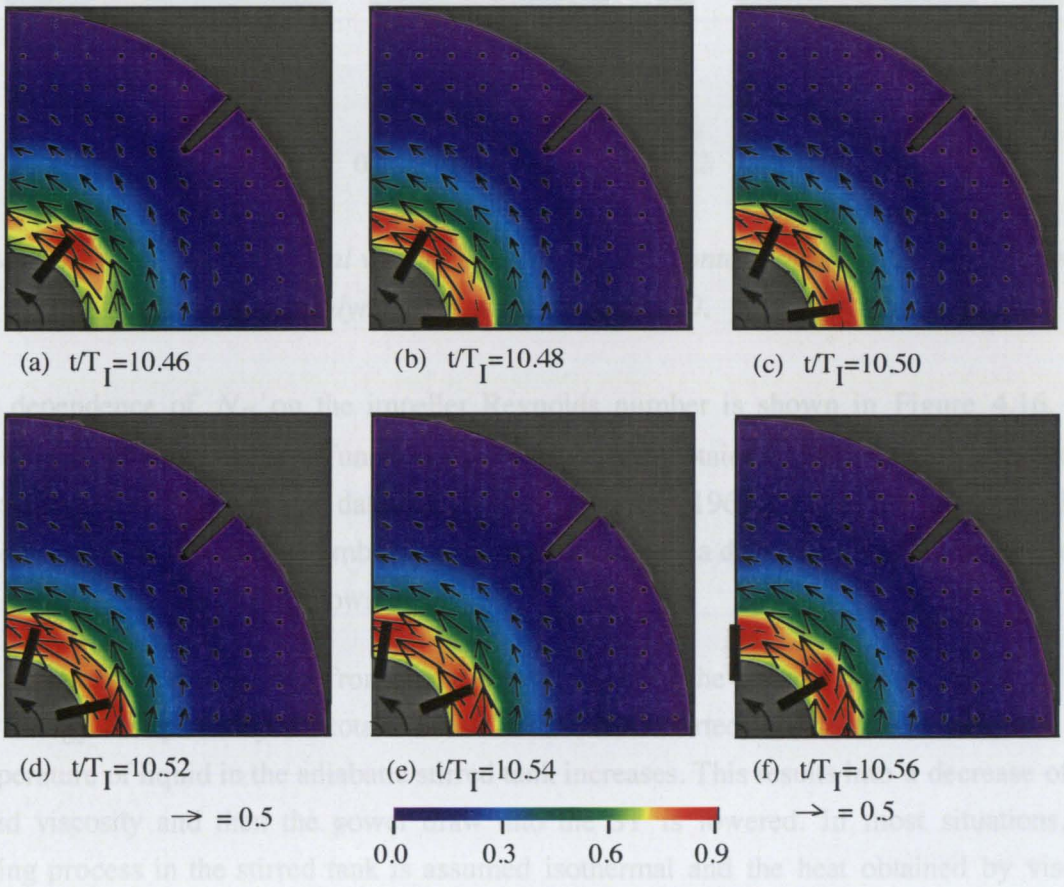

Figure 4.14 *Normalised speed maps overlaid with the radial-tangential projection of the velocity vector at the impeller centre plane from the dynamic simulation at Re=10.*

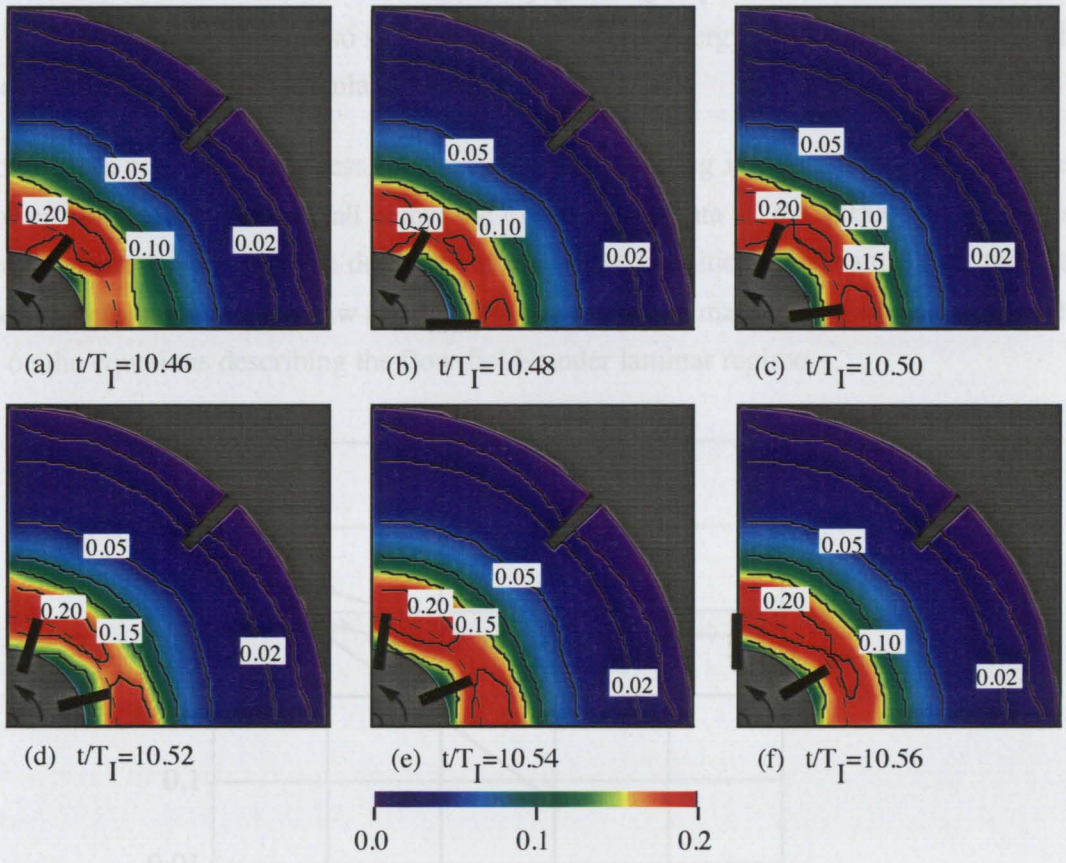

Figure 4.15 *Normalised total viscous stress maps and contour plots at the impeller centre plane from the dynamic simulation at Re=10.*

The dependence of N_P on the impeller Reynolds number is shown in Figure 4.16. The power number is an inverse function of Re, and data obtained from the 3D simulations overestimates the experimental data found by Bates *et al.* (1963). All three models predicted an equal value of the power number and the reason for such a deviation from the experimental data could be explained as follows.

The power draw is estimated from the volume integral of the viscous dissipation in the ST. The energy dissipated by the total viscous stress is converted into heat, and with time, the temperature of liquid in the adiabatic stirred tank increases. This results into a decrease of the liquid viscosity and then the power draw into the ST is lowered. In most situations, the mixing process in the stirred tank is assumed isothermal and the heat obtained by viscous dissipation is exchanged through the ST surfaces with the surrounding ambient. This kind of heat transfer was not accounted for in the present calculation of the viscous dissipation. Therefore, the results on the power number obtained from the 3D simulations over-predict the measured data. However, the correct decay of N_P with Reynolds number is predicted.

Moreover, a change in the slope of the power draw curve is observed at the $Re = 10$. This slope change of the power draw, at increased impeller rotational speeds, was obtained only in the results of 3D simulations. This is caused by growing importance of the radial and axial flows at $Re > 10$ that must be also supplied by the kinetic energy from the impeller, and this was not predicted by the 2D simulations.

In addition, the total viscous stress diminishes with increasing impeller rotational speed and the power number estimations fall below the experimental data at $Re > 1000$. This suggests that the viscous stress is not the dominant stress in the transition from laminar to turbulent regime. Therefore, the power draw for $Re > 1000$ must be estimated in a different way as that based on the equations describing the flow fields under laminar regime.

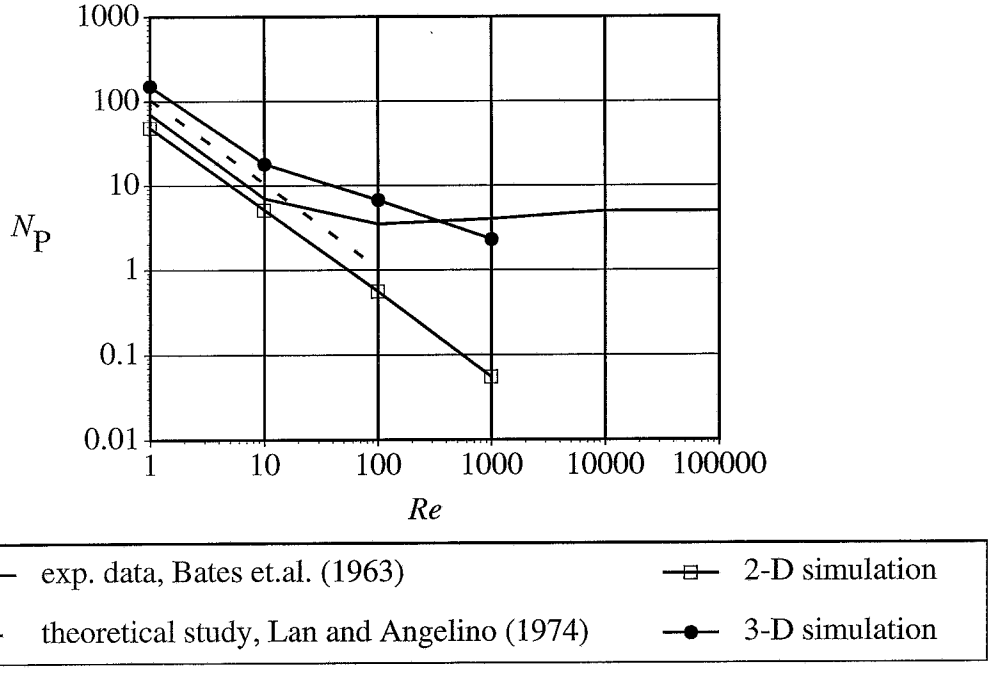

Figure 4.16 Calculated Power number compared with experimental data.

4.3.4 Conclusions

Three models were used to predict the hydrodynamics of stirred tanks. The steady-state results obtained using the moving ring approach were equivalent, for small Reynolds numbers, to those based on the blades set approach and with those from the dynamic model.

The predictions confirmed the results from the 2D simulations that the presence of baffles in the stirred tank decreases the tangential flow rate and the mixing efficiency and this gives origin to stagnant regions. Therefore, the mixing performance of the Rushton impeller in the ST, operating under laminar regime, can be improved using the multiple impellers or impellers of large diameters. This finding is in agreement with experimental studies reported in the literature (Nagata, 1955; Hoogendoorn and Den Hartog, 1967; Metzner *et al.*, 1961).

Comparisons of the calculated Power number with experimental data showed some deviations and the estimates from the 3D simulations were significantly higher than those from the 2D simulations. In addition, the 3D results showed that the models based on laminar flow equations are not suitable for the flow field and the power draw predictions of the ST agitated at $Re > 1000$.

4.4 Summary of Conclusions

Two and three-dimensional simulations of mixing process in stirred tanks with the Rushton impeller were performed using the commercial code FIDAP 7.6. The flow hydrodynamics in the baffled and unbaffled stirred tanks was investigated using the steady-state and dynamic models.

The 2D numerical simulations confirmed the axis-symmetric flow field in the stirred tanks. The results showed that the tangential flow rate of the baffled tank is smaller than that of the unbaffled tank and these results were confirmed also by the 3D simulations. The results of simulations showed that more regions that are stagnant occurred in the baffled tank than in the tank without baffles. The removal of baffles improves the tangential flow rate and mixing efficiency. In general, the ST with the Rushton impeller exhibits poor mixing under laminar regime and multiple impellers or the impellers of large diameters should be used to improve the uniformity of flow field in the ST.

The total viscous stress was found inversely proportional to the impeller rotational speed. The correct trend of dependence of the total viscous stress on the Reynolds number was predicted by numerical simulations.

Power numbers estimated from the results of 2D simulations were lower than experimental data of Bates *et al.* (1963) but the estimations from the 3D simulations over-predicted the experimental values. The discrepancies were attributed to the method used for the approximation of the power draw. Moreover, it was found that the models based on the laminar flow equations are not suitable for the flow field predictions in the ST at $Re > 1000$. Consequently, more sophisticated models should be used in the transition from laminar to turbulent regime and in fully developed turbulent regime.

5. Turbulent Mixing – 3D CFD Study

5.1 Introduction

Computational fluid dynamics — CFD — has become a tool that is more regularly and frequently used by researchers, designers, and engineers in the chemical industry. The growing importance of CFD is accompanied by demands to validate the results of numerical predictions against experimental data.

A major goal for CFD developers is to provide the user with more robust, flexible and applicable programs. The features implemented into CFD packages, such as various mesh-generating programs, methods to improve the convergence, relaxation, upwinding, and stability schemes are only a few examples that extend their capability. At the same time, models are also being improved to simulate processes that involve radiation, combustion, and turbulence, in single or multiphase flows.

A new feature for simulation of flows in rotating machinery, released only recently, allows now transient-dynamic simulations of rotating impellers in ST with baffles. This is an alternative to the standard pseudo steady-state approaches, where difficulties are felt to prescribe boundary conditions in the impeller region due to interactions between impeller and baffles.

Transient-dynamic simulation of the baffled ST can eliminate the problem of impeller-baffle interactions using one of two novel numerical schemes (Hamill *et al.*, 1994). The first, the *clicking-mesh* method, is easier to apply but has more restrictions than the second, the

sliding-mesh method, which is naturally more attractive but also computationally more expensive to use.

The clicking-mesh method assumes only one mesh in the computational domain. The impeller is considered a motionless object and the baffles are very thin surfaces that make part of the rotating ST walls. The computational domain for integration using the method of sliding-mesh is formed by two meshes. The first mesh is attached to the fixed objects and the second rotates-slides relative to the fixed mesh. It is convenient the same node locations are shared by both meshes at the sliding interface, so that no interpolation is necessary between neighbouring nodes. Disadvantages of the clicking-mesh method are related to the facts that the time step of computation must scale with the tangential size of the grid elements and that the computational domain must only be composed of regular and uniform elements.

Version 7.6 of FIDAP includes the *moving body constraint* capability, that is a particular sliding method that can used for the transient simulation of the baffled stirred tank. The user can define constraints for any nodal degree of freedom in such a way that the boundary conditions are applied and released during a numerical prediction as a function of time and position. In other words, at time step i, the blades of the impeller match with some grid elements and exactly at these locations are prescribed the constrained variables. At the next time step, $i+1$, other locations of computational domain coincide with the positions of the blades, and the same constrained variables are defined at different locations.

This chapter deals with the simulation and predictions of turbulent flow in the baffled ST impelled by the Rushton impeller, and the analysis of the impact of the particular imposed boundary conditions on these predictions is made. This chapter is divided on two main parts:

- *Steady-State Predictions,*
- *Dynamic Model Predictions.*

Steady-state simulations and predictions are discussed in Section 5.1. Various sets of boundary conditions for the *moving ring* steady-state model are analysed and the importance of proper boundary conditions is addressed. The major disadvantage of the moving ring approach is that the details of flow in the impeller region can not be revealed and the resort to experimental data is always necessary.

Numerical simulations presented in Section 5.3 use the *moving body constraint capability* allowing a better insight on the flow in the impeller region. Understanding of flow details in the impeller region is important for design studies of the impeller and for mixing optimisation. The drawback of a transient simulation remains in the increased computational and time expense.

Despite of a growing amount of numerical predictions published in the literature, it is still a challenging task to model the ST hydrodynamics. The problem is very complex and difficult

to resolve numerically, because of the three-dimensionality, time-dependency and turbulence character. The main difficulties are related with boundary conditions in the impeller region.

An analysis of all entities involved in the stirred tank with the Rushton impeller is provided here, together with the associated boundary conditions. The moving ring approach is analysed in detail in Section 5.2, with the objective of deriving the most suitable set of boundary conditions. Results of numerical predictions using various sets of boundary conditions are studied and compared to experimental data. The comparison of simulation results with experimental data for first order quantities, such as the velocity and pressure, is the most common in the literature. Additionally, a novel analysis of the Reynolds stresses is provided and compared to data measured by LDV and presented in Chapter 3. The advantages and limitations of the steady-state modelling of the ST are given at the end of this section.

The investigation of time dependent turbulent mixing is performed in Section 5.3 by means of the transient-dynamic simulation and comparison of the results from the steady-state data and the transient simulation is provided. A new approach for simulations of turbulent flows in the ST is derived and tested. The results are compared to experimental data and to data obtained from the steady-state models.

CFD predictions, presented in the next sections, reinforce the confidence into CFD as a valuable tool for ST reactor research, design, and development of new industrial applications.

5.2 Steady-State Predictions

The objectives of steady-state predictions are outlined in Section 5.2.1. The moving ring approach is described in Section 5.2.2 and the applied boundary conditions for all models used are introduced in Section 5.2.2. Section 5.2.4 presents the results of numerical predictions and compares them to those obtained experimentally. The main findings from steady-state predictions are summarised in Section 5.2.5.

5.2.1 Objectives of this work

The Rushton impeller in a baffled ST was under investigation for $Re = 5000$. According to Tatterson (1991), such flow belongs to the transition from laminar to turbulent regime, but Oldshue (1997) claimed that such a transition typically occurs in the range from $Re = 10$ to 1000, as observed in this experimental study. Chapter 4 showed clearly that the predictions based on the laminar flow equations are not suitable for these high impeller Reynolds numbers, and in this Chapter the stirred tank will be studied always operating under turbulent regime.

The stirred tank can be divided on four regions: impeller region, impeller discharge flow region, baffle region and bulk of the tank. The flow field is most violent near the impeller

region. The impeller discharge flow region is characteristic with a strong jet of radial flow that originates from the Rushton impeller and this flow is accomplished with high levels of the turbulence. The power draw introduced through the impeller is all dissipated by the viscous stress at the small-scale motions and converted into heat. Most of the power draw is dissipated in the regions of the impeller and the discharge flow. Theoretical predictions of the energy dissipation rate found in the literature differ from author to author, but in the recent study of Zhou and Kresta (1996) it is reported that around 40% of the total power input is dissipated in these two regions. The impeller region and the impeller discharge flow region occupy only a small but crucial portion of the stirred tank (around 10%). Therefore, a proper choice of boundary conditions in these regions is essential for a reasonable agreement between the numerical predictions and experimental data.

The analysis of all entities used in the moving ring approach, is provided and six steady-state models with different sets of boundary conditions are derived and validated. The boundary conditions implemented for physical or virtual boundaries lead to significant differences in the CFD predictions, as shown by the velocity and turbulent features of the ST hydrodynamics. The main objective of this study is to select the best model based on the proper set of boundary conditions by comparing the simulation predictions with the LDV data presented in Chapter 3. Additional comparisons are carried out against the results published in the literature and with the overall flow parameters — Flow number and Power number. The shear Reynolds stress predictability at the impeller centre is also discussed.

5.2.2 Computational model description and moving ring approach

The 3D computational domain of integration is formed by a single quarter ($\pi/2$ segment) of the ST with the baffle located in the plane that passes through $\pi/4$. A schematic representation of the geometry of the simulated problem and of the ST computational domain can be seen in Figure 5.1.

The moving ring, as shown in Figure 5.2, is the tank region swept by the blades of the impeller. The steady-state predictions were performed using the moving ring approach in order to avoid the impeller-baffle interactions and time-dependency of the predicted flow fields.

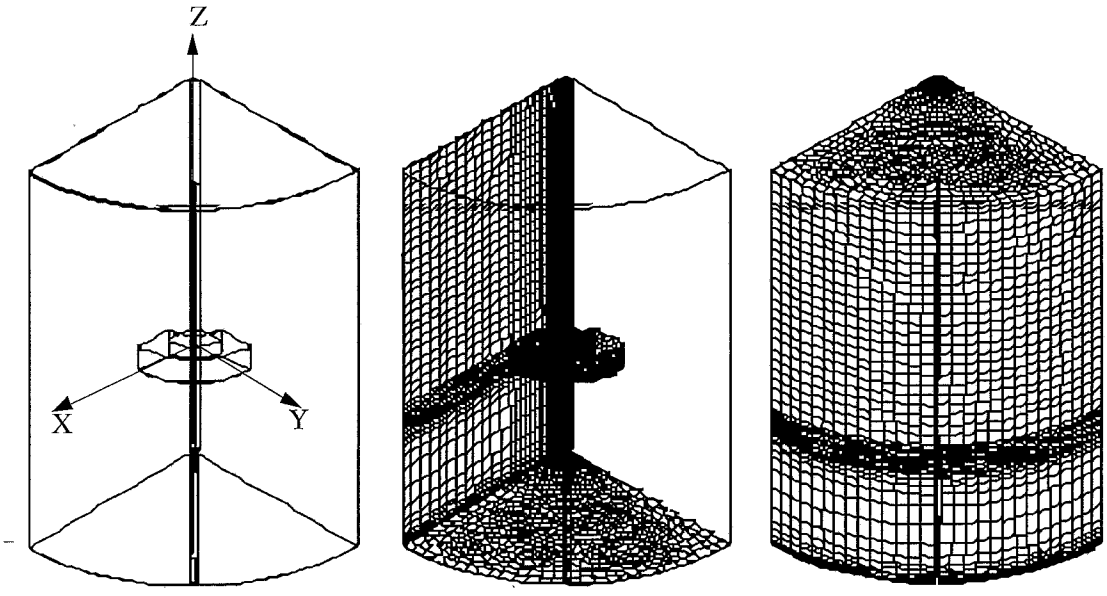

Figure 5.1 *Schematic representation of the ST geometry and of the mesh of computational domain.*

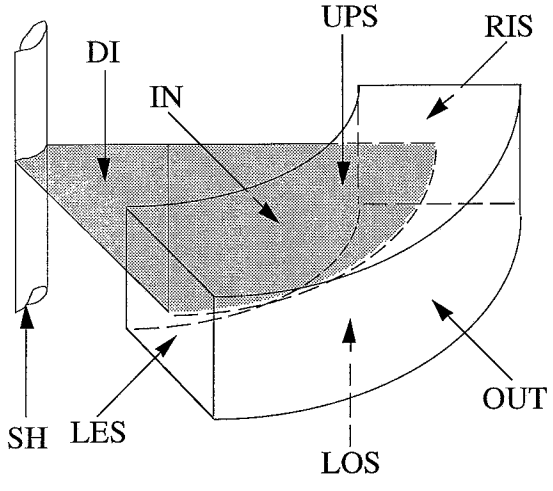

Figure 5.2 *Moving ring approach and entities specified in the steady-state simulations: SH-shaft, DI-impeller disk, IN-inflow surface, UPS and LOS-upper and lower surfaces, LES and RIS-left and right surfaces, and OUT-outflow surface.*

The moving ring region is replaced by a virtual fluid body that can be delimited by the surface entities. Consequently, the moving ring represents the only source of momentum transferred from the real blades into the ST. For this approach, the boundary conditions must be specified on the following entities:

- *inflow surface of impeller region;*
- *upper and lower surface of impeller region;*
- *left and right surface of impeller region;*
- *outflow surface of impeller region.*

Descriptions of these moving ring entities follow.

- ***The inflow surface of impeller region, IN***

This entity is drawn by the inner vertical-edge of the rotating blade where the flow enters the impeller region. Generally, it is very difficult to prescribe boundary conditions at the inflow surface, due to the lack of experimental data. There is a possibility to derive some relevant boundary conditions from the analysis of impeller region as a control volume. This can be performed by the application of some theoretical assumptions, such as that of the two-dimensional flow within the impeller region, but their introduction is questionable due to the flow complexity in this region. Since the knowledge of the flow at this entity is insufficient, its boundary conditions are often let free, and the flow field in this entity is computed by the CFD simulator assuming non-zero velocities and zero total viscous stresses at the surface. This was the methodology used in the present simulations.

- ***The upper and lower surfaces of impeller region, UPS and LOS***

Only few experimental data can be found on this surface entity in the literature, but some experimental values are available on the vicinity of the top and bottom edges of the impeller blades. This data can be approximated as the boundary conditions for this entity. An alternative is to specify a reasonable flow field at these surfaces. For instance, in one of the proposed models introduced later in this chapter, it is assumed that the axial flow does not enter the impeller region through these surfaces. However, the LDV study of the impeller region (see Chapter 3) found that this assumption does not reflect the real ST hydrodynamics, and thus, it is preferable not to specify explicitly the boundary conditions of the velocity at the UPS and LOS. Taking this option, the non-zero velocities and zero total viscous stresses conditions are implicitly defined at the surfaces. This is acceptable as was discussed in Chapter 3.

- ***The left and right surfaces of impeller region, LES and RIS***

These entities arise only when a part of the entire ST volume is taken to be a computational domain and must have employed the periodic boundary conditions. Since the approach of the moving ring is an analogy of the time-averaged LDV experiments, obtained experimental data are very useful to define the boundary conditions at the LES and RIS (as in model 5 introduced later). Another alternative is the assumption of zero flows through the UPS and LOS surfaces. In this case, the tangential velocity at the LES, RIS is a known function of the radius while the radial velocity is calculated from an assumption of a 2D flow in the impeller region.

- ***The outflow surface of impeller region, OUT***

This is the only surface entity of the moving ring approach, where the boundary conditions can be prescribed without too many difficulties. This is due to sufficient experimental data at

the OUT entity in the literature. The component of the axial velocity is negligible at the OUT entity due to assumption of the pure radial jet and the rotational flows. The radial and tangential velocities vary along the vertical edge of the blade in the form of a parabolic profile. Generally, the velocity components at the corners of the blades are at approximately 10% of the velocity vector magnitude at the impeller centre plane.

The ratio between the magnitude of the radial and of the tangential velocity components also varies with the axial co-ordinate. This variation is expressed as the *angularity parameter*, χ which can be defined as:

$$\chi = \tan^{-1}\left(\frac{V_\theta}{V_r}\right) \tag{5.1}$$

and from the LVD study for the standard ST it depends on the axial position along the blade tip as shown in Figure 5.3. The radial velocity component, V_r, decreases with distance from the zero axial co-ordinate and consequently, the radial jet of the impeller discharge flow is less intense near the blade corners. The velocity boundary conditions to specify the OUT entity can be obtained by combination of the angularity parameter, χ, and the velocity at the tip of an impeller. For example, the angularity parameter will be approximated for model 1 by the function as plotted in Figure 5.3.

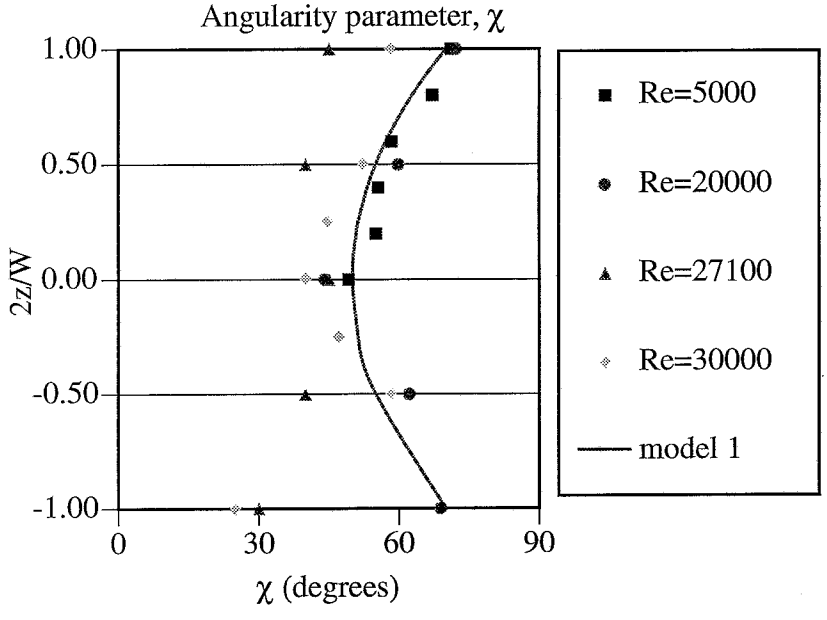

Figure 5.3 *The measured angularity parameter distribution from data obtained by Wu and Patterson (1989) at Re=30000; Mavros et al. (1996) at Re=27000; and from the present LDV study for Re=5000 and Re=2000.*

The moving ring entities were discussed in previous paragraphs. In order to perform the ST simulations, the specification of boundary conditions is necessary not just at the moving ring

entities but also at the all fixed and rotating entities of the ST tank. Additional entities used in the present geometrical model are divided on:

- *impeller disk;*
- *impeller shaft;*
- *stirred tank bottom;*
- *stirred tank wall;*
- *liquid surface;*
- *reference and periodic surfaces.*

Descriptions of these entities and the boundary conditions specified follow.

- ***The impeller disk, DI***

The impeller disk supports the blades that are equidistantly distributed around it and this entity is replaced by the rotationally moving fluid. The component of the tangential velocity was defined on the impeller disk as a linear function of the radii and the velocity magnitude depended on the rotational velocity of the impeller. The radial and axial velocities were defined as zero. This entity plays an important role for the flow that enters the volume swept by the blades of the impeller. It should not be omitted in any model, since it determines the flow separation between the top and bottom flow regions in the ST.

- ***The impeller shaft, SH***

The impeller shaft entity specifies the surface of the rotating shaft where the impeller is mounted. The impeller shaft enters the tank from the top and coincides with the axial axis of co-ordinate system. In previous works found in the literature, the shaft modelling was omitted, but Bakker *et al.* (1994) demonstrated the importance of its modelling for correct numerical predictions. The shaft modelling is mostly important for consistent predictions of the tangential velocity in the top portions of the ST, where additional stresses are produced and not negligible.

The SH entity was modelled specifying the tangential velocity while the radial and axial velocity components were zero. Problems were encountered in the case where the shaft is connected to the bottom of stirred tank. In this case, numerical discontinuity was introduced into the specification of boundary conditions at the edges of impeller shaft and tank bottom. A possible alternative is to model the tip of the shaft in the shape of a cone, as shown in Figure 5.4a. FIDAP 7.6 package does not allow the exact cone modelling and an approximation to a similar shape is seen as an unnecessary complication of the model geometry. For this reason, in the present models the shaft ends at a small distance from the flat tank bottom. It was assumed that the existence of a small gap (see Figure 5.4b) has negligible affect on the flow field near the tank bottom. Such reasoning is supported by the fact that all velocity components are very small in this region.

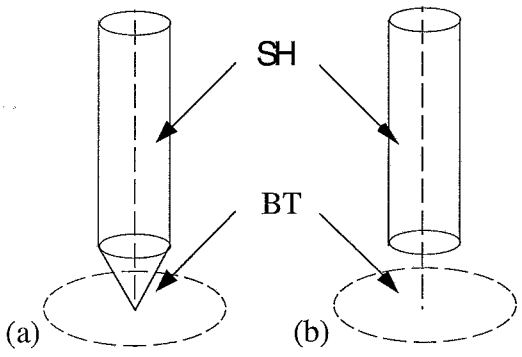

Figure 5.4 *A schematic representation on how to avoid inconsistency of the boundary conditions at the tank bottom, BT: (a) an ideal solution and (b) a small gap creation.*

- ***The stirred tank bottom, BT***

All velocity components are set to zero at the flat bottom of the stirred tank. Problems were detected for the simulation where the shaft and bottom entities shared a common surface. As previously described, this gives origin to an infinite stress difference, resulting into the strong flow perturbations observed near the solid surface. The problem can be solved as mentioned in the paragraph on the SH entity.

- ***The stirred tank wall, WA***

The non-slip boundary conditions are defined at the wall of a tank including the baffle.

- ***The liquid surface, TO***

A central air vortex is formed at the liquid surface, mainly at the high rotational speeds of the impeller. This is accompanied by air suction into the bulk of the tank and therefore, the boundary conditions must be carefully defined here. It is preferable to model the liquid surface as a flat free surface, where the axial velocity is zero.

- ***The reference and periodic surfaces, REF and PER***

Assuming the flow field symmetry in the ST, the periodic boundary conditions must be specified at the vertical planes of the computational domain. Thus, all the variables solved at the REF surface ($\theta = 0$) are identical to those at the PER surface ($\theta = \pi / 2$).

The geometry and the entities of the ST computational model were described in the previous paragraphs. The simulations of turbulent mixing in the ST are accomplished using the boundary conditions specified at these entities and using the equations that are presented next.

The flow in these simulations is considered incompressible and isothermal and the liquid as Newtonian. Numerical simulations are accomplished by the solution of the equations of conservation of mass and momentum. The equations for turbulent flow are similar to those presented in the previous chapter but now they do not form a closed system. All the flow variables, such as the velocity or pressure, are time averaged and decomposed into the mean (represented with the over-bar) and periodic-fluctuating (represented with the prime) components. This decomposition applied to the conservation equations, generate additional variables and equations that must be derived in order to close the system of equations.

The equation of mass conservation for liquids of constant density, ρ, is given by

$$\frac{\partial \overline{U}_i}{\partial x_i} = 0 \tag{5.2}$$

where $\overline{U}_i$ is the mean component of the velocity vector in the x_i direction. The conservation of momentum can be written for turbulent flow as

$$\frac{\partial\left(\rho\overline{U}_i\right)}{\partial t} + \overline{U}_j \frac{\partial\left(\rho\overline{U}_i\right)}{\partial x_j} = \frac{\partial}{\partial x_j}\overline{\sigma}_{ij} + \rho g_i \tag{5.3}$$

Here, $\overline{\sigma}_{ij}$ is the *total mean stress tensor* and g_i is the component of the gravitational acceleration. The terms on the left hand-side of Equation 5.3 represent the net mean accumulation rate of momentum within the control volume and the net mean transport of momentum across the faces of the control volume. The terms on the right hand-side represent the forces per unit volume acting on the faces of the fluid element, and the mean body force per volume acting within the fluid element.

The total mean stress $\overline{\sigma}_{ij}$ in turbulent flow is composed by:

$$\overline{\sigma}_{ij} = -\overline{p}\,\delta_{ij} + \overline{\tau}_{ij} + \overline{\tau}^t_{ij} \tag{5.4}$$

where $\overline{p}$ is the mean hydrodynamic pressure, δ_{ij} is the Kronecker delta, $\overline{\tau}_{ij}$ is the mean viscous stress tensor and $\overline{\tau}^t_{ij} = -\rho\overline{u_i v_j}$ is the *Reynolds stress tensor*. By comparing Equation 5.4 with the definition of total stress tensor in laminar flow, the additional *Reynolds stress tensor* term appears due to turbulence.

Introducing Equation 5.4 into Equation 5.3 results in:

$$\frac{\partial\left(\rho\overline{U}_i\right)}{\partial t} + \overline{U}_j \frac{\partial\left(\rho\overline{U}_i\right)}{\partial x_j} = -\frac{\partial \overline{p}}{\partial x_i} + \mu\frac{\partial^2 \overline{U}_i}{\partial x_j^2} - \frac{\partial}{\partial x_j}\rho\left(\overline{u_i u_j}\right) + \rho g_i \tag{5.5}$$

The Reynolds stress tensor seems to be similar to that of the viscous stress, and in some turbulent flow situations, it is related with the mean shear rate tensor, $\bar{\varepsilon}_{ij}$, using the parameter *turbulent viscosity*, μ_t, as:

$$-\rho\overline{(u_i u_j)} = 2\mu_t \bar{\varepsilon}_{ij} \tag{5.6}$$

However, in the case of turbulent flow, the turbulent viscosity is a property of the flow field, not of the liquid as the dynamic molecular viscosity, μ, in the case of laminar flow. Applying dimensional analysis and analogy between eddies and molecular viscosities, the turbulent viscosity can be determined as:

$$\mu_t = \rho c_\mu k^{3/2}/\varepsilon \tag{5.7}$$

where c_μ is the flow field constant, k is the local *average turbulent kinetic energy* and ε is the local *rate of the turbulent kinetic energy dissipation.*

The two additional transport equations, one for the kinetic energy and one for the rate of energy dissipation, must be derived and solved in order to compute the Reynolds stress tensor. Unfortunately, these equations can be closed only by using some semi-empirical constants.

The transport equations for the turbulent kinetic energy, k, and the rate of the turbulent kinetic energy dissipation, ε, are incorporated into the standard $k-\varepsilon$ turbulence model. This standard model is valid only for isotropic turbulence, the case where the velocity fluctuations are equal in all directions.

Various works in the literature and the LDV measurements in Chapter 3 showed that the assumption of isotropic turbulence is not acceptable for the most important regions of the stirred tank. The incapability of the standard model to predict *anisotropic turbulence* is due to the linear relation of the Reynolds stress and the shear rate (see Appendix C). Some alternative forms to this linear relation were reported in the literature. Quadratic or higher order dependence between the Reynolds stresses and the shear rate tensor can provide a mechanism necessary for prediction of anisotropic turbulence, but it introduces some additional constants. Speziale (1987) proposed a quadratic function between the Reynolds stresses and the mean rates of the shear and its non-linear model contains only one additional constant to the standard $k-\varepsilon$.

The non-linear Speziale's model (1987) was used in the present simulations and the Reynolds stress is defined by:

$$-\rho\overline{u_i u_j} = -\frac{2}{3}\rho k\delta_{ij} + 2\mu_t\varepsilon_{ij} + 4c_{sp}c_\mu\frac{k}{\varepsilon}\mu_t(\varepsilon_{ik}\varepsilon_{kj} + \varepsilon_{ij} - \frac{1}{3}(\varepsilon_{mn}\varepsilon_{mn} + \varepsilon_{mm})\delta_{ij})$$
$$\dot{\varepsilon}_{ij} = -\frac{\partial u_i}{\partial x_k}\varepsilon_{kj} - \frac{\partial u_j}{\partial x_k}\varepsilon_{ki} \tag{5.8}$$

where the $\varepsilon_{ij}, \varepsilon_{ik}, \varepsilon_{kj}, \varepsilon_{mn}, \varepsilon_{mm}$ are components of the shear rate tensor; the $\dot{\varepsilon}_{ij}$ is the truncated Oldroyd derivative of the ε_{ij}; the c_{sp} is Speziale's constant and the c_μ is constant from the standard $k-\varepsilon$ model.

The constants for the standard $k-\varepsilon$ model arise in the transport equations of the turbulent kinetic energy and the rate of energy dissipation (see Appendix C). These constants were derived and optimised upon many cases of turbulent flows (Launder and Spalding, 1974) and it is not an objective of this study to modify them just in order to fit the ST hydrodynamics. The values of the constants c_μ, c_1, c_2, c_3 and $\sigma_k, \sigma_\varepsilon$ used in the standard $k-\varepsilon$ model and the value of additional constant c_{sp} from the Speziale's turbulence model are listed on Table 5.1.

Table 5.1 Constants used in the Speziale's turbulence model.

c_μ	c_1	c_2	c_3	σ_k	σ_ε	c_{sp}
0.09	1.44	1.92	0.80	1.00	1.30	1.68

A more detailed discussion on the closure problem for turbulent flow and Speziale's model is given in Appendix C.

After this introduction of the computational model, boundary conditions and equations used to model the turbulent mixing, some details on the ST simulations follow.

The non-linear, turbulent and steady-state problem was solved in the 3D space. The equations describing the flow throughout the flow domain are discretized with finite elements using eight node bricks, with tri-linear velocity and discontinuous constant pressure approximations. The system of ordinary differential equations is solved on each element of the computational domain using the segregated solver for each independent variable.

The CR method (Conjugate Residual method, FIDAP 7.6) provided the solution for the symmetric linear equation system and the GMRES method (Generalised Minimal Residual method, FIDAP 7.6) was used for the non-symmetric system of equations. All simulations were performed on the 3D computational domain using 45684 nodal points and 50445 elements generated automatically using the FI-GEN mesh generator (FIDAP 7.6). The simulations required 42MB of the core memory for each independent variable and the computational time was of the order of 7 hours in an IBM RS6000 machine, model 3CT.

The convergence criterion was set to DTOL = 0.001 for all degrees of freedom (the three velocity-components, pressure, kinetic energy and energy dissipation) in all simulations.

5.2.3 Boundary conditions models for the moving ring

The hydrodynamics of the ST (Figures 3.1 and 3.2), was predicted for $Re = 5000$ corresponding to a frequency of the rotational shaft, $N = 0.55\text{Hz}$. All dimensions, operating parameters, and fluid properties agree with those for LDV experiments reported in Chapter 3.

The following text provides the boundary conditions for the present models and is subdivided on two parts:

- *specification of velocity components;*
- *specification of turbulence parameters.*

Six models of different boundary conditions were tested by *specifying the velocity components* with the goal to demonstrate the importance of the imposed boundary conditions on the ST predictions.

- ***Specification of velocity components***

In the first part of this text is given a summary of boundary conditions for the impeller entities of all models used.

- **model 1** specifies the profiles of the radial and tangential velocity components at the OUT entity, as measured by LDV. These profiles are of a parabolic shape and the velocity components are functions of the axial co-ordinate, as defined by the values of the *angularity parameter*, χ, found from LDV experiments and shown in Figure 5.3.

- **model 2** specifies a constant value for V_r and V_θ at the OUT entity. Both velocity components are equal to the tip velocity of the impeller and the axial velocity is assumed negligible.

- **model 3** assumes that the flow from the bulk of a stirred tank does not enter the impeller region through the entities UPS, LOS and considers the axial velocity as negligible. The velocity components, V_r and V_θ, are constant and equal to the tip velocity of the impeller at the OUT entity, and are functions of the radius, r, at the UPS, LOS entities.

- **model 4** is similar to the model of Bakker (1994), where the profiles of the radial and tangential components are specified in the shape of a parabolic function at the OUT entity. The velocity profiles in this model are considered as functions only of the axial co-ordinate and the dependence on the angularity parameter, as in model 1, is not applied. Both V_r and V_θ are equal to the tip velocity of the impeller at the value of $z = 0$ at the OUT entity.

- **model 5** was created based on LDV data, as measured in Chapter 3. The velocity components, V_r and V_θ, values are approximated by polynomial functions of the axial position for different radii inside the impeller region.

- **model 6** was derived with the purpose to define the boundary conditions within the impeller region independently of the experimental data. The velocity components V_r and V_θ, are equal at the same radii within the moving ring and specified as parabolic functions of the axial and radial co-ordinates. The parabolic function assumed that the tangential velocity vector at the OUT blade corners is 10% of the tangential velocity vector at the centre of the blade tip. The magnitudes of the tangential velocity component at the impeller centre line increased linearly with the radius.

The basic differences between models 1 through 6 are illustrated in Figure 5.5. Here, in *grey* are shown the regions where velocity boundary conditions are explicitly specified and in *white* the regions where the implicit boundary conditions are used (non-zero velocities and zero stresses).

The detailed list of the boundary conditions for each model is found in Tables 5.2 through 5.7.

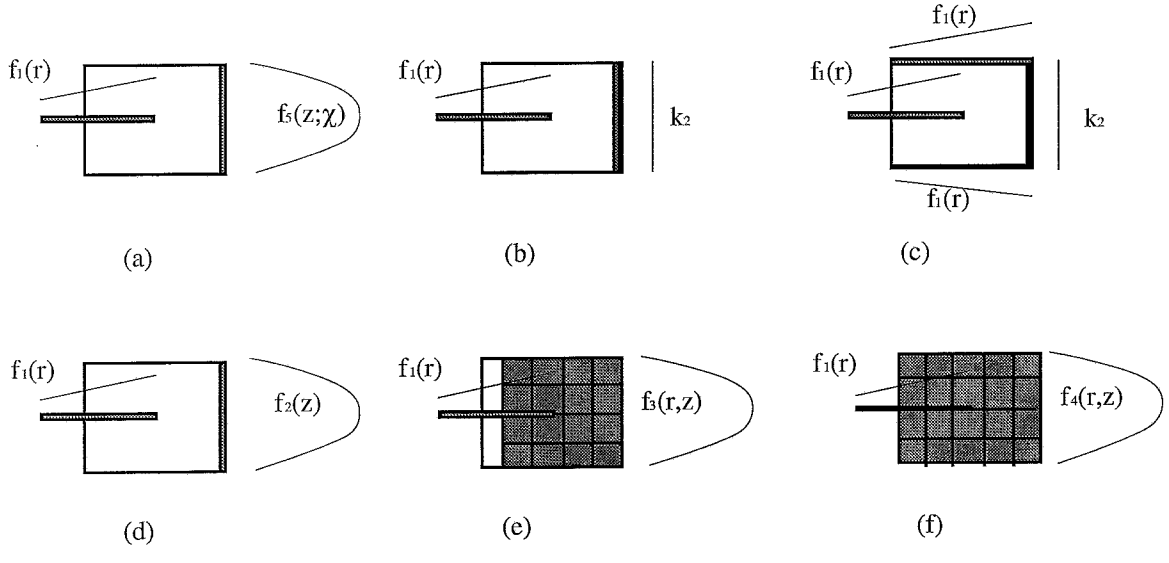

Figure 5.5 *2D illustration of the velocity boundary conditions specified for: (a) model 1; (b) model 2; (c) model 3; (d) model 4; (e) model 5 and (f) model 6.*

In Figure 5.5 the boundary conditions are shown on the blade edges of radial cuts of the moving ring, and extending these into the angular direction will form the surface entities of the moving ring, as shown in Figure 5.2. The shape of the velocity profile is depicted by a thin curve in the normal direction to the associated entity. For example, in Figure 5.5a, the velocity profile along the impeller disk is defined as a function that increases linearly with the radius while the parabolic profile of velocity is specified at the OUT entity.

The stress conditions are introduced into the models implicitly when the velocities are defined, and the values corresponding to models 1 through 6 can be found in Tables 5.2 through 5.7. The equations necessary to derive the boundary conditions in terms of the stresses are associated with each surface and are given (valid only for incompressible flows) in the cylindrical co-ordinate system as:

$$\begin{aligned} \tau_{rr} &= -p + 2\mu\frac{\partial V_r}{\partial r} & \tau_{r\theta} &= \mu\left[r\frac{\partial}{\partial r}\left(\frac{V_r}{r}\right) + \frac{1}{r}\frac{\partial V_r}{\partial \theta}\right] \\ \tau_{\theta\theta} &= -p + 2\mu\left(\frac{1}{r}\frac{\partial V_\theta}{\partial \theta} + \frac{V_r}{r}\right) & \tau_{\theta z} &= \mu\left[\frac{\partial V_\theta}{\partial z} + \frac{1}{r}\frac{\partial V_z}{\partial \theta}\right] \\ \tau_{zz} &= -p + 2\mu\frac{\partial V_z}{\partial r} & \tau_{rz} &= \mu\left[\frac{\partial V_r}{\partial z} + \frac{\partial V_z}{\partial r}\right] \end{aligned} \tag{5.9}$$

where the p is pressure, μ is the dynamic molecular viscosity and the stresses are indexed as introduced in Chapter 3 and Appendix C.

The velocity boundary conditions on Tables 5.2 through 5.7 are specified using the following symbols: the impeller radius, R; and the angular velocity, $\omega = 2\pi N$, where N is the frequency of the impeller rotation. Moreover, the constants and functions are specified as:

$$\begin{aligned} k_1 &= \omega r_{shaft} & f_3(r,z) &\cong (LDVdata) \\ k_2 &= \omega R & f_4(r,z) &= \omega r(1 - 0.009z^2) \\ f_1(r) &= \omega r & f_5(z,\chi) &= \omega R(1 - 0.009z^2) \\ f_2(z) &= \omega R(1 - 0.009z^2) & \chi(V_r / V_\theta) &= 44.5° + 1605z \end{aligned}$$

Table 5.2 Model 1 boundary conditions.

entity	V_r	V_θ	V_z	*shear stress*	*normal stress*
SH	*0*	k_1	*0*	$\tau_{rz} = 0$	$\tau_{rr} = 0$
DI	*0*	$f_1(r)$	*0*	$\tau_{zr} = 0$	$\tau_{zz} = 0$
IN	*free*	*free*	*free*	$\tau_{zr} = \tau_{r\theta} = 0$	$\tau_{rr} = 0$
UPS, LOS	*free*	*free*	*free*	$\tau_{zr} = \tau_{z\theta} = 0$	$\tau_{zz} = 0$
LES, RIS	*free*	*free*	*free*	$\tau_{\theta r} = \tau_{\theta z} = 0$	$\tau_{\theta\theta} = 0$
OUT	$f_5(z)$	$f_5(z)$	*0*	$\tau_{iy} \neq 0$	$\tau_{rr} \neq 0$
BT	*0*	*0*	*0*	$\tau_{zr} = \tau_{z\theta} = 0$	$\tau_{zz} = 0$
WA	*0*	*0*	*0*	$\tau_{zr} = \tau_{r\theta} = 0$	$\tau_{rr} = 0$
TO	*free*	*free*	*0*	$\tau_{zr} = \tau_{z\theta} = 0$	$\tau_{zz} = 0$

Table 5.3 Model 2 boundary conditions.

entity	V_r	V_θ	V_z	*shear stress*	*normal stress*
SH	*0*	k_1	*0*	$\tau_{rz} = 0$	$\tau_{rr} = 0$
DI	*0*	$f_1(r)$	*0*	$\tau_{zr} = 0$	$\tau_{zz} = 0$
IN	*free*	*free*	*free*	$\tau_{zr} = \tau_{r\theta} = 0$	$\tau_{rr} = 0$
UPS, LOS	*free*	*free*	*free*	$\tau_{zr} = \tau_{z\theta} = 0$	$\tau_{zz} = 0$
LES, RIS	*free*	*free*	*free*	$\tau_{\theta r} = \tau_{\theta z} = 0$	$\tau_{\theta\theta} = 0$
OUT	k_2	k_2	*0*	$\tau_{rz} = 0$	$\tau_{rr} \neq 0$
BT	*0*	*0*	*0*	$\tau_{zr} = \tau_{z\theta} = 0$	$\tau_{zz} = 0$
WA	*0*	*0*	*0*	$\tau_{zr} = \tau_{r\theta} = 0$	$\tau_{rr} = 0$
TO	*free*	*free*	*0*	$\tau_{zr} = \tau_{z\theta} = 0$	$\tau_{zz} = 0$

Table 5.4 Model 3 boundary conditions.

entity	V_r	V_θ	V_z	*shear stress*	*normal stress*
SH	*0*	k_1	*0*	$\tau_{rz} = 0$	$\tau_{rr} = 0$
DI	*0*	$f_1(r)$	*0*	$\tau_{zr} = 0$	$\tau_{zz} = 0$
IN	*free*	*free*	*free*	$\tau_{zr} = \tau_{r\theta} = 0$	$\tau_{rr} = 0$
UPS, LOS	$f_1(r)$	$f_1(r)$	*0*	$\tau_{iy} \neq 0$	$\tau_{zz} = 0$
LES, RIS	*free*	*free*	*free*	$\tau_{\theta r} = \tau_{\theta z} = 0$	$\tau_{\theta\theta} = 0$
OUT	k_2	k_2	*0*	$\tau_{rz} = 0$	$\tau_{rr} \neq 0$
BT	*0*	*0*	*0*	$\tau_{zr} = \tau_{z\theta} = 0$	$\tau_{zz} = 0$
WA	*0*	*0*	*0*	$\tau_{zr} = \tau_{r\theta} = 0$	$\tau_{rr} = 0$
TO	*free*	*free*	*0*	$\tau_{zr} = \tau_{z\theta} = 0$	$\tau_{zz} = 0$

Table 5.5 Model 4 boundary condition.

entity	V_r	V_θ	V_z	*shear stress*	*normal stress*
SH	*0*	k_1	*0*	$\tau_{rz} = 0$	$\tau_{rr} = 0$
DI	*0*	$f_1(r)$	*0*	$\tau_{zr} = 0$	$\tau_{zz} = 0$
IN	*free*	*free*	*free*	$\tau_{zr} = \tau_{r\theta} = 0$	$\tau_{rr} = 0$
UPS, LOS	*free*	*free*	*free*	$\tau_{zr} = \tau_{z\theta} = 0$	$\tau_{zz} = 0$
LES, RIS	*free*	*free*	*free*	$\tau_{\theta r} = \tau_{\theta z} = 0$	$\tau_{\theta\theta} = 0$
OUT	$f_2(z)$	$f_2(z)$	*0*	$\tau_{iy} \neq 0$	$\tau_{rr} \neq 0$
BT	*0*	*0*	*0*	$\tau_{zr} = \tau_{z\theta} = 0$	$\tau_{zz} = 0$
WA	*0*	*0*	*0*	$\tau_{zr} = \tau_{r\theta} = 0$	$\tau_{rr} = 0$
TO	*free*	*free*	*0*	$\tau_{zr} = \tau_{z\theta} = 0$	$\tau_{zz} = 0$

Table 5.6 Model 5 boundary conditions.

entity	V_r	V_θ	V_z	*shear stress*	*normal stress*
SH	*0*	k_1	*0*	$\tau_{rz} = 0$	$\tau_{rr} = 0$
DI*	*0*	$f_1(r)$	*0*	$\tau_{zr} = 0$	$\tau_{zz} = 0$
IN	*free*	*free*	*free*	$\tau_{rz} = \tau_{r\theta} = 0$	$\tau_{rr} = 0$
UPS, LOS	$f_3(r, z)$	$f_3(r, z)$	*free*	$\tau_{iy} \neq 0$	$\tau_{zz} = 0$
LES, RIS	$f_3(r, z)$	$f_3(r, z)$	*free*	$\tau_{iy} \neq 0$	$\tau_{\theta\theta} \neq 0$
OUT	$f_3(r, z)$	$f_3(r, z)$	*free*	$\tau_{iy} \neq 0$	$\tau_{rr} \neq 0$
BT	*0*	*0*	*0*	$\tau_{zr} = \tau_{z\theta} = 0$	$\tau_{zz} = 0$
WA	*0*	*0*	*0*	$\tau_{zr} = \tau_{r\theta} = 0$	$\tau_{rr} = 0$
TO	*free*	*free*	*0*	$\tau_{zr} = \tau_{z\theta} = 0$	$\tau_{zz} = 0$

* the DI entity is only specified in the region that does not belong to the volume swept by the blades

Table 5.7 Model 6 boundary conditions.

entity	V_r	V_θ	V_z	*shear stress*	*normal stress*
SH	*0*	k_1	*0*	$\tau_{rz} = 0$	$\tau_{rr} = 0$
DI	*0*	$f_1(r)$	*0*	$\tau_{zr} = 0$	$\tau_{zz} = 0$
IN	$f_4(r,z)$	$f_4(r,z)$	*free*	$\tau_{iy} \neq 0$	$\tau_{rr} \neq 0$
UPS, LOS	$f_4(r,z)$	$f_4(r,z)$	*free*	$\tau_{iy} \neq 0$	$\tau_{zz} = 0$
LES, RIS	$f_4(r,z)$	$f_4(r,z)$	*free*	$\tau_{iy} \neq 0$	$\tau_{\theta\theta} \neq 0$
OUT	$f_4(r,z)$	$f_4(r,z)$	*free*	$\tau_{iy} \neq 0$	$\tau_{rr} \neq 0$
BT	*0*	*0*	*0*	$\tau_{zr} = \tau_{z\theta} = 0$	$\tau_{zz} = 0$
WA	*0*	*0*	*0*	$\tau_{zr} = \tau_{r\theta} = 0$	$\tau_{rr} = 0$
TO	*free*	*free*	*0*	$\tau_{zr} = \tau_{z\theta} = 0$	$\tau_{zz} = 0$

The six models differ in the specification of the velocity boundary conditions. The turbulent flow field in the ST was modelled using two kinds of *specification of turbulence parameters.*

- ***Specification of turbulence parameters***

FIDAP 7.6 allows the specification of k and ε, or alternatively, of the *turbulent intensity*, I, and the *characteristic length scale*, L_s, related by:

$$k = I \cdot U^2/100$$
$$\varepsilon = A \cdot k^{3/2}/L_s \qquad (5.10)$$

where U is the magnitude of the velocity and A is a constant.

Information about k and L_s can be obtained from experimental data. For example, works of Wu and Patterson (1989) and Yianneskis *et al.* (1987) are frequently used to define the boundary conditions for k at the tip of the impeller. Wu and Patterson (1989) also reported the distributions of the characteristic length scales, L_s, based on LDV results. According to their results, L_s was about 1/10 of the blade width, W, at the corners of the impeller blade, and about $W/4$ at the centreline of the impeller. The length scales were much larger away from the impeller discharge flow. The authors claimed that $A = 0.85$ was the most adequate value, but in the present work, it was set to unity for simplicity. Kresta and Wood (1991) reported the value of $L_s = W/2$ as a length scale of the trailing vortices.

Turbulent flow was modelled for the six models using two kinds of turbulence approximations. The first type of boundary conditions, *TA1,* defines the constant turbulent intensity as $I = 50\%$, and the length scale as $L_s = W/4$ at the OUT entity. The relevant parameters to specify the turbulence can be plotted as shown in Figure 5.6. The specified constant of the turbulent intensity, I, was found at the impeller centre line from LDV measurements presented in Chapter 3, and was approximated on the entire OUT entity. LDV data on the turbulent intensity expresses the total turbulence that consists from the random and pseudo-turbulence contributions, as explained in Appendix B, and these were not separated in the *TA1*. The experimental results of Wu and Patterson (1989) on the macro-scale, L_s, at the impeller centre line were adopted for the OUT entity. The rate of the energy dissipation was calculated using Equation 5.10.

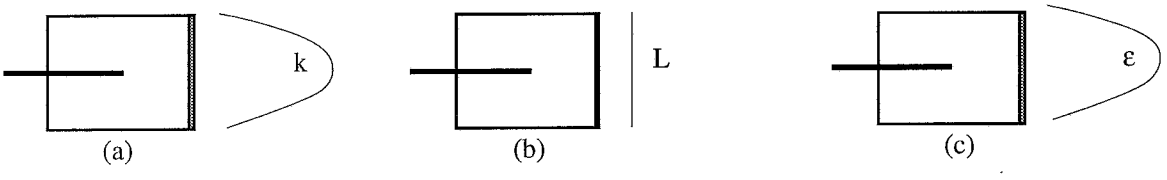

Figure 5.6 *2D illustration of the boundary conditions specified in the TA1 turbulence approximation and showing profiles of: (a) turbulent kinetic energy; (b) macro-scale length and (c) the rate of the energy dissipation.*

Boundary conditions in the second turbulent approximation, *TA2*, were derived from LDV results in the impeller region (Chapter 3). Assuming the moving ring approach, only the random turbulence quantity should be taken into account while the periodic component called pseudo-turbulence must be eliminated. This because the impeller region is averaged and approximated by the set of surface entities (see Figure 5.2)

Since LDV measurements were not performed using a rotating frame of reference, in order to approximate the magnitude of the random contribution of the turbulent kinetic energy to the total kinetic energy, the following assumptions were considered:

- Isotropic turbulence at the OUT impeller entity and the measured radial velocity fluctuation is used as characteristic value for all the fluctuating velocities, then $k = 3(\overline{v_r^2})/2$. This assumption is adopted from the study of Zhou and Kresta (1996) on local isotropy for the radial flow impeller.

- The *random fluctuating* velocity is only one third of the magnitude of the measured total fluctuating velocity. This value is a rough estimate based on the experimental work of Wu and Patterson (1989).

Then, the following equation can be used as an estimation of the random kinetic energy that is imposed in *TA2*:

$$k_{random} \approx (\overline{v_r^2})/2 \tag{5.11}$$

Taking the last equation and data of the LDV study in Chapter 3, a comparison to the results of Wu and Patterson (1989) can be performed, as shown in Figure 5.7. As can be seen, the approximation of the random kinetic energy from LDV data is in a reasonable agreement with the experimental data of Wu and Patterson (1989).

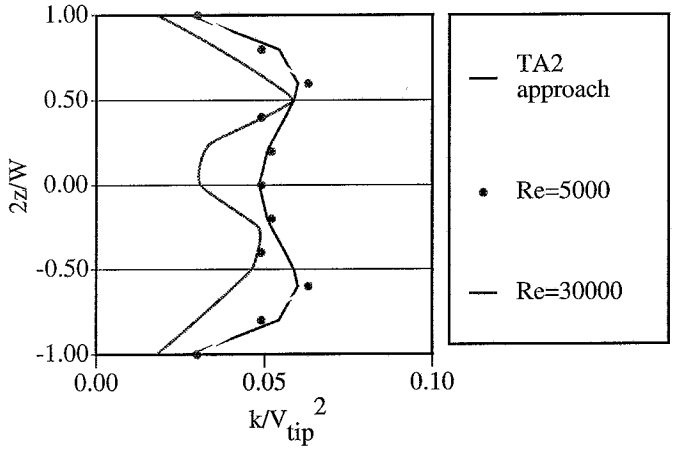

Figure 5.7 *Comparison of the estimate of the random turbulent kinetic energy used in TA2 approach and data obtained at Re=5000 (from LDV study in Chapter 3) and those found by Wu-Patterson (1989).*

A double peak profile of the turbulent kinetic energy (only the random part) was defined at the OUT entity in *TA2* turbulent approximation. The k boundary condition at the UPS, LOS entities were defined as constant in accordance with results found in the impeller region by LDV. Data on the turbulent macro-scale, L_s, at the OUT entity was defined in accordance to the results of Wu and Patterson (1989). The rate of the energy dissipation, ε, was calculated

using Equation 5.10 and the profiles of boundary conditions in *TA2* approximation are shown schematically in Figure 5.8.

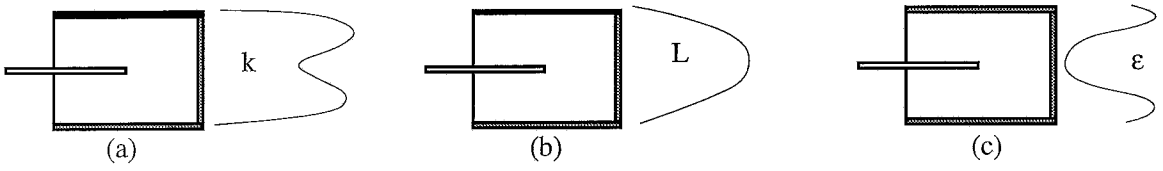

Figure 5.8 *The 2D illustration of the boundary conditions specified in the TA2turbulence approximation and showing profiles of: (a) turbulent kinetic energy; (b) macro-scale length; and (c) rate of the energy dissipation.*

5.2.4 Results

This section is subdivided on five subsections following the criteria that was used for the validation of numerical predictions with experimental data:

- *Velocity patterns;*
- *Flow number;*
- *Turbulent kinetic energy and the rate of the kinetic energy dissipation;*
- *Power number;*
- *Reynolds stresses predictability.*

The choice of the most appropriate model for steady-state predictions is selected on its ability to predict correctly the mentioned criteria. At the end of this section a discussion related to the moving ring approach and the boundary conditions specified by stresses is presented.

5.2.4.1 Velocity patterns

The shape of the velocity fields and the magnitudes of the velocity components obtained from predictions of the models studied are not affected significantly by the turbulent boundary conditions applied (*TA1* and *TA2*). The maximum difference in the predicted velocity components is around 10% for a few locations in the stirred tank. Flow patterns of the Rushton impelled ST using the *TA2* approach are shown in Figure 5.9 and Figure 5.10. The interpolated maps of speed (composed from all velocity components) are overlaid with the radial-axial projections of the velocity vector and normalised by the velocity at the impeller tip, V_{tip}. The vertical plane behind the baffle, at the angle $\theta = 3\pi/8$, is shown in Figure 5.9. It can be observed that models 2 and 3, defined with the uniform velocity distribution at the OUT entity, produce the stronger jet of radial flow than the other models. As the result, the higher Flow number values can be expected in predictions of model 2 and model 3.

The radial jet is redirected to the axial direction near the wall of a stirred tank and this flow change gives origin to two vertical vortices. The circulation of the top vortex above the

impeller, however, is disrupted at about $2/3$ of the tank height, H. Since similar behaviour is not observed in front of the baffle and at the plane passing through the baffle ($\theta = \pi/4$, see Figure 5.10), the baffle presence contributes to the pattern. This fact has not been reported in the previous numerical works, but this phenomenon was observed in the experimental work of Mavros *et al.* (1996).

The region of highest speed is located at the tip of the impeller and confirms the image of the radial jet coming out from the impeller. Noteworthy is the three spots of high magnitude of speed, observed on the speed map of model 3 near the impeller region. As can be seen, the flow enters at the highest velocity through the IN entity from where it is pumped to the impeller discharge flow through the OUT surface. This phenomenon is caused by the $V_z = 0$ boundary condition prescribed at the UPS, LOS entities. A similar phenomenon was not observed in the experiments, and model 3 is considered as incapable of the correct ST predictions. The velocity patterns from the predictions using the models 1, 4, 5 and 6 using the parabolic velocity distribution at the OUT entity are very similar. Therefore, it is not possible to select the most reasonable model from results presented in Figure 5.9 and Figure 5.10. The flow enters the impeller region through all surfaces but the OUT surface, where it is pumped at the highest velocity into the discharge flow region.

Figure 5.10 shows the flow field maps at the $\theta = \pi/4$ vertical plane that coincides with the plane passing through a baffle. Additional vortices are not formed in the top part of the ST at this plane, as well as at the vertical planes in front of a baffle. Present results on the flow field somehow differ from those of Bakker *et al.* (1994) obtained by numerical simulation. The vertical vortices are not so extended into the axial direction and the flow field in the present simulations is more declined inward to the ST. The vortex centres are closer to the impeller discharge flow than those from predictions of Bakker *et al.* (1994) but the angular dependence of the vortex centre was confirmed in the present predictions. The vector maps of the models 1, 4, 5, and 6 are very similar, and only further examinations can offer more information about each model reliability to predict the stirred tank hydrodynamics.

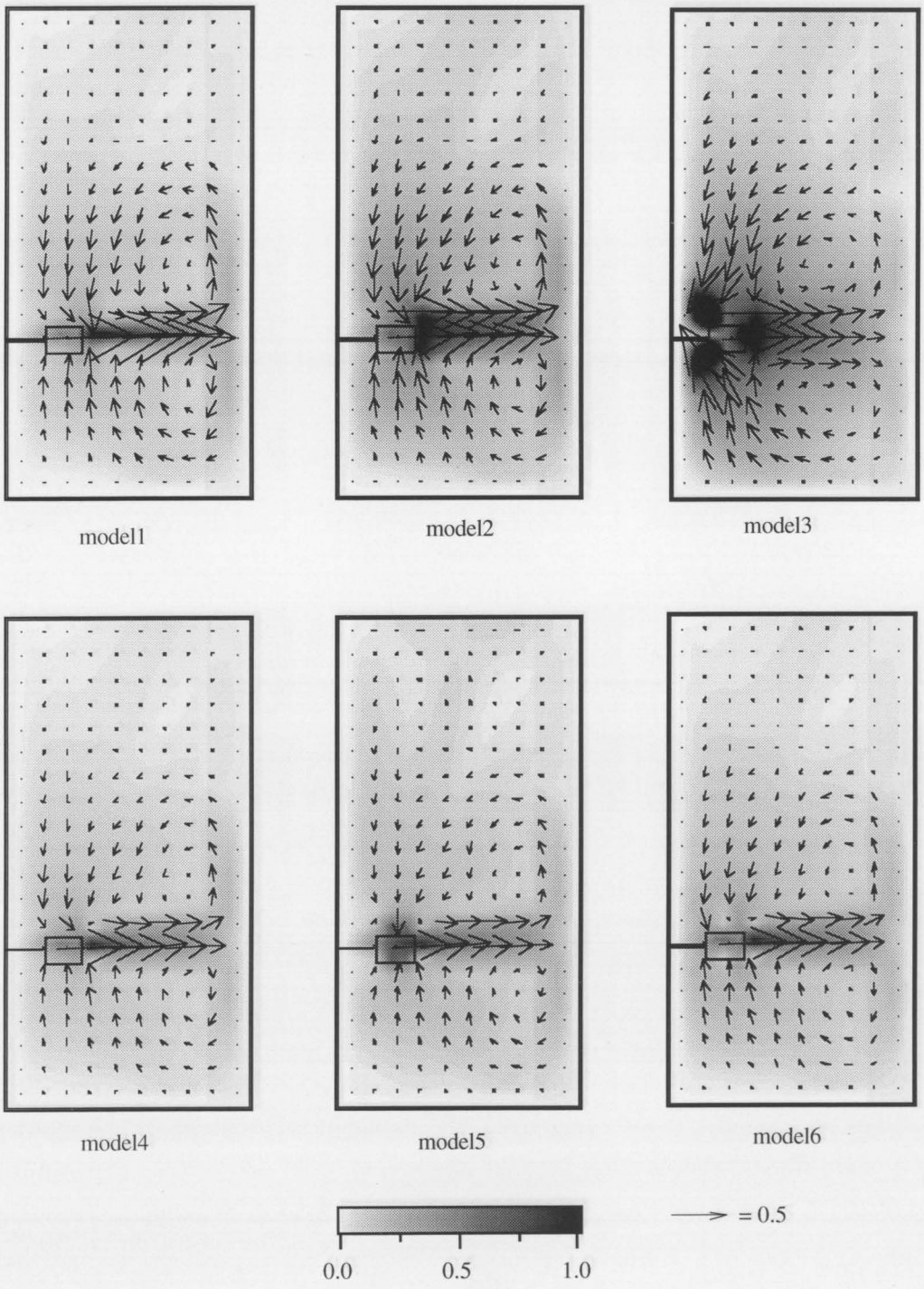

Figure 5.9 *Normalised speed maps overlaid with the radial-axial projection of the velocity vector at the vertical plane behind a baffle from steady-state simulations at Re=5000.*

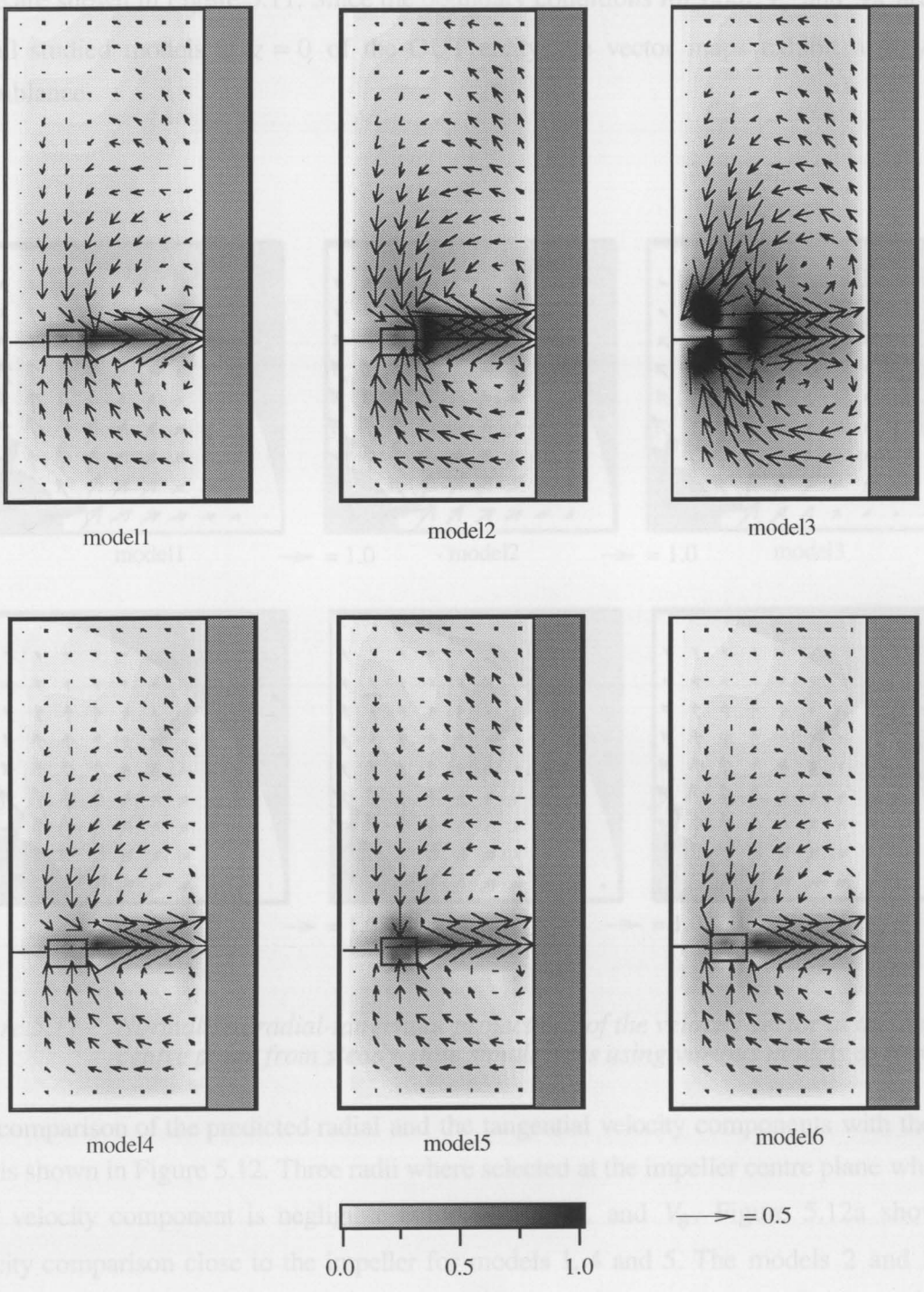

Figure 5.10 Normalised speed maps overlaid with the radial-axial projection of the velocity vector at the vertical plane passing through the baffle from steady-state simulations at Re=5000.

Vector plots from the radial and the tangential velocity components at the impeller centre plane are shown in Figure 5.11. Since the boundary conditions for both V_r and V_θ are equal for all studied models at $z = 0$ of the OUT entity, the vector maps exhibit a very close resemblance.

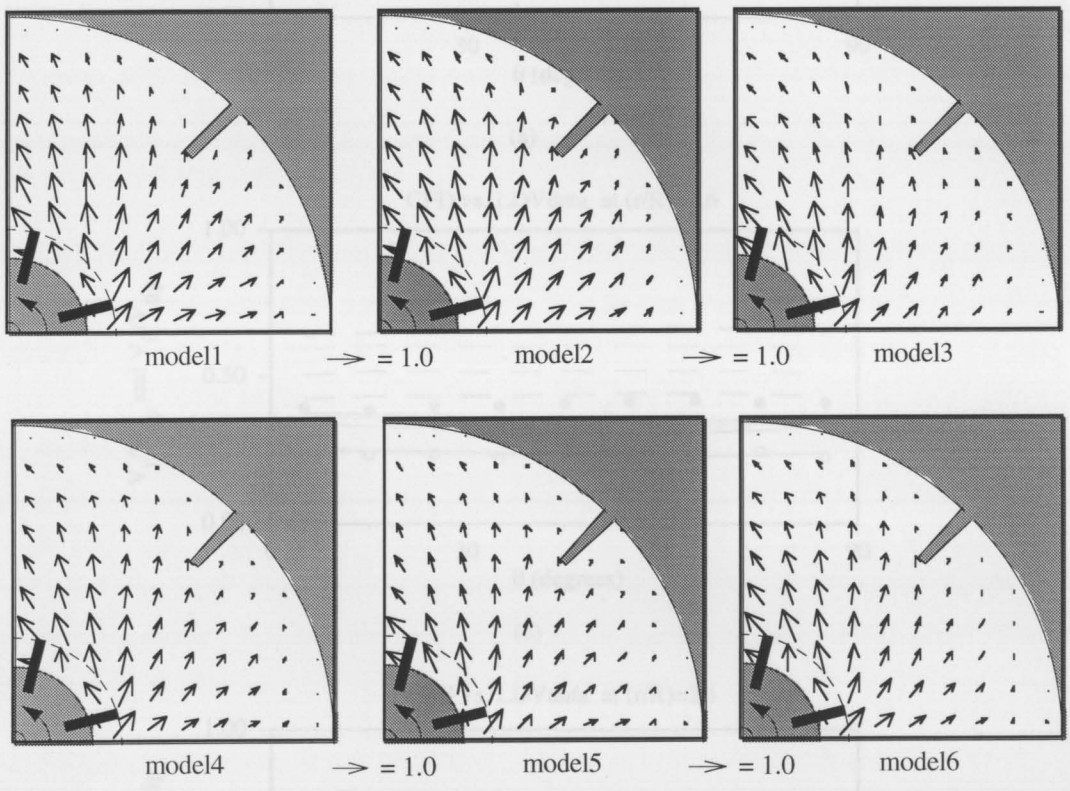

Figure 5.11 *Normalised radial-tangential projections of the velocity vector at the impeller centre plane from steady-state simulations using various models at Re=5000.*

The comparison of the predicted radial and the tangential velocity components with the LDV data is shown in Figure 5.12. Three radii where selected at the impeller centre plane where the axial velocity component is negligible comparing to V_r and V_θ. Figure 5.12a shows the velocity comparison close to the impeller for models 1, 4 and 5. The models 2 and 3 were excluded from these considerations due to predictions of a very strong radial jet and in the case of model 3 due to unrealistic flow picture observed in Figure 5.9 and Figure 5.10. The results of model 6 are not plotted in Figure 5.12 since they are quantitatively equal to those of model 4. As can be seen, the closest values for the radial and tangential components are found from models 4 (6) and model 5 while model 1 over-predicts the measured data. The comparisons at radii far away from the impeller are shown in Figure 5.12c. Predictions from all steady-state models are of higher magnitudes than those measured experimentally.

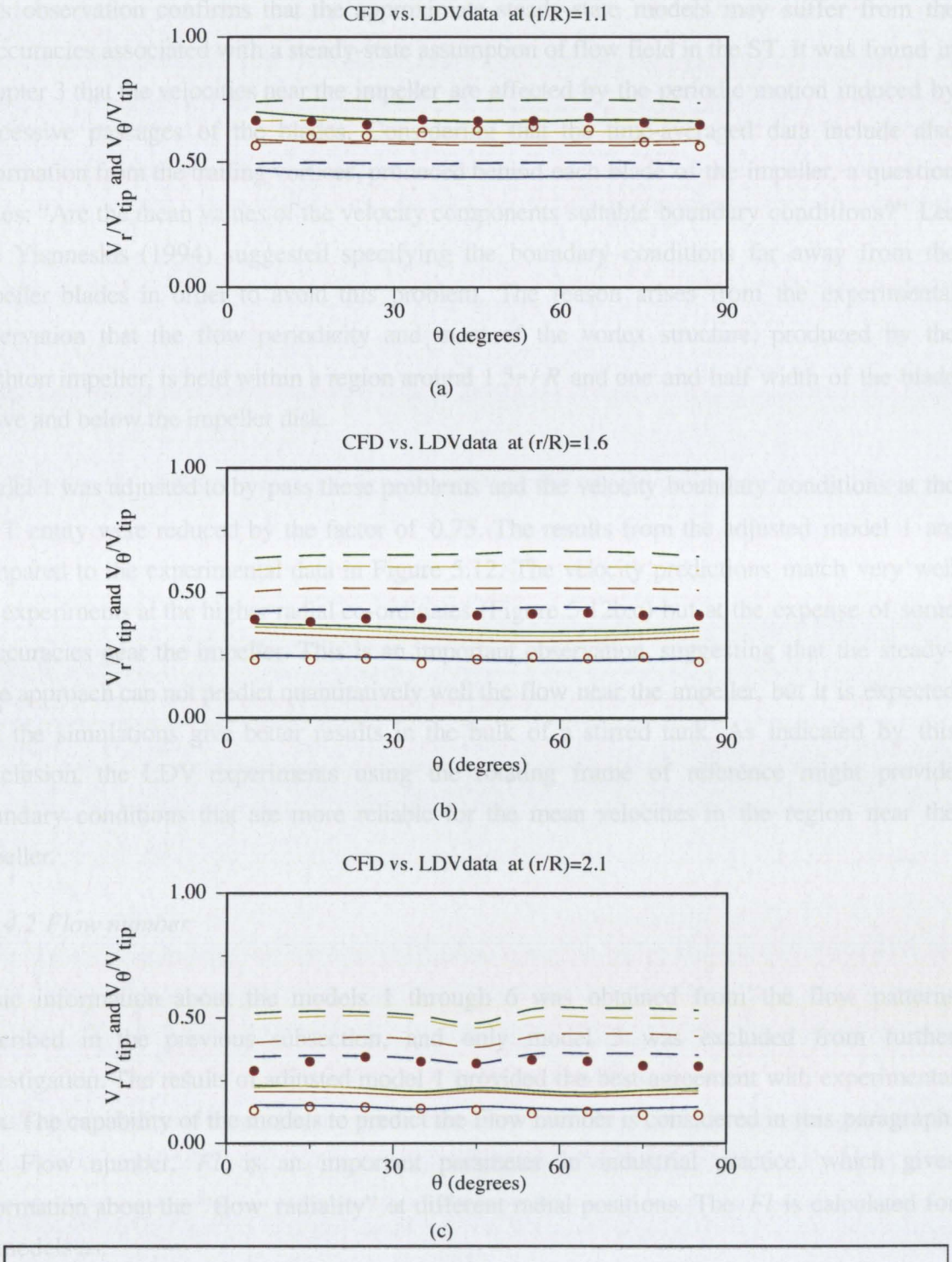

Figure 5.12 Comparison of LDV data with the results of numerical simulations at the three radii and for Re=5000.

This observation confirms that the approximate steady-state models may suffer from the inaccuracies associated with a steady-state assumption of flow field in the ST. It was found in Chapter 3 that the velocities near the impeller are affected by the periodic motion induced by successive passages of the blades. Considering that the time-averaged data include also information from the trailing vortices, produced behind each blade of the impeller, a question arises: "Are the mean values of the velocity components suitable boundary conditions?" Lee and Yianneskis (1994) suggested specifying the boundary conditions far away from the impeller blades in order to avoid this problem. The reason arises from the experimental observation that the flow periodicity and most of the vortex structure, produced by the Rushton impeller, is held within a region around $1.5r/R$ and one and half width of the blade above and below the impeller disk.

Model 1 was adjusted to by-pass these problems and the velocity boundary conditions at the OUT entity were reduced by the factor of 0.75. The results from the adjusted model 1 are compared to the experimental data in Figure 5.12. The velocity predictions match very well the experiments at the higher radial co-ordinates (Figure 5.12b,c) but at the expense of some inaccuracies near the impeller. This is an important observation, suggesting that the steady-state approach can not predict quantitatively well the flow near the impeller, but it is expected that the simulations give better results in the bulk of a stirred tank. As indicated by this conclusion, the LDV experiments using the rotating frame of reference might provide boundary conditions that are more reliable for the mean velocities in the region near the impeller.

5.2.4.2 Flow number

Basic information about the models 1 through 6 was obtained from the flow patterns described in the previous subsection, and only model 3 was excluded from further investigation. The results of adjusted model 1 provided the best agreement with experimental data. The capability of the models to predict the Flow number is considered in this paragraph. The Flow number, Fl, is an important parameter in industrial practice, which gives information about the "flow radiality" at different radial positions. The Fl is calculated for all models as:

$$Fl = \frac{Q_r}{8NR^3} = \frac{1}{2}\int_{-z_l}^{z_u} dz \int_{o}^{\pi/2} rV_r d\theta \tag{5.12}$$

or

$$Fl = \frac{Q_r}{NR^3} = \int_{-z_l}^{z_u} dz \int_{0}^{\pi/4} rV_r d\theta \tag{5.13}$$

where the integration limits in the axial direction, $-z_l$ and z_u, for $r/R = 1.0$, is at the edges of the impeller blade and for $r/R = 1.5$ and $r/R = 2.0$ extends to the location where the velocity V_r is still oriented in the direction of the impeller discharge flow.

Two integration domains were applied in order to see the difference between the Flow number predicted in the region in the front of a baffle ($\pi/4$ domain) and of the Flow number predicted within the whole $\pi/2$ segment. Table 5.8 shows results of the Flow number integrated on the $\pi/4$ domain (Equation 5.13) and on the $\pi/2$ domain (Equation 5.12). The results were calculated on the set of six models using the *TA1* turbulence approximation.

Table 5.8 Flow number results from predictions using TA1 turbulence approximation.

	Flow number					
domain	$\pi/4$			$\pi/2$		
model	$r/R = 1.0$	$r/R = 1.5$	$r/R = 2.0$	$r/R = 1.0$	$r/R = 1.5$	$r/R = 2.0$
1	1.02	1.97	2.76	1.02	1.98	2.83
2	1.74	2.50	3.26	1.74	2.50	3.31
3	1.74	2.88	2.82	1.74	2.91	3.04
4	0.95	1.60	2.22	0.95	1.61	2.29
5	0.74	1.33	1.86	0.74	1.34	1.91
6	0.95	1.66	2.24	0.95	1.67	2.32

Flow numbers calculated on the two integration domains differ slightly at $r/R = 1.5$ and $r/R = 2.0$ in favour of the $\pi/2$ domain. This means that the radial flow is slightly higher in the region behind the vertical plane passing through a baffle (in direction of the rotating impeller) than in the region in front of it. The Flow number dependence on the radial co-ordinate is shown in Figure 5.13. Results from the studied models are compared to the experiments of Gunkel and Weber (1975), Wu and Patterson (1989), and Stoots and Calabrese (1995). The results produced by model 4 and model 6 compare very well with the experiments of Gunkel and Weber (1975) while the results of model 5 are quite close to the experiments of Wu and Patterson (1989). Models 1, 2 and 3 overestimate the Flow number values. The models 2 and 3 can be rejected at this point, since the *Fl* value at the tip of the impeller is almost double the measured value. This over-prediction is due to the uniform velocity profile imposed at the OUT entity. Small differences were observed in the case of model 5 comparing to the models 4 and 6. The use of the angularity parameter in model 1 resulted in a small over-prediction of the Flow number.

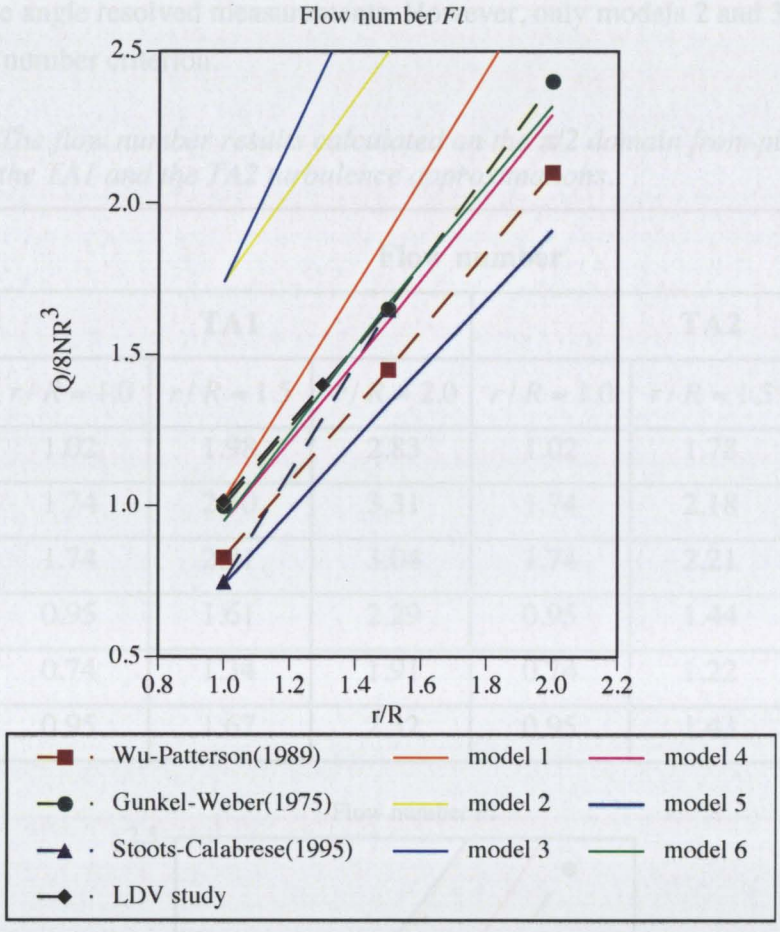

Figure 5.13 *Flow number as a function of the radius from simulations using TA1 turbulent approximation.*

Flow number predictions, using the *TA2* turbulence approach, differ from those obtained using *TA1*, mainly in regions far away from the impeller. The results on the calculated values of *Fl* on the $\pi/2$ domain and using the *TA1* and the *TA2* are summarised in Table 5.9.

The results are similar at $r/R = 1.0$ since identical boundary conditions of the velocity are specified at the OUT entity. However, small differences are observed at higher radial co-ordinates. The dependence of the Flow number on the radial co-ordinate for predictions using the *TA2* approximation is shown in Figure 5.14. The results of the studied models are compared against experiments of Gunkel and Weber (1975), Wu and Patterson (1989), and against those of Stoots and Calabrese (1995). Smaller deviations from the experimental data are observed than in the predictions using the *TA1* approach (Figure 5.14).

Figure 5.14 illustrates that some differences exist between the experimental data of the various authors. The LDV study of Chapter 3 and data of Gunkel and Weber (1975) might suffer, near the impeller, from the fact that data was obtained in a fixed frame of reference. Therefore, the measured radial velocities are higher than those reported by Wu and Patterson

(1989) using the angle resolved measurements. However, only models 2 and 3 can be rejected using the Flow number criterion.

Table 5.9 *The flow number results calculated on the π/2 domain from predictions using the TA1 and the TA2 turbulence approximations.*

	Flow number					
	TA1			TA2		
model	$r/R = 1.0$	$r/R = 1.5$	$r/R = 2.0$	$r/R = 1.0$	$r/R = 1.5$	$r/R = 2.0$
1	1.02	1.98	2.83	1.02	1.78	2.63
2	1.74	2.50	3.31	1.74	2.18	2.93
3	1.74	2.91	3.04	1.74	2.21	2.96
4	0.95	1.61	2.29	0.95	1.44	2.11
5	0.74	1.34	1.91	0.74	1.22	1.81
6	0.95	1.67	2.32	0.95	1.43	2.11

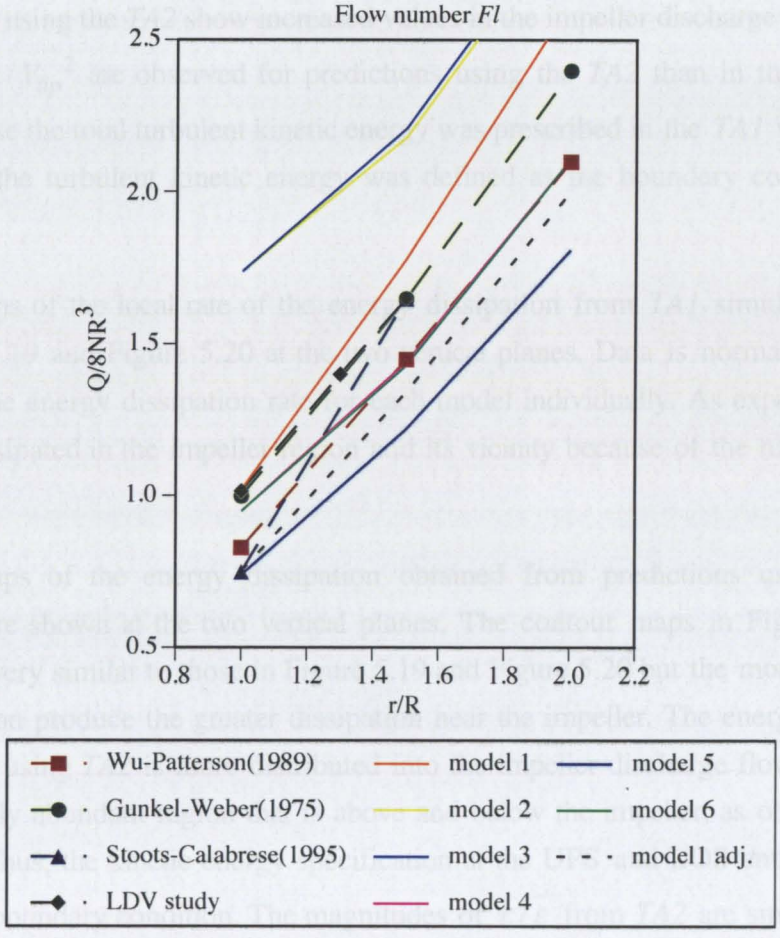

Figure 5.14 *Flow number as a function of the radius; calculated from simulations using the TA2 turbulent approximation.*

5.2.4.3 Turbulent kinetic energy and the rate of dissipation of the kinetic energy

The contour maps of the normalised turbulent kinetic energy, k/V_{tip}^2, are shown for all six models in Figure 5.15 and Figure 5.16. The turbulence was modelled using the *TA1* approximation and the results are shown at the angles $\theta = \pi/4$ and $\theta = 3\pi/8$ (behind the baffle in direction of the rotating impeller). A first analysis shows that regions of maximum kinetic energy are within the impeller discharge flow and the impeller region. Model 3 predicts extremely high levels of the kinetic energy due to the violent flow entering the impeller region through the IN entity as discussed in Section 1.3.4.1.

As can be seen, the results for models 1, 2, 4 and 5 show very similar patterns, characteristic with small differences near the impeller due to different boundary conditions imposed for the velocity. Figure 5.17 and Figure 5.18 show contour maps of the kinetic energy for the *TA2* approximation. The predictions using the *TA1* and *TA2* are very close in the bulk of the tank but they differ in the impeller vicinity. The turbulent kinetic energy, k/V_{tip}^2, of the *TA1* approach is concentrated mostly in the impeller vicinity, while the turbulent kinetic energies from predictions using the *TA2* show increased values in the impeller discharge flow. Smaller magnitudes of k/V_{tip}^2 are observed for predictions using the *TA2* than in those using the *TA1*. This because the total turbulent kinetic energy was prescribed in the *TA1* while only the random part of the turbulent kinetic energy was defined as the boundary condition in the *TA2*approach.

The contour maps of the local rate of the energy dissipation from *TA1* simulations can be seen in Figure 5.19 and Figure 5.20 at the two vertical planes. Data is normalised with the mean value of the energy dissipation rate for each model individually. As expected, most of the energy is dissipated in the impeller region and its vicinity because of the highest velocity gradients.

The contour maps of the energy dissipation obtained from predictions using the *TA2* approximation are shown at the two vertical planes. The contour maps in Figure 5.21 and Figure 5.22 are very similar to those in Figure 5.19 and Figure 5.20 but the models using the *TA1*approximation produce the greater dissipation near the impeller. The energy dissipation from the models using *TA2* is more distributed into the impeller discharge flow and into the more energetically abundant region that is above and below the impeller, as observed in the contour maps. Thus, the kinetic energy specification at the UPS and LOS entities appear to be a reasonable boundary condition. The magnitudes of $\varepsilon/\bar{\varepsilon}$ from *TA2* are smaller than that from the *TA1*.

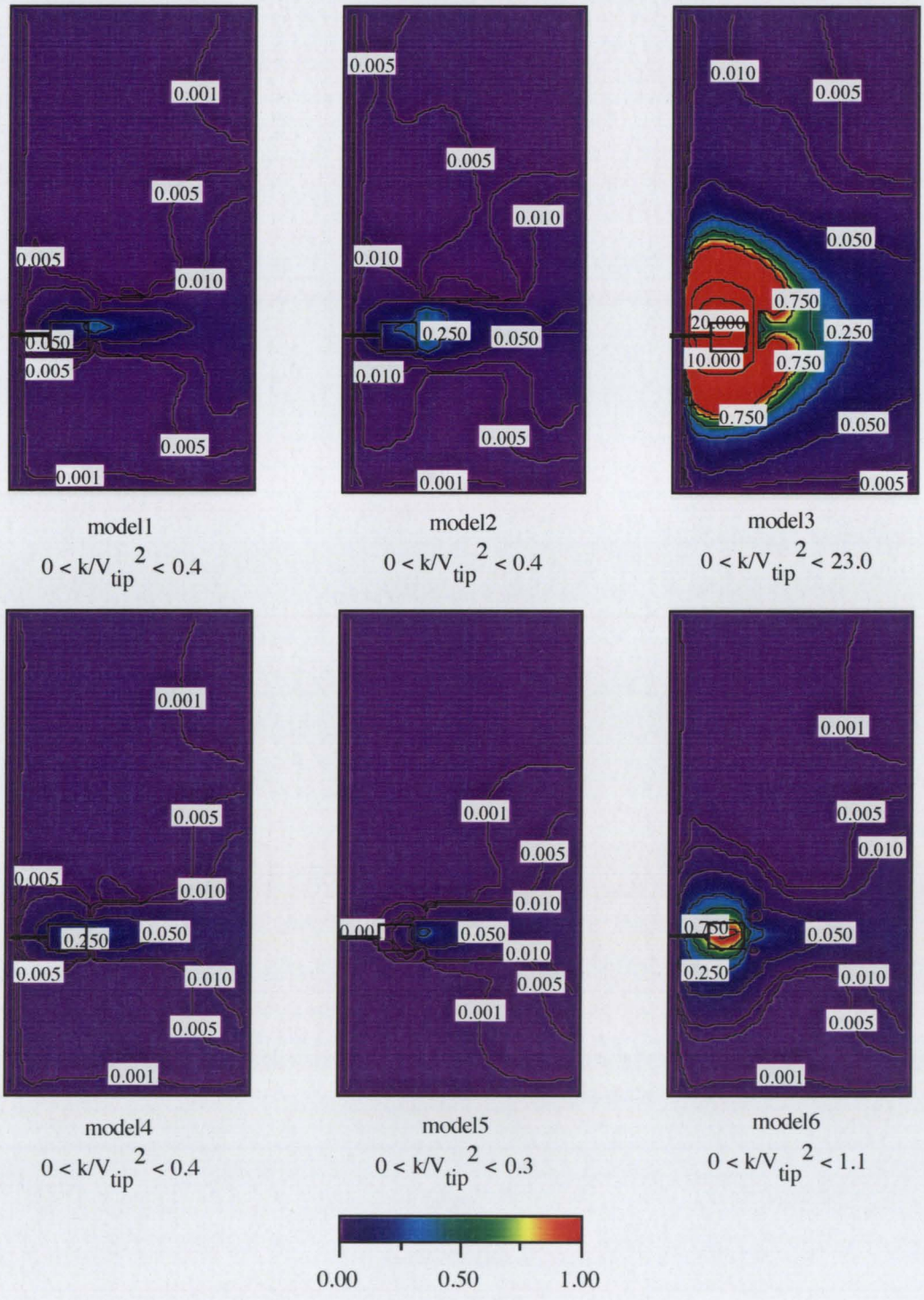

Figure 5.15 *Normalised turbulent kinetic energy maps and contour plots at the vertical plane behind the baffle from steady-state simulations at Re=5000 and using the TA1 boundary conditions.*

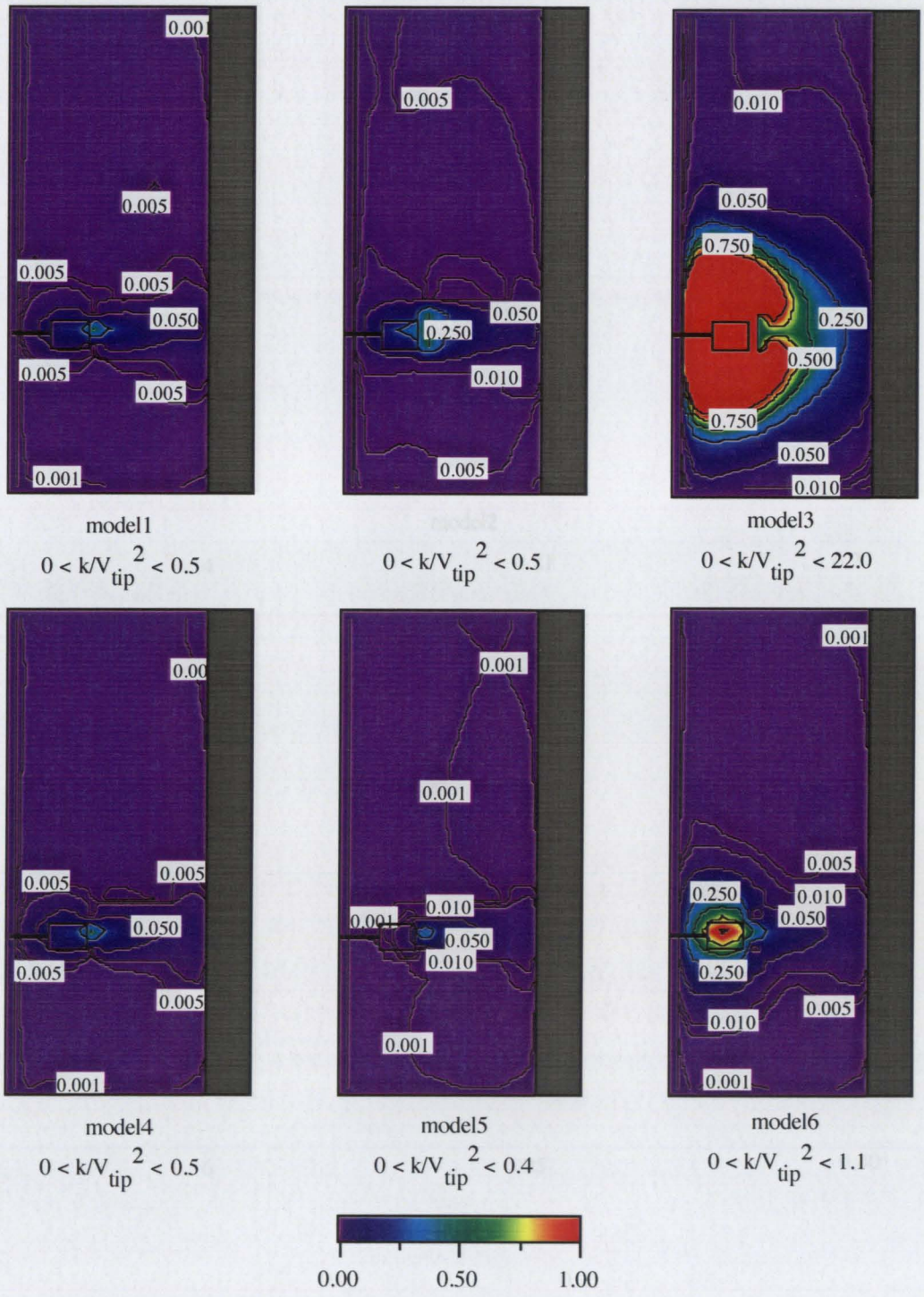

Figure 5.16 *Normalised turbulent kinetic energy maps and contour plots at the vertical plane passing through the baffle from steady-state simulations at Re=5000 and using the TA1 boundary conditions.*

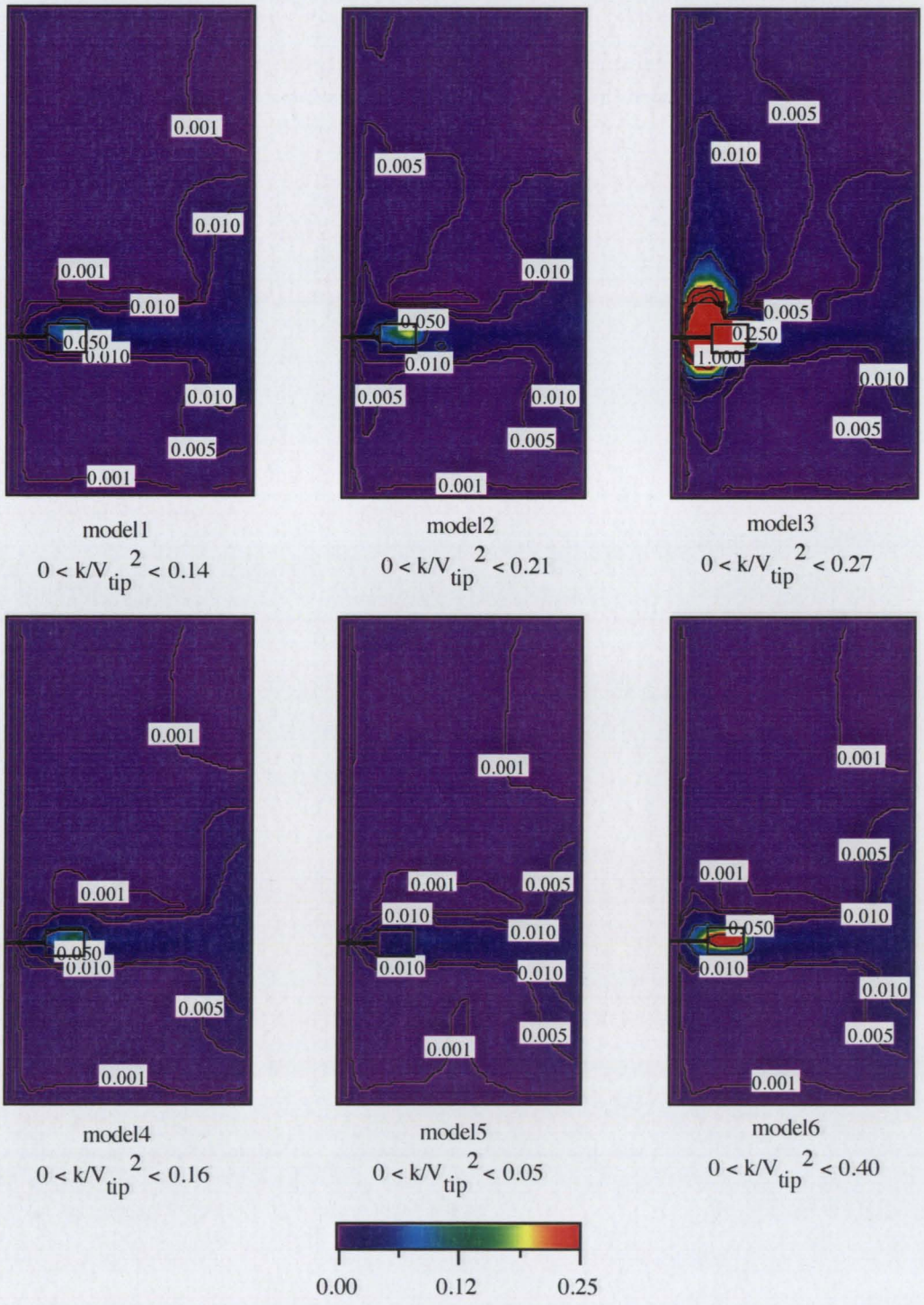

Figure 5.17 *Normalised turbulent kinetic energy maps and contour plots at the vertical plane behind the baffle from steady-state simulations at Re=5000 and using the TA2 boundary conditions.*

Figure 5.18 *Normalised turbulent kinetic energy maps and contour plots at the vertical plane behind passing through the baffle from steady-state simulations at Re=5000 and using the TA2 boundary conditions.*

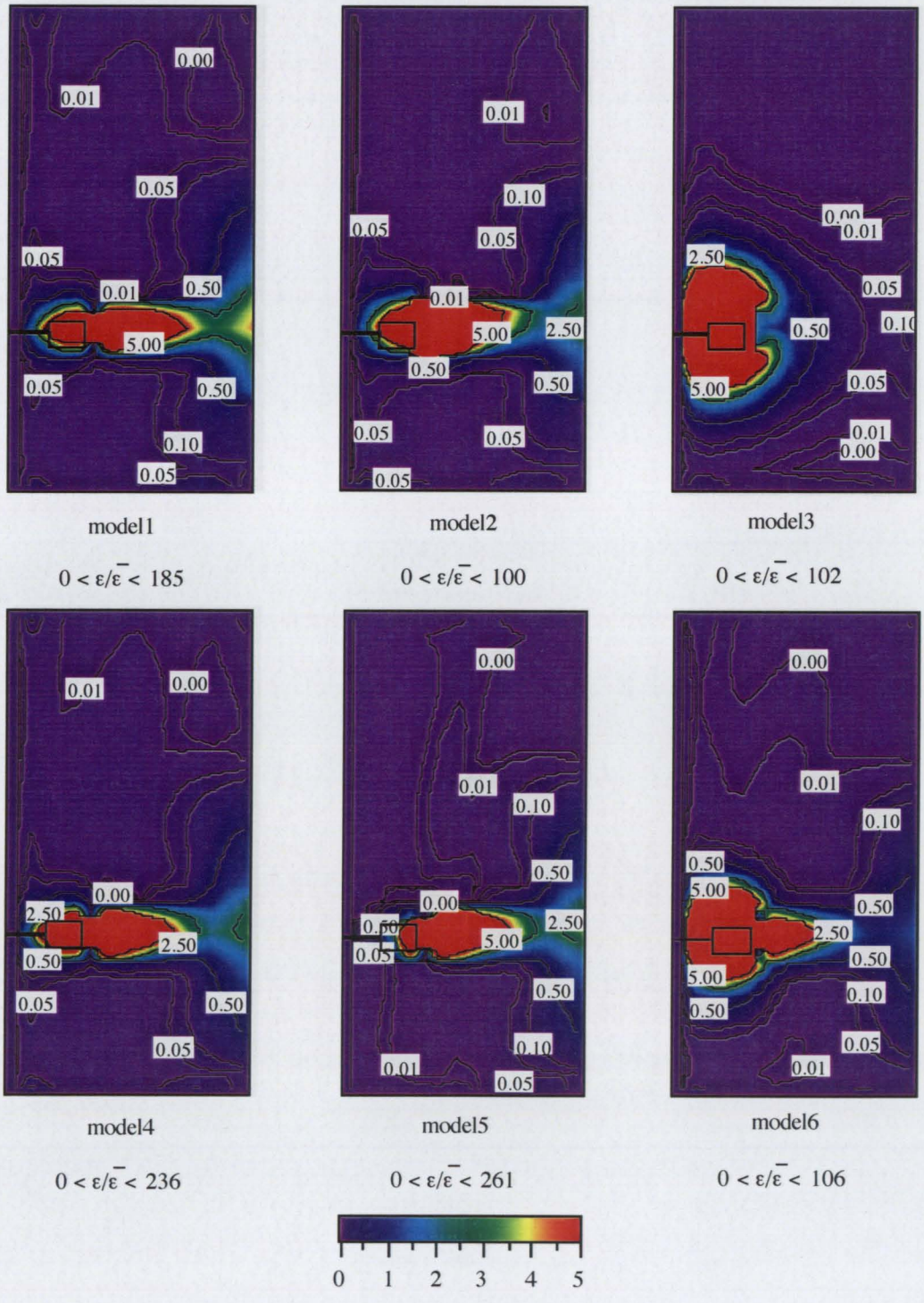

Figure 5.19 *Normalised energy dissipation maps and contour plots at the vertical plane behind the baffle from steady-state simulations at Re=5000 and using the TA1 boundary conditions.*

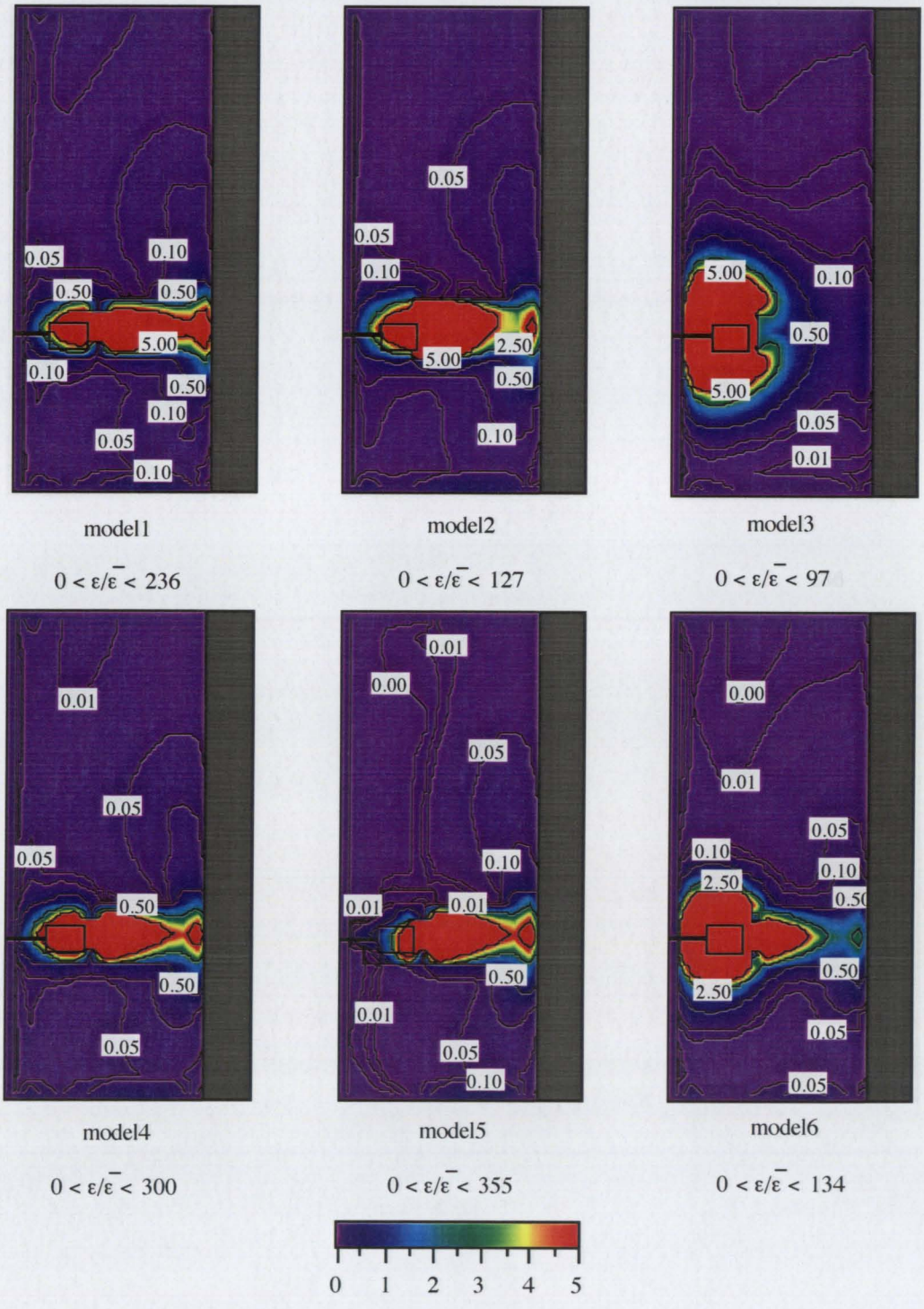

Figure 5.20 *Normalised energy dissipation maps and contour plots at the vertical plane passing through the baffle from steady-state simulations at Re=5000 and using the TA1 boundary conditions.*

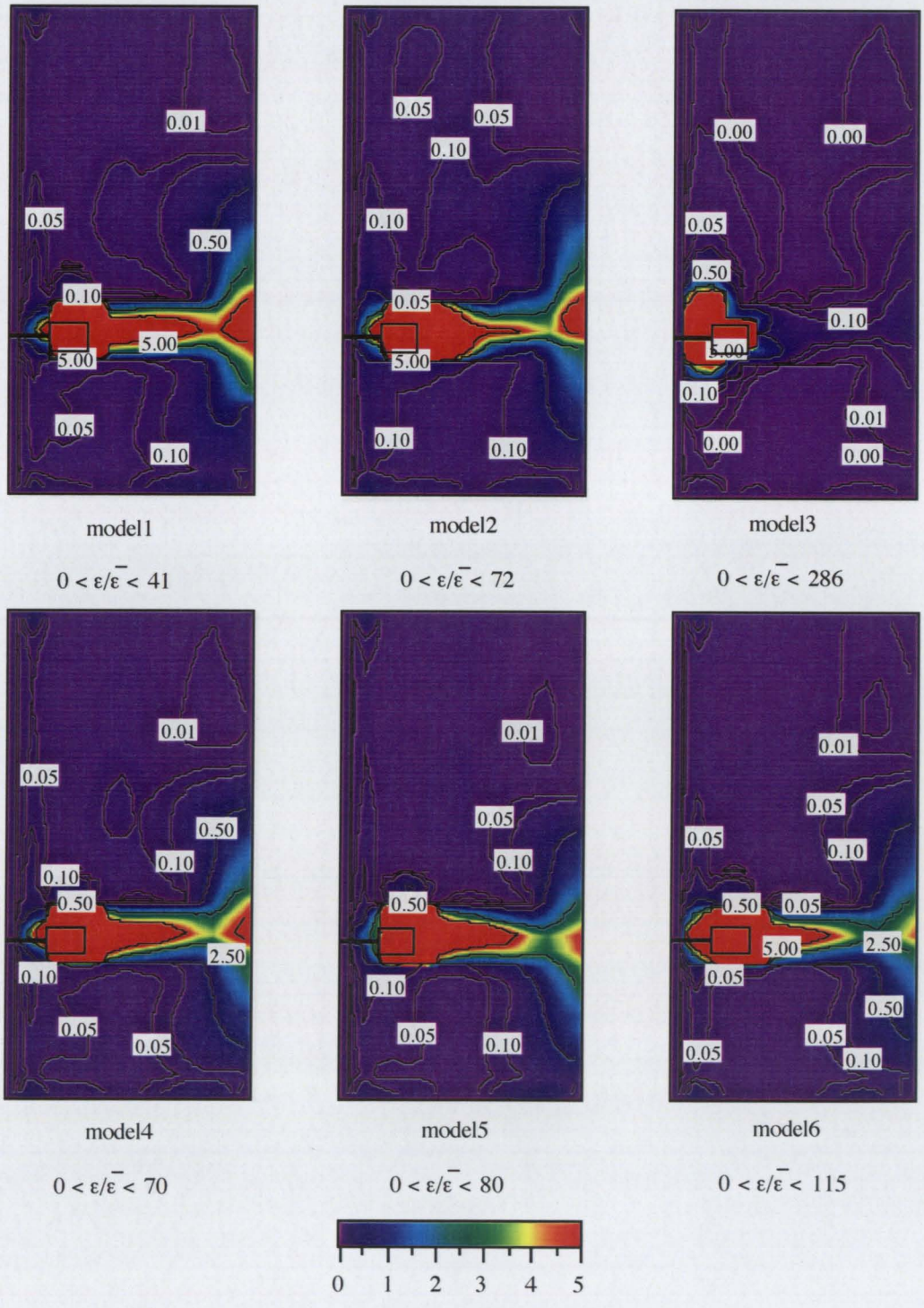

Figure 5.21 *Normalised energy dissipation maps and contour plots at the vertical plane behind the baffle from steady-state simulations at Re=5000 and using the TA2 boundary conditions.*

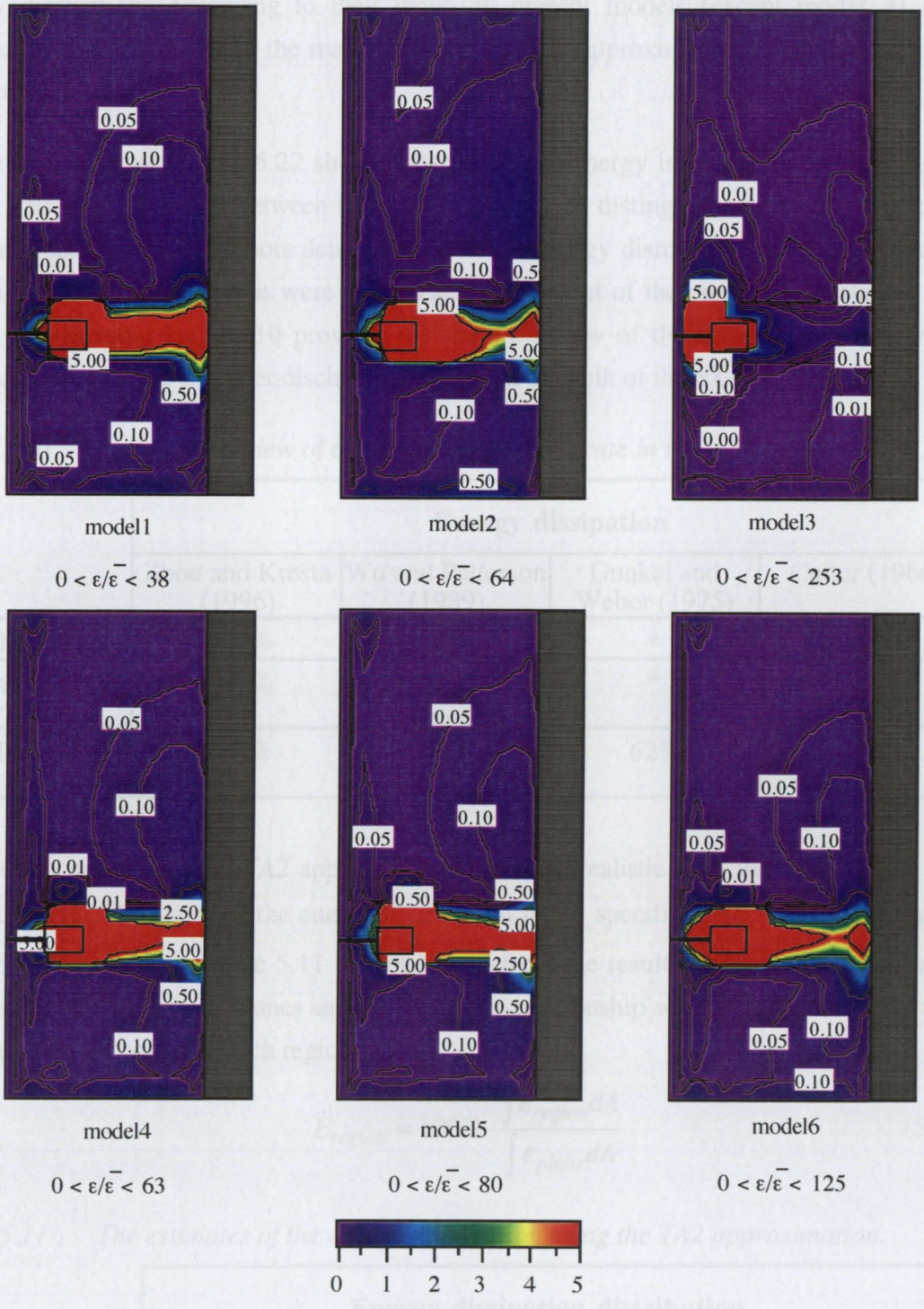

Figure 5.22 *Normalised energy dissipation maps and contour plots at the vertical plane passing through the baffle from steady-state simulations at Re=5000 and using the TA2 boundary conditions.*

The models using the *TA2* approximation produce data closer to the work of Wu and Patterson (1989) who reported data near the impeller up to 30 times the mean value of the energy dissipation. According to their work, all present models (except model 3) offer reasonable values in terms of the magnitude but the *TA2* approximation is considered as the more reliable one.

Figure 5.19 through Figure 5.22 show that most of the energy is dissipated within a small region and the differences between the models can not be distinguished from the presented contour maps. Therefore, a more detailed study of the energy distribution must be performed for the ST. Three main regions were defined and the amount of the energy dissipated in each region is estimated. Table 5.10 provides a literature review of the dissipated energy in the impeller region, in the impeller discharge flow and in the bulk of the ST.

Table 5.10 Literature review of the dissipated energy rate in three ST main regions .

	Energy dissipation			
	Zhou and Kresta (1996)	Wu and Patterson (1989)	Gunkel and Weber (1975)	Cutter (1966)
impeller region	15.3%	30%	*	20-25%
discharge flow region	28.2%	30%	*	35-50%
bulk of the tank	56.5%	40%	62%	25-40%

** 38% in both regions*

Simulations employing the *TA2* approximation are more realistic than those using the *TA1* approximation. Estimates of the energy distribution in the specific region, E_{region}, are given on Table 5.11. Data on Table 5.11 was estimated from the results of the energy dissipation obtained at the two vertical planes and the following relationship was used for the calculation of the energetic content of each region:

$$E_{region} = 100\% \cdot \frac{\int \varepsilon_{region} dA}{\int \varepsilon_{plane} dA} \tag{5.14}$$

Table 5.11 The estimates of the energy distribution using the TA2 approximation.

	Energy dissipation distribution					
	model 1	**model 2**	**model 3**	**model 4**	**model 5**	**model 6**
impeller region	35%	38%	40%	42%	38%	48%
discharge flow region	22%	15%	0.3%	17%	15%	11%
bulk of the tank	43%	47%	59.7%	41%	47%	51%

The results of predictions from the models 1 through 6 have a tendency to overestimate the energy dissipated in the impeller region and the bulk of the tank, and to underestimate the dissipated energy in the impeller discharge flow region. The observed tendency arises from the approximation of the steady-state simulations using the moving ring that is another limitation of this approach to the ST. At this point, no selection between the models can be done and further validation is necessary.

5.2.4.4 Power number

The power number, N_P, is directly related to the specified turbulence parameters and it is used here to validate the numerical predictions. The power input is introduced into the fluid throughout the impeller and consequently dissipated at very small scales and transformed into heat. The power draw, P, from the impeller into the ST is defined as

$$P = 4\rho \int_0^{\pi/2} \varepsilon dV_Q = \rho \bar{\varepsilon} V_Q \tag{5.15}$$

where ε is the rate of the turbulent kinetic energy dissipation, ρ is the fluid density and V_Q is the total volume of a stirred tank.

The average value of the rate of the kinetic energy dissipation as the power per unit of mass is defined as:

$$\bar{\varepsilon} = \frac{P}{m} = \frac{\int \varepsilon dV_Q}{\int dV_Q} \tag{5.16}$$

where m is the mass of liquid. Then the power number, N_P, can be normalised as:

$$N_P = \frac{P}{\rho N^3 D^5} \tag{5.17}$$

Table 5.12 shows the results of the power number, N_P, as calculated from predictions of the models 1 through 6 employing the *TA1* and *TA2* turbulence approximations and the reference value found experimentally by Bates *et al.* (1963). The results on the power number for both turbulent approximations are also shown in Figure 5.23. These results confirmed that simulations using the *TA1* over-predicted the measured data in general. Only the use of model 5 with the *TA1* approaches to the reference value. The results on the Power number computed from predictions using the *TA2* approximation (except model 3) are closer to the reference value. This is due to the definition of the random turbulent kinetic energy on the boundary condition. The model 1, 2 and 6 offer the best data using this validation criterion.

Table 5.12 *Power number results from predictions using the TA1 and the TA2 turbulence approximations.*

	N_P						
	model 1	model 2	model 3	model 4	model 5	model 6	ref. value
TA1	9.2	16.7	960	7.3	4.4	16.2	5.0
TA2	4.9	4.6	142.5	3.4	2.3	4.7	5.0

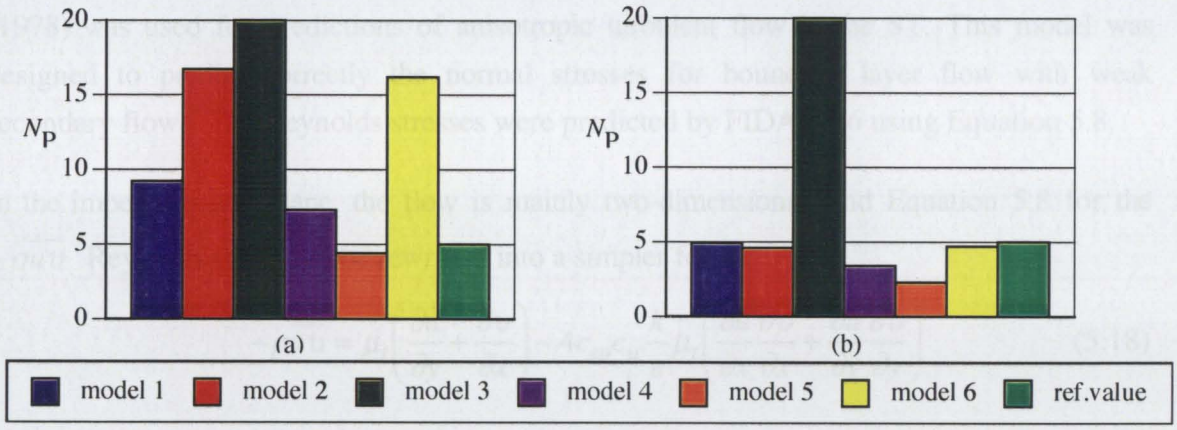

Figure 5.23 *Power number calculated from simulations using steady-state models and (a) TA1 and (b) TA2 boundary conditions.*

5.2.4.5 Predictability of the Shear Reynolds stress

In the Navier-Stokes equations that are averaged with respect to time, some additional terms arise. Considering the statistical description of turbulence, more unknowns than available equations appear, and this situation is called *closure problem* (see Appendix C for details). These terms are a double or a triple correlation between the components of the velocity or between the fluctuations of the velocity and the density. The correlation between the fluctuations of the velocity components are known as the *Reynolds stresses*. They account for the forces generated on the fluid purely by velocity fluctuations and the components in all directions of a co-ordinate system form the Reynolds stress tensor. This tensor is symmetric and contributes to the mean stress tensor. The components of the mean stress tensor aligned on a diagonal are the *normal stresses* while the off-diagonal components are the *shear stresses*.

The shear stresses play an important role in the transfer of momentum and they can be thought as a divergence of the stress because it exchanges momentum between the turbulence

and the mean flow. Moreover, these stresses decay rapidly in the absence of a source of turbulence.

The Reynolds stresses are generally unknown, and the closure problem is solved by relating this quantity to the mean flow features such as the mean shear rate. One of the first closure approaches is known as *Prandtl's mixing theory* and another example is the *Boussinesq's model.* In more recent models, the Reynolds stresses are related as a non-linear function of the mean strain rate, and are known as *anisotropic models.*

The shear Reynolds stress, $-\rho\overline{uv}$, is the last validation criterion for the simulations in this work. This quantity was investigated by LDV, as reported in Chapter 3, and the results showed an anisotropic behaviour of flow at the impeller centre plane. The model of Speziale (1978) was used for predictions of anisotropic turbulent flow in the ST. This model was designed to predict correctly the normal stresses for boundary layer flow with weak secondary flows. The Reynolds stresses were predicted by FIDAP 7.6 using Equation 5.8.

In the impeller centre plane, the flow is mainly two-dimensional, and Equation 5.8 for the $-\rho\overline{uv}$ Reynolds stress can be rewritten into a simpler form:

$$-\rho\overline{uv} = \mu_t\left(\frac{\partial u}{\partial y}+\frac{\partial v}{\partial x}\right) - 4c_{sp}c_{\mu}\frac{k}{\varepsilon}\mu_t\left(\frac{\partial u}{\partial x}\frac{\partial v}{\partial x}+\frac{\partial u}{\partial y}\frac{\partial v}{\partial y}\right) \tag{5.18}$$

where μ_t is the turbulent viscosity, and u and v are the velocity fluctuations in the Cartesian co-ordinate system.

The second term on the right-hand side of Equation 5.18 accounts for the anisotropic turbulence since the first term on the right-hand side can be found in the standard $k-\varepsilon$ model that is valid only for the isotropic turbulence.

Figure 5.24 shows the comparison of the predicted Reynolds stresses, using model 1 and the adjusted model 1, to the data obtained by LDV at three different radial positions. This data is expressed as the ratio of the maximum shear stress in the ST, which corresponds to that at the tip of the impeller:

$$-\frac{\overline{uv}}{V_{tip}^{\,2}} = f(r/R;\theta) \tag{5.19}$$

Figure 5.24 displays a good qualitative and quantitative agreement between the adjusted model 1 and experimental data for all radii. Model 1 over-predicts the measured quantity that is mainly due to limitations of the steady-state simulation, as explained in Section 5.2.4.1. This limitation results into inaccurate results of the velocity components near the impeller.

The problem is not felt in predictions of the Reynolds stress, because the contribution of pseudo-turbulence was already eliminated from the experimental data.

An increase of values of the shear Reynolds stress is observed in the close proximity of the baffle (Figure 5.24c). The magnitude and sign of the shear Reynolds stress obtained experimentally are in good agreement with data from the steady-state simulation using the adjusted model 1.

These results suggest that CFD simulations produce reasonable predictions of the first order quantities (mean velocities)but also of the second order quantities such as the shear Reynolds stress.

The contour maps of the Reynolds stress are presented in Figure 5.25 at the impeller centre plane. These contour maps show results from the simulation of model 1 using *TA2* conditions and LDV data at $Re = 5000$. The contour map of LDV data contains also the contribution from pseudo-turbulence, and thus the magnitude near the impeller is higher than that obtained from the simulations. In the regions far away from the impeller, the effect of pseudo-turbulence vanishes and the magnitudes exhibit a reasonable agreement.

The break of the axis-symmetric flow in the regions far away from the impeller, found in LDV study of Chapter 3, was confirmed also by the results of numerical simulations.

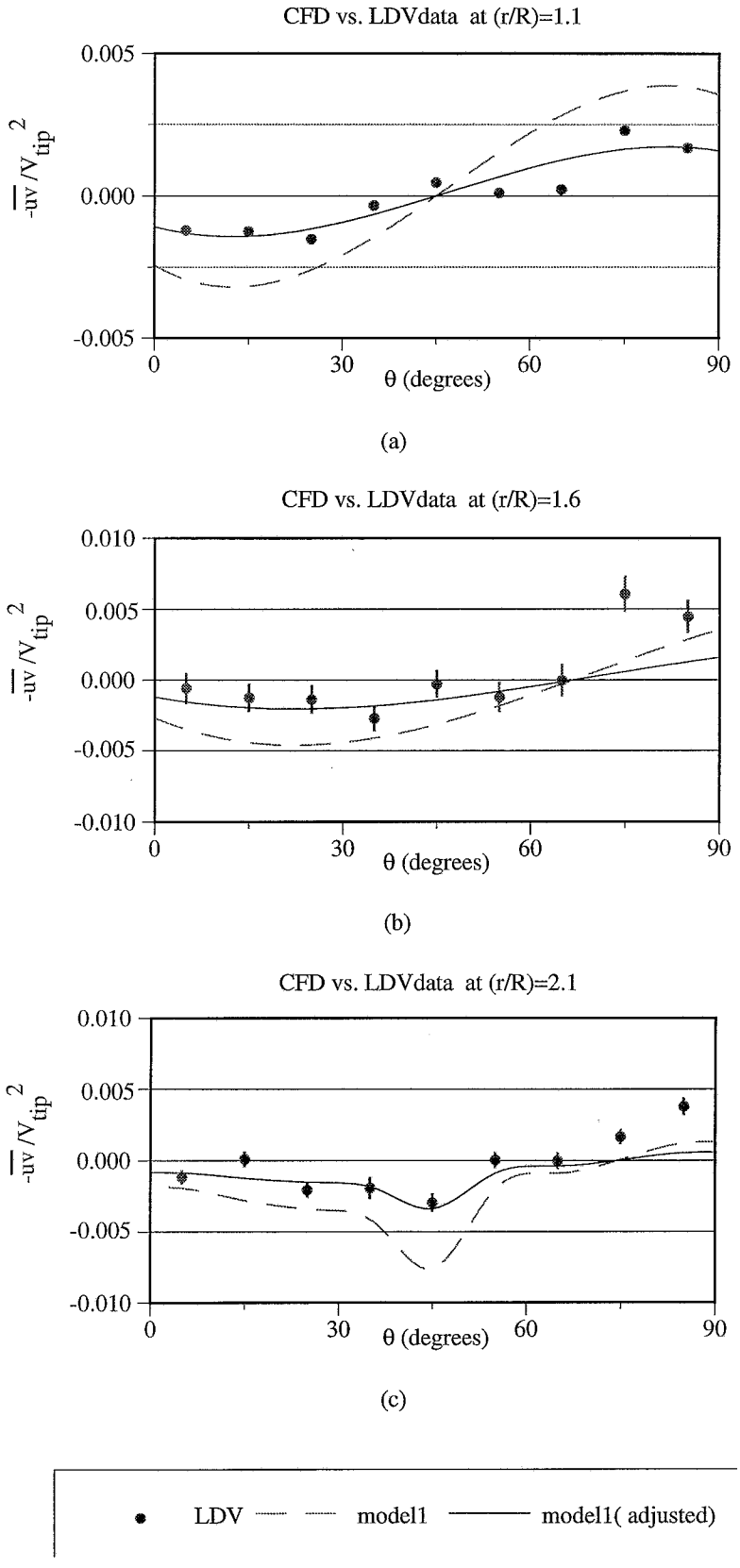

Figure 5.24 *Comparison of the shear Reynolds stress prediction with LDV data at various radii of the impeller centre plane (z=0) and for Re=5000.*

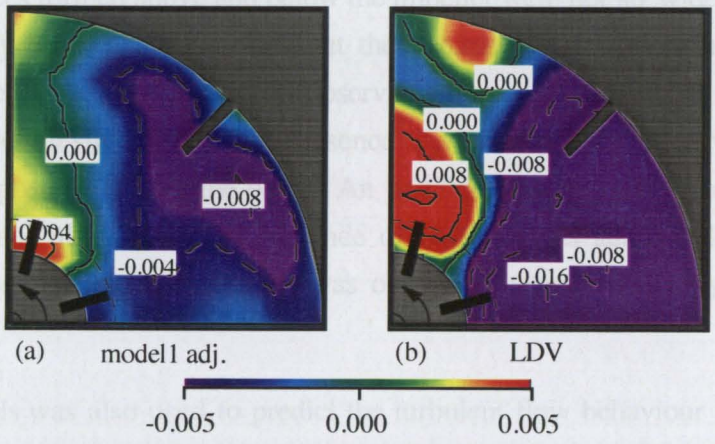

Figure 5.25 *The contour maps of the shear Reynolds stress at the impeller centre plane: (a) numerical prediction of model 1; (b) LDV data without elimination of pseudo-turbulence.*

5.2.5 Conclusions from steady-state simulations of ST

Single-phase, 3D simulations of the ST impelled with the Rushton impeller were performed using the set of six models. All models predicted very similar flow patterns. However, models 2 and 3 with the uniform boundary condition for the velocity at the OUT entity promoted more violent mixing in the radial and axial directions resulting into the overestimation of the Flow number. Model 3 with definition of a zero axial flow at the UPS, LOS entities was not appropriate for the ST predictions. This because the pattern obtained differs from experimental data and the overall numbers such as the Power number and Flow number were highly overpredicted. Models 1, 4, 5 and 6, where a parabolic profile was specified as the velocity boundary condition, produced higher radial and the tangential velocity components at the impeller centre plane than those from the measured data. This observation was attributed to limitations of the steady-state ST simulations. In addition, models 5 and 6 were more complex and demanded more boundary conditions than the others. Model 5, where the boundary conditions were specified in accordance to the LDV data did not offer the best predictions, as might be expected. This is probably related with time-averaging of the data measured or with the uncertainties coming from the intersection of the measuring volume by the passages of the blades during the LDV experiments. The first and fourth models were the easiest to implement into the CFD package, and offered very close predictions of the ST, with minimal recourse to experimental data. It is believed that model 1 gives better predictions than the other models due to boundary conditions using specification the angularity parameter observed experimentally and because of its positive impact on the velocity components predicted near the impeller. The velocity boundary conditions of model 1 were adjusted in order to approximate the measured data more closely. This adjusted model 1 predicted very well the velocities apart from the impeller region, but at the expense of poor predictions in the impeller vicinity.

The two main vortices formed above and below the impeller were not so widened and straight as those reported by Bakker *et al.* (1994) but their shape was more inward declined. The angular dependence of the vortex centres, observed in work of Bakker *et al.* (1994), was confirmed by the present simulations. The presence of a baffle affects the flow in the ST and a secondary flow appeared behind the baffle. An additional vortex was obtained in the top part of the stirred tank also due to the presence of baffles. This additional vortex was not reported in previous numerical works, but was observed experimentally by Mavros *et al.* (1996).

The set of six models was also used to predict the turbulent flow behaviour in the ST, using two turbulent approaches *TA1* and *TA2*. Both approximations were derived from experimental data reported in Chapter 3, but the *TA1* includes pseudo-turbulence. A previous sugestion that the pseudo-turbulence should be subtracted from the boundary conditions in the moving ring approach was confirmed by the present results. The *TA1* boundary conditions resulted in the overprediction of the turbulent flow but significant improvements were achieved using the *TA2* in all aspects studied. The pattern of turbulent flow was very similar for the entire set of models in the bulk of the ST, but imposed boundary conditions for the impeller played a very important role near the impeller. Analysis of figures showing the kinetic energy and the rate of kinetic energy dissipation concluded the existence of some discrepancies between the *TA2* results and experimental data found in the literature. The definition of a constant kinetic energy at the UPS, LOS entities was found to improve the predictions of the turbulent quantities studied. This specification is usually omitted in the ST predictions but this boundary condition can eventually overcome the wrong estimates of the energy distribution. The magnitudes of the kinetic energy, from the *TA2* approach, compare reasonably with the investigation of Wu and Patterson (1989).

The shear stresses produced by the impeller depend on the design of the blades and have impact, for example, on the resistance of cells of mixed biological materials, as well as on the coalescence and dispersion in the gas-fluid mixtures. CFD predictability of the shear Reynolds stress showed a good agreement with experimental data. This is a very important observation but it should be emphasised here that the contribution of pseudo-turbulence was not predicted by the steady-state models.

To summarise, the adjusted model 1 with the *TA2* turbulence specifications gives very good agreement with experimental data in the regions far away from the impeller. Likewise, reasonable predictions are provided for the overall flow characteristics of the ST such as the Power number and the Flow number.

5.3 Dynamic Model Predictions

The unsteady-dynamic predictions of the baffled ST agitated by the Rushton impeller are reported here. Two models with different boundary conditions were solved using the moving boundary constraint capability, included in FIDAP 7.6 that can resolve the time dependent interactions between the impeller and the baffles. The flow hydrodynamics was computed using the anisotropic model of turbulence proposed by Speziale (1987) and described in the first part of this chapter.

This section is organised into five subsections. The objectives of this study are given in Section 5.3.1 and a general description of the dynamic models used is given in Section 5.3.2. More detailed information on the entities of dynamic models is reported in Section 5.3.3, simultaneously with the list of boundary conditions applied on these entities. The results of numerical simulations in Section 5.3.4 are validated using the same criteria as those for the steady-state predictions. Finally, the last Section 5.3.5 provides a summary of conclusions obtained from dynamic predictions.

5.3.1 Objective of this work

Two new approaches to solve the hydrodynamics of the ST are presented here as two additional models, model 7 and model 8. They are derived and tested to predict the flow field of the stirred tank for $Re = 5000$.

The results of dynamic simulations are validated in accordance with the criteria used in the previous steady-state predictions. Thus, the field patterns of liquid velocity, kinetic energy, and the energy dissipated distribution into the three main ST's regions are presented. These results are used for quantifying the Flow and Power numbers, which represent important overall characteristics of the stirred tank. Special attention is drawn on the predictability of the shear Reynolds stresses, $\overline{\tau}^{t}_{xy}$, that are compared with data measured by LDV.

Differences between the results of the dynamic and those of the steady-state simulation are addressed focusing on the advantages and disadvantages of each case.

5.3.2 Dynamic model description

Time dependent simulations of the Rushton impeller in the ST were performed using the sliding-mesh approach. The characteristics of the impeller and the dimensions of the tank were presented in Figures 3.1 and 3.2. As in the steady-state simulations, only the $\pi/2$ segment was used for the present predictions, since this allows substantial savings in computational time. The working fluid was water that filled the tank to the height H at room temperature.

The three-dimensional problem was defined as time-dependent, isothermal and for a Newtonian liquid. The impeller region that belongs to the moving grid consists of regular elements (equally spaced in the axial, radial and tangential directions). The grid elements in the reminder of the computational domain were created automatically using the automatic mesh generator (FI-GEN based on the paving/plastering algorithm) and with various sizes and shapes to accommodate for the presence of the baffle. A total number of 18070 nodal points with 20466 linear order surface elements (eight node bricks, with tri-linear velocity and discontinuous constant pressure approximations) was used in the present simulations. The equations of momentum containing the transient terms were solved using the implicit backward Euler scheme for time integration. Fixed time increments were used corresponding to single jumps of the blades on successive elements in the impeller region.

The segregated solver was chosen for the solution of the non-linear system of equations due to the large number of independent variables (three-velocity components, pressure, kinetic energy and energy dissipation). The main advantages of the segregated solver are the faster computation of systems of equations and the smaller disk storage requirements. The symmetric system of linear equations was solved using the conjugate residual method (CR) with a maximum of 500 iterations. The non-symmetric system was solved using the generalised minimal residual method (GMRES) with a maximum of 1500 iterations. The simulations required 16MB of the core memory for each independent variable and the computational time was of the order of 200 hours in an IBM RS6000 machine, model 3CT.

The convergence criterion DTOL = 0.001 was adjusted for each variable at the end of each time increment. Discontinuous approximation of the pressure was turned on for all elements of the computational domain and the conservation of mass was verified at each time step after reaching the convergence criteria (PUPDATE option in FIDAP 7.6).

Time dependent simulations started with fluid at rest and continued until the moment when the velocity patterns of the ST were established and appeared as flow fields exhibiting periodic behaviour. The number of revolutions of the impeller to achieve the flow periodicity in the ST depends on the grid density and on the impeller Reynolds number predicted. The number of time steps necessary to resolve a simple single revolution was $N_{ts} = 48$.

5.3.3 List of entities and boundary conditions in the dynamic models

Two models were specified to predict the hydrodynamics of turbulent flow in the ST. Model 7 consists from boundary conditions of the velocity that arise from the nature of the blade motion. Hence, only the tangential velocity component was defined along the blade as a function of radius while the radial and axial components were assumed negligible. The centrifugal effect at the tip of the blades was included explicitly in the model 8. Different

boundary conditions for dynamic models 7 and 8 were accomplished within the MBC — Moving Boundary Constraint — entity as described later.

Boundary conditions applied for dynamic models are reported in the following text that is categorised by these entities

- *impeller shaft;*
- *impeller disk;*
- *impeller blades — MBC;*
- *stirred tank bottom;*
- *stirred tank wall;*
- *liquid surface;*
- *reference and periodic entities.*

In addition, at the end of this section is given a table listing all boundary conditions.

- ***The shaft, SH***

This rotating entity enters the tank from the top and is identical to the axial axis of the cylindrical co-ordinate system. The entity is modelled in the same way as discussed in Section 5.2. This means that only the component of tangential velocity is non-zero and uniform along the shaft.

- ***The impeller disk, DI***

Boundary conditions for this entity coincide with those applied in the steady-state simulation (see Section 5.2) and only the tangential velocity is non-zero, being a function of the radius and of the rotational speed of the impeller.

- ***The impeller blades, MBC***

The impeller blades were modelled as thin (one element thick) 3D entities equally separated in the disk by a $2\pi/6$ angle. Thus, only two blades belong to the present computational domain in a single time step. Boundary conditions are time dependent and defined using the moving body constraint—MBC subroutine. A FORTRAN subroutine was developed that simulates the rotational motion of the blades and the temporal change of node locations where the boundary conditions are prescribed. The conditions set for the MBC entity originate the two different models: model 7 and model 8.

In model 7, only the tangential velocity was defined at the blades of the impeller and its magnitude depended on the radius as illustrated in Figure 5.26a. The radial and axial velocities at the blades were defined as zero. Definition of the turbulence parameters, in model 7, is based on the LDV experiments from this study and Wu and Patterson (1989). At the tip of the impeller blade a double peak profile of the random turbulent kinetic energy was imposed, and it was assumed that the contribution of pseudo-turbulence to the total turbulent kinetic energy will be generated by the impeller motion. At the top and bottom of the

horizontal edges of the blades, constant random kinetic energy was specified according to data found in the LDV study. In this way, the k,ε values at the blades corresponded to the *TA2* approximation used in the steady-state models (see Figure 5.8a in Section 5.2). Figure 5.26c represents the specification of the turbulent kinetic energy in model 7. The rate of the energy dissipation was specified in the same way as in the *TA2* approach of the steady-state models (see Figure 5.8c). This implies that the macro-length scale has a parabolic profile at the blade tip and according to the results of Wu and Patterson (1989).

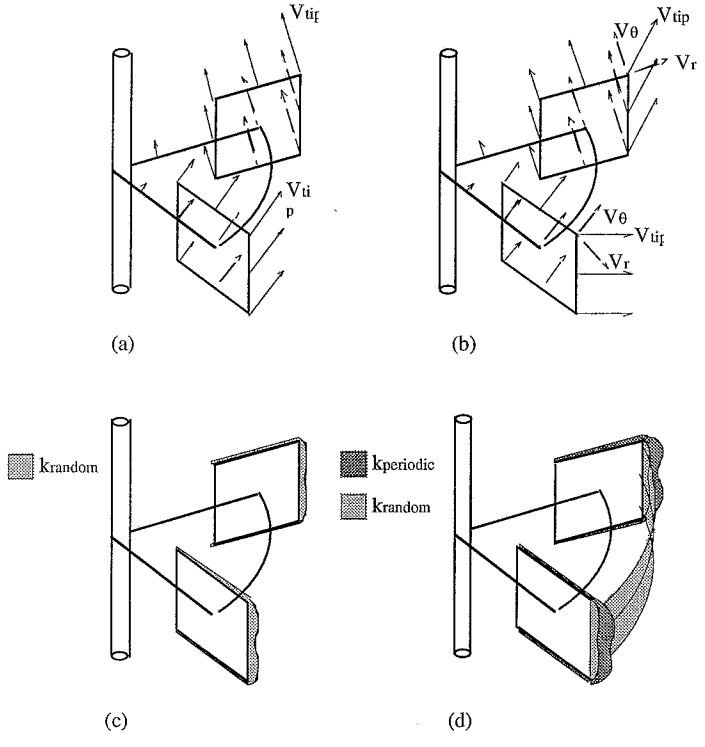

Figure 5.26 Sschematic representation of boundary conditions for dynamic simulations presented in terms of the velocity vectors (a, b) and the turbulent kinetic energy (c, d) for model 7(a, c) and model 8 (b, d).

In model 8, the tangential velocity was defined as that in model 7. However, in this case, the boundary condition for the radial velocity was not set to zero at the blade tip and its magnitude was equal to the magnitude of the tangential velocity, as illustrated in Figure 5.26b. This is a singular condition, in order to account for the tangential discontinuity of the radial velocity at the interface of the tip of the blade and liquid. The boundary conditions for modelling the turbulent flow were approached in a novel strategy. The random kinetic energy was defined not only at the blade tip but at the entire curved-surface drawn by the tip of the blade (identical to the OUT surface of the moving ring approach in steady-state simulations) and the contribution of pseudo-turbulence was superimposed to the random value only at the tip of blades (see Figure 5.26d). Thus, the total turbulent kinetic energy was defined at the tip of the impeller blade, as shown in Figure 5.26d, and the random kinetic energy at the curved-

surface drawn by the tip of the blade. The rate of the energy dissipation was specified as in model 7.

- ***The stirred tank bottom, BT***

All velocities were set to zero at the tank bottom and because in its vicinity there is a region of high velocity gradients, a denser grid was created in the normal direction to the tank bottom.

- ***The stirred tank wall, WA***

This entity was modelled as a solid surface that includes the baffle located in the middle of $\pi/2$ computational domain. All of the velocity components were constrained to null.

- ***The liquid surface, TO***

This entity was defined as in the steady-state simulations (see section 5.2). Only the axial velocity was set to zero at the liquid surface of the ST. Mass flow was not allowed in direction normal to the liquid surface and the formation of a central air vortex was assumed non-existent.

- ***The reference and periodic entities, REF and PER***

Periodic boundary conditions must be imposed on the surfaces where the flow field is repeated in space as in Section 5.2 for the reference and periodic entities , but now modified for the blade motion. Since the computational domain is the $\pi/2$-segment, and the angle between the two blades of the Rushton impeller is only $2\pi/6$, the part of the REF and PER surfaces swept by the impeller must be excluded from the regions of periodic boundary conditions (see Figure 5.27).

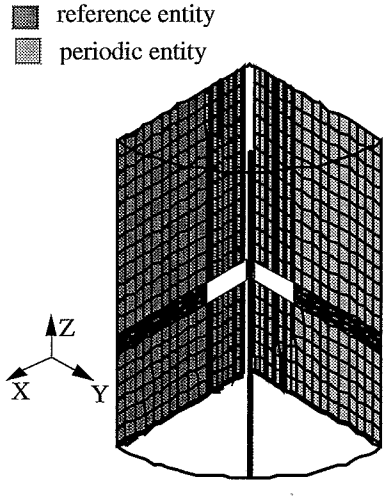

Figure 5.27 Schematic representation s of REF and PER entities.

This is particularly important at the instant of time when one blade matches the reference or periodic entities. None of the blades pass, at the same instant of time, through the other entity. In one of the excluded regions it is imposed the blade motion and in the other is imposed the observed previous condition in time. It was found that this localised discontinuity, has a small effect on the overall flow and vanishes with increased impeller rotational speed. The reference and periodic entities of dynamic models are shown in Figure 5.27. The list of boundary conditions used in the present dynamic models 7 and 8 is given on Table 5.13.

Table 5.13 Boundary conditions for dynamic models of the stirred tank.

entity	V_r	V_θ	V_z	*shear stress*	*normal stress*
SH	*0*	k_1	*0*	$\tau_{rz}=0$	$\tau_{rr}=0$
DI	*0*	$f_1(r)$	*0*	$\tau_{zr}=0$	$\tau_{zz}=0$
MBC	*0 and* V_θ *	$f_1(r)$	*0*	$\tau_{\theta r}=\tau_{\theta z}=0$	$\tau_{\theta\theta}=0$
BT	*0*	*0*	*0*	$\tau_{zr}=\tau_{z\theta}=0$	$\tau_{zz}=0$
WA	*0*	*0*	*0*	$\tau_{zr}=\tau_{r\theta}=0$	$\tau_{rr}=0$
TO	*free*	*free*	*0*	$\tau_{zr}=\tau_{z\theta}=0$	$\tau_{zz}=0$

* the zero condition is valid for model 7 and in model 8 $V_\theta = V_r$ at the impeller radius; $k_1 = \omega R; f_1(r) = \omega r$.

5.3.4 Results

Numerical predictions from both dynamic models of the stirred tank are presented next, following the same strategy as introduced in the first part of this Chapter. The results are subdivided on six subsections:

- *Time evolution of velocity patterns;*
- *Velocity patterns;*
- *Flow number;*
- *Turbulent kinetic energy and the rate of the kinetic energy dissipation;*
- *Power number;*
- *Shear Reynolds stress predictability.*

These predictions are compared with experimental data and with steady-state predictions of the previous chapter. All maps and vector plots will be presented as time averaged results obtained from the last half of impeller revolution simulated.

5.3.4.1 Time evolution of velocity patterns

The dynamic simulations of the Rushton impelled ST started at time zero when the fluid was at rest. Then, the blades started to move and set the fluid into motion, first near the impeller. The energy introduced to the fluid through the impeller accumulated with time and forced the liquid to move through the entire bulk of the tank. Tangential and radial flows dominated in the earliest stages of simulation but the axial flow increased with time to the point when the two vertical vortices were totally established in the ST. The simulation continued until a pseudo steady-state was attained at 16 differently positioned checkpoints. The checkpoints were selected at different horizontal planes of the ST and at radial co-ordinates slightly higher than the impeller radius, at locations near the baffle and in regions near the wall. This set of checkpoints was assumed to give the appropriate information on the flow periodicity.

The diagrams of calculated speed from the three velocity components are shown in Figure 5.28 for some checkpoints along the time normalised by the period of the impeller revolution. The value of the speed is normalised by V_{tip} and as can be seen, the periodic flow patterns at the impeller centre plane were established after a few seconds (see check points P_1 and P_2). The influence of the passages of the blades is evident from the histogram of point P_1 in Figure 5.28. The fluid flow below the impeller enters a periodic state after approximately five impeller revolutions (see P_7 and P_8 check points). More revolutions of the impeller were necessary to drive the flow in the top part of the tank to the quasi-periodic state (checkpoints P_3, P_4, P_5 and P_6). The small perturbations plotted at check points P_5 and P_7 are due to the periodic flow nature and an extent of the flow periodicity can be studied in this way. Approximately 12 to 13 impeller revolutions were necessary to obtain the quasi-periodic flow field in the ST.

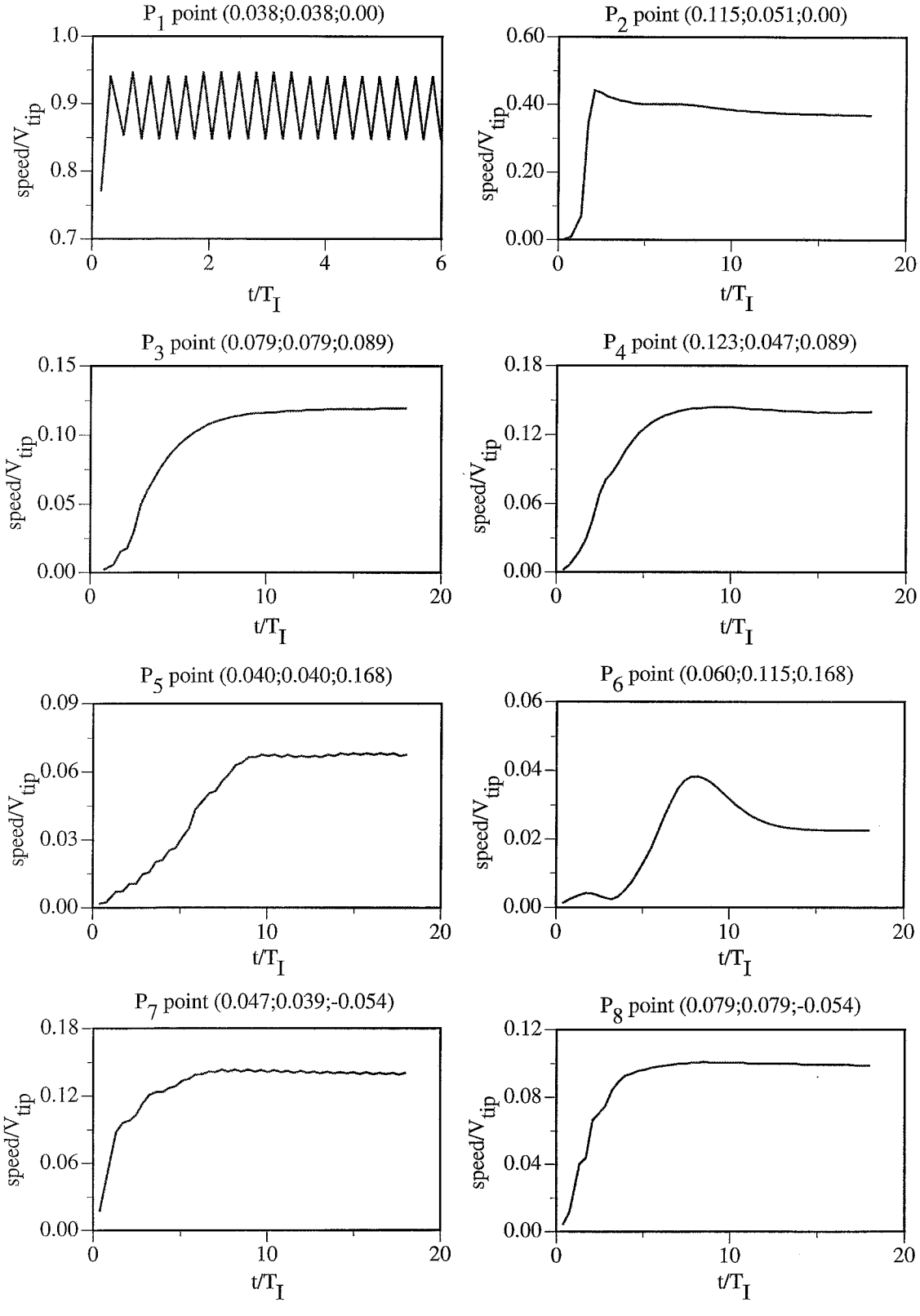

Figure 5.28 *Histograms of the normalised speed obtained from simulation of the dynamic model 7at various ST positions (referred to the Cartesian co-ordinate system).*

5.3.4.2 Velocity patterns

Interpolated maps of the speed are overlaid by the vector plots of the velocity in Figure 5.29 for the dynamic models 7 and 8. The results are shown at the two vertical planes, corresponding to the angular co-ordinates $\theta = \pi/4$ (plane passing through the baffle) and $\theta = 3\pi/8$ (behind the baffle in direction of the impeller rotation). Since dynamic simulations were performed, the results from the last half of impeller revolution solved were spatially averaged in order to plot the velocity maps in Figure 5.29a-f. Figure 5.29a,b,d,e shows the velocity vector plots and the existence of two vertical vortices can be observed. The radial flow generated by the impeller pumps the fluid towards the wall where is redirected to the axial direction. The vortex centres are located as those in the results of steady-state simulations and a good agreement of the flow pattern is obtained. The top vortex is also disrupted behind the baffle as observed in the steady-state predictions. The vortex centre depends on the tangential co-ordinate, θ, as was reported by Bakker (1994).

Figure 5.29c,f shows the speed map overlaid by the radial-tangential projections of the velocity vector at the impeller centre plane. The results are also averaged from the last half of impeller revolution solved in order to make a comparison with the steady-state predictions. The highest velocities are observed at the impeller radius as expected. The vector plots in Figure 5.29c,f illustrate that model 8 predicts the flow directed more into the radial direction than that of the model 7, where the tangential flow dominates. Model 1 (adjusted) presents the results from the steady-state simulations. A detailed comparison of the results from dynamic models is given in Figure 5.30 at the three radial positions at the impeller centre plane. The comparison with experimental data shows that model 8 predicts higher radial velocities than model 7, because of the radial velocity included in the boundary conditions of model 8. The predicted components of the radial and the tangential velocity are closer to experimental data near the impeller, but both models over-predict data obtained by LDV measurements in the regions far away from the impeller

The baffle region is illustrated in Figure 5.31. As can be seen, the vortex behind the baffle is predicted very well qualitatively by both dynamic models. However, model 7 and model 8 overestimated the magnitudes of velocity vectors found experimentally.

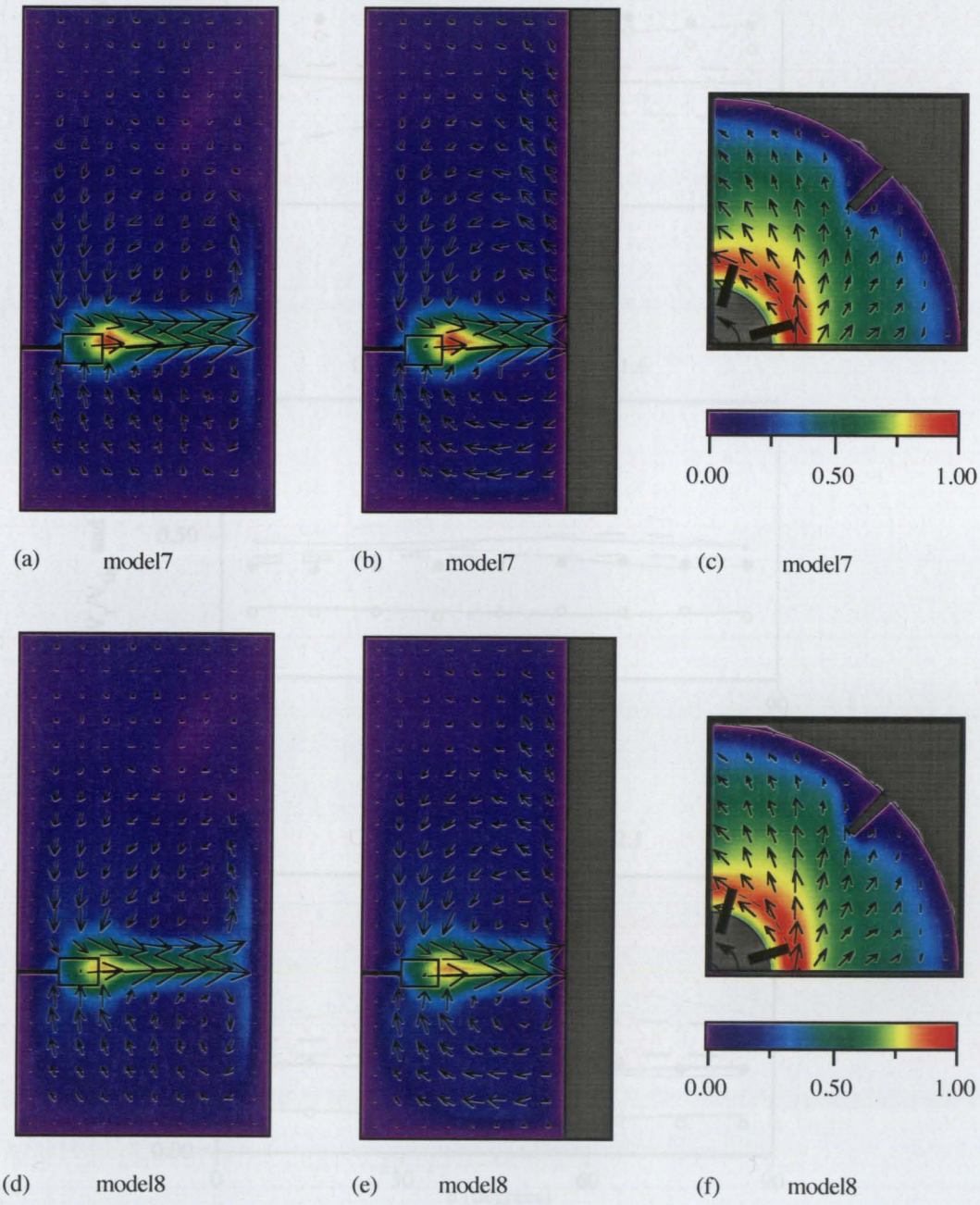

Figure 5.29 *Normalised speed maps overlaid with the projections of the velocity vector from dynamic simulations using the models 7 and 8 at the tangential co-ordinates $\theta=\pi/4$ (a, d); $\theta=\pi/2$ (b, e); and at the impeller centre plane (c, f).*

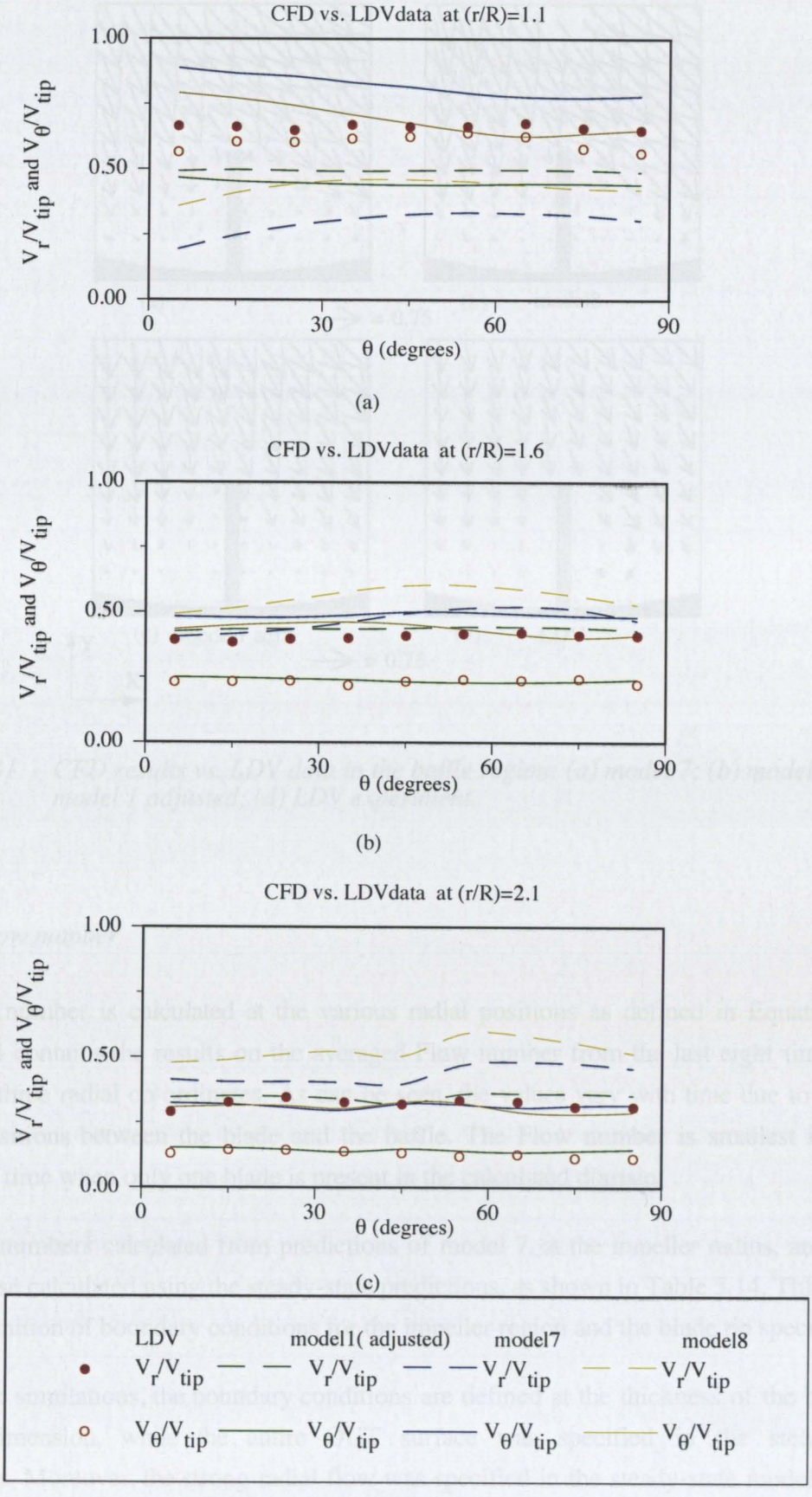

Figure 5.30 Comparison of the results at three radii of the impeller centre plane.

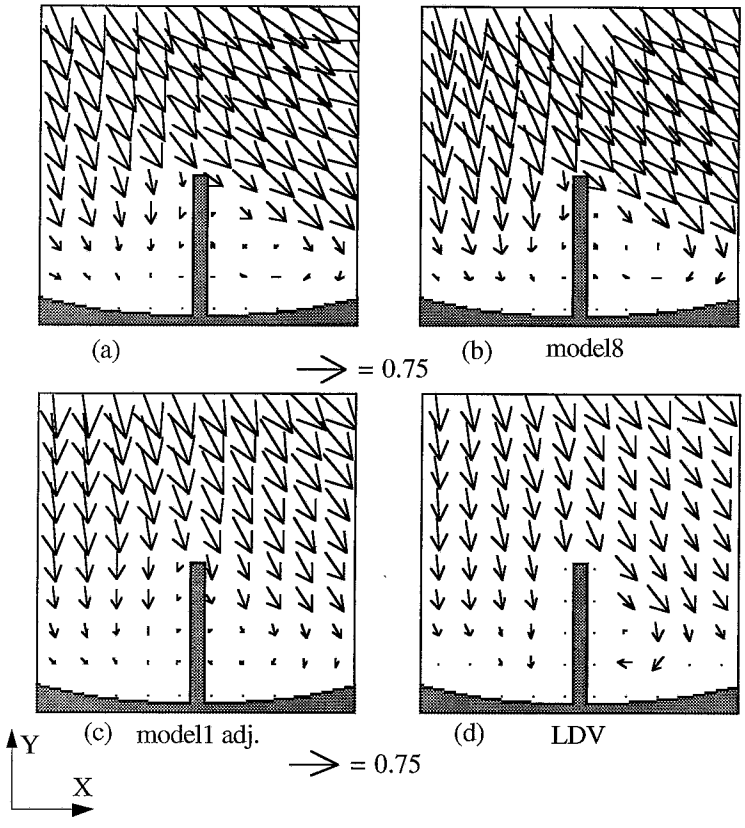

Figure 5.31 *CFD results vs. LDV data in the baffle region: (a) model 7; (b) model 8; (c) model 1 adjusted; (d) LDV experiment.*

5.3.4.3 Flow number

The Flow number is calculated at the various radial positions as defined in Equation 5.6. Table 5.14 contains the results on the averaged Flow number from the last eight time steps and at the three radial co-ordinates. As can be seen, the values vary with time due to various relative positions between the blade and the baffle. The Flow number is smallest in those instants of time when only one blade is present in the calculated domain.

The Flow numbers calculated from predictions of model 7, at the impeller radius, are nearly half of those calculated using the steady-state predictions, as shown in Table 5.14. This fact is due to definition of boundary conditions for the impeller region and the blade tip specifically.

In dynamic simulations, the boundary conditions are defined at the thickness of the blade, in angular dimension, while the entire OUT surface was specified in the steady-state simulations. Moreover, the strong radial flow was specified in the steady-state models in the contrary with dynamic simulations.

Table 5.14 Flow number calculated from dynamic prediction of the stirred tank.

	$Q_r \times 10^4$			$Fl = \frac{Q_r}{8NR^3}$		
Time (s)	$r/R = 1.0$	$r/R = 1.5$	$r/R = 2.0$	$r/R = 1.0$	$r/R = 1.5$	$r/R = 2.0$
36.02	3.04	8.66	12.51	0.55	1.57	2.28
36.06	2.99	8.71	12.52	0.54	1.58	2.28
36.10	2.95	8.71	12.51	0.54	1.58	2.28
36.14	2.81	8.66	12.40	0.51	1.58	2.27
36.18	2.74	8.60	12.46	0.50	1.56	2.26
36.22	2.66	8.56	12.45	0.48	1.56	2.26
36.26	2.90	8.59	12.47	0.53	1.56	2.27
36.30	2.93	8.63	12.49	0.53	1.57	2.27
36.34	3.04	8.66	12.51	0.55	1.57	2.28
average				**0.52**	**1.57**	**2.27**

The integration limit in the axial direction is at the edges of the impeller blade for positions at the $r/R = 1.0$ and for radii $r/R = 1.5$ and $r/R = 2.0$ extends to the location where the V_r velocity is still in direction of the discharge flow.

The comparison of the Flow numbers predicted by dynamic models 7 and 8, steady-state model and experimental data is shown in Figure 5.32. Model 7 under-predicts the Flow number near the impeller region and the result at $r/R < 1.5$ is qualitatively close to data of Stoots and Calabrese (1995). Better agreement with data of Gunkel and Weber (1975) and Wu and Patterson (1989) is obtained at $r/R > 1.5$. The results on the Flow number from model 1 over-predict data of the dynamic model due to specified boundary conditions. Model 8 gives reasonable predictions near the impeller but highly overestimates the radial jet flow in the regions away from the impeller.

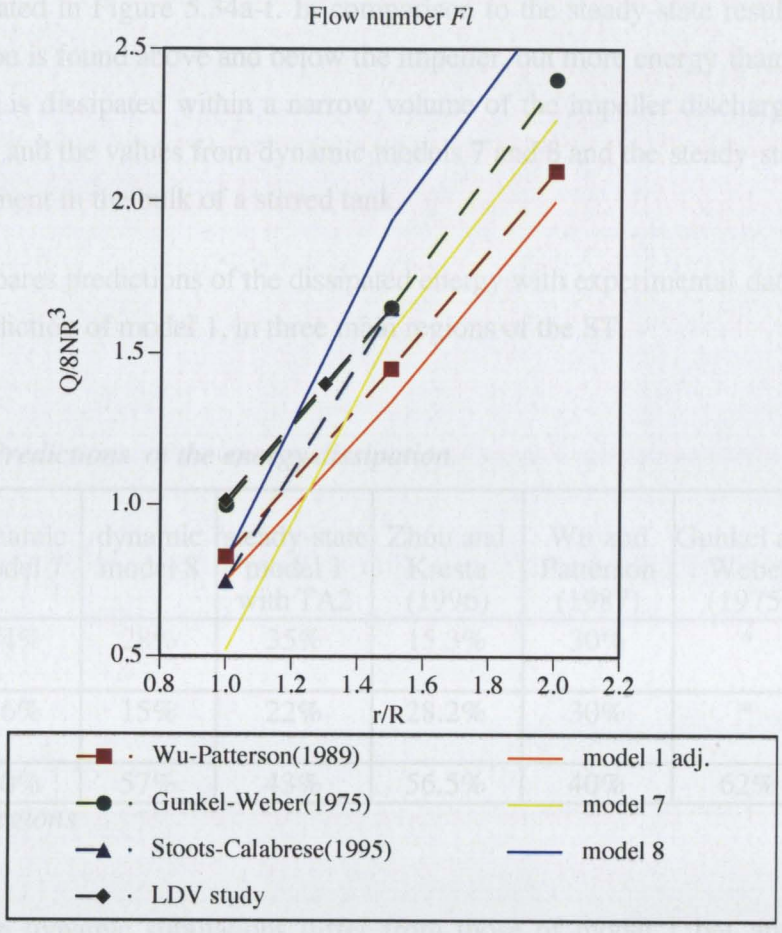

Figure 5.32 Flow number as a function of the radius - predictions versus experimental data.

5.3.4.4 Turbulent kinetic energy and the rate of kinetic energy dissipation

Figure 5.33a,b,d,e shows interpolated maps of the kinetic energy overlaid by the contour maps from models 7 and 8 at the two angles: $\theta = \pi/4$ and $\theta = 3\pi/8$, respectively. Most of the kinetic energy is contained within the impeller region and the discharge flow. An increase in the kinetic energy is observed near the wall due to the sudden change of flow direction, but the smaller energetic content is found in the bulk of the ST. The k values predicted by dynamic models are smaller in the magnitude near the impeller than those obtained from the steady-state predictions. Very good agreement in the bulk of the ST and in the discharge flow region can be concluded. Model 8 in comparison to model 7 produced higher level of turbulence due to the boundary conditions. The maps of the turbulent kinetic energy agree qualitatively very well but differ in the magnitudes. The contour maps predicted by model 7 and 8 are given in Figure 5.33c,f at the impeller centre plane. Quantitative differences between the two are evident and the ST content is mixed by a more violent flow in the case of model 8.

Figure 5.34 shows the rate of kinetic energy dissipation, ε, normalised by the averaged value in the ST. Most of the energy is dissipated in the impeller vicinity, along the wall and the

baffle, as illustrated in Figure 5.34a-f. In comparison to the steady-state results, a region of higher dissipation is found above and below the impeller, but more energy than in the steady-state predictions is dissipated within a narrow volume of the impeller discharge flow region. The magnitudes and the values from dynamic models 7 and 8 and the steady-state models are in a good agreement in the bulk of a stirred tank.

Table 5.15 compares predictions of the dissipated energy with experimental data and with the steady-state prediction of model 1, in three main regions of the ST.

Table 5.15 Predictions of the energy dissipation.

	dynamic model 7	dynamic model 8	steady-state model 1 with TA2	Zhou and Kresta (1996)	Wu and Patterson (1987)	Gunkel and Weber (1975)	Cutter (1966)
impeller region	24%	28%	35%	15.3%	30%	*	20-25%
discharge flow	16%	15%	22%	28.2%	30%	*	35-50%
tank bulk	60%	57%	43%	56.5%	40%	62%	25-40%

** 38% in both regions*

The results from dynamic simulations differ from those of model 1 but are close to the experimental data of Gunkel and Weber (1975) in terms of the dissipation in the bulk of the tank. It is difficult to draw any conclusions from the estimates of the energy dissipated in the impeller region and the discharge flow region because the values found in the literature also vary noticeably.

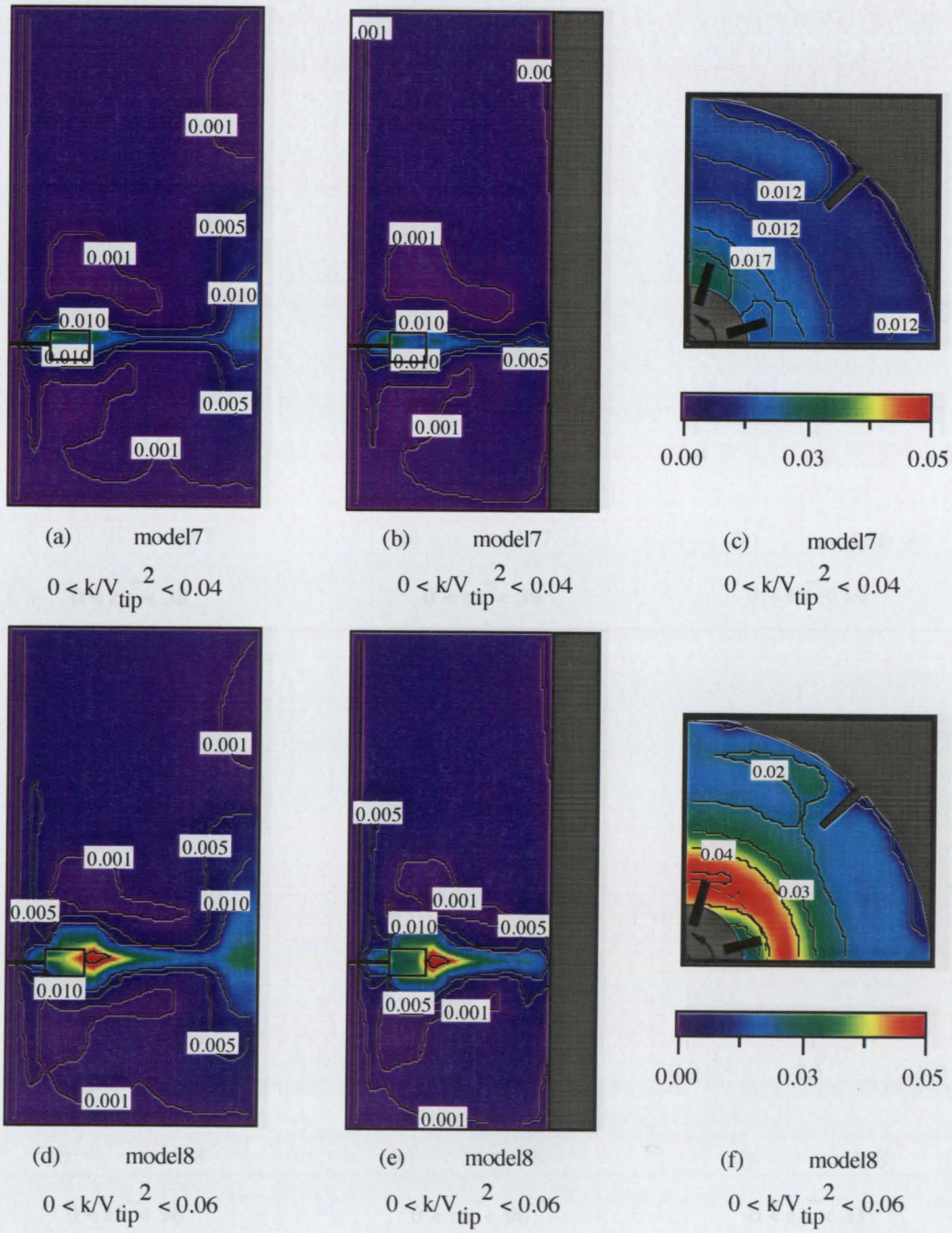

(a) model7 $0 < k/V_{tip}^2 < 0.04$

(b) model7 $0 < k/V_{tip}^2 < 0.04$

(c) model7 $0 < k/V_{tip}^2 < 0.04$

(d) model8 $0 < k/V_{tip}^2 < 0.06$

(e) model8 $0 < k/V_{tip}^2 < 0.06$

(f) model8 $0 < k/V_{tip}^2 < 0.06$

Figure 5.33 *Normalised turbulent kinetic energy maps and contour plots from dynamic simulations using the models 7 and 8 at the tangential co-ordinates $\theta=\pi/4$ (a, d); $\theta=\pi/2$ (b, e); and at the impeller centre plane (c, f).*

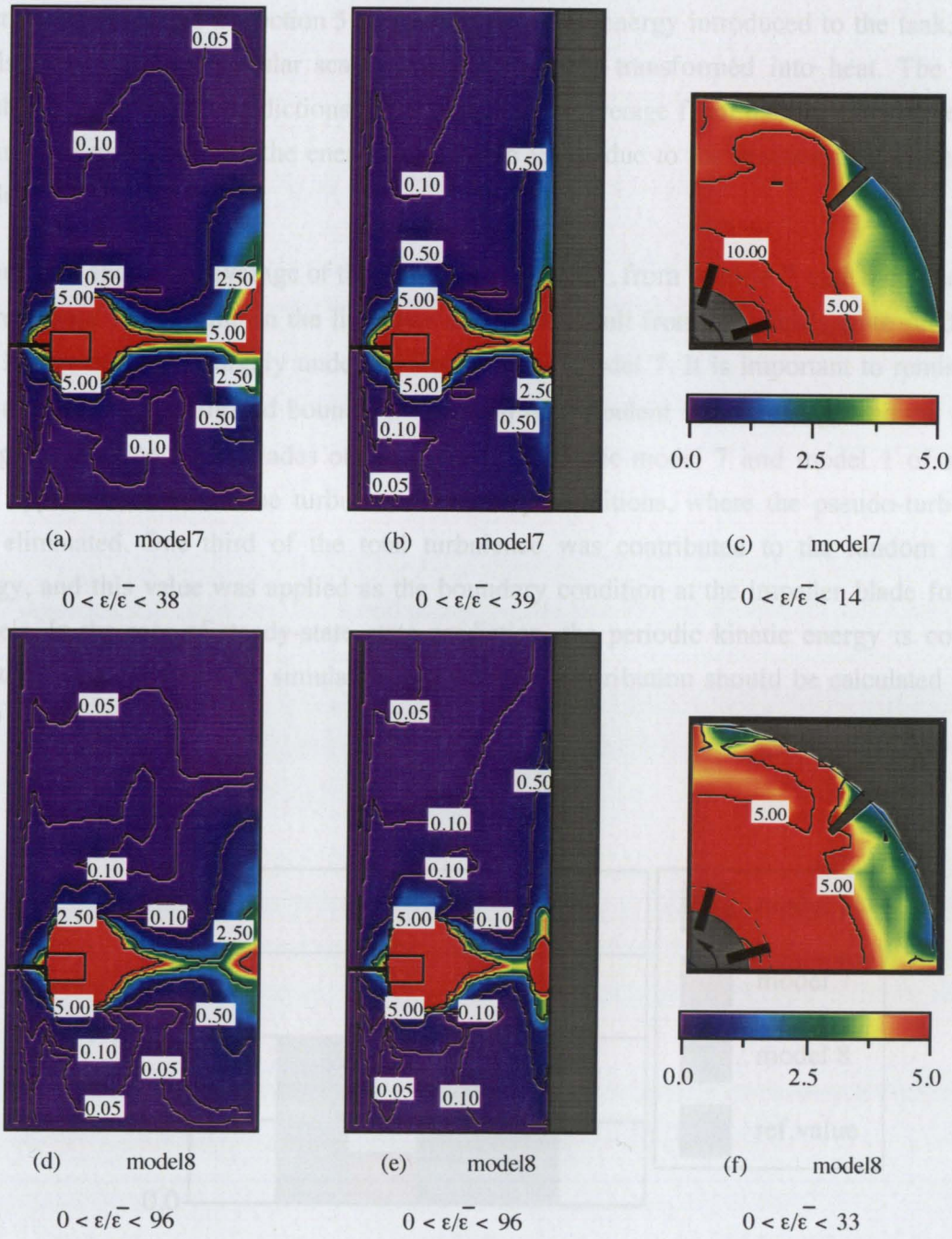

(a) model7 $0 < \varepsilon/\bar{\varepsilon} < 38$

(b) model7 $0 < \varepsilon/\bar{\varepsilon} < 39$

(c) model7 $0 < \varepsilon/\bar{\varepsilon} < 14$

(d) model8 $0 < \varepsilon/\bar{\varepsilon} < 96$

(e) model8 $0 < \varepsilon/\bar{\varepsilon} < 96$

(f) model8 $0 < \varepsilon/\bar{\varepsilon} < 33$

Figure 5.34 *Normalised dissipation energy maps and contour plots from dynamic simulations using the models 7 and 8 at the tangential co-ordinates $\theta=\pi/4$ (a, d); $\theta=\pi/2$ (b, e); and at the impeller centre plane (c, f).*

5.3.4.5 Power number

The Power number is another overall characteristic used to specify the ST in industrial practice. As explained in Section 5.2, it is related to the energy introduced to the tank, which is dissipated at the molecular scales and consequently transformed into heat. The Power number from dynamic predictions is calculated as an average from the last eight time steps because the mean value of the energy dissipation varies due to the position of a blade to the baffle.

Figure 5.35 shows the average of the Power number, N_P, from models 7 and 8 compared to the reference value found in the literature and to the result from the steady-state prediction. The Power number is highly under-predicted by the model 7. It is important to remind that N_P depends on the implied boundary condition for turbulent kinetic energy and the rate of energy dissipation at the blades of the impeller. Dynamic model 7 and model 1 of steady-state approach use the same turbulence boundary conditions, where the pseudo-turbulence was eliminated. One third of the total turbulence was contributed to the random kinetic energy, and this value was applied as the boundary condition at the impeller blade for both models. In the case of steady-state state prediction, the periodic kinetic energy is correctly omitted, but in the dynamic simulation, the periodic contribution should be calculated by the CFD code.

Figure 5.35 The numerical predictions of the Power number and the reference value from Bates et al. (1963).

The results from model 7 show, however, that N_P is roughly three times less than the expected value. This fact supports the idea that CFD modelling is not able to generate the pseudo-turbulence. Therefore, the total kinetic energy including the periodic and random contributions should be prescribed as the boundary condition at the moving blades, as was done in model 8. Model 8 produced better results but some discrepancies still exist.

5.3.4.6 *Predictability of Shear Reynolds stress*

The shear Reynolds stress, $\overline{\tau}^{t}_{xy}$, was introduced in the Section 5.2 and in the Chapter 3. Figure 5.36 shows the comparison of the shear Reynolds stress, $-\overline{uv}/V_{tip}^{2}$ with measured data. The predicted values are in a good agreement with experiments near the impeller but with increasing distance from the impeller, the results of dynamic model 7 under-predicted the experimental data. Very similar trend was observed by Ahlstedt (1996) for the normal components of the Reynolds stress tensor. Model 8 gave qualitatively similar results as model 7. The quantitative aspect is very close to the results of steady-state predictions and a good indication of the trend near the baffle is shown in Figure 5.36c. Data in Figure 5.36a contains only the random contribution to the shear Reynolds stress. Noteworthy is the fact that the magnitude of studied quantity predicted by model 7 is of the same order as that of the experimental data. Model 8 exhibited a stronger periodicity due to different boundary conditions but these results are not shown in Figure 5.36a since no elimination of the pseudo-turbulence was performed.

The contour maps of shear stress studied using models 7 and 8 are compared with LDV data and with the results from steady-state model 1 in Figure 5.37. The results are presented at the impeller centre plane that was found as the most important region by the present experimental study. LDV data, however, contains also a contribution from pseudo-turbulence that is not predicted by numerical studies.

An extent of this periodic component could be quantified by subtraction of the numerical data from experimental data. Model 8 predictions approximated to the image obtained by steady-state predictions qualitatively better than model 7. The quantitative information from these contours maps can be somehow distorted due to an interpolation of the results at the examined surface plane.

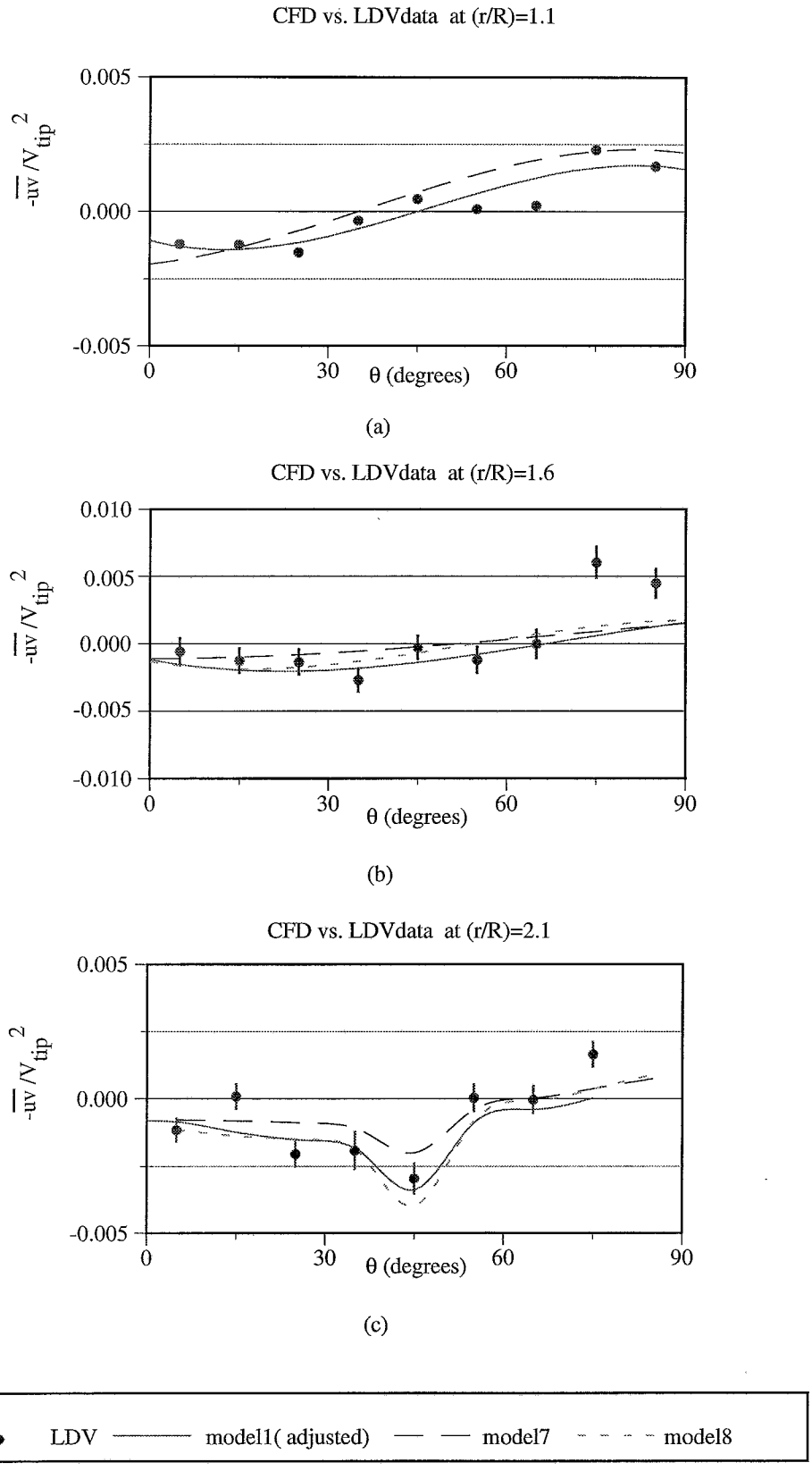

Figure 5.36 Comparison of dynamic models prediction of the shear Reynolds stress with LDV data at various radii of the impeller centre plane (z=0) and at Re=5000.

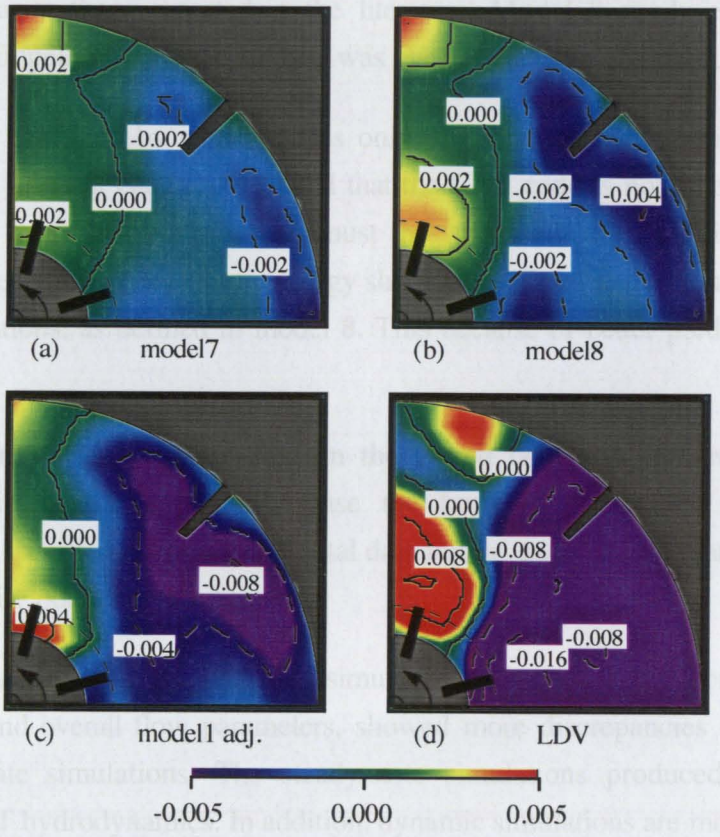

Figure 5.37 Contour maps of the shear Reynolds stress at the impeller centre plane: (a) model 7; (b) model 8; (c) model 1adjusted; (d) LDV data.

5.3.5 Conclusions from dynamic predictions of ST

Dynamic simulation of the ST was performed under turbulent conditions using the anisotropic turbulence model of Speziale (1978). The motion of the impeller blades was simulated using the sliding-mesh technique. The periodic flow nature was observed on a set of checkpoints and the time necessary to achieve the quasi-periodic state was determined as 12-13 impeller revolutions.

Predicted flow patterns were qualitatively very close to those obtained experimentally and to those from the steady-state simulation. The flow predicted by model 7 was dominated mainly by the tangential flow due to boundary condition specified at the impeller blades. Better modelling results were obtained using the boundary conditions of model 8.

The formation of an additional vortex behind the baffle, reported in the steady-state model, was confirmed by the dynamic predictions. The results from models 7 and 8 near the baffle agree qualitatively well with experimental data but the velocity magnitude was over-predicted as compared to data obtained using LDV technique.

The overall flow parameters were calculated and a very small Flow number was found near the impeller in the predictions using model 7. The results far away from the impeller were

quantitatively similar to those reported in the literature. Model 8 produced a quite good prediction near the impeller but the radial flow was overestimated at higher radial distances.

The Power number predicted by model 7 was only one third of the experimental value of Bates *et al.* (1963). Thus, it can be concluded that the CFD code is not able to generate the pseudo-turbulence, and this contribution must be specified as a particular boundary condition. Consequently, the total kinetic energy should be defined as the boundary condition for dynamic simulations, as defined in model 8. This because of better predictions obtained using model 8.

Dynamic simulations of the turbulent flow in the stirred tank are still dependent on the recourse to experimental data. This because the boundary conditions for turbulence parameters must be specified using experimental data but no experimental data are necessary to specify the velocity boundary conditions.

The analysis of the results from dynamic simulations, based on the comparisons with experimental data and overall flow parameters, showed more discrepancies than the results from the steady-state simulations. The steady-state simulations produced more realistic predictions of the ST hydrodynamics. In addition, dynamic simulations are more expensive in terms of the computational time and disk storage and therefore, the steady-state simulations are preferable for practical computations of mixing in the stirred tanks.

6. Mixing and Chemical Reactions

6.1 Introduction

Knowledge of the flow field is of essential importance for the understanding and numerical simulations of the processes that occur in mixing devices. Hydrodynamics of the stirred tank was studied in previous chapters, and the information obtained can be taken as the first and necessary step towards the next goal — to resolve the applications where a mixing is coupled with the transport of chemical species with/without chemical reactions. These applications occur in many processes of the chemical industry and are still subject to study due to its complexity.

The eventual optimisation of performance of the stirred tank reactor — STR, depends upon the ability to predict the conversion, distribution of species, and the reaction selectivity, because they can be affected by the mixing efficiency. According to Villermaux and Falk (1996), most of the effort in this area has been concerned with the mixing of only miscible fluids and with a use of simple reaction schemes that involved one or two chemical reactions. Industrial needs are more demanding and address complex situations involving viscous and non-Newtonian liquids, multiphase media dispersions, and the cases of mixing where a large spectrum of species and reactions is involved simultaneously. Nevertheless, the applications of mixing with non-reactive tracer or simple reaction schemes must be first accomplished in order to proceed with more complicated and realistic problems.

This Chapter introduces and describes some methods used in the modelling of reactive flows in the liquid-phase under laminar and turbulent regime. The main objective is to provide the necessary information for future simulations of mixing with chemical reactions. The

capabilities and perspectives of CFD to simulate the standard stirred tank reactor, is illustrated with the results from the numerical simulation of a non-reactive tracer and its transport in the STR. The effects of flow regime and the importance of tracer injector position on the tracer transport are discussed.

The main body of this chapter is meant to be introductory to the problems of mixing with chemical reactions and is organised into six sections. The subject of mixing with chemical reactions is introduced in Section 6.2 where the possible problems to be faced in numerical simulations are also outlined. The methods used for numerical predictions of laminar mixing with chemical reactions are given in Section6.3. The Section 6.4 is dedicated to computational methods for turbulent reactive flows. The existing CFD tool is employed for predictions of a neutral tracer in the STR in Section 6.5. The conclusions and major findings are reported in the last section.

6.2 Coupling of mixing and chemical reaction

The goal of mixing is to implement homogeneous fields of any specific variable (concentration or temperature) in the reactor. This is particularly important in systems involving more than one species and multiple chemical reactions. In such cases, the selectivity of reactions can be maximised and consequently the by-product minimised from the side reactions. In order to control such mixing process, it is necessary to understand how the reactants contact and to have a clear picture of the physics that occur before and during the reaction.

Chemical reactions start on a molecular level and this fact implies a great difficulty for numerical simulations of a STR. There are two extreme cases of what can happen before a chemical reaction takes place. In the fist case, the reactants are premixed (at the molecular scale) before the initialisation of a reaction and then a *perfectly mixed* reactor can be assumed. If the reactants are introduced into the reactor separately, the matter is more complicated due the convection and diffusion processes that precedes the contact of reactants. This situation is referred as the *non-premixed* chemical reactor. Here, the reactor hydrodynamics can have an influence on the effects at the molecular scale and can determine the *reactor mixidness*. The term mixidness is used to evaluate the reactor performance in term of the overall mixing and it is thought as the opposite of *segregation*. Segregation are the mechanisms that creates the concentration differences in the reactor bulk, and with this concept the mixing quality can be analysed. The intensity of segregation can be viewed as the maximum relative concentration-difference and, for example, the simple introduction of reactants through a feed pipe creates automaticaly initial segregation problems.

Various length and time scales are involved in the mixing process of the standard STR. The reactants fed into the STR are spread through the bulk of the tank mainly by the convective

terms that depends on the macro-mixing. Simultaneously, the effects on the scales smaller than macro-mixing scale proceed and these are very important for the predictions of the yield on a specific reaction product within a complex reaction system (Bakker and Van Akker, 1994). In general, the mixing process can be characterized by the following stages:

- *overall circulation and large-scale convection*, that are characterised by large vortex motions occurring on the scale of reactor and that are responsible for the mixing between regions of different velocities;

- *turbulent diffusion,* that equalises locally the concentration differences on the large-scales and is promoted by the velocity fluctuations under conditions of the turbulent flow;

- *decreasing of fluid elements* and *breaking down of eddies* into smaller parts by acting of the shear and of the elongation forces;

- *viscous-convective mixing*, that depends on the viscosity and which acts at the small scales in order to reduce the thickness of liquid *laminae*,

- *viscous-diffusive mixing* or molecular diffusion, that is effective at the molecular scale and only inside the smallest eddies.

Mixing processes pass through all these stages and therefore the spectrum of reactant concentrations in the reactor can be quite large. The first two mentioned stages account for the macro-mixing that can be easily computed by CFD tools, in the term of *blending times.* The blending time depends on the liquid flow pattern, and it determines how fast the species are uniformly dispersed in the STR. Macro-mixing is also described in terms of residence time distributions.

The last three stages are often reported as the micro-mixing process. Many times it is simply assumed ho have a characteristic time equal to the diffusion time needed to smooth out the concentration differences at the smallest length scales. Standard CFD modelling takes no explicit account on these length scales effects and therefore, it can not be directly applied to solve the micro-mixing problem. Consequently, there is need to develop some additional theories. These theories can be based on main assumptions of local flow conditions, such as the segregation or dissipation of the turbulent kinetic energy. Different and distributed characteristic times of the micro-mixing will be found in the reactor bulk, due to the spatial distribution of the energy dissipation as found in Chapter 5 for the STR.

Macro and micro-mixing can be generically handled as it will be introduced in the next sections. But the *meso-mixing* is another additionally important mechanism of mixing in the STR. Baldyga and Bourne (1992) reported that the meso-mixing occur in the semi-batch and continuously operated STR, where the reactant liquid feeding velocity can strongly interact

with the surrounding velocity field. The meso-mixing is faster than the macro-mixing but slower than the micro-mixing, but the effects of both meso and micro-mixing are generally coupled in the STR.

All mentioned stages of the mixing process should be included in the numerical model of mixing with chemical reaction. This is a rather complicated task because the processes at various stages can interact mutually and they usually occur at the same instant of time. Moreover, each mixing stage may have different impacts on chemical reactions. In these cases, it is advisable to apply the concept of the *rate-limiting step* in order to simplify the mixing process simulation. With this concept, the slowest mixing stage controls the process and becomes the crucial stage for numerical simulation.

The following situations can arise if the characteristic times of the different mixing stages are compared with the characteristic reaction time, t_R

- $t_{micro} << t_R$; the reaction is slow, and the micro-mixing does not have any impact on the product formation, and the reaction chemical kinetics is the rate controlling step;
- $t_{micro} \approx t_R$; the reaction is of the finite rate, both the micro-mixing and the reaction kinetics are equally important and none of the mechanisms can be neglected;
- $t_{micro} >> t_R$; the reaction is practically instantaneous, the reaction rate is determined mainly by the mixing at the smallest length scales (micro-mixing).

The characteristic *reaction time*, t_R, can be estimated as the inverse value of the chemical reaction rate, that depends on chemical reaction order and the reaction conditions.

The macro-mixing influences indirectly the micro-mixing through the rates of the local energy dissipation. Laminar flow conditions are always assumed on the local smallest-scales in many models, as it will reported in the next section. These small-scales are placed into a turbulent surrounding of larger scales in the case of turbulent reactive flows. Current models for turbulent reactive mixing do not describe the interactions between the macro and micro-scale mechanisms. This should be a goal for the future development because such models would account also for the incomplete macro and micro-mixing.

6.3 Computational methods for laminar reactive flows

Laminar mixing was discussed in detail in Chapter 4 and the macro-mixing pattern was presented at various planes of the ST. It was concluded that the Rushton type of impeller is inadequate for mixing under a laminar regime due to a poor overall mixing performance. Thus, the regions in the top parts of the reactor were almost stagnant and a different type of

impellers or the multiple configurations of the Rushton impeller were recommended to enhance the reactor uniformity.

The meso and micro-mixing processes are almost identical in the laminar regime and can be sought as a single process. A physical picture of the micro-mixing is fundamental to determine its mechanism. Two approaches are commonly used for this purpose. The first approach is based on the concept called *striation* while the second approach uses the *description of mass transfer.*

Complex motions in the STR result into deformation of fluid elements and their break up on the smaller parts. These parts are then stretched and deformed by the shear and elongation forces resulting into thinner elements called striations. These striations keep their original identity and travel through the reactor. The average distance between two adjacent layers of a deformed element of liquid is called the *striation thickness.* This space variable can be used with the equation of molecular diffusion as the characteristic path length, and then used for numerical predictions of micro-mixing.

If the concentration difference between the two adjacent layers is reduced by diffusion to 90% (Fourier number, $Fo \cong 0.1$), the time for diffusion within two layers is defined as:

$$Fo = \frac{\mathcal{D}t}{x^2} \Rightarrow t_D \cong 0.1\frac{\lambda_K{}^2}{\mathcal{D}} \tag{6.1}$$

where the t is time; the λ_K is the Kolmogorov micro-scale and the $\mathcal{D}$ is diffusion coefficient. The diffusion time, t_D, is an important parameter related to the micro-mixing time. The striation thickness decreases upon mixing and the local diffusion rate can increase with time. The striation thickness time decay, with a simple model assuming only shear deformation, can be approximated as a function of the average shear rate as:

$$\frac{\delta}{\delta_0} = \left(1+\left(\bar{\varepsilon}_{ij}t\right)^2\right)^{-1/2} \cong \left(\bar{\varepsilon}_{ij}t\right)^{-1} \tag{6.2}$$

where the $\bar{\varepsilon}_{ij}$ is the local averaged shear rate and the δ, δ_0 is striation and initial striation thickness, respectively. The *initial striation thickness*, δ_0, is in fact an initial scale for segregation. The gradual reduction of the striation thickness can in this way, be quantified in term of the averaged shear rate. Applying the last equation into Equation 6.1, and rearranging the diffusion time expressed in terms of the initial thickness, $\delta_0 \approx \lambda_K$, the averaged shear rate, and diffusion coefficient:

$$t_D = \left(\frac{0.1\delta_0{}^2}{\mathcal{D}\bar{\varepsilon}_{ij}{}^2}\right)^{1/3} \tag{6.3}$$

Naturally, that this characteristic time is only valid, if this time is smaller than the time the striation thickness takes to vanish, i.e. the *flow time* or stretching time.

Ottino (1994) proposed for this problem another micro-mixing parameter, the *flow time* or stretching time, t_F, as the ratio between the averaged value of the shear rate and the local shear, ε (relative elongation):

$$t_F(t) = \left(\frac{1}{t} \int_0^t \frac{\bar{\varepsilon}_{ij}}{\varepsilon_{ij}} dt \right)^{-1} \tag{6.4}$$

The flow time, t_F, is determined by the local continuous decrease of the striation thickness and Ottino (1994) proposed the following approximation (see Villermaux and Falk, 1996):

$$t_F = \left(\frac{2\nu}{\dot{\varepsilon}} \right)^{1/2} \frac{1}{eff(t)} \tag{6.5}$$

where, ν, is the liquid kinematic viscosity, $\dot{\varepsilon}$ is the local rate kinetic energy dissipation, and $eff(t)$ an efficiency parameter. The main difficulty is related to the estimation of efficiency parameter, $eff(t)$, that usually lies between 0 to 2/3 (Villermaux and Falk, 1996). The flow time includes the effects of the total deformation rate and can be used to describe the micro-mixing in laminar flow.

The lowest value between the two parameters, t_D and t_F, might determine the extent of micro-mixing. The t_F equation predicts a stronger reduction of striation for higher energy input. Then, according to Thoenes (1994), the following situations can happen:

- $t_D > t_R$ and $t_F >> t_R$, reaction is limited by the micro-mixing;
- $t_D > t_R$ and $t_F \approx t_R$, the striation deformation promotes the transport and the chemical reaction;
- $t_D > t_R$ and $t_F < t_R$, a situation very close to the perfectly mixed reactor where the micro-mixing is not important.

Another kind of models for simulations of laminar mixing are those based on the concept of mass transfer across the interfacial area formed between the two segregated components-reactants. The reciprocal value of multiplication of the mass transfer coefficient and of the reaction area may be considered as the micro-mixing characteristic time. The area of reaction is time dependent, and inverse proportional to the striation thickness. Then for a batch process with the residence time, t_{rtd}, the time averaged volumetric mass transfer coefficient, $k_L a$ is (Thoenes, 1994):

$$\overline{k_L a} = \frac{2\bar{\varepsilon}_{ij}}{3\delta_0\sqrt{\pi}}\sqrt{\mathcal{D}t_{rtd}} \tag{6.6}$$

The idea of the mass transfer coefficient is explored in the IEM— Interaction by Exchange with the Mean — model of Villermaux (1972) which will be described in a latter section. The IEM model is based on small fluid elements as particles with associated concentration, which travel through the reacting mixture and exchange the mass with it. The reaction is contained within the particles that are surrounded by fluid with concentration equal to the mean value of the reactor bulk. The mass flux is thus driven by the concentration difference between the particle and its close environment.

6.4 Computational methods for turbulent reactive flows

This section describes the effects of turbulence on the mixing with chemical reaction. Basic features of turbulent mixing in the stirred tank were studied in Chapter 5 and more details on the concepts of turbulent flow are given in Appendix C. The statistical turbulence is used here to explain difficulties encountered in the numerical simulations of mixing with chemical reactions. This goal is demonstrated here on the energy spectra of velocity and concentration fluctuations and the problems for simulations are stressed by comparison of the equations of mass conservation under laminar and turbulent regimes.

Mixing in the STR operated under a turbulent regime embrace a wide range of length and time scales. These scales promote a macroscopic heterogeneity that is related with the velocity gradients and local differences of the dissipated energy. If a chemical reaction is present in such a flow, it can generate the micro-gradients of the concentration that have an additional influence on the product yield.

The physical picture of the various scales involved in the turbulent reactive flows can be obtained from the energy spectra. These spectra has been studied by various researches (Von Karman, 1939; Kolmogorov, 1941; Brodkey, 1967, and Tatterson, 1991) and they describe how the turbulent flow energy is transferred from large flow scales to the smaller scales. The energy spectrum of velocity fluctuations can be obtained from experimentally measured velocity data, at the points separated by distance, a, then arranged in the autocorrelation function and by Fourier analysis of this data. Considering a turbulent flow, the fluctuation velocities at the two points can be correlated as:

$$Q_{ij}(a) = \overline{u_i(x)u_j(x+a)} \tag{6.7}$$

where the u_i, u_j are velocity fluctuations at the certain space locations (x and $x+a$). The values of Reynolds stresses can be obtained by vanishing the distance between the two points (see also Appendix B). This special kind of the velocity correlation is used to understand the turbulence and to get a notion of relations between the various quantities studied. Fast Fourier

Transformation —FFT of the Q_{ij} results into the energy spectrum of velocity fluctuations. According to Tatterson (1991), the energy spectrum describes behaviour between the two points, which is brought about by the velocity fluctuations. The spectrum is obtained in the frequency domain or in the wave-number space, w, that can be considered as the reciprocal value of the length scale. In addition, the length scales can be obtained by the integration of the normalised Q_{ij} function called *Eulerian correlation coefficient*, R_{ij}:

$$R_{ij}(a) = \frac{\overline{u_i(x)u_j(x+a)}}{\sqrt{\overline{u_i^2(x)}}\sqrt{\overline{u_j^2(x+a)}}} \tag{6.8}$$

The integral length scale also called macro-scale, L_S can be calculated by:

$$L_S = \int_0^\infty Rij(a)da \tag{6.9}$$

For the higher Reynolds numbers, the spectrum of the velocity fluctuations can be approximated as $E_u(w) \propto w^{(-5/3)}$, where the w is the wave-number. A graphical representation of the energy spectrum of velocity fluctuations is shown in Figure 6.1.

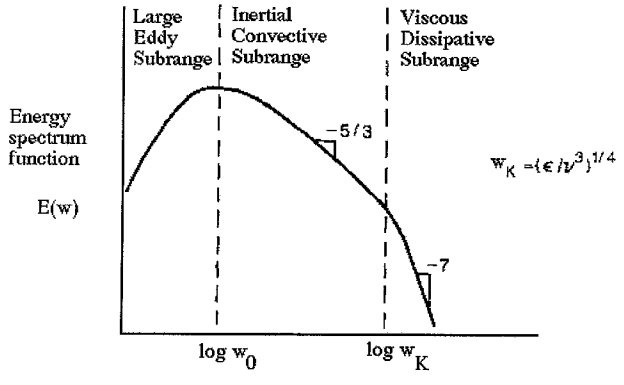

Figure 6.1 *The energy spectrum of velocity fluctuations (from Tatterson, 1991).*

As can be seen in Figure 6.1, the energy spectrum is divided into three different sub-ranges. Large eddies occur in the sub-range where the wave-number is below w_0. The inertial convective sub-range begins at the w_0 (corresponding to the integral scale, L_S) and ends at the wave number w_K, associated with the Kolmogorov micro-scale, λ_K. These two length-scales can be expressed as (Fox, 1996):

$$L_S = \frac{3\pi \int_0^\infty w^{-1}E_u(w)dw}{4\int_0^\infty E_u(w)dw} \tag{6.10}$$

$$\lambda_K = \left(\frac{\nu^3}{\varepsilon}\right)^{1/4} \tag{6.11}$$

In this sub-range, the turbulent kinetic energy is transported from the large-scale motions (in the order of the reactor diameter) to the small-scale eddies. Laminar flow conditions are assumed in the viscous dissipative sub-range, occurring below the λ_K scale, where the kinetic energy is converted into an internal energy by the action of viscous forces.

The length scale distribution of the turbulent reactive flow may be represented also by the energy spectrum of the concentration fluctuations. The function f_c, in the analogy with the R_{ij}, can be taken as:

$$f_c(a) = \frac{c(x)c(x+a)}{\sqrt{\overline{c^2(x)}}\sqrt{\overline{c^2(x+a)}}} \tag{6.12}$$

This function contains an information on how the concentration at one point correlates with the concentration at another point. The Figure 6.2 shows a typical energy spectrum of the concentration fluctuations (Tatterson, 1991).

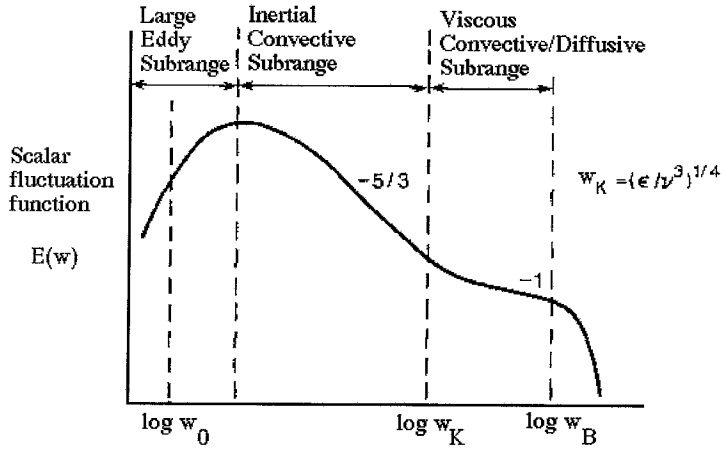

Figure 6.2 The energy spectrum of concentration fluctuations(from Tatterson, 1991).

The energy spectrum of concentration fluctuations contains one sub-range more than that of the velocity fluctuations. The difference is found in the viscous convective and diffusive sub-ranges. As the result, the concentration fluctuations spectra extend into much higher values of the wave number (to the smaller length scales) than those of the velocity fluctuations. In addition, the energy spectrum of the concentration fluctuations extends even more for flows with higher Schmidt number ($Sc = \nu/\mathcal{D}$) values. For $Sc > 1$, the usual case of liquids, the molecular diffusion occurs only near the Batchelor scale, λ_B:

$$\lambda_B = \left(\frac{\nu\mathcal{D}^2}{\varepsilon}\right) = \lambda_K Sc^{(-1/2)} \tag{6.13}$$

As depicted in Figure 6.2, the Batchelor spectrum may be approximated by $E_\phi \propto w^{(-1)}$. According to Ottino (1994), in the statistical theory of turbulence is implicit the concept that all turbulent flows at high Reynolds number should be in fact the same. The idea of universal flows at the very small scales is supported by the energy spectra experimentally obtained. The conclusion for numerical simulations of the turbulent reactive flow is obvious: "the smaller length scales should also be resolved for the cases where turbulent mixing is coupled with a specie transport or chemical reactions".

Numerical models for the turbulent reactive flow must employ the equations of the conservation of mass, momentum, energy (for non-isothermal problem), and the conservation equations of mass for all species present in the system. The equations for conservation of mass and momentum were introduced in previous chapters. The equation of mass conservation for the single specie is described next, individually for laminar and turbulent flows. The same equation can be applied for each species for multi-component systems.

The specie mass balance over a small volumetric fluid element can be givens as it follows. Temporal change of mass in the volume element plus the input of mass into the element must be equal to the sum of the output of mass from the fluid element and the rate of production of specie in the volume element by a chemical reaction. This can be mathematically described as (Bird, 1960)

$$\frac{\partial \rho_A}{\partial t} + \frac{\partial n_{Ai}}{\partial x_i} = r_A \tag{6.14}$$

where the $n_{Ai}$is mass flux component of specie A in the i-direction; and the r_A is the rate of production of specie per volume unit by chemical reaction. The equation of mass conservation for a mixture of more species can be derived by summation of these equations for all components present in the system.

More useful equations are derived in terms of the mass fraction, w_A, or the molar concentrations, C_A, using the assumption of constant density and diffusion coefficients:

$$\frac{\partial w_A}{\partial t} + \frac{\partial}{\partial x_i}(U_i w_A) = \mathcal{D}_A\left(\frac{\partial^2 w_A}{\partial x_i \partial x_i}\right) + r_A \tag{6.15}$$

$$\frac{\partial C_A}{\partial t} + U_i \frac{\partial C_A}{\partial x_i} = \mathcal{D}_A\left(\frac{\partial^2 C_A}{\partial x_i \partial x_i}\right) + R_A$$

where the $\mathcal{D}_A$is molecular diffusivity; the r_A, R_A are the mass and molar chemical reaction production rates, respectively. Here, only the ordinary diffusion term will be assumed and if the specie is produced by a chemical elementary reaction the R_A is defined as equal to kC_A^2 or $k\overline{C}_A\overline{C}_B$, where the k is the specific reaction rate.

By applying the rules for statistical description of turbulence, the concentration of the specie C_A can be replaced by the time averaged mean concentration value, $\overline{C}_A$, and the turbulent concentration fluctuation, c_A.

$$C_A = \overline{C}_A + c_A \tag{6.16}$$

If this decomposition is introduced into Equation 6.15, some additional terms arise for the turbulent flow:

$$\frac{\partial \overline{C}_A}{\partial t} + \overline{U}_i \frac{\partial \overline{C}_A}{\partial x_i} + \frac{\partial \overline{u_i c_A}}{\partial x_i} = \mathcal{D}_A \frac{\partial^2 \overline{C}_A}{\partial x_i \partial x_i} + R_A \tag{6.17}$$

The third term on the left hand-side of Equation 6.17 is called *turbulence mass flux*, $\overline{u_i c_A}$, and has an analogy in the turbulent momentum flux, $\tau_{ij}^t = -\rho \overline{u_i u_j}$ studied in the previous chapters.

If the specie inside of the balanced volume element is produced by chemical reaction, the term R_A can be expressed using the terms, $k\left(\overline{C_A}^2 + \overline{c_A^2}\right)$ or $k\left(\overline{C}_A \overline{C}_B + \overline{c_A c_B}\right)$. The additional terms, by comparing with the production rates in laminar flow, express the production rate of specie by concentration fluctuations $\overline{c_A^2}$ or $\overline{c_A c_B}$, and these must be closed in order to solve the conservation equation. For this purpose, some additional relations must be defined. However, the closure of terms related with the concentration fluctuations is a quite difficult task and is usually based on the semi-empirical relations with known turbulence quantities.

The analyses of the energy spectra showed that some extra length and time scales arise in the problem involving chemical reactions. Moreover, the additional terms appeared in the equations for turbulent reactive flows. Both these facts make the numerical simulations of the turbulent reactive flows more difficult than in the cases of laminar reactive flows.

Moreover, the linking of small-scale and large-scale effects is fundamental for the successful computational attack of turbulent reactive flows. The small scales effects in the STR could be coupled with macro-mixing patterns available from previous CFD simulations. The comparisons of CFD predictions with the experimental data in Chapter 5, showed that the macroscopic patterns of the STR are well predicted. However, can CFD tool be useful for predictions of the turbulent reactive flows? The shortcoming is related with the manner which the non-linear terms are discretized for the numerical solution. It should be noted that the molecular scales, at which the reactants are contacted, are not achievable with common CFD tools. CFD simulation does not resolve the sub-grid scales of the concentration field, where the micro-mixing occurs, and the local non-linear reaction rates are replaced by the grid-level (macro-mixing) averages. In this way, CFD simulations of the non-premixed reactor with chemical reaction can be misleading.

The most common computational methods used to predict the turbulent reacting flows are given in the following subsections. They are divided on two parts by the method applied to resolve the effects on macro-scale and micro-scale:

- *moment methods;*
- *micro-mixing models.*

The first part will introduce the moment methods that will be applied in simulations of the non-reactive tracer, as it will be described in Section 6.5. The second part on the micro-mixing methods will be organised in two groups presented as the phenomenological and mechanistic models.

6.4.1 Moment methods

This is a classical approach based on the decomposition of variables into the average and fluctuation components (see Equation 6.16). Additional terms appear in the mass conservation for specie, as seen from Equations 6.17. The last term on the left hand-side of Equation 6.17 is called turbulent mass flux representing the transport term due to turbulence. Another difficulty is introduced by the extra terms from the reaction rate, R_A, due to the variance and covariance of concentration fluctuations, $-k(\overline{c_A^2})$ and $-k(\overline{c_A c_B})$ respectively. Both mentioned terms are not closed and can only be approximated.

Then the *transport equation of concentration variance* can be used to close the concentration fluctuations term and in a simplified form is expressed as:

$$\frac{\partial \overline{\phi^2}}{\partial t} + \bar{u}_i \frac{\partial \overline{\phi^2}}{\partial x_i} + \frac{\partial}{\partial x_i} \overline{u_i \phi^2} = -2\overline{u_i \phi} \frac{\partial \overline{\Phi}}{\partial x_i} - 2\varepsilon_\phi \tag{6.18}$$

where the ϕ^2 is the scalar, variance or co-variance, and the ε_ϕ is the *scalar dissipation.*

The turbulent mass flux term, $\overline{u_i c_A}$, represents the transport of mass by the concentration and velocity fluctuations in the inertial sub-range of the energy spectrum. The closures for the turbulent transport term $\overline{u_i c_A}$ and the new term $\overline{u_i c_A{}^2}$ from the *transport equation of variance,* $\overline{\phi^2}$ (for example, $\overline{c_A{}^2}$) are commonly performed using the *gradient-diffusion theory*. Then, by applying the gradient diffusion theory for the flows of constant density:

$$\overline{u_i \phi} = -\mathcal{D}_t \frac{\partial \overline{\Phi}}{\partial x_i} \quad \text{and} \quad \overline{u_i \phi^2} = -\mathcal{D}_t \frac{\partial \overline{\phi^2}}{\partial x_i} \tag{6.19}$$

where the $\mathcal{D}_t$ is the turbulent diffusion given as:

$$\mathcal{D}_t = \frac{\rho c_\mu k^2}{Sc_t \varepsilon} = \frac{\rho \mu_t}{Sc_t} \tag{6.20}$$

where the Sc_t is the turbulent Schmidt number. It should be noted that the $\mathcal{D}_t$ in Equation 6.20 was substituted by the local characteristics of turbulent flow such as the turbulent kinetic energy, k, and the rate of turbulent kinetic energy dissipation, ε.

The scalar dissipation, ε_ϕ, arising from the transport equation of variance Equation 6.18 describes a decay of the scalar variance due to molecular diffusion. It acts at the molecular scales and using the Corrsin's model (1964) can be expressed as:

$$\begin{aligned} \varepsilon_\phi &= 2\mathcal{D}\overline{\frac{\partial c_A}{\partial x_i}\frac{\partial c_A}{\partial x_i}} = \frac{\overline{\phi^2}}{\tau_\phi} = \frac{\overline{\phi^2}}{\tau_u} \\ \frac{\overline{c_A{}^2}}{\tau_u} &= 2\mathcal{D}\overline{\frac{\partial c_A}{\partial x_i}\frac{\partial c_A}{\partial x_i}} \end{aligned} \tag{6.21}$$

where the *scalar mixing time*, τ_ϕ is given by:

$$\tau_\phi = \frac{1}{2}\left[4\left(\frac{\lambda^2}{\varepsilon}\right)^{(1/3)} + \left(\frac{\nu}{\varepsilon}\right)^{(1/2)} \ln Sc\right] \tag{6.22}$$

The scalar mixing time, τ_ϕ is sought to be proportional with the turbulence time, τ_u contained in the previously mentioned $k-\varepsilon$ turbulent models:

$$\tau_\phi \approx \tau_u = c\frac{k}{\varepsilon} \tag{6.23}$$

This idea comes from an assumption that the diffusion by velocity fluctuations is similar to the diffusion by concentration fluctuations. According to Fox (1996) this expression is valid only for cases where:

- velocity and scalar fluctuations are generated by the same integral-scale mechanism,
- the scalar spectrum is fully developed,
- the rate of scalar mixing is controlled by the rate of production of a scalar variance at the large scale (cascade process is in an equilibrium).

The problem is now to close the reaction term having the form of $-k(\overline{c_A c_B})$. This because the triple-correlations from the equation of variance are in Equation 6.18 neglected for simplicity. In laminar flows, the covariance of concentration fluctuations can be ignored and the reaction rate is computed by Arrhenius' law assuming a model controlled by the reaction kinetics. The concentration covariance in turbulent flow is determined by the micro-mixing and can not be resolved exactly by the standard CFD tools. Toor (1969) proposed the following relation in order to close the concentration covariance, $\overline{c_A c_B}$, for a simple reaction $A + B \rightarrow R$ in the one dimensional reactor under turbulent regime as:

$$\overline{c_A c_B} = -I_S \overline{C_{A0}}\,\overline{C_{B0}} \tag{6.24}$$

where the $\overline{C_{A0}}, \overline{C_{B0}}$ are averaged values of each specie concentration in the separate feed jets of an ideal-tubular reactor. The I_S is the intensity of segregation meaning a decay law for the one-dimensional reactor. In the limit of instantaneous reaction ($k \to \infty$), the reactants A and B can not coexist and the $\overline{c_A c_B} \to -\overline{C_A}\,\overline{C_B}$ in order to keep the average reaction rate finite. For the limit of slow reaction can be assumed that $\overline{c_A c_B} << \overline{C_A}\,\overline{C_B}$, and the reaction rate depends only on the kinetics of reaction. *Toor's hypothesis* assumes that the concentration covariance depends only on the hydrodynamic and not on the reaction rate. The analysis of the one-dimensional reactor showed that the covariance of fast and slow reactions is equal at any position along the reactor. Unfortunately, this is valid only for one-dimensional reactor.

The model of Toor (1969) does not offer reliable results for the more complicated reaction system and the better models were needed. Dutta and Tarbell (1989) argued that not the covariance but the intensity of segregation, I_S, is independent of the reaction rate (see Wang and Tarbell, 1993) and developed the three-environment — 3E — model where:

$$\overline{c_A c_B} = -I_S\left(\overline{C}_{A0}\overline{C}_B + \overline{C}_{B0}\overline{C}_A - \overline{C}_A\overline{C}_B\right) \tag{6.25}$$

where the $\overline{C_A}, \overline{C_B}$ are the mean concentration distributions at the reactor outlet. In both models (Toor, 1969 and the 3E model), the concentration covariance is related to a non-reactive flow. Therefore, they have problems to predict correctly the reactive flows, mainly in term of the concentration variance, $\overline{c_A{}^2}$. The use of second-order methods (Equation 6.17) should help because they account for a change of the concentration distribution by the chemical reaction but additional triple-correlation terms appear such as $\overline{C_A c_A c_B}; \overline{C_B}\,\overline{c_A{}^2}; \overline{c_A{}^2 c_B}$. These terms are also unclosed and often neglected as in Equation 6.18. The models thus derived produce the better results but still not satisfactory and other approaches were developed to avoid the difficulties related to the concentration covariance.

Most of the models were originally developed for the combustion applications. An assumption of the finite rate chemical reactions and that these are primarily controlled by the action of turbulent mixing is very common. The most known is the *eddy-break-up* model (Magnussed and Hjertager, 1976) where the reaction rate is a function of the mean concentration level of fuel, oxidants, or products. An empirical constant, A_c, controls the strength and the polarity of reaction is needed for such a model:

$$r_i = -A_c \rho \nu_{ni} \frac{C_{ni}}{\tau_u} \tag{6.26}$$

Spalding (1971) replaced the concentration variable in the eddy-break-up model by the fluctuating concentration variance, $\overline{c_{ni}^2}$ of fuel, oxidants, or products. The value of fluctuating concentration variance can be obtained from the transport equation of variance (Equation 6.17).

More sophisticated models are those where the controlling step of the mixing is evaluated using a minimum function. One of the examples is the model of Ziman (1990) based on Corrsin's analysis:

$$r_i = \min(k_{ij}\overline{C_i}\overline{C_j}, \overline{C_i}/t_m, \overline{C_j}/t_m) \tag{6.27}$$

$$t_m = 2\frac{k}{\varepsilon} + 1.54\sqrt{\frac{\nu}{\varepsilon}}\ln Sc \tag{6.28}$$

The minimum function selects the lowest reaction rate that is determined as the kinetic-laminar rate or the rate at which the least abundant species is micro-mixed, t_m.

Commercial CFD packages can contain some of the modified combustion approaches and it depends on the user and his experience to choose the most suitable for a specific application.

6.4.2 Micro-mixing models

Micro-mixing is accomplished by small-convective motions in the viscous-convective sub-range, near the Kolmogorov micro-scale, and by the molecular diffusion in the viscous-diffusive sub-range, near the Batchelor concentration length scale (Tatterson, 1991). Knowledge of the mixidness at the molecular scale is necessary to predict the reactor performance. CFD predictions giving the averaged macro-scale fields of velocity, pressure, kinetic energy, and energy dissipation should be supplied by the models that take care of the events within each element grid volume. This can be achieved by the micro-mixing models.

Micro-mixing models are *phenomenological* and require an empirical information to determine the values of essential parameters (Fox, 1996). They model only a few dominant mechanisms and are attractive because of their simplicity and small computational demands. The Lagrangian approach is usually employed for the micro-mixing models and the small particles of specific specie are tracked from the macro-scale down to the Kolmogorov scale. Moreover, it is assumed that the reactants have no effect on the velocity field until the Batchelor scale is reached. The reactants are contacted at the Batchelor scale and consequently, the reaction zones are created while the molecular diffusion starts at the same time.

The models of micro-mixing should interpret deformations, stretching and striations of fluid elements and also the *engulfment* of fresh liquid into deforming elements. The laminae are placed into the energy dissipating vortices of turbulence. These vortices are stretched and

rotated and the size of local unmixed regions is further reduced. A graphical representation of the *engulfment mechanism* can be seen in Figure 6.3.

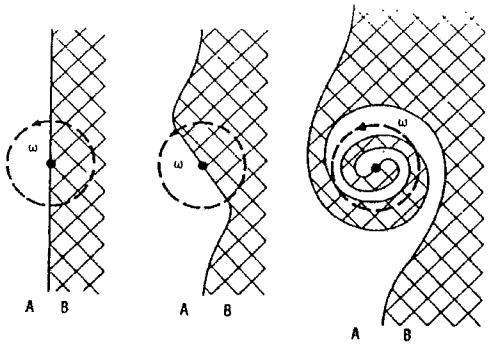

Figure 6.3 *Schematic representation of engulfment mechanism of the species A and B (from Thoenes, 1994).*

The micro-mixing models described here are split on two sections:

- *phenomenological models;*
- *mechanistic models.*

The phenomenological models (Section 6.4.2.1) are those where the processes are described by formal interaction and the segregation decays without having basis in the real mechanisms of micro-mixing. The second possibility how to approach the micro-mixing are *mechanistic models* reported in Section 6.4.2.2.

6.4.2.1 Phenomenological models

The phenomenological model proposed by Curl (1963) is known as the CRD — *Coalescence-Re-Dispersion* — model. In this model, the mixing takes place by random and instantaneous coalescence of droplets of the two reactants and by subsequent re-dispersion into an identical pair of droplets. According to Dutta and Tarbell (1989), these droplets are seen, in turbulence analogy, as some isotropic turbulent eddies and the coalescence rate as a measure of the rate of turbulent micro-mixing. Homogenisation of the reactor composition is attained through the coalescence at a certain frequency while a chemical reaction goes on within the particles. Another model called the IEM — *Interaction by Exchange with Mean* — was developed by Villermaux and Devillon (1972). Assuming the homogeneous mixing, the result of interactions of one fluid particle with its neighbours is represented by an equivalent mass-transfer flux. Micro-mixing of this model is based on the concentration difference, as driving force, and the exchange rate is characterised by the micro-mixing time, t_m:

$$\frac{dC_i}{d\alpha} = k_m(\overline{C}_i - C_i) + r_i \qquad (6.29)$$

where the α is the age of element and the t_m can be calculated by Equation 6.28.

The 3E — *Three-Environment* — model of Ritchie and Togby (1979) assumes the two-reactants entering the reactor (entering environment, EE) and the one environment leaving(LE) the reactor. The EE is described as totally segregated and the LE as well-mixed. Micro-mixing is modelled by the transfer of mass from the EE to the LE region, and the transfer coefficient is an inverse value of the micro-mixing parameter (see Dutta and Tarbell, 1989). The last model was extended later to the 4E — *Four-Environment* — model with two separate EE and LE regions that can interact mutually.

The engulfment model of Baldyga and Bourne (1990) is based on a growth of volume of the engulfed fluid, V_{ei}:

$$\frac{dV_{ei}}{d\alpha} = EV_{ei} \tag{6.30}$$

where $E \approx (\varepsilon / \nu)^{1/2}$; and the mass balance for the engulfed fluid of volume V_{ei}, and the composition C_i (see Ottino, 1994) is given by

$$\frac{d(V_{ei}C_i)}{d\alpha} = E\overline{C}_i V_{ei} + r_i V_{ei} \tag{6.31}$$

Then by combination of Equation (6.32) and Equation (6.33) is obtained:

$$\frac{dC_i}{d\alpha} = E\left(\overline{C}_i - C_i\right) + r_i \tag{6.32}$$

6.4.2.2 Mechanistic models

Baldyga and Bourne (1984) described the molecular diffusion and chemical reaction within a small vortex of shrinking laminae-structure, on the fluid mechanical approach. They assumed that the equations of diffusion and reaction can be solved over the slab regions with the thickness, 2δ , in time, t, while the initial thickness was $2\delta_0$ and the initial time was t_0. Moreover, the initial thickness $2\delta_0$ was equal to the Kolmogorov length, λ_K, and the equation can be written as

$$\frac{\partial C_i}{\partial t} + U\frac{\partial C_i}{\partial x} = \mathcal{D}\frac{\partial^2 C_i}{\partial x^2} + r_i \tag{6.33}$$

The rate of shrinkage was given by:

$$U = \frac{-(\varepsilon / \nu)^{1/2} x}{\left(4 + \varepsilon t^2 / \nu\right)^{1/2}} \tag{6.34}$$

where the ε is rate of the energy dissipation and the x is co-ordinate within a slab thickness. The mean lifetime of the energy-dissipated vortex was defined by:

$$t = 12(\nu/\varepsilon)^{1/2} \tag{6.35}$$

In addition, it was assumed that after each eddy lifetime the number of eddies doubles, so the eddies are formed by the geometric progression of two. All eddies were considered to form the important part of the fine dissipating structure. The eddy scale was twelve times of the λ_K, and the eddies can be pictured as the vortices which engulfed the fluid to form a partially segregated laminae (Tatterson, 1991). Non-dimensional form of Equation (6.33) was given as:

$$\frac{\partial C_i}{\partial T} = \left(\frac{\delta_0}{\delta}\right)\frac{\partial^2 C_i}{\partial \bar{X}^2} + \frac{{\delta_0}^2 r_i}{\mathcal{D}c_{j0}} \tag{6.36}$$

where the C_i, T, X are dimensionless concentration, time, and distance (x/δ). The initial thickness δ_0 was one half of the Kolmogorov micro-scale and had following non-dimensional form:

$$\frac{\delta_0}{\delta} = \left[1 + \frac{T^2 Sc^2}{32} - \sqrt{\left(1 + \frac{T^2 Sc^2}{32}\right)^2 - 1}\right]^{(-1/2)} \tag{6.37}$$

6.5 Application of CFD package for non-reactive mixing in STR

The importance of mixing process was recognised in many areas of the chemical industry and the increasing demands for its optimisation are aimed by numerical simulations. Application of CFD packages can be very useful for this purpose.

The hydrodynamics study of the ST was introduced in the earlier chapters and the key concepts of numerical predictions of mixing with chemical reactions were explained in previous sections of this chapter. The knowledge and results obtained on the ST hydrodynamics are used here to perform *numerical predictions of a tracer in non-premixed STR.*

6.5.1 Model description and objectives

Mixing in the batch STR is examined here using dynamic simulations of non-reactive tracer diffusion and transport under laminar and turbulent flow regimes. The effect of flow regime on the tracer transport and diffusion is addressed.

The objective is to visualise the tracer transport in the STR and to reveal the effect of location of the tracer injection on time necessary for homogenisation of the reactor contents. This time parameter can be characterised as the *blending time* that is important for the comparisons of the STR's performances.

The tracer is injected through four feeding pipes that are equidistantly distributed within the STR. The computational domain of integration is formed by single quarter of the STR, identical to that used in the previous chapter, and the particular feeding pipe is always located at the vertical plane that passes through the baffle (see Figure 6.4). Its was assumed that the feeding pipe is very thin and has no influence on the flow field in the stirred tank. Therefore, only the feeding pipe outlet was modelled as a very small sphere. The location of this sphere in the STR will be referred as the injection point that is the additional entity of computational domain comparing with those described in the steady-state simulations of the ST hydrodynamics. Here the simulations are limited to dynamic computation of the tracer transport and diffusion in 3D space while the impeller rotation is modelled using the moving ring approach.

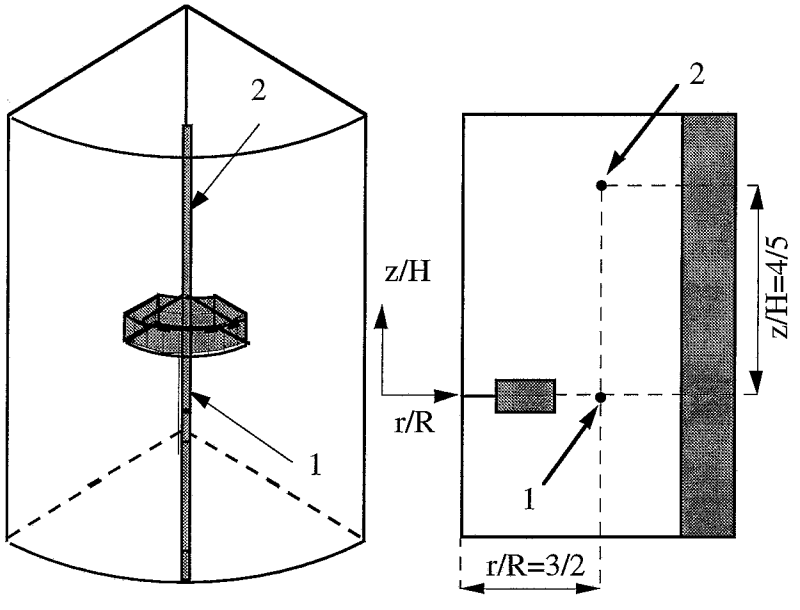

Figure 6.4 *Graphical representation of two locations of the tracer injection where (1) stands for the first injection point — FIP, and (2) for SIP.*

The flow is considered incompressible, isothermal and fluid with tracer Newtonian. Flow fields in the STR operating under laminar and turbulent regimes were adopted from previous steady-state simulations of the stirred tank. Thus, the local values of all the relevant variables (three velocity components, pressure, turbulent kinetic energy and the rate of turbulent kinetic energy dissipation) were assumed as steady. As the result, only 'the equation of mass

conservation for the tracer, as single specie, was solved here. In this case, the source term is not considered and the conservation equation can be written for laminar regime as:

$$\frac{\partial C_n}{\partial t} + U_i \frac{\partial C_n}{\partial x_i} = \mathcal{D} \frac{\partial^2 C_n}{\partial x_i \partial x_i} \tag{6.38}$$

The terms on the left-hand side of Equation 6.38 represent the local temporal change of concentration of the tracer and the tracer convection. The term on the right-hand side expresses the tracer diffusion. The convective term dominates in the equation while contribution by diffusion process is very small.

In the case of turbulent flow, all of the variables are time-averaged and the tracer conservation equation is given by:

$$\frac{\partial \overline{C}_n}{\partial t} + \overline{U}_i \frac{\partial \overline{C}_n}{\partial x_i} + \frac{\partial \overline{u_i c_n}}{\partial x_i} = \mathcal{D}_t \frac{\partial^2 \overline{C}_n}{\partial x_i \partial x_i} \tag{6.39}$$

where the $\mathcal{D}_t = \mu_t / \rho Sc_t$ is turbulent diffusivity with the μ_t signifying the turbulent viscosity and the Sc_t is the turbulent Schmidt number. In this work, it was assumed that $Sc_t = 0.9$. By comparing Equation 6.38 with Equation 6.39 additional term called turbulent mass flux arises and this can be closed using the following expression:

$$\overline{u_i c_n} = -\mathcal{D}_t \frac{\partial \overline{C}_n}{\partial x_i} \tag{6.40}$$

The presented equations were solved numerically using the associated boundary conditions.

The boundary conditions were defined at the entities representing the injection point, wall, tank bottom, shaft, and liquid surface. A zero convective flow was applied on the tank wall including the baffle and bottom entities. Free liquid surface was modelled as flat with zero convective flow in the normal direction. Diffusional flows through these entities were assumed negligible. The computational domain with non-zero thickness at the wall and the bottom would stop also the diffusional flows but it was not objective of this work to introduce an additional geometrical complexity into the present model. The walls with a zero-thickness are therefore assumed as satisfactory due to negligible values of the tracer mass that is diffused in/out of the computational domain.

The impeller shaft was modelled as the solid entity of non-zero thickness having an impermeable surface, SH, for the convective and diffusional flows.

The periodic boundary conditions were imposed at the vertical planes of computational domain. The surface entities REF and PER (see Figure 5.27) were balanced at each computed time-step and the mass entering and leaving from the computational domain was always

equivalent. The mass balance was based on the convective terms since diffusion terms are negligible.

The mass balance over the entire external surfaces of the computational domain showed that the present model is free of any leaks.

The tracer injection was simulated as instantaneous. This was accomplished using different initial boundary condition of the tracer concentration in location of the injection from those in the reactor bulk. The tracer injection was specified within a group of small finite elements that form a discretized sphere. Two locations of the tracer injection were studied. The first injection point — FIP, is positioned in the impeller discharge flow region, and the second injection point — SIP — located in the top part of the reactor, as can be seen from Figure 6.4. The summary of initial boundary conditions for the present simulations is introduced in Table 6.3. It was assumed that the introduction of tracer does not disturb the flow fields in the STR.

Table 6.3 Initial boundary conditions for a tracer predictions.

Modelling of points of injection	Physical properties of injected tracer	Mass fraction of tracer
sphere radius $r_S = 0.003\text{m}$	density $\rho_A = 1000\text{kgm}^{-3}$	injected specie $w_A(0) = 0.1$
sphere volume $V_S = 1.1 \cdot 10^{-7}\text{m}^3$	viscosity $\mu_A = 0.001\text{Pa} \cdot \text{s}$	initial in STR $w_A(0) = 0.001$
reactor volume $V = 3.0 \cdot 10^{-2}\text{m}^3$	diffusivity $\mathcal{D}_A = 6.8 \cdot 10^{-10}\text{m}^2\text{s}^{-1}$	after injection $\overline{w_A} = 0.0011$

The tracer injection modelled in this way results into discontinuity of initial boundary conditions for the numerical simulation. In order to obey the law of mass conservation, CFD package can generate negative concentrations in some locations of computational domain. This situation occurs near the location of injection and is physically inconsistent. The *clipping method* can be used to change the sign of variable in order to avoid the negative tracer concentration. However, the simulations are affected by mentioned discontinuity also in the case of using the clipping method. The clipping should be employed, however, for studies where a chemical reaction is present, otherwise the reaction mechanism can be violated. For example, an irreversible reaction can be simulated, as it was reversible without the use of the clipping. In the study of non-reactive tracer, the use of the clipping is not necessary.

The equations describing the mass conservation were discretized and solved by FIDAP 7.6. The grid of domain was created by automatic mesh generator using the quadrilateral elements. Total number of finite elements is 54324 and these were arranged in forms of eight node bricks.

The system of ordinary differential equations is solved on each element of the computational domain using the segregated solver. The conjugate residual method, CR (FIDAP 7.6), provided the solution for the symmetric linear equation system and the GMRES (Generalised Minimal Residual method, FIDAP 7.6) for the non-symmetric system of equations.

Dynamic predictions were performed using the implicit backward Euler scheme. The time-step equal to 0.001s was used for computations in the range of time from 0.0s to 0.1s and the time-step of 0.01s was used for time range between 0.1s to 20s. The simulation was stopped when the tracer was equally distributed in the reactor. To put this in a context, it was less then ten impeller revolutions.

The simulations required 12MB of the core memory and the computational time was of the order of 15 hours in IBM RS6000 machine, model 3CT. The convergence criterion was set to DTOL = 0.001.

6.5.2 Calculated quantities

The non-reactive tracer simulations were performed separately at two locations of the tracer injection and using the laminar and turbulent flow equations. The impeller Reynolds number corresponded to 5000and the flow fields were taken from the predictions of the ST hydrodynamics, reported in Chapter 5.

The tracer concentration in the STR corresponds to the value of injected mass at the beginning and is expressed as the mean mass fraction:

$$\overline{w_A} = \frac{1}{V}\int_V w_A(x,y,z)dV \tag{6.41}$$

The value of $\overline{w_A}$ should be constant but it varies with time due to discontinuity introduced using the initial boundary conditions. This temporal variation will be given by $\Delta w_A = \overline{w_A(t)} - \overline{w_A}$, where the $\overline{w_A(t)}$ is the mean mass fraction calculated at time, t.

The tracer transport in the STR will be presented by temporal images expressing the local normalised concentration differences. This is provided using the quantity:

$$\left(w_A(x,y,z,t) - \overline{w_A}\right)/\left(w_{A\ \max}(x,y,z,t) - \overline{w_A}\right) \tag{6.42}$$

where the $w_A(x,y,z,t)$is the local tracer fraction with its maximum value $w_{A\ \max}(x,y,z,t)$. Time variable will be always normalised by the single period of impeller revolution, T_I.

The effects of location of the injection and of the flow regime on the tracer transport are presented as temporal evolutions of the intensity of segregation. The intensity of segregation quantifies the level of the reactor heterogeneity and is defined as:

$$I_S = \frac{\sigma^2}{{\sigma_0}^2} = \frac{\frac{1}{V}\int_V \left[w_A(x,y,z,t) - \overline{w_A(t)}\right]^2 dV}{\frac{1}{V}\int_V \left[w_A(x,y,z0) - \overline{w_A(0)}\right]^2 dV} \tag{6.43}$$

The intensity of segregation decays with time and the curve of this decay can be used to specify the blending time parameter for desired level of the segregation. The value of blending time depends on the impeller type, impeller rotational velocity, location of the feed injection, number of feed pipes, and on the physical properties of the mixed fluid.

6.5.3 Results from non-reactive tracer simulations

The simulations of non-reactive tracer, injected in the impeller discharge flow region, provide the following picture of the tracer transport throughout the STR.

Starting in the FIP, the tracer cloud spreads and flows mainly in the radial direction through the impeller centre plane until it reaches the tank wall. The cloud splits on two equivalent parts due to the impact at the wall, and one part enters the top and second part the bottom vortex of the STR. Both parts enlarge along the wall in the axial and tangential directions. At the same time, the clouds separate from the wall vicinity and expand inward to the tank. Then, two separated tracer clouds extend in direction parallel with the tank bottom. Finally, the cloud in the top part of the STR turns downward and the cloud in the bottom part upward to the impeller region. After passing through the impeller region, the tracer enters the impeller discharge flow region and process repeats periodically but now with the smaller tracer concentrations.

This is shown in Figure 6.5 and Figure 6.6 from the frontal view on the STR. Figure 6.5 and Figure 6.6 represent temporal images of the tracer mass-fraction differences according to quantity defined in Equation 6.42. Temporal expansion of the tracer cloud in 3D space is visualised by coloured regions where the opacity of colours increases exponentially with the magnitude of the presented quantity. The regions where the presented quantity equals to zero are transparent, and those regions where the value of this quantity is equal to unity are completely opaque. Time is normalised by the single period of the impeller revolution. Figure 6.7 and Figure 6.8 show the tracer-cloud expansion but from the top view of the STR. The series of 2D images in Figure 6.7 and Figure 6.8 is reconstructed by summation of the local quantities (Equation 6.42) along the vertical direction of the STR.

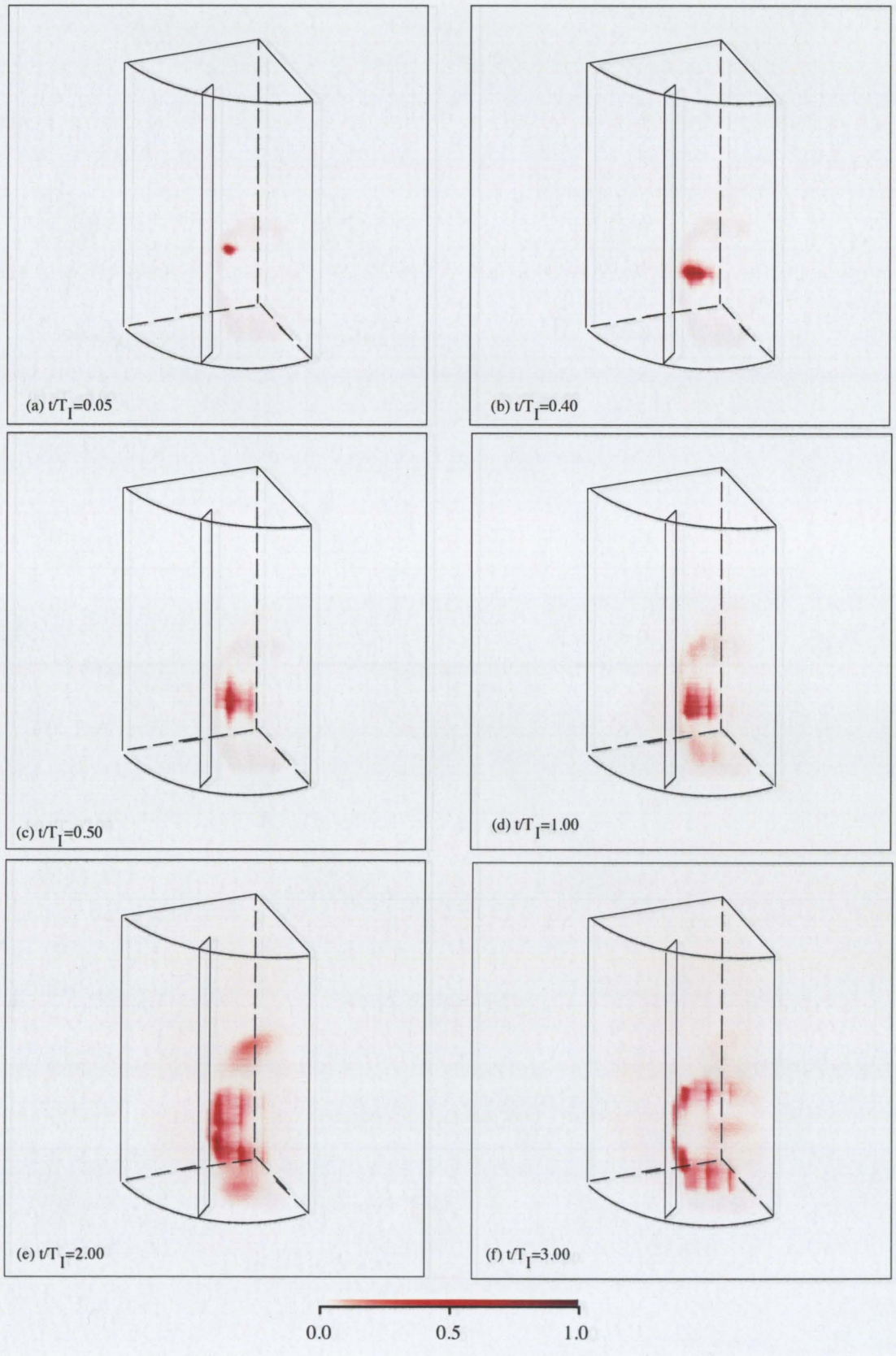

Figure 6.5 *Frontal view on temporal images of expansion of the tracer cloud at Re=5000 using laminar flow equations.*

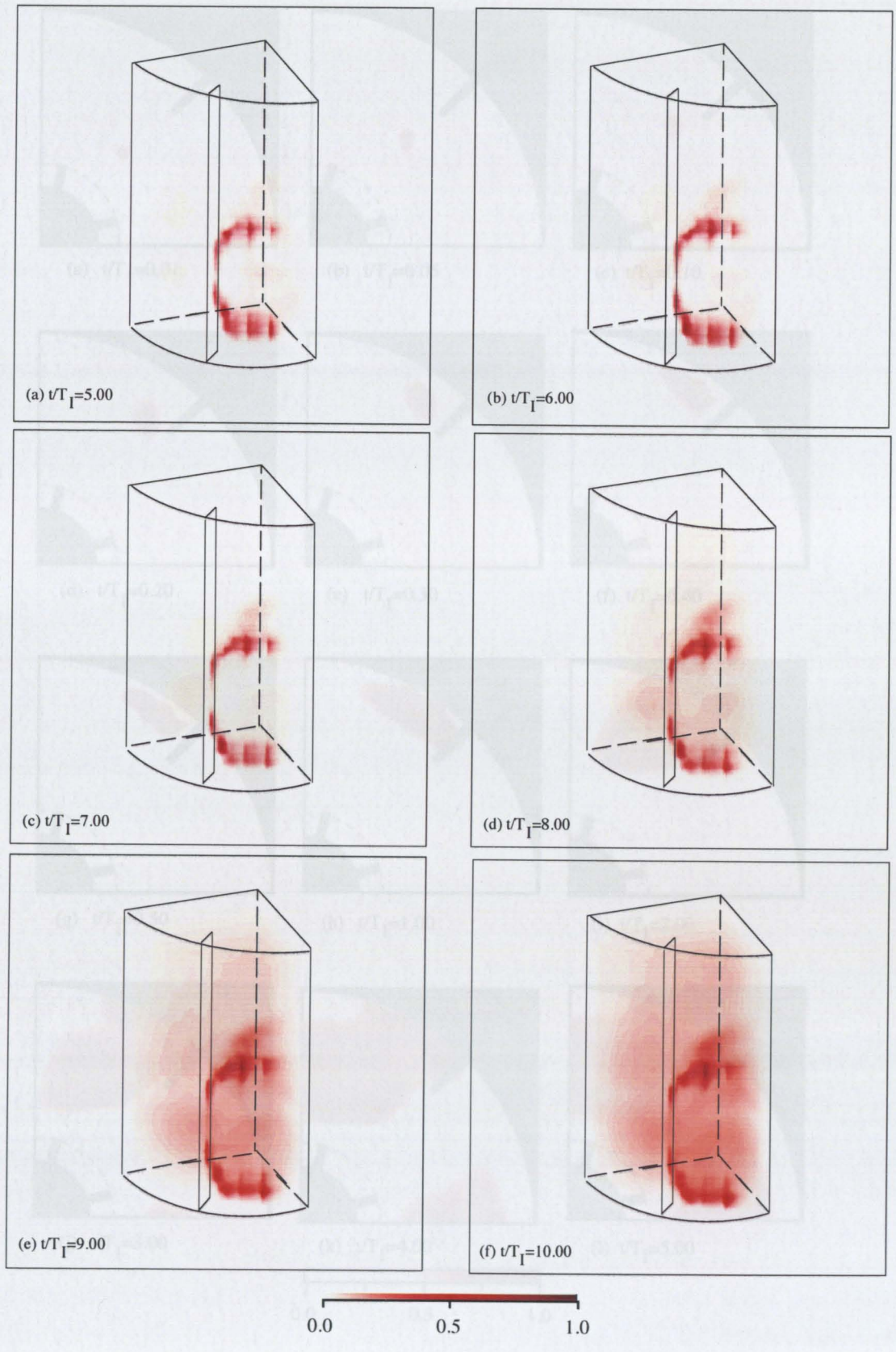

Figure 6.6 *Frontal view on temporal images of expansion of the tracer cloud at Re=5000 using laminar flow equations.*

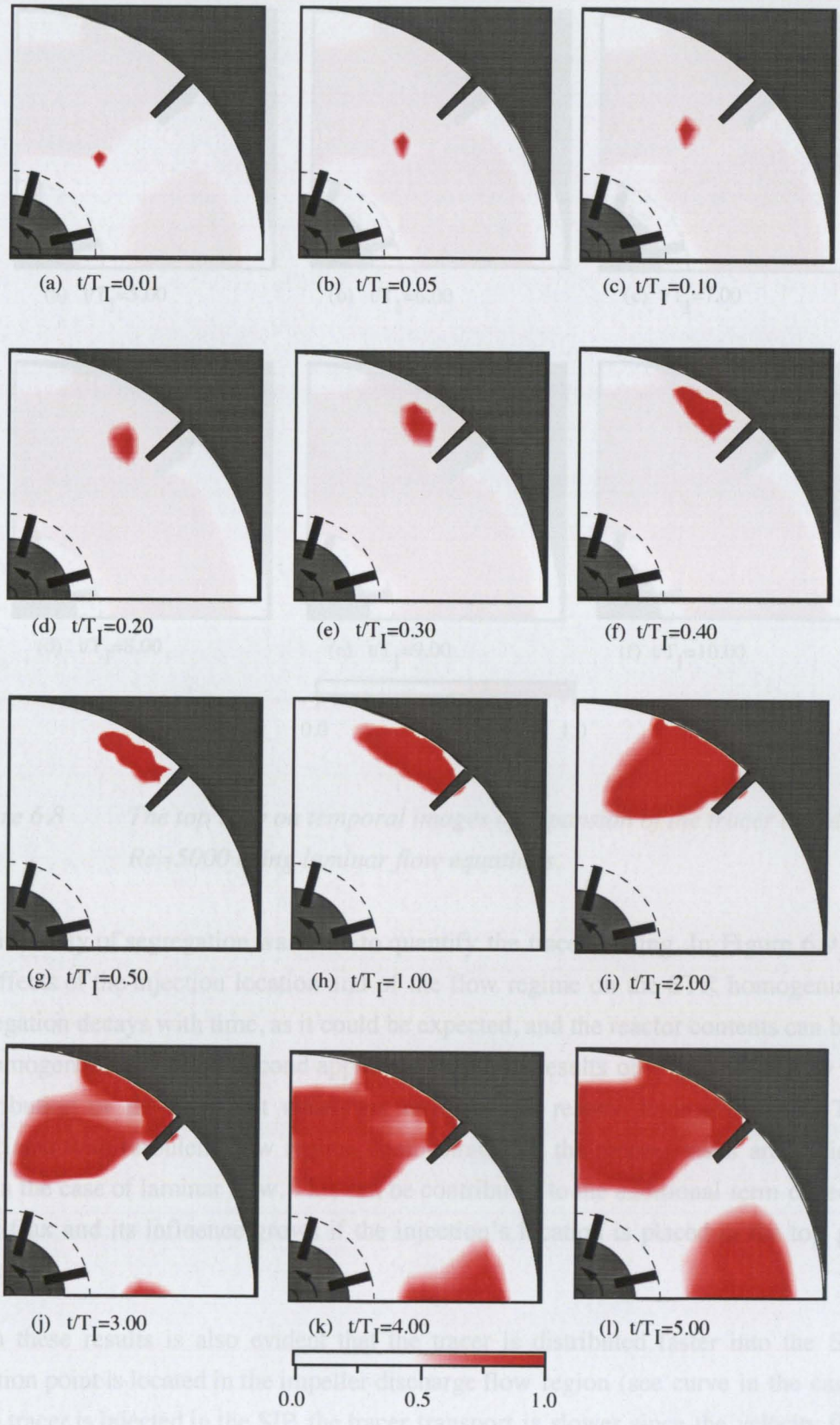

Figure 6.7 *The top view on temporal images of expansion of the tracer cloud at Re=5000 using laminar flow equations.*

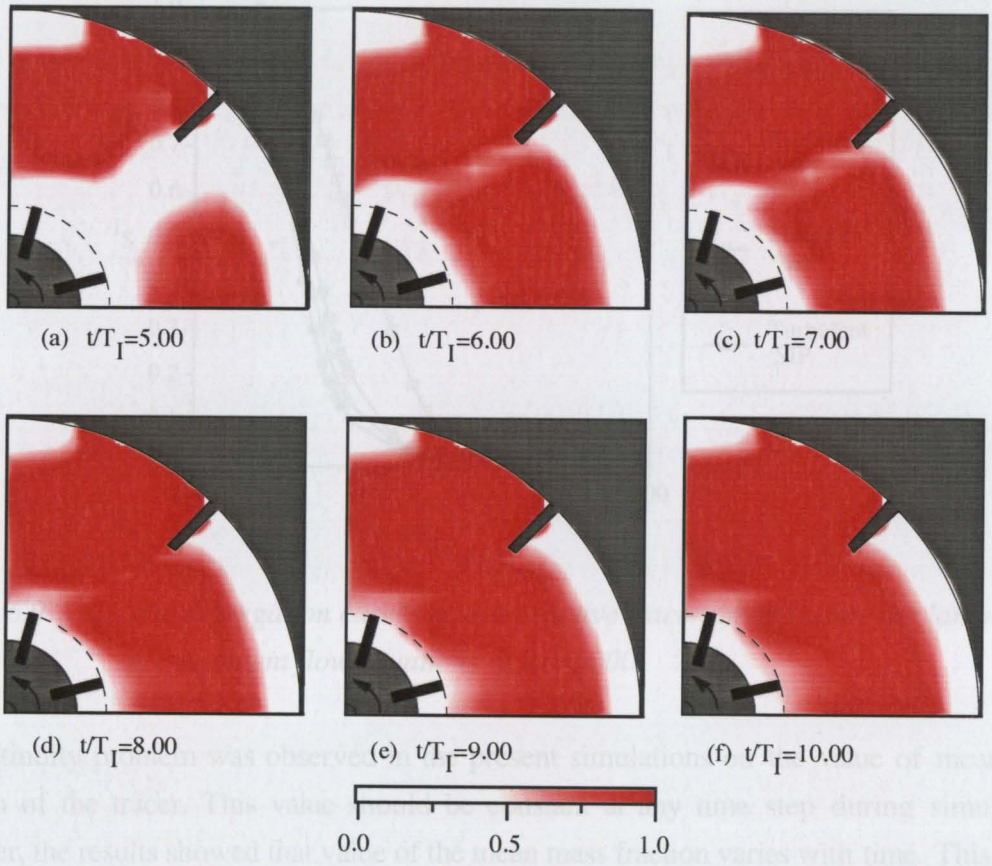

Figure 6.8 *The top view on temporal images of expansion of the tracer cloud at Re=5000 using laminar flow equations.*

The intensity of segregation was used to quantify the tracer mixing. In Figure 6.9 are shown the effects of the injection location and of the flow regime on the STR homogenisation. The segregation decays with time, as it could be expected, and the reactor contents can be regarded as homogeneous after one second approximately. The results on Figure 6.9 show clearly the contribution of the turbulent mass-flux term on the reactor homogenisation. The curves associated with turbulent flow regime demonstrate that the mixing tasks are achieved faster that in the case of laminar flow. This can be contributed to the additional term called turbulent mass-flux and its influence grows if the injection's location is placed in the top part of the reactor.

From these results is also evident that the tracer is distributed faster into the STR if the injection point is located in the impeller discharge flow region (see curve in the case of FIP). If the tracer is injected in the SIP, the tracer transport is slower since the velocity field in this region is not so violent than that in the impeller discharge flow region. The tracer is dispersed into the reactor bulk more slowly while a value of blending time increases.

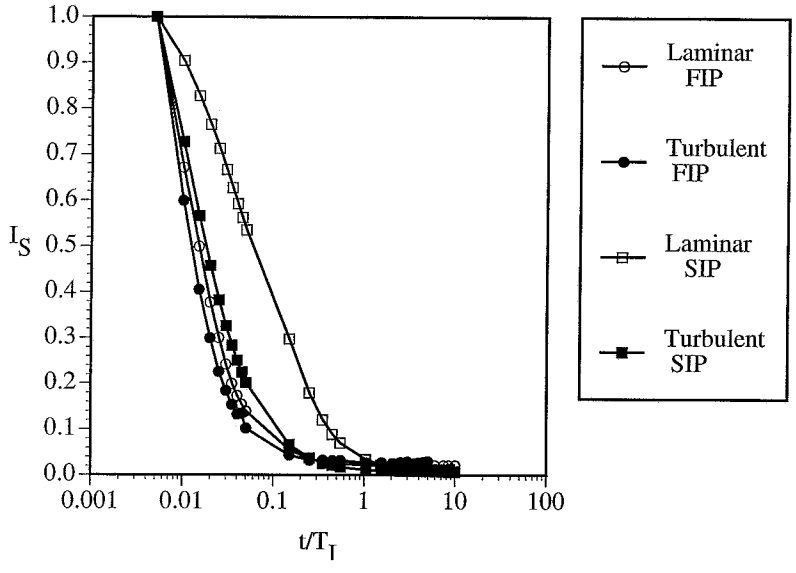

Figure 6.9 *The segregation curves of non-reactive tracer mixing using the laminar and turbulent flow equations at Re=5000.*

Discontinuity problem was observed in the present simulations on the value of mean mass fraction of the tracer. This value should be constant at any time step during simulations, however, the results showed that value of the mean mass fraction varies with time. This fact is due to previously mentioned discontinuity of initial boundary conditions and non-uniform volumes of the computational grid elements. An example of such variation is plotted in Figure 6.10 for the simulation including the injection at SIP.

As can be seen, the difference from the mean tracer fraction, Δw_A, exhibits with time an oscillatory behaviour. The magnitude of this oscillation and associated variation of the tracer mass can attain as much as 10% of the value of the mass tracer injected. But, for the case of FIP this magnitude was elevated up to maximum about 30%.

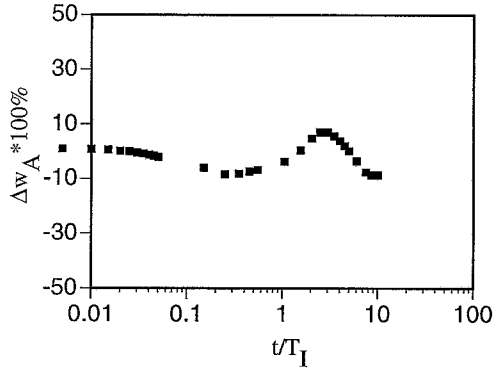

Figure 6.10 *The variation of mean concentration of tracer in the STR.*

Numerous studies were performed in order to suppress this variation of the averaged mass fraction. The studies accomplished by changes of different numerical methods for the time

integration, decreasing of time step, decreasing of injected tracer-mass, and change of the initial injection volume. Tested changes did not offer a significant improvement. The use of a non-uniform grid may also have an effect on the results predicted. And, it is believed that an increase of the computational grid density could partially solve the problem. These problems could be minimised in the future predictions by the gradual and not-instantaneous injection of the tracer into the STR but this at the increased computational expense.

6.6 Conclusions

Numerical methods to compute the reactive flow mixing in laminar and turbulent regimes were described in this chapter. The problems encountered for numerical predictions of such flows were explained theoretically and the methods used to avoid these difficulties commented. This can be a good starting point for the further investigation of chemical reactions in the STR.

The tracer injection and the consequent transport of mass of the tracer were studied in the STR using the dynamic-transient simulations. The hydrodynamics of the STR was assumed as steady-state and taken from previous simulations of laminar and turbulent regime. The effects of flow regimes and the location of injection on the blending time were studied. The results showed clearly that the tracer is distributed faster in the STR operated under turbulent regime. The study of the location of injection confirmed the fact that homogenisation of the STR is achieved faster if the injection pipes are located in the impeller discharge flow region that at the top of the reactor. Differences in the blending time parameter for the STR under turbulent and laminar regime are very small for practical applications. The last conclusion suggests that the reactive mixing of the STR at the Reynolds number studied can be computed quite well using the equations for the laminar flow model. It can be expected that with the increasing Reynolds number also the difference between the reactor performance working under different flow conditions will be enhanced.

7. Conclusions and Suggestions for Future Work

7.1 Conclusions

The hydrodynamics of the stirred tank mechanically agitated by the Rushton impeller was studied experimentally and by numerical simulations. The mixing process was considered as a single-phase, isothermal and Newtonian problem. Experimental investigation was performed using the LDV technique and the numerical simulations were carried out using the commercial CFD package — FIDAP 7.6.

The experimental study focused on four regions of the ST — impeller discharge flow region, impeller region, impeller centre plane, and baffle region. Data on velocity and stresses were obtained using the fixed frame of reference. The profiles of the radial and tangential velocities measured near the tip of the impeller were found independent of the angular co-ordinate and this leads to the assumption of the flow field in the ST as the axis-symmetric. Measured data were later used to derive the proper boundary conditions for the numerical predictions. Data focused on the region of the impeller discharge flow were found consistent with other data reported in the literature. The flow hydrodynamics was studied at the impeller centre plane with increasing Reynolds number. The presence of pseudo-turbulence was felt in the data obtained near the impeller due to periodic passages of the blades and its contribution to the measured data was eliminated using the spectral analysis. The anisotropic flow behaviour in the stirred tank was clearly demonstrated by the contour maps of the shear Reynolds stress. Similar fields of the velocity, kinetic energy, and shear stresses were observed on the results at various Reynolds numbers and these features were found to scale with the rotational velocity of the impeller. An analysis of the experimental uncertainties showed that higher order quantities, such as the shear Reynolds stresses, are measured with larger errors than

those related to the first order quantities such as the velocity. Moreover, the uncertainty depended on the spatial location and the local velocity.

The flow field in the stirred tank under laminar flow conditions was predicted numerically by solving the equations of the conservation of mass and momentum on a two and three-dimensional domains. The effect of the presence of a baffle was studied and the flow rate found for small Reynolds numbers in the baffled tank was lower than that in the tank without baffles. The computed viscous stresses were inversely proportional to the rotational velocity of the impeller. The resulting lack of information on the vertical flow in the ST in the two-dimensional simulations lead to the need of three-dimensional predictions. Two steady-state models and the time-dependent simulation of a 3-D flow showed similar results for $Re < 10$ either for the baffled and unbaffled stirred tanks. The most important fact is that the Rushton impeller was found as inadequate for the laminar mixing purposes due to a poor overall circulation produced and a large dead zone occurrence in the stirred tank. The presence of a baffle diminished the homogenisation of the ST and its removal is strongly recommended for laminar flow regime. The results showed that the models based on the laminar flow equations are not suitable for flow predictions of the ST's agitated at higher impeller Reynolds numbers than the $Re > 100$.

Turbulent flow predictions of the ST were performed using the steady-state approach called moving ring. The importance of imposed boundary conditions on the entities of a moving ring was demonstrated on the predictions using a set of models with different boundary conditions. Despite of the fact that similar flow patterns were obtained from all the models studied, a detailed analysis of the various hydrodynamic parameters revealed the significant deviations. Therefore, the most convenient model was selected and this selection was based on the comparisons with experimental data of the velocity and shear Reynolds stress. Direct comparison of the measured and predicted shear Reynolds stresses was reported and the results showed good agreement. The distribution of the characteristics of turbulent flow, such as the kinetic energy and the rate of the kinetic energy dissipation was obtained and discussed. In addition, the overall criteria like the Power and Flow numbers were calculated and compared with the experimental data. The study showed some difficulties to predict numerically the flow near the impeller. This was contributed to the effects of pseudo-turbulence and to the fixed frame of reference used to obtain the experimental data as basis for the boundary conditions in the impeller region. As a compromise, the model whose predictions approached the most closely to all examined criteria was adjusted to predict correctly the hydrodynamics in a region where the pseudo-turbulence already decayed. Using this procedure, a very good agreement with experiments was obtained. The main attributes of the present steady-state model 1 are the good predictions of all quantities of industrial interest and the low computational expenses. The simplicity of the model, however, is accompanied by the need of recourse to experimental data required for the turbulence boundary conditions.

The new model was derived for dynamic predictions of turbulent flow. This model was based on the sliding mesh approach and its predictions showed more discrepancies with experimental data and confirmed that the CFD is incapable to generate the contribution of pseudo-turbulence. A need of experimental data was found necessary also in the dynamic simulations of the ST working under a turbulent regime. At the present, the use of transient simulations of the stirred tank is recommended only for studies of the impeller design rather then for the industrial applications of mixing. This is due to a substantial computational expense and to the fact that the results produced are still not satisfactory. In general, the CFD tools can do a very good job in the predictions of hydrodynamics of the ST. This work can be considered as an important contribution to the growing confidence into CFD tools and their capability to predict satisfactorily the hydrodynamic processes.

Non-reactive tracer study in the stirred tank using CFD package focused on both the influence of flow regime and the location of tracer's injection on the homogenisation in the STR. The homogenisation was achieved faster if the reactant was injected in the impeller discharge flow region as in the case where injected in the region at the reactor top. The study of effect of flow regime on the tracer transport in the STR demonstrated the faster mixing under conditions of turbulent regime than in the laminar conditions but this difference was negligible from a practical point of view. This suggests that laminar flow model might be sufficient for predictions of a non-reactive tracer at moderate Reynolds numbers.

Finally, intensive mixing of the stirred tank with the Rushton impeller is concentrated into a very small region thus turning the use of these devices less effective and non-economical for practical applications. An improvement can be achieved by using more than one impeller in the stirred tank or by employing of a more efficient impeller, that would enhance the overall mixing.

7.2 Suggestions for Future Work

The results of present work showed that CFD tools predict the mixing features of the ST well. It can also be stressed here that both the experimental research and the numerical predictions should continue in order to contribute to the better understanding and numerical predictability of the stirred tank hydrodynamics, its performance and mixing quality. The analysis of reported results points to the following suggestions for the future work:

- The rotating frame of reference should be employed in future experimental work in order to avoid the effects of pseudo-turbulence on the data measured. In this way, the separation of the random turbulence contribution embedded in total turbulence is easier and comparison with the results from simulations more precise. The rotating machinery resolver or the coupling of LDV data acquisition with an encoder of the blade's position would be satisfactory for this purpose but the small data rate during the data acquisition

could make such measurements very difficult. More attention should be paid to the flow field apart from the regions affected by pseudo-turbulence. Detailed data on those regions would give a possibility to prescribe the boundary conditions at the locations different from the impeller region. The boundary conditions in the impeller region could therefore remain with definitions of the preferable flow directions only. This kind of approach might offer a better applicability of CFD tools for the predictions of mixing process in the ST.

- Dynamic model of the stirred tank could be confined to the small region around the impeller in order to study the vortex system evolving behind each blade. The shortcoming lays in the increased computational resources necessary to predict the effects observed experimentally. Numerical simulations and the comparison of its results with the experiments might offer some interesting findings on the effects of the impeller rotation, impeller size and its shape on the vortex system.

- Steady-state modelling of the stirred tank is preferable at the present time due to less computational expense necessary and due to the better results produced than those from the transient simulations. The difficulties reported in the predictions near the impeller might be solved in the following way. Taking the boundary conditions of the model 1 as the initial boundary conditions in the ST, good intermediate predictions of the flow hydrodynamics can be obtained. The future simulation will employ, however, only the laminar flow equations in order to avoid the complexity introduced by a turbulent regime. In this way, the parameters due to turbulence such as the kinetic energy, rate of the kinetic energy dissipation, and the Reynolds stresses will not be computed but the new model could account for them in the terms called sources. The additional stresses (arising from turbulence) will be implemented as the source terms and these should well substitute the effects of turbulence at the higher Reynolds numbers. As mentioned, the boundary conditions derived in model 1 will be utilised as the initial conditions of a steady-state prediction and equations of the conservation of momentum will contain the mentioned source terms. This combination should generate good predictions in the entire bulk of the stirred tank and such predictions will offer the new boundary conditions in the impeller region obtained from the post-processing analysis of the solution. Moreover, the terms observed in turbulent flow will still be present and the modified Navier-Stokes equations will be implemented without additional empirical constants due to turbulence. The source terms will be based on the stresses measured experimentally and normalised by the square of rotational velocity of the impeller. In this way, a quite simple model built from the equations of the conservation of mass and modified equation of momentum should be sufficient for predictions of a large range of Reynolds number. This formulation of a stirred tank model will be free of any additional recourse to experiments and free of empirical constants used in the statistical turbulence. The model inputs for the sources

can be based on the results of present thesis. However, this kind of numerical simulation might introduce a problem of numerical instability.

- An interaction of hydrodynamics of the mixing reactor with chemical reactions can be better studied by using PDF methods. The reason is that such tools compute directly and without approximations the terms difficult to close. Thus, obtained results could be compared to the results of CFD simulations performed using the assumption of a perfectly mixed computational grid volume.

- Industrial needs appoint clearly to the models for semi-batch and continuous mixing processes. The extension of the present models for such purposes is straightforward and could be employed not only for the single-phase but also for multi-phase applications.

Literature References

- Ahlstedt, H., and Lahtinen, M., "Calculation of Flow Field in a Stirred Tank with Rushton Turbine Impeller", *3rd CFX International Users Conference*, 1-17 (1996).
- Angst, W., Bourne, J.R., and Dell'ava, P., "Mixing and Fast Chemical Reaction-IX: Comparison Between Models and Experiments", *Chem. Eng. Sci.*, **39**(2), 335-342 (1983).
- Angst, W., and Bourne, J.R., "Mixing and Fast Chemical Reaction-IV", *Chem. Eng. Sci.*, **37**(4), 585-590 (1982).
- Angst, W., Bourne, J.R., and Sharma, R.N., "Mixing and fast chemical reaction-V: Influence of Diffusion within the Reaction Zone on Selectivity", *Chem. Eng. Sci.*, **37**(8), 1259-1264 (1982).
- Armenante, P.M., Luo, Ch., Chou, Ch., Fort, J., and Medek, J., "Velocity Profiles in a Closed, Unbaffled Vessel: Comparison Between Experimental LDV Data and Numerical CFD Predictions", *Chem. Eng. Sci.*, **52**(20), 3483-3492 (1997).
- Bakker, A., Myers, K.J., Ward, R.W., and Lee, C.K., "The Laminar and Turbulent Flow Pattern of a Pitched Blade Turbine", *Trans IChemE*, **74**, 485-491 (1996).
- Bakker, A., and Van Den Akker, E. A., "Single-Phase Flow in Stirred Reactors", *Trans IChemE*, **72**, 583-593 (1994).
- Bakker, A., Laroche, R.D., Wang, M.H., and Calabrese, R.V., "Sliding Mesh Simulation of Laminar Flow in Stirred Reactors", *Trans IChemE*, **75**, 42-44 (1997).
- Bakker, A., and Fasano, J. B., "Time Dependent, Turbulent Mixing and Chemical Reaction in Stirred Tanks", *AIChE Symposium Series - Industrial Mixing Technology*, **90**(299), 71-77, 1994.

- Bakker, A., and Van Den Akker, E. A., "A Computational Study of Chemical Reactors on the Basis of Micromixing Models", *Trans IChemE*, **72**, 733-738 (1994).
- Baldyga, J., and Bourne, J.R., "Mixing and Fast Chemical Reaction-VIII: Initial Deformation of Material Elements in Isotropic, Homogeneous Turbulence", *Chem. Eng. Sci.*, **39**(2), 329-334 (1983).
- Baldyga, J., and Bourne, J.R., "A Fluid Mechanical Approach to Turbulent Mixing and Chemical Reaction-Part III, Computational and Experimental Results for the New Micromixing Model", *Chem. Eng. Commun.*, **28**, 259-281 (1984).
- Baldyga, J., and Bourne, J.R., "Simplification of Micromixing Calculations-I. Derivation and Application of New Model", *Chem. Eng. J.*, **42**, 83-92 (1989).
- Baldyga, J., "Turbulent Mixer Model with Application to Homogeneous, Instantaneous Chemical Reactions", *Chem. Eng. Sci.*, **44**(5), 1175-1182 (1989).
- Baldyga, J., and Bourne, J.R., "Some Consequences for Turbulent Mixing of Fine-Scale Intermittency", *Chem. Eng. Sci.*, **47**(15), 3943-3948 (1992).
- Baldyga, J., Bourne, J.R., and Yang, Y., "Influence of Feed Pipe Diameter on Mesomixing in Stirred Tank Reactors", *Chem. Eng. Sci.*, **48**(19), 3383-3390 (1993).
- Baldyga, J., and Bourne , J.R., "Comparison of Engulfment and IEM Micromixing Models", *Chem. Eng. J.*, **45**, 25-31 (1990).
- Baldyga, J., "A Closure Model for Homogeneous Chemical Reactions", *Chem. Eng. Sci.*, **49**(12), 1985-2003 (1994).
- Baudou, C., Xuereb, C., and Bertrand, J., "3-D Hydrodynamics Generated in a Stirred Vessel by a Multiple-propeller System", *Can. J. Chem. Eng.*, **75**, 653-663 (1997).
- Bates, R. L., Fondy, P. L., and Corpstein, R. R., "An Examination of Some Geometrical Parameters of Impeller Power", *Ind. Eng. Chem. Process Des. Dev.*, **2**(4), 310 (1963)
- Belevi, H., Bourne, J.R., and Rys, P., "Mixing and Fast Chemical Reaction-II: Diffusion-Reaction Model for the CSTR", *Chem. Eng. Sci.*, **36**(10), 1649-1654 (1981).
- Bell, W.A., "Spectral Analysis of Laser Velocimetry Data with the Slotted Correlation Method", *American Institute of Aeronautics and Astronautics -86-1102*, , 1-12 (1986).
- Benedict , L.H., and Gould, R.D., "Uncertainty Estimates for any Turbulence Statistics", *Proceedings of LDV Conference, Lisbon, Portugal*, (1996).
- Bird, R.B., Stewart, W.E., and Lightfoot, E.N., *Transport Phenomena*, John Wiley and Sons, New York, 1960.
- Bolzern, O., and Bourne, J.R., "Mixing and Fast Chemical Reaction-VI. Extension of the Reaction Zone", *Chem. Eng. Sci.*, **38**(7), 999-1003 (1983).
- Bourne, J.R., Kozicki, F., and Rys, P., "Mixing and Fast Chemical Reaction-I. Test Reactions to Determine Segregation", *Chem. Eng. Sci.*, **36**(10), 1643-1648 (1981).

- Bourne, J.R., Kozicki, F., Moergeli, U., and Rys, P., "Mixing and Fast Chemical Reaction-III: Model-Experiment Comparisons", *Chem. Eng. Sci.*, **36**(10), 1655-1663 (1981).
- Bourne, J.R., and Rohani, S., "Mixing and Fast Chemical Reaction-VII: Deforming-Reaction Zone Model for the CSTR", *Chem. Eng. Sci.*, **38**(6), 911-916 (1983).
- Bourne, J.R., and Hilber, C.P., "The Productivity of Micromixing-Controlled Reactions: Effect of Feed Distribution in Stirred Tanks", *Trans IChemE*, **68**(P.A), 51-56 (1990).
- Bourne, J.R., and Yu, S.Y., "Investigation of Micromixing in Stirred Tank Reactors Using Parallel Reactions", *Ind. Eng. Chem. Res.*, **33**(1), 41-55 (1994).
- Bourne, J.R., and Toor, H.L., "Simple Criteria for Mixing Effects in Complex Reactions", *AIChE J.*, **23**, 602-613 (1977).
- Bouwmans, I., Bakker, A., and Van Den Akker, H.E.A., "Blending Liquids of Differing Viscosities and Densities in Stirred Vessels", *Chem. Eng. Sci.*, **75**(A8), 777-783 (1997).
- Buchhave, P., George Jr., W.K., and Lumley, J.L., "The Measurement of Turbulence with the Laser-Doppler Anemometer", *Ann. Rev. Fluid Mech.*, **11**, 443-503 (1979).
- Calabrese, R.V., and Stoots, C.M., "Flow in the Impeller Region of a Stirred Tank", *Chem. Eng. Prog.*, 43-50 (1989).
- Chang, P.C., Mou, C.Y., and Lee, D.J., "Micromixing Effects in a Stirred Tank: The Random Replacement IEM Model", *Chem. Eng. Sci.*, **51**(11), 2601-2606 (1996).
- Ciofalo, M., Brucato, A., Grisafi, F., and Torraca, N., "Turbulent Flow in Closed and Free-Surface Unbaffled Tanks Stirred by Radial Impellers", *Chem. Eng. Sci.*, **51**(14), 3557-3573 (1996).
- Corrsin, S., "The Isotropic Turbulent Mixer", *AIChE J.*, **10**, 870-877 (1964).
- Curl, R.L., "Dispersed Phase Mixing: Theory and Effects in Simple Reactors", *AIChE J.*, **9**(2), 175-181 (1963).
- Cutter, L.A., "Flow and Turbulence in a Stirred Tank.", *AIChE J.*, **12**, 35-45 (1966).
- Distelhoff, M.F.W., Marquis, A.J., Nouri, J.M., and Whitelaw, J.H., "Scalar Mixing Measurements in Batch Operated Stirred Tanks", *Can. J. Chem. Eng.*, **75**, 641-652 (1997).
- Dong, L., Johansen , S. T., and Engh, T. A., "Flow Induced By an Impeller in an Unbaffled Tank-II. Numerical Modelling", *Chem. Eng. Sci.*, **49**(20), 3511-3518 (1994).
- Durst, F., Melling, A., and Whitelaw, J.H., *Principles and Practice of Laser-Doppler Anemometry* , Academic Press Inc., New York, 1976.
- Dutta, A., and Tarbell, J.M., "Closure Models for Turbulent Reacting Flows", *AIChE J.*, **35**(12), 2013-2027 (1989).

- Dyster, K.N., Koutsakos, E., Jaworski, Z., and Nienow, A.W., "An LDA Study of the Radial Discharge Velocities Generated by a Rushton turbine: Newtonian fluids, Re>5", *Trans IChemE*, **71**(A), 11-23 (1993).
- *FIDAP7.6 manuals*, FDI Inc., Evanston, IL, USA, 1991-1997.
- Fox, R.O., and Villermaux, J., "Unsteady-State IEM Model: Numerical Simulation and Multiple-Scale Perturbation Analysis Near Perfect-Micromixing Limit", *Chem. Eng. Sci.*, **45**(2), 373-386 (1990).
- Fox, R.O., and Grier, M.R., "Numerical Simulation of Turbulent Reacting Flows using PDF Methods", *AIChE Symposium Series*, **89**(293), 49-54, 1993.
- Fox, R.O., "Computation of Turbulent Reactive Flows: First-Principles Macro/Micromixing Models Using Probability Density Function Methods", *Chem. Eng. Sci.*, **47**(9), 2853-2858 (1992).
- Fox, R.O., "The Fokker-Plank Molecular Mixing Closure for PDF Modelling of Turbulent Flows", *AIChE Symposium Series*, **88**(286), 83-87 (1992).
- Fox, R. O., "Computational Methods For Turbulent Reacting Flows in the Chemical Process Industry", *Revue De L'Institut Français du Pétrole*, **51**(2), 215-243 (1996).
- Gao, F., and O'Brien, E.E., "Direct Numerical Simulations of Reacting Flows in Homogeneous Turbulence", *AIChE J.*, **37**(10), 1459-1470 (1991).
- Goetz, S., Sperling, R., Liepe, F., and Jembere, S., "Numerical Determination of the Three-Dimensional Velocity Distribution in a Baffled Pitched-Blade Impeller Stirred Vessel", *Chem. Eng.&Tech.*, **20**(9), 596-605 (1997).
- Guichardon, P., Falk, L., Fournier, M.C:, and Villermaux, J., "Study of Micromixing in a Liquid-Solid Suspension in a Stirred Reactor", *AIChE Symposium Series*, **91**(305), 123-130 (1995).
- Guichardon, P., Falk, L., and Villermaux, J., "Extension of a Chemical Method for the Study of Micromixing Process in Viscous Media", *Chem. Eng. Sci.*, **52**(24), 4649-4658 (1997).
- Gunkel, A.A., and Weber, M.E., "Flow Phenomena in Stirred Tanks, Part I&II", *AIChE J.*, **21**(5), 931-949 (1975).
- Hamill, I.S., Hawkins, I.R., Jones , I.P., Lo, S.M., and Splawski, B.A., "The Application of CFDS-FLOW-3D to Single and Multi-Phase Flows in Mixing Vessels", *AIChE J. - Unpublished*, 1-21 (1997).
- Hannon, J., "Modelling of Micromixing with Chemical Reaction in CFDS-FLOW3D", *AIChE Symposium Series* , **90**(299), 71-78 (1994).

- Harvey, P.S., and Greaves, M., "Turbulent Flow in an Agitated Vessel Part I: A Predictive Model & Part 2: Numerical Solution and Model Predictions", *Trans IChemE*, **60**, 195-210 (1982).
- Harvey III, A. D., L, Lee, C. K., Rogers, and S., "Steady-State Modelling and Experimental Measurement of a Baffled Impeller Stirred Tank", *AIChE J.*, **41**(10), 2177-2186 (1995).
- Hockey, R.M., and Nouri, J. M., "Turbulent Flow in a Baffled Vessel Stirred by a 60 degrees Pitched Blade Impeller", *Chem. Eng. Sci.*, **51**(19), 4405-4421 (1996).
- Hoogendoorn, C.J., and Den Hartog, A.P., "Model Studies on Mixers in the Viscous Flow Region", *Chem. Eng. Sci.*, **22**(1), 1689-1701 (1967).
- Jaworski, Z., Wyszynski, M.L., Moore, I.P.T., and Nienow, A.W., "Sliding Mesh CFD-A Predictive Tool in Stirred Tank Design", *Proceedings of the Institution of Mechanical Engineers, part E: Journal of Process Mechanical Eng.*, **211**(E3), 149-156 (1997).
- Kresta, S., and Wood, P.E., "Prediction of the Three-Dimensional Flow in Stirred Tanks", *AIChE J.*, **37**(3), 448-460 (1991).
- Le Lan, A., and Angelino, H., "Theoretical Study of the Power Consumption of a Radial Type Impeller ", *First European Conf. on Mixing and Centrifugal Separation*, **A2**, 11-21 (1974).
- Lee, K. C., and Yianneskis, M., "The Extent of Periodicity of the Flow in the Vessels Stirred by Rushton Impeller", *AIChE Symposium Series - 299*, **90**(299), 5-18 (1994).
- Lee, K. C., and Yianneskis, M., "Transient Temperature Measurements in a Stirred Vessel with Liquid Crystal Tracers", *ASME 2nd Biennial European Joint Conference*, 1-8 (1994).
- Lee, K. C., and Yianneskis, M., "A Liquid Crystal Thermographic Technique for the Measurements of Mixing Characteristics in Stirred Vessels", *Trans IChemE*, **75**(A), 746-754 (1997)
- Lee, K. C., and Yianneskis, M., "Turbulence Properties of the Impeller Stream of a Rushton Turbine", *AIChE J.*, **44**(1), 13-24 (1998).
- Letellier, C., Le Sceller, L., and Gouesbet, G., "Recovering Deterministic Behaviour from Experimental Time Series in Mixing Reactor", *AIChE J.*, **43**(9), 2194-2202 (1997).
- Li, K.T., and Toor, H.L, "Turbulent Reactive Mixing with a Series-Parallel Reaction: Effect of Mixing on Yield", *AIChE J.*, **32**(8), 1312-1320 (1986).
- Magnussen, B.F., and Hjertager, B.W., "On Mathematical Modelling of Turbulent Combustion with Special Emphasis on Soot Formation and Combustion", *16th Int. Symp. on Comb.*, 719-729 (1976).

- Mann, R., Togatorop, A., Senior, P.R., Graham, P., and Edwards, R.B., "Evaluating Mixing in Stirred Reactors by 3-D Visualisation", *Trans IChemE*, **75**(A8), 755-762 (1997).
- Manna, L., "Comparison Between Physical and Chemical Methods for the Measurement of Mixing Times", *Chem. Eng. J.*, **67**, 167-173 (1997).
- Mavros, P., Xuereb, C., and Bertrand, J., "Determination of 3-D Flow Fields in Agitated Vessels by Laser-Doppler Velocimetry: Effect of Impeller Type and Liquid Viscosity on Liquid Flow Patterns", *Trans IChemE*, **74**, 658-668 (1996).
- Mehta, R.V., and Tarbell, J.M., "An Experimental Study of the Effect of Turbulent Mixing on the Selectivity of Competing Reactions", *AIChE J.*, **33**(7), 1089-1101 (1987).
- Menon, R., and Larson, C., "Turbulence Measurements in Liquid Flows Using a Dedicated LDV System ", *TSI Inc. report*, (1987).
- Metzner, A.B., Feehs, R.H., Ramos, H.L., Otto, R.E., and Tuthill, J.D., "Agitation of Viscous Newtonian and Non-Newtonian Fluids", *AIChE J.*, **7**(1), 3-9 (1961).
- Middletton, J.C., Pierce, F., and Lynch, P.M., "Computations of Flow Fields and Complex Reaction Yield in Turbulent Stirred Reactors and Comparison with Experimental data", *Chem.Eng.Res.Des.*, **64**, 18-22 (1986).
- Montes, J.L., Boisson, H.C., Fort, I., and Jahoda, M., "Velocity Field Macro-Instabilities in an Axially Agitated Mixing Vessel", *Chem. Eng. J.*, **67**, 139-145 (1997).
- Moo-Young, M., Tichar, K., and Takahashi, F. A. L., "Blending Efficiencies of Some Impellers in Batch Mixing", *AIChE J.*, **18**, 178-182 (1972).
- Mujumdar, A.S., Huang, B., Wolf, D., Weber, M.E., and Douglas, W.J.M., "Turbulence Parameters in a Stirred Tank", *Can. J. Chem. Eng.*, **48**, 475-483 (1970).
- Natu, R.R., and Shenoy, U.V., "A New Micromixing Model for Turbulent Reactors", *Chem. Eng. Sci.*, **45**(8), 2147-2154 (1990).
- Oldshue, J. Y., "Heed This Advice in Scalling Up Mixers", *Chem. Eng. Prog.*, 70-73 (1997).
- Ottino, J.M, "Mixing and Chemical Reactions - A Tutorial", *Chem. Eng. Sci.*, **49**(24A), 4005-4027 (1994).
- Pericleous, K.A., and Patel, M.K., "The Modelling of Tangential and Axial Agitators in Chemical Reactors", *Phys.Chem.Hydrodynamics*, **8**, 105-123 (1987) .
- Pettersson, M., and Rasmuson, A.C., "Hydrodynamics of Suspensions Agitated by Pitched-Blade Turbine", *AIChE J.*, **44**(3), 513-527 (1998).
- Pinho, F.T., Piqueiro, F.M., Proenca, M.F., and Santos, A.M., "Power and Mean Flow Characteristics in Mixing Vessels Agitated by Hyperboloid Stirrers", *Can. J. Chem. Eng.*, **75**(5), 832-842 (1997).

- Pope, S.B., "PDF Methods for Turbulent Reactive Flows", *Prog. Energy Comb. Sci.*, **11**, 131-192 (1985).
- Ranade, V.V., and Joshi, J.B., "Flow Generated by Disc Turbine: Part I-Experimental", *Chem. Eng. Res. Des.*, **68**, 19-33 (1990).
- Ranade, V.V., and Joshi, J.B., "Flow Generated by Disc Turbine: Part II-Mathematical Modelling and Comparison with Experimental Data", *Chem. Eng. Res. Des.*, **68**, 34-50 (1990).
- Ranade, V. V., and Dommeti, S.M.S., "Computational Snapshot of Flow Generated By Axial Impellers in Baffles Stirred Vessels", *Trans IChemE*, **74**, 476-484 (1996).
- Ranade, V.V., "Efficient Computational Model for Simulating Flow in Stirred Vessels: A Case of Rushton Turbine", *Chem. Eng. Sci.*, **52**(24), 4473-4484 (1997).
- Ranade, V.V., and Bourne, J.R., "Reactive Mixing in Agitated Tanks", *Chem. Eng. Commun.*, **99**, 33-53 (1991).
- Ranade, V.V., Bourne, J.R., and Joshi, J.B., "Fluid Mechanics and Blending in Agitated Tanks", *Chem. Eng. Sci.*, **46**(8), 1883-1893 (1991).
- Ranade, V. V., "Decoupling of Micro- and Macromixing in Turbulent Reacting Flow", *AIChE J.*, **38**(3), 466-470 (1992).
- Reed, X. B., Princz, M., and Hartland, S., "Laser Doppler Measurements of Turbulence in a Standard Stirred Tank", *Proc. 2nd Eur. Conference on Mixing,* Cambridge, England, B1-B26 (1977).
- Ritchie, B.W., and Togby, A.M., "A Three-Environment Micromixing Model for Chemical Reactors with Arbitrary Separate Feedstreams", *Chem. Eng. J.*, **17**, 173-182 (1979).
- Rutherford, K., Lee, K. C., Mahmoudi, S. M. S., and Yianneskis, "Hydrodynamic Characteristics of Dual Rushton Impeller Stirred Vessels", *AIChE J.*, **42**(2), 332-346 (1996).
- Sachs, J. P., and Rushton, J. M., "Discharge Flow from Turbine-type Mixing Impellers", *Chem. Eng. Prog.*, **50**(12), 597-603 (1954).
- Schaefer, M., Hoefken, M., and Durst, F., "Detailed LDV Measurements for Visualisation of the Flow Field Within a Stirred-Tank Reactor Equipped with a Rushton Turbine", *Chem. Eng. Sci.*, **75**(A8), 729-736 (1997).
- Shames, I. H., *Mechanics of Fluids (third edition),* McGraw-Hill, New York, 1992.
- Shiue, S. J., and Wong, C. W., "Studies on Homogenisation Efficiency of Various Agitators in Liquid Blending", *Can. J. Chem. Eng.*, **62**, 602-609 (1984)
- Spalding, D. B., "Concentration Fluctuations in a Round Turbulent Free Jet", *Chem. Eng. Sci.*, **26**, 95-107 (1971).

- Speziale, C. G., "On Non-linear K-l and K-e Models of Turbulence", *J. Fluid Mech.*, **178**, 459-475 (1987).
- Stoots, C. M., and Calabrese, R. V., "Mean Velocity Field Relative to a Rushton Turbine Blade", *AIChE J.*, **41**(1), 1-11 (1995).
- Strizhak, P., Ali, F., and Menzinger, M., "Inhomogenities of CSTR on a Macroscale Due to Spatial Dependence of Micromixing Time -The BZ Reaction", *J. Phys. Chem.*, **102**(1), 188-191 (1998).
- Sturesson, C., Theliander, H., and Rasmuson, A., "An Experimental (LDA) and Numerical Study of the Turbulent Flow Behaviour in the Near Wall and Bottom Regions in an Axially Stirred Vessel", *AIChE Symposium Series - 305*, **91**, 102-114 (1995).
- Tatterson, G.B., *Fluid Mixing and Gas Dispersion in Agitated Tanks*, McGraw-Hill, 1991.
- Tennekes, H., and Lumley, J. L., *A First Course in Turbulence*, The MIT Press, 1972.
- Thoenes, D., *Chemical Reactor Development*, Kluwer Academic Publishers, Dodrecht, 1994.
- Thoma, S., Ranade, V.V., and Bourne, J.R., "Interaction Between Micro and Macro-Mixing during Reactions in Agitated Tanks", *Can. J. Chem. Eng.*, **69**, 1135-1141 (1991).
- Tiljander, P., Ronnmark, B., and Theliander, H., "Characterisation of Three Different Impellers using the LDV-Technique", *Can. J. Chem. Eng.*, **75**, 787-793 (1997).
- Togatorop, A., Mann, R., and Schofield, D. F., "An Application of CFD to Inert and Reactive Tracer Mixing in a Batch Stirred Vessel", *AIChE Symposium Series - 299*, **90**(299), 19-32 (1994).
- Toor, H.L., "Turbulent Mixing of Two Species with and without Chemical Reactions", *Ind. Eng. Chem. Fundamentals*, **8**(4), 655-659 (1969).
- Tsai, K., and Fox, R. O., "PDF Modelling of Turbulent Mixing and Chemical Reactions in a Tubular Jet Reactor", *AIChE Symposium Series - 305*, **91**(305), 31-38 (1995).
- Tsai, K., and Fox, R. O., "Modelling the Scalar Dissipation Rate for a Turbulent Series-Parallel Reaction", *Chem. Eng. Sci.*, **51**(10), 1929-1938 (1996).
- Tsai, K., and Fox, R. O., "PDF Simulation of a Turbulent Series-Parallel Reaction in an Axisymetric Reactor", *Chem. Eng. Sci.*, **49**(24B), 5141-5158 (1994).
- Tsai, K., and Fox, R. O., "PDF Modelling of Turbulent-Mixing Effects on Initiator Efficiency in a Tubular LDPE Reactor", *AIChE J.*, **42**(10), 2926-2939 (1996).
- *TSI manuals*, , TSI Inc., St.Paul, MN, USA, 1991.
- Uhl, V.W., and Gray, J.B., *Mixing: Theory and Practice I&II*, Academic Press Inc., New York, 1967.

- Van Der Molen, K., and Van Maanen, H.R.E, "Laser-Doppler Measurements of the Turbulent Flow in Stirred Vessels to Establish Scaling Rules", *Chem. Eng. Sci.*, **33**, 1161-1168 (1978).
- Van't Riet, K., Smith, J.M., and Bruijn, W., "Real and Pseudo-Turbulence in the Discharge Stream from a Rushton Turbine", *Chem. Eng. Sci.*, **31**, 407-412 (1976).
- Van't Riet, K., and Smith, J. M., "The Trailing Vortex System Produced by Rushton Turbine Agitators", *Chem. Eng. Sci.*, **30**, 1093-1105 (1975).
- Villermaux, J., and David, R., "Recent Advances in the Understanding of Micromixing Phenomena in Stirred Reactors", *Chem. Eng. Commun.*, **21**, 105-122 (1983).
- Villermaux, J., "Macro and Micromixing Phenomena in Chemical Reactors", *Chemical Reactor Design and Technology, NATO ASI Series, Serie E*, (10), 191-243.
- Villermaux, J., and Falk, L., "Recent Advances in Modelling Micromixing and Chemical Reaction", *Revue De L'Institut Français du Pétrole*, **51**(2), 205-213 (1996).
- Villermaux, J., and Devillon, J.C., "Representation de la coalescence et de la redispersion des domaines de segregation dans un fluide par un modele de interaction phenomenologique", *2nd Int. Symp. Chem. React. Eng.*, **B113** (1972).
- Villermaux, J., Falk, L., and Fournier, M.C., "Potential Use of a New Parallel Reaction System to Characterise Micromixing in Stirred Reactors", *AIChE Symposium Series - 299*, **90**(299), 50-54 (1994).
- Wang, D.M., and Tarbell, J.M., "Closure Models for Turbulent Reacting Flows with a Nonhomogeneous Concentration Field", *Chem. Eng. Sci.*, **48**(23), 3907-3920 (1993).
- Wang, Y.-D., and Mann, R., "Partial Segregation in Stirred Batch Reactors: Effect of Scale-up on the Yield of a Pair of Competing Reactions", *Trans IChemE*, **70**(A), 282-290 (1992).
- Webster's New College Dictionary, Houghton Mifflin Company, 1976
- Wu, H., and Patterson, G.K., "Laser-Doppler Measurements of Turbulent-Flow Parameters in a Stirred Mixer", *Chem. Eng. Sci.*, **44**(10), 2207-2221 (1989).
- Xu, Y., and McGrath, G., "CFD Predictions of Stirred Tank Flows", *Trans IChemE*, **74**, 471-475 (1996).
- Yianneskis, M., Popiolek, Z., and Whitelaw, J.H., "An Experimental Study of the Steady and Unsteady Flow Characteristics of Stirred Reactors", *J. Fluid Mech.*, **175**, 537-555 (1987).
- Zhou, G., and Kresta, S. M., "Distribution of Energy Between Convective and Turbulent Flow For Three Frequently Used Impellers", *Trans IChemE*, **74**, 379-389 (1996).
- Zhou, G., and Kresta, S. M., "Impact of Tank Geometry on the Maximum Turbulence Energy Dissipation Rate for Impellers", *AIChE J.*, **42**(9), 2476-2490 (1996).

A. Co-ordinate System Transformations

A.1 Transformation of Cartesian co-ordinate system

The transformation of the frame of reference, used in the LDV measurements (see Chapter3), into a different Cartesian co-ordinate system is described here. The choice of the measurement system shown in Figure A.1 was made using the rules based on the appropriate selection of the coincidence window (for details see Section 3.4.3) and on the technical limitations.

The measured data were transformed into the new co-ordinate system shown in Figure A.2 in order to compare the experimental results with those of the numerical simulation. The new co-ordinate system was used for the presentation of the results in Section 3.4.1 and can be obtained by a clockwise rotation of the measurement frame of reference followed by the horizontal flip.

The recalculation of measured data to the transformed frame of reference was made using the following relations:

$$\begin{aligned} \phi &= 5\pi/4 \\ X &= x\cos(\phi) + y\sin(\phi) \\ Y &= -x\sin(\phi) + y\cos(\phi) \\ U_t &= U_m\cos(\phi) + V_m\sin(\phi) \\ V_t &= -U_m\sin(\phi) + V_m\cos(\phi) \end{aligned} \tag{A.1}$$

where U_m and V_m are the velocities in the x and y directions of the frame of reference, while U_t, and V_t the are velocities in the X and Y directions of the transformed co-ordinate system, respectively.

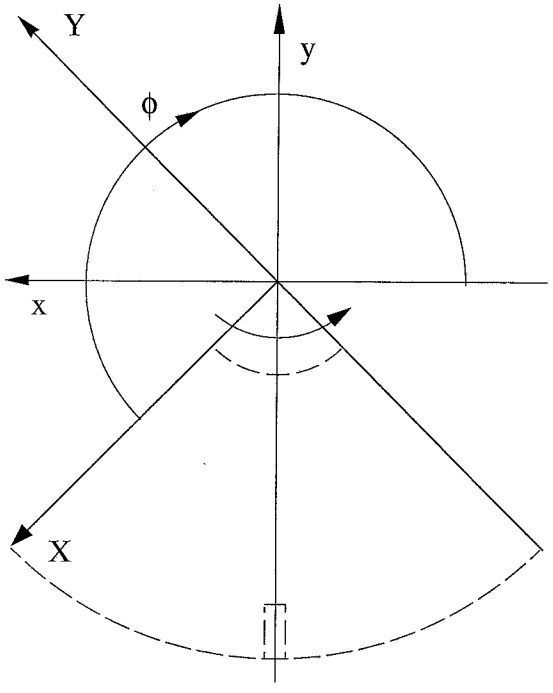

Figure A.1 Measurement frame of the reference used in LDV.

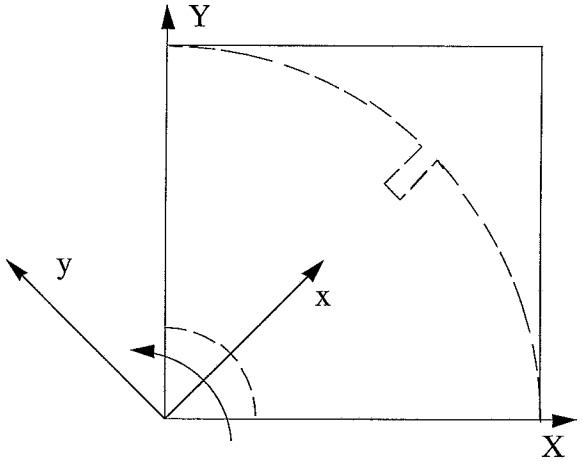

Figure A.2 Frame of reference for the presentation of results.

Applying the velocity decomposition into the mean and fluctuating parts of the velocity:

$$\begin{aligned} U_m &= \overline{U}_m + u_m; \quad V_m = \overline{V}_m + \upsilon_m \\ U_t &= \overline{U}_t + u_t; \; V_t = \overline{V}_t + \upsilon_t \end{aligned} \tag{A.2}$$

and using the heuristic rules known in the theory of turbulence, the Reynolds stress can be measured using the equation:

$$\overline{u_m \upsilon_m} = \overline{U_m V_m} - \overline{U}_m \overline{V}_m \tag{A.3}$$

It can be easily demonstrated, by using the vector transformations above that the Reynolds stress measured can be transformed as:

$$\begin{aligned} \overline{u_t^2} &= 1/2(\overline{u_m^2} + \overline{2u_m \upsilon_m} + \overline{\upsilon_m^2}) \\ \overline{\upsilon_t^2} &= 1/2(\overline{u_m^2} - \overline{2u_m \upsilon_m} + \overline{\upsilon_m^2}) \\ \overline{u_t \upsilon_t} &= 1/2(\overline{\upsilon_m^2} - \overline{u_m^2}) \end{aligned} \tag{A.4}$$

and the standard deviations from the mean velocities in each direction can be expressed as:

$$\begin{aligned} \sigma_{U_m} &= \sqrt{\overline{u_m^2}}; \quad \sigma_{V_m} = \sqrt{\overline{\upsilon_m^2}} \\ \sigma_{U_t} &= \sqrt{\overline{u_t^2}}; \; \sigma_{V_t} = \sqrt{\overline{\upsilon_t^2}} \end{aligned} \tag{A.5}$$

where $x, y, \overline{U}_m, \overline{V}_m, \sigma_{U_m}, \sigma_{V_m}, \overline{u_m \upsilon_m}$ are values obtained in the measurement frame of reference and these are transformed into $X, Y, \overline{U}_t, \overline{V}_t, \sigma_{U_t}, \sigma_{V_t}, \overline{u_t \upsilon_t}$ on the new frame of reference.

A.2 Transformation to cylindrical co-ordinate system

The results in Sections 3.4.1 and 3.4.2 were presented in the cylindrical co-ordinate system. The measurement-Cartesian and the transformed-cylindrical system share the same origin, as shown in Figure A.3 and their co-ordinates are related by:

$$\begin{aligned} r^2 &= x^2 + y^2 \\ \theta &= \arcsin\left(\frac{y}{r}\right) \end{aligned} \tag{A.6}$$

where r and θ are the radial and tangential co-ordinates of the cylindrical system.

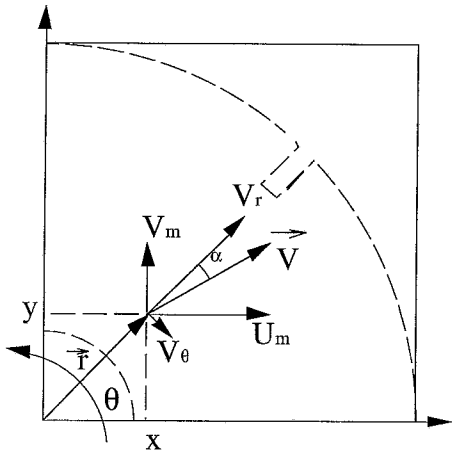

Figure A.3 Cylindrical frame of reference.

The vector, $\vec{r}$, of the system origin and the measured point is called the directional vector. The angle, α, between the directional and the velocity vector $\vec{V}$, can be calculated from:

$$\begin{aligned}
\vec{V} &= U_m{}^2 + V_m{}^2 \\
\vec{V} &= \overline{\vec{V}} + \vec{v} \\
\alpha &= a\cos\left(\frac{xU_m + yV_m}{|\vec{r}||\vec{V}|}\right) \\
V_r &= \left|\overline{\vec{V}}\right|\cos\alpha \\
V_\theta &= \left|\overline{\vec{V}}\right|\sin\alpha
\end{aligned} \tag{A.7}$$

where $\vec{V}$ is the velocity vector and V_r and V_θ are the radial and tangential velocity, respectively. Applying the velocity decomposition to both of the velocities results into:

$$\begin{aligned}
V_r &= \overline{V}_r + v_r \\
V_\theta &= \overline{V}_\theta + v_\theta
\end{aligned} \tag{A.8}$$

The transformations of the normal and tangential stresses can be accomplished in a similar way as the transformation of the Reynolds stress between the two Cartesian systems, and then can be written:

$$\begin{aligned}
\overline{v_r^2} &= \left|\overline{U_m}^2 + \overline{u_m^2} + \overline{V_m}^2 + \overline{v_m^2}\right|\overline{\cos^2\alpha} - \overline{V_r}^2 \\
\overline{v_\theta^2} &= \left|\overline{U_m}^2 + \overline{u_m^2} + \overline{V_m}^2 + \overline{v_m^2}\right|\overline{\sin^2\alpha} - \overline{V_\theta}^2 \\
\overline{v_r v_\theta} &= \left|\overline{U_m}^2 + \overline{u_m^2} + \overline{V_m}^2 + \overline{v_m^2}\right|\overline{\sin\alpha\cos\alpha} - \overline{V_r}\ \overline{V_\theta}
\end{aligned} \tag{A.9}$$

Note that the angle α is calculated from the mean and fluctuating velocities by:

$$\alpha = a\cos\frac{x(\overline{U}_m + \sqrt{\overline{u_m^2}}) + y(\overline{V}_m + \sqrt{\overline{v_m^2}})}{\left|\sqrt{x^2+y^2}\right|\left|\sqrt{\left(\overline{U_m}^2 + \overline{V_m}^2\right) + \left(\overline{u_m^2} + \overline{v_m^2}\right)}\right|} \tag{A.10}$$

B. Elimination of the periodic turbulence

This appendix describes the LDV data processing in order to eliminate the contribution of pseudo-turbulence from the total turbulence. Simultaneous measurements of two velocities in the $x-y$ plane were performed using the coincidence mode of LDV data acquisition. As noted in some previous works published in the literature (ex. Van't Riet, 1976; Wu and Patterson, 1989), the data near the impeller consists from the periodic and random parts where the periodic part is caused by regular passages of the blades of the impeller. Then, the measured turbulence quantity, q_{total}, can be decomposed in two parts:

$$q_{total} = q_{periodic} + q_{random} \tag{B.1}$$

The periodic contribution can be eliminated by using the angle-resolved measurements as described by Yianneskis *et al.* (1989) or Stoots and Calabrese (1995). This technique was not used in the present LDV experiments. Thus, the data measured near the impeller were affected by the pseudo-turbulence that diminished in the regions far away from the impeller. In the present work, the periodic contribution of pseudo-turbulence was removed from the total turbulence using the high-pass filtering and the low frequencies corresponding to the impeller rotational frequency and its multiple were filtered out.

LDV measurement is complicated by the nature of the velocity signal that originates from the random arrivals of particles to the LDV measurement volume. Therefore, a special treatment must be taken in the statistical analysis of LDV data. The method of Bell (1986) uses the random correlation in which the estimate of the correlation function is computed by a special slotting technique and the disadvantage of a non-uniform time interval between the data obtained is resolved as it follows. The time of data acquisition in a measured location is divided into the "n-slots"(see FigureB.1a) and the two successive velocities are multiplied. The time difference between successive velocity data is determined and placed into the slot best representing this difference (see Figure B.1a). The average value of all multiples of successive velocity data found in each slot is calculated at the end. The averaged values are placed at the slot centre as the estimate of a correlation function (see Figure B.1b).

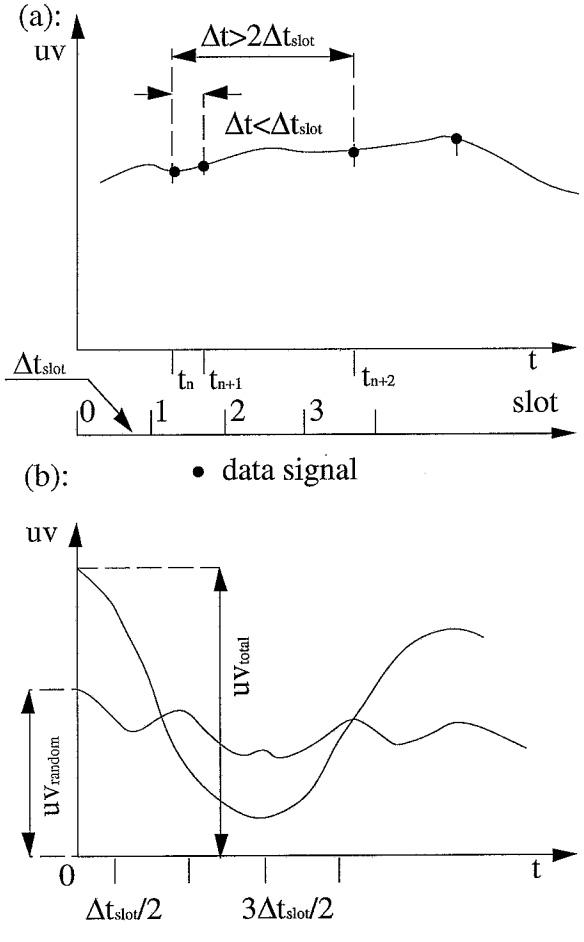

Figure B.1 (a) Principle of the slotting technique; (b): The R(uv) correlation function

The slotting technique was performed here using a Pascal program where the time range corresponding to the one slot is calculated as:

$$\Delta t = \frac{t_{last} - t_{first}}{\text{number of points in range}} \tag{B.2}$$

and the maximum spectrum frequency, $F\max$, by:

$$F\max = \frac{1}{2\Delta t} \tag{B.3}$$

The FFT — Fast Fourier Transformation — from the correlation function estimate (using $N_{pts} = 8192$) offers the frequency spectra. By data filtering using the high-pass filter, the random contribution of a required total turbulence quantity can be separated. The filtered data are then converted back using the inverse FFT to the correlation function (see Figure B.3). The amplitude of the new correlation at a zero time can be expressed as the covariance of two velocity fluctuations, $\overline{uv}_{random}$, which represents the statistical quantity desired.

Data from the correlation technique were filtered in the LabView 2.0 software. The block diagram of data filtering is shown in Figure B.2. The front panel and the $\overline{UV}$-correlation plots are displayed in Figure B.3. Two successive high-pass filters (Chebyshev) were used to filter out frequencies smaller than the double of the blade frequency, F_b. The blade frequency, as can be seen at the plot "power spectra before", exhibits the highest magnitude at the frequency about $F \approx 3Hz$, corresponding to the $N/6$ of the impeller rotational frequency, $N = 0.5Hz$. As reported by Wu and Patterson (1989), the first two components of the Fourier series should be removed (up to double of the blade frequency). The frequency range for the filter was slightly larger than double of the blade frequency in order to remove all the adjusted range.

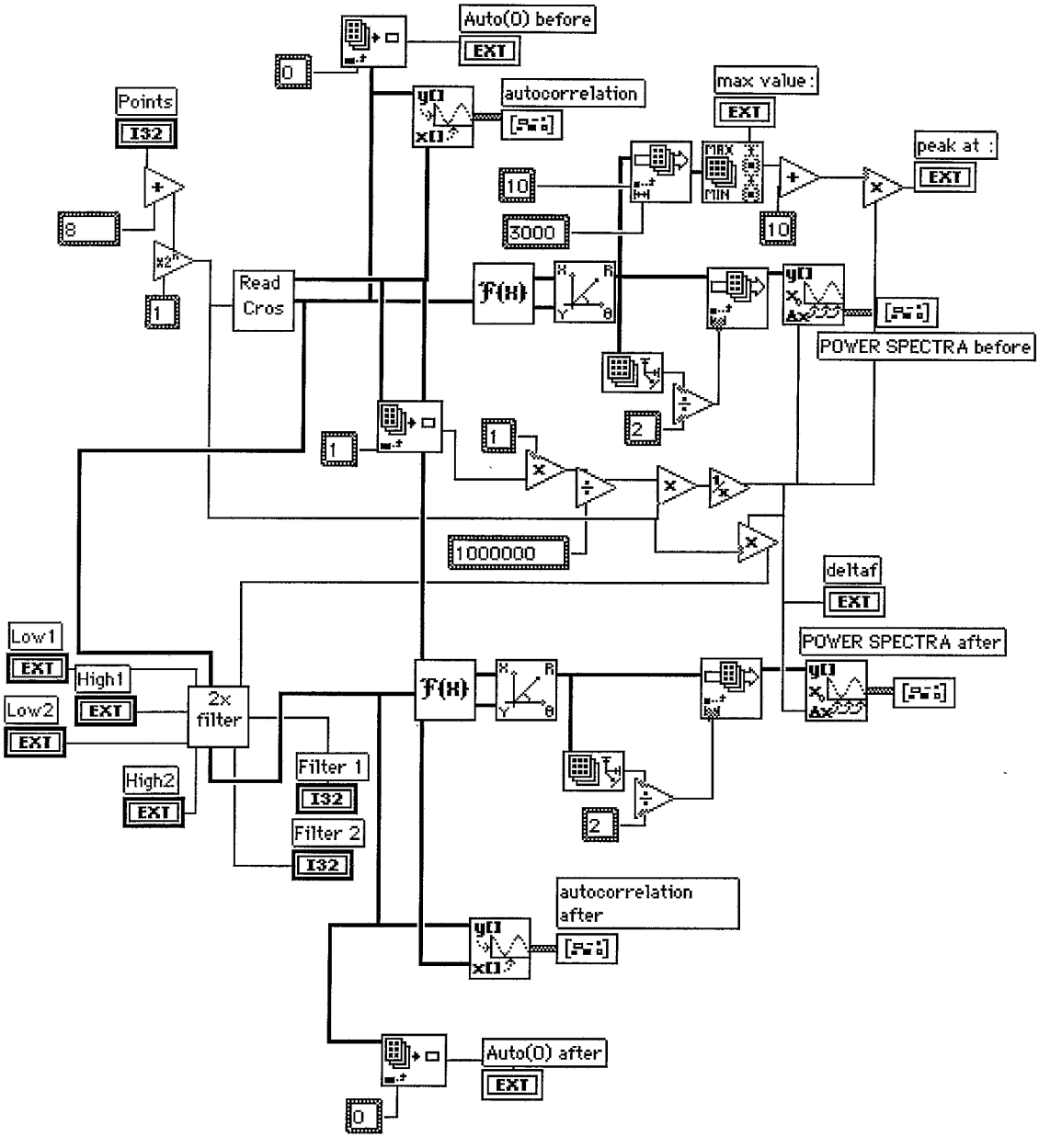

Figure B.2 Block diagram of LDV data filtering using LabView software.

All points measured at r/R =1.1 were filtered twice in order to eliminate the frequencies smaller than $7Hz$. This range of frequency allowed the removal of the two highest frequency peaks (the first at around $F \approx 3Hz$ and the second at $F \approx 6Hz$). The desired random variable is provided by the value of the correlation function at the zero time after filtering (Figure B.3):

$$R_{uv}(0) = \overline{u_m v_m} = \overline{U_m V_m} - \overline{U}_m\ \overline{V}_m = \overline{\left(U_m - \overline{U}_m\right)\left(V_m - \overline{V}_m\right)} \qquad \text{(B.4)}$$

The amplitude of a sine like curve corresponds to the total covariance of the $\overline{UV}$ quantity, while the smaller amplitude represents the filtered correlation and the random part of the covariance, $\overline{(u_m v_m)}_{random}$.

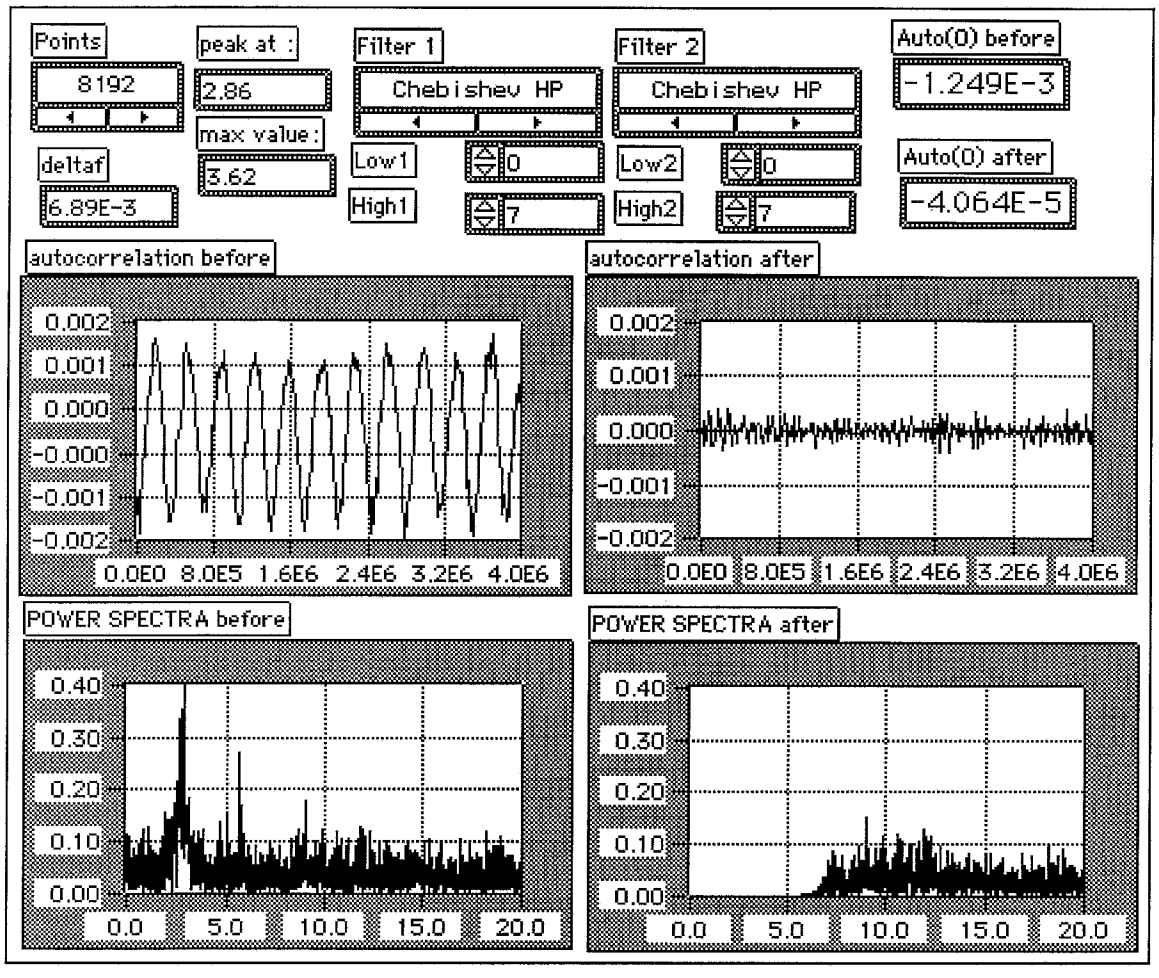

Figure B.3. Front panel of LDV data filtering using LabView software.

C.The Closure Problem in Turbulent Flow and Speziale's Non-Linear Model

C.1 Description of the closure problem for turbulent flow

The equation of momentum conservation for the flow under laminar regime is given by:

$$\frac{\partial U_i}{\partial t}+\frac{\partial}{\partial x_j}\left(U_iU_j\right)=-\frac{1}{\rho}\frac{\partial p}{\partial x_i}+\frac{\partial}{\partial x_j}\left(\nu\frac{\partial U_i}{\partial x_j}\right) \tag{C.1}$$

where the U_i is the velocity component in the i direction of Cartesian co-ordinate system, p is the pressure, ν is the kinematic viscosity and ρ is the fluid density. Equation C.1 is written using the double-index scheme where the indexes i and j represent two orthogonal directions of the co-ordinate system. This scheme allows a simple description of the complete system of equations and that for the x direction is given by:

$$\frac{\partial U}{\partial t}+\frac{\partial}{\partial y}(UV)=-\frac{1}{\rho}\frac{\partial p}{\partial x}+\frac{\partial}{\partial y}\left(\nu\frac{\partial U}{\partial y}\right) \tag{C.2}$$

where U is the velocity in the x direction $(i=x)$, V is the velocity in the y direction $(j=y)$ and V_z is the axial velocity in the z direction of Cartesian co-ordinate system. The first term on the left side in Equations C.1 and C.2 means a temporal change of momentum for the balanced volume element and the second term denotes the momentum convection into a

volume of considered element. The terms on the right-hand side of Equations C.1 and C.2 express the changes in the volume element by the pressure and the viscous forces acting on this element, respectively.

The stresses can be written by repeated indexes ($ii;ij;jj$), where the first index indicates the normal direction to the considered plane and the second denotes direction in the Cartesian system. For example, the shear stress is written by mixed indices while the normal stress by two identical indices.

The variables in the statistical turbulence are decomposed onto the mean and the fluctuating parts:

$$U_i = \overline{U_i} + u_i \quad \text{and} \quad P = \overline{P} + p \tag{C.3}$$

where U_i and P stand for the instantaneous velocity and the instantaneous pressure, respectively. For the Cartesian co-ordinate system using the $x;y;z$ co-ordinates, the mean velocities are denoted by $\overline{U};\overline{V};\overline{V}_z$ while the fluctuation components by $u;v;w$.

Equation of momentum conservation for turbulent flow is given by introducing Equation C.3 into Equation C.1 and the linear terms have the form:

$$\overline{\frac{\partial U_i}{\partial x_i}} = \frac{\partial}{\partial x_i}\overline{(\overline{U_i} + u_i)} = \frac{\partial \overline{U_i}}{\partial x_i} \tag{C.4}$$

Since the time-average of the fluctuating velocity is zero by definition (Tennekes and Lumley, 1972) the second term in the parenthesis in Equation C.4 can be dropped out. As can be seen, the linear terms do not cause problems but the additional term arises for the non-linear term:

$$\overline{\frac{\partial (U_i U_j)}{\partial x_j}} = \frac{\partial}{\partial x_j}\overline{\left[(\overline{U_i} + u_i)(\overline{U_j} + u_j)\right]} = \frac{\partial}{\partial x_j}\overline{\left[\overline{U_i}\,\overline{U_j} + u_i u_j\right]} = \frac{\partial}{\partial x_j}(\overline{U_i}\,\overline{U_j} + \overline{u_i u_j}) \tag{C.5}$$

Then, the time-averaged equation of momentum conservation for turbulent flow can be written as:

$$\frac{\partial \overline{U_i}}{\partial t} + \frac{\partial}{\partial x_j}(\overline{U_i}\,\overline{U_j}) = -\frac{1}{\rho}\frac{\partial \overline{P}}{\partial x_i} + \frac{\partial}{\partial x_j}\left(\nu \frac{\partial \overline{U_i}}{\partial x_j}\right) - \frac{\partial}{\partial x_j}(\overline{u_i u_j}) \tag{C.6}$$

The last term on the right-hand side of Equation C.6 is additional in comparison with Equation C.1 and it is called the Reynolds stress.

Three equations of the momentum conservation (see Equation C.2) are available for turbulent flow plus the one equation of the mass conservation given as:

$$\frac{\partial U_i}{\partial x_i} = 0 \tag{C.7}$$

These four equations (three times Equation C.2 plus Equation C1.7) contain ten unknown variables (three velocities, pressure and six Reynolds stresses). The Reynolds stress tensor consists of nine terms but only six of them are unknown because the terms with mixed indices are equivalent (i.e., $\overline{uv} = \overline{vu}$). These unknown terms are not closed and this situation is often reported as the *closure problem.*

There are various possibilities to resolve the closure problem. The first most known possibility is referred as the eddy viscosity concept. This concept is based on the assumption of isotropic flow behaviour and on an analogy between the viscous stress and the Reynolds stress. From dimensional analysis the Reynolds stress is given by:

$$\overline{u_i u_j} = -\nu_t\left(\frac{\partial \overline{U}_i}{\partial x_j} + \frac{\partial \overline{U}_j}{\partial x_i}\right) + \frac{2}{3}\rho k \delta_{ij} \tag{C.8}$$

where $\nu_t = \mu_t / \rho$ is the eddy or turbulent viscosity, k is the turbulent kinetic energy and δ_{ij} is the Oldroyd derivative. By applying dimensional analysis and assuming a similarity between the turbulent and the molecular viscosity, can be written:

$$\nu_t \propto \frac{k^{1/2}}{L_s} \Rightarrow \nu_t = c_\mu \frac{k^{3/2}}{\varepsilon} \tag{C.9}$$

where L_s is the characteristic macro-scale of turbulent flow, ε is the rate of kinetic energy dissipation and c_μ is a model constant. To close the Reynolds stresses, two additional variables: k and ε are introduced, and additional equations must be written for them. The transport equation for the turbulent kinetic energy is given as:

$$\frac{\partial k}{\partial t} + \frac{\partial \overline{U}_j k}{\partial x_j} = \nu_t\left(\frac{\partial \overline{U}_i}{\partial x_j} + \frac{\partial \overline{U}_j}{\partial x_i}\right)\frac{\partial \overline{U}_i}{\partial x_j} + \frac{\partial}{\partial x_j}\left(\frac{\nu_t}{\sigma_k}\frac{\partial k}{\partial x_j}\right) - \varepsilon \tag{C.10}$$

while k and ε can be expressed by:

$$k = \frac{1}{2}\overline{u_i u_j} \tag{C.11}$$

$$\varepsilon = \nu \overline{\frac{\partial u_i}{\partial x_k} \frac{\partial u_j}{\partial x_k}} \tag{C.12}$$

The simplified form of the transport equation for the rate of kinetic energy dissipation is expressed using the production term, P_t, as:

$$\frac{\partial \varepsilon}{\partial t} + \frac{\partial}{\partial x_j} \overline{U}_j \varepsilon = \frac{\partial}{\partial x_j} \left(\frac{\nu_t}{\sigma_\varepsilon} \frac{\partial \varepsilon}{\partial x_j} \right) + c_1 \frac{\varepsilon}{k} P_t - c_2 \frac{\varepsilon^2}{k} \tag{C.13}$$

The closure problem can be solved now, because there are thirteen equations (Equation C.7; three times of Equation C.6; six times Equation C.8 for the Reynolds stresses; Equation C.9, plus Equation C.10 and Equation C.13 for the kinetic energy and energy dissipation, respectively) for thirteen variables $(\overline{U}, \overline{V}, \overline{V}_z, \overline{p}, \overline{uu}, \overline{uv}, \overline{uw}, \overline{vv}, \overline{vw}, \overline{ww}, k, \varepsilon, \nu_t)$. The shortcoming is that within the available Equations C.6 through C.13, there are five constants that must be supplied to the model. These constants have a semi-empirical nature and the most often used set of constants was validated on various cases of turbulent flow (see Chapters 4 and 5).

The isotropic $k-\varepsilon$ model is inadequate for many situations of scientific interest. More realistic solutions can be obtained using the second-moment closures where each Reynolds stress is solved by the transport equation similar to those for k and ε variables. Moreover, these methods reflect reality where the Reynolds stresses are generated, dissipated, and transported at different length-scales. The transport equation for the Reynolds stresses can be derived:

$$\begin{aligned} \frac{\partial}{\partial t} \overline{u_i u_j} + \frac{\partial}{\partial x_k} (\overline{U_k}\, \overline{u_i u_j}) &= -(\overline{u_i u_k} \frac{\partial \overline{U_j}}{\partial x_k} + \overline{u_j u_k} \frac{\partial \overline{U_i}}{\partial x_k}) \\ &- \frac{\partial}{\partial x_k} \left[\overline{u_i u_j u_k} + \overline{\frac{p}{\rho}(u_i \delta_{ik} + u_j \delta_{ik})} - \nu \frac{\partial}{\partial x_k} (\overline{u_i u_j}) \right] + \overline{\frac{p}{\rho} (\frac{\partial u_i}{\partial x_j} + \frac{\partial u_j}{\partial x_i})} - 2\nu \overline{\frac{\partial u_i}{\partial x_k} \frac{\partial u_j}{\partial x_k}} \end{aligned} \tag{C.14}$$

where the terms on the left side represent the unsteady term and the convection by mean flow. The first term on the right-hand side of Equation C.14 means the production of Reynolds stress by the mean strain. The second term on the right side consists of diffusion of the Reynolds stress by turbulence, pressure and viscous effects. The third term on the right side denotes the pressure-strain interactions and the last term on the right side is the viscous destruction of Reynolds stress.

However, these equations also need some approximations for unknown (triple) correlation and another disadvantage is that they also contribute to higher computational and time expenses to obtain the slotution.

A different option relative to the isotropic turbulence models and the second order closures is to account for the effects of anisotropy, and it means an extension of Equation C.8 with additional terms. These closures are called non-linear and contain some additional terms. They are higher order function of the strain rate and the Speziale's model (1978) is an example that is briefly described in next section.

C.2 The Reynolds stress equation in non-linear Speziale's model of turbulent flow

The Reynolds stress reported in Chapter 5was predicted using this equation:

$$-\rho\overline{u_i u_j} = -\frac{2}{3}\rho k\delta_{ij} + 2\mu_t s_{ij} + 4c_{sp}c_\mu \frac{k}{\varepsilon}\mu_t(s_{ik}s_{kj} + \dot{s}_{ij} - \frac{1}{3}(s_{mn}s_{mn} + \dot{s}_{mm})\delta_{ij})$$
$$\dot{s}_{ij} = -\frac{\partial u_i}{\partial x_k}s_{kj} - \frac{\partial u_j}{\partial x_k}s_{ki} \qquad \text{(C.15)}$$

Note that the second term on the right side represents a linear dependence on the strain rate and is identical to that used in the aforementioned standard k-ε model. Additional terms on the right-hand side of Equation C.15 sign represent a higher-order dependence on the flow variables that are known. The advantage of this model is that it contains only the one model constant, c_{sp}, more than the standard k-ε model.

The shear Reynolds stress, τ_{xy}^t, was studied in Chapter 5 and measured in Chapter 3 at the plane passing through the impeller centre. Since the axial velocity and its derivations at this plane was negligible, Equation C.15 can be rewritten into:

$$-\rho\overline{uv} = \mu_t\left(\frac{\partial U}{\partial y} + \frac{\partial V}{\partial x}\right) - 4c_{sp}c_\mu \frac{k}{\varepsilon}\mu_t \left[\begin{array}{l} \left(\frac{\partial U}{\partial x}\frac{\partial V}{\partial x} + \frac{\partial U}{\partial y}\frac{\partial V}{\partial y} + \frac{3}{4}\frac{\partial U}{\partial z}\frac{\partial V}{\partial z}\right) \\ -\frac{1}{4}\left(\frac{\partial V_z}{\partial x}\frac{\partial V_z}{\partial y} - \frac{\partial U}{\partial z}\frac{\partial V_z}{\partial y} - \frac{\partial V}{\partial z}\frac{\partial V_z}{\partial x}\right) \end{array}\right] \qquad \text{(C.16)}$$

Then Equation C.16 can be simplified using some mathematical manipulations into:

BIBLIOTECA F.E. PORTO

$$-\rho\overline{uv} = \mu_t\left(\frac{\partial U}{\partial y}+\frac{\partial V}{\partial x}\right)-4c_{sp}c_\mu\frac{k}{\varepsilon}\mu_t\left(\frac{\partial U}{\partial x}\frac{\partial V}{\partial x}+\frac{\partial U}{\partial y}\frac{\partial V}{\partial y}\right) \tag{C.17}$$

Finally, Equation C.17 was implemented into FIDAP 7.6 package as a FORTRAN subroutine for the computation of studied shear Reynolds stress.

FACULDADE DE ENGENHARIA
UNIVERSIDADE DO PORTO
BIBLIOTECA
0000043759

FACULDADE DE ENGENHARIA

Rua dos Bragas 4099 PORTO CODEX PORTUGAL
Telef.: 351 2 323201 • Fax: 351 2 319280 • Telex: 27323 FEUP P